

Cerebral Venous Blood Volume:
Methodology for In Vivo Measurement and
Implications for BOLD fMRI

Jing Jean Chen, M. Sc.
Department of Biomedical Engineering
McGill University, Montreal, Canada

March 10, 2009

A thesis submitted to McGill University in partial fulfillment of the
requirements for the degree of Doctor of Philosophy

© Jing Jean Chen, 2009

Table of Contents

List of Figures	vii
List of Tables	ix
Acknowledgments	xi
Contributions of Authors	xiii
Other Publications	xv
List of Abbreviations and Symbols	xvii
Abstract	xix
Résumé	xxi
Original Contributions	xxiii
Chapter 1 Introduction	1
Chapter 2 Background	5
2.1 Functional Physiology	6
2.1.1 Neuronal Activation	7
2.1.2 Cerebral Vasculature	9
2.1.3 Neurovascular Coupling	11
2.2 Blood Properties and Physiology	13
2.3 BOLD Contrast Mechanisms and Measurement	15
2.3.1 The BOLD Effect	15
2.3.2 BOLD Contrast Mechanisms	17
2.3.3 Measurement of BOLD	19
2.3.4 Detection of BOLD	21
2.4 CBF Measurement	23
2.5 CBV Measurement	26
2.6 CMRO ₂ Measurement and BOLD Modeling	30
2.7 BOLD Signal Dynamics	34
2.8 High-field Imaging	37
2.8.1 Relaxation Characteristics	38
2.8.2 SNR and RF Characteristics	39
2.8.3 Functional MRI	40
Chapter 3 Deoxygenation-Induced Transverse Relaxation Effects in Blood at 3 Tesla ...	43
3.1 Preface	43
3.2 Abstract	46
3.3 Introduction	47
3.4 Theory	48
3.5 Methods	49
3.6 Results	51
3.7 Discussion	56
3.8 Acknowledgments	58

Chapter 4	Development of VERVE at 3 Tesla	59
4.1	Tissue T_2 Relaxometry at 3 T	59
4.1.1	Background	59
4.1.2	Methods	61
4.1.2.1	MR Acquisition	61
4.1.2.2	Data Analysis	63
4.1.3	Results	65
4.1.4	Discussion	67
4.2	Blood T_1 Relaxometry	68
4.2.1	Background	68
4.2.2	Methods	68
4.2.2.1	MRI Acquisition	68
4.2.2.2	Data Processing	70
4.2.3	Results	70
4.2.4	Discussion	71
4.3	Gradient-Echo BOLD Effects in VERVE	73
4.3.1	Background	73
4.3.2	Results	75
4.4	Spin-Echo BOLD Effects in VERVE	78
4.4.1	Sensitivity to the $\Delta\text{CBF}-\Delta\text{CMR}_{\text{O}_2}$ Ratio	79
4.4.2	Sensitivity to Baseline Venous Oxygenation	81
4.4.3	Sensitivity to the Resting State CBV_v and ΔCBV_v Fractions	82
4.5	VERVE Parameter Optimizations	84
4.5.1	Field Inhomogeneities	84
4.5.2	Contrast and Noise	86
4.5.3	Power Deposition and SNR	88
4.5.4	Cerebral Spinal Fluid Suppression	90
4.5.5	Summary	91
Chapter 5	BOLD-Specific Flow-Volume Relationship during Neuronal Activation	93
5.1	Preface	93
5.2	Abstract	96
5.3	Introduction	97
5.4	Materials and Methods	99
5.4.1	MRI Acquisition	99
5.4.1.1	Venous CBV Measurement	99
5.4.1.2	CBF Measurement	101
5.4.2	Stimulation Paradigm	102
5.4.3	Data Processing	102
5.4.4	Simulations	104
5.5	Results	105
5.6	Discussion	110
5.7	Acknowledgments	115
Chapter 6	Contributions to the Post-Stimulus BOLD Undershoot	117
6.1	Preface	117
6.2	Abstract	120
6.3	Introduction	121

6.4	Materials and Methods.....	123
6.4.1	Stimulation Paradigm.....	123
6.4.2	MRI Acquisition	124
6.4.3	Data Analysis	125
6.4	Results and Discussion	127
6.5.1	Results.....	127
6.5.2	Discussion.....	133
6.5.2.1	CBF Post-Stimulus Undershoot.....	134
6.5.2.2	Venous Compliance	135
6.5.2.3	BOLD Post-Stimulus Response.....	137
6.6	Acknowledgments.....	141
Chapter 7	Conclusions.....	143
7.1	Summary	143
7.2	Future Work.....	145
Appendix I	Ethics Approval for Human Studies	149
Appendix II	Whole Human Blood T ₂ Relaxometry Supplementary Material.....	153
A2.1	Blood T ₂ Variations with Elapsed Time	153
A2.2	Cross-Validation of T ₂ Relaxometry Methodology.....	154
A2.3	In Vivo Blood Water Diffusion Coefficient	156
Appendix III	ASL and PET Cross-Validation of Cerebral Blood Flow Measurement ..	159
A3.1	Preface.....	159
A3.2	Abstract.....	162
A3.3	Introduction.....	163
A3.4	Methods and Materials.....	166
A3.4.1	Experimental design.....	166
A3.4.2	Magnetic resonance imaging	167
A3.4.3	Positron emission tomography.....	168
A3.4.4	Data analysis	171
A3.5	Results.....	174
A3.5.1	Physiological monitoring.....	174
A3.5.2	Regions of interest (ROI).....	174
A3.5.3	Activation time-course.....	175
A3.5.4	FAIR vs. PET.....	177
A3.5.5	Correlation analysis	179
A3.6	Discussion	180
A3.7	Acknowledgments.....	184
Bibliography	185

List of Figures

Figure 1.1	Brodmann's cytoarchitonic map of the adult human brain.....	2
Figure 2.1	Vascularization varies across the cortical layers.....	5
Figure 2.2	Schematic of excitatory process.....	6
Figure 2.3	Cerebral ATP consumption.....	7
Figure 2.4	The cerebral vasculature.	10
Figure 2.5	Schematic of a red blood cell.....	14
Figure 2.6	BOLD signal and underlying neuronal activity.	16
Figure 2.7	The human cerebral microvascular composition.	17
Figure 2.8	The magnetic field disturbance produced by a blood vessel.	18
Figure 2.9	Gradient- and spin-echo BOLD contrast.	20
Figure 2.10	Sequence diagram for simultaneous BOLD and CBF acquisition.....	25
Figure 2.11	Gradient-echo BOLD and MION imaging of activation.	28
Figure 2.12	CBV measurements by MION and VASO.	29
Figure 2.13	The deoxy-hemoglobin dilution model.....	32
Figure 2.14	Generation of BOLD transient response by the Balloon Model.....	35
Figure 2.15	Positive and negative BOLD responses in the primate visual cortex.	36
Figure 2.16	The relative specific absorption rate (SAR) for turbo spin-echo.....	37
Figure 2.17	Spin-echo BOLD sensitivity variation with field strength.....	40
Figure 2.18	BOLD contrast variation with field strength.....	41
Figure 3.1	Measured whole blood T_2 and model fits.	52
Figure 3.2	Blood T_2 enhancement variations.	53
Figure 4.1	The segmented EPI sequence diagram.	61
Figure 4.2	The schematic diagram of the multi-echo CPMG sequence.....	62
Figure 4.3	Sample brain relaxometry data from a single subject.....	64
Figure 4.4	GM and WM dependence on CPMG refocusing interval.....	66
Figure 4.5	The Look-Locker sequence diagram.....	69
Figure 4.6	The blood R_1 (T_1^{-1}) variation with oxygenation.	70
Figure 4.7	VERVE [105] sequence diagram with EPI readout.....	72
Figure 4.8	VERVE gradient-echo BOLD effect (I).	74
Figure 4.9	VERVE gradient-echo BOLD effect (II).	75
Figure 4.10	VERVE gradient-echo effect (I & II combined).....	76
Figure 4.11	T_2 -weighted vs. T_2^* -weighted VERVE readout.	77
Figure 4.12	The VERVE calibration factor vs. ΔY_v at 3 T.....	79

Figure 4.13	VERVE calibration variation with n .	80
Figure 4.14	The influence of baseline Y_v on VERVE calibration.	81
Figure 4.15	VERVE calibration sensitivity to venous blood fraction.	82
Figure 4.16	The TSE-VERVE sequence diagram.	84
Figure 4.17	VERVE parameter optimization contour plots.	86
Figure 4.18	VERVE SNR vs. readout bandwidth.	88
Figure 4.19	Comparison of EPI- and TSE-VERVE SNR images.	91
Figure 5.1	CBV_v and CBF activation maps.	105
Figure 5.2	CBV_v and CBF average time courses.	106
Figure 5.3	Fits of $rCBF$ and $rCBV_v$ to a power-law model.	109
Figure 5.4	Effect of α mis-estimation on calibrated BOLD.	110
Figure 6.1	CBV_v , CBF and BOLD activation maps.	128
Figure 6.2	Average CBV_v , CBF and BOLD time courses.	129
Figure 6.3	Measured and modeled time courses.	130
Figure 6.4	Summary of post-stimulus transient parameters.	131
Figure 6.5	Visual and sensorimotor transient parameters.	132
Figure A2.1	Diffusion measurements in blood and water.	157
Figure A3.1	Functional MRI experimental protocol.	169
Figure A3.2	PET experimental protocol.	170
Figure A3.3	Sample ROIs.	173
Figure A3.4	BOLD and FAIR time courses.	175
Figure A3.5	PET and FAIR CBF comparison.	178
Figure A3.6	Correlation between PET and FAIR.	179

List of Tables

Table 3.1	Diffusion and exchange model parameters.....	54
Table 3.2	Physiological and model parameters.....	55
Table 3.3	Effect of physiological parameters on $T_{2,0}$	56
Table 4.1	Cortical grey matter T_2 variation with refocusing interval.....	65
Table 4.2	Cortical white matter T_2 variation with refocusing interval.....	66
Table 5.1	Group-average CBF and CBV_v values.....	108
Table A2.1	Comparison of T_2 measured by CPMG and segmented EPI.....	155
Table A3.1	PET CBF measurements.....	176
Table A3.2	FAIR and PET CBF comparison.....	178

Acknowledgments

I am deeply indebted to my supervisor, Professor Bruce Pike, for his tireless guidance, illimitable knowledgeability, unwavering faith and inexhaustible patience. His unfailing encouragement, optimism and kindness made my Ph. D. years a uniquely nurturing, inspiring and memorable experience that taught me more than I had ever dreamt.

Of course, my school life would have never been the same without the generous help and companionship of my lab-mates, Ives Levesque, Ilana Leppert, Michael Ferreira, Jennifer Campbell, Clarisse Mark, Christine Tardif, Claire Cohalan (my proofreader!), Charmaine Chia, Eric Stinson, Katerina Klepousniotou, Karma Advani, Leili Torab and Vivian Woo. I owe much to their high academic standards and willing guinea-pig'ism. I would like to extend my gratitude to Drs. Jan Warnking, Bojana Stefanovic, Ernst Meyer, Keith Worsley, and Andrew Janke for their input, and to my colleagues, Zografos (Aki) Caramanos, Alex Carmel-Veilleux, Irina Kezele and Vladimir Fonov for sharing their knowledge. I also thank the MR techs, Louise Marcotte, Ron Lopez and David Costa, whose quick thinking and ready humour kept me from breaking down time and again (except on April Fool's). I am especially thankful to André Cormier for his diligence and his dedication to making my life easier. Furthermore, the input of my supervisory committee members, Drs. Henrietta Galiana, Jean Gotman and Louis Collins is much appreciated. More thanks go to Jean-François Malouin and Sylvain Milot for guarding me against the villainy of computer problems, and to Jennifer Chew, Pina Sorrini, Lina Vuch, H el ene Day and Stacey Peixoto for their patience and support.

For their curiosity, perseverance and grey matter, I heartily thank everyone who volunteered for my studies. For their indispensable accommodation, I thank the staff at the Royal Victoria Hospital blood laboratory. I am grateful to my family and friends for putting up with me through the past 4 years. I am also obliged to the Natural Sciences and Engineering Research Council, the Canadian Institutes of Health Research, le Fonds

de la recherche en santé due Québec and the Montreal Neurological Institute for their financial support.

Finally, this thesis is dedicated to my mother, whose love, courage and sacrifices fill every page.

Contributions of Authors

I am the first author of all manuscripts included in this thesis, and have performed all of the work described in chapters 1 to 7, which included:

1. the conception of theoretical simulations;
2. the implementation and testing of new sequence designs;
3. the design of studies and the corresponding experimental protocols;
4. the collection and analysis of all experimental data;
5. the writing of all manuscripts.

All the above was supervised by Dr. G. Bruce Pike.

Other Publications

The following are additional peer-reviewed conference publications that were produced over the course of this Ph. D. project that have not been included in this thesis:

1. Jean J Chen and G. Bruce Pike. Venous CBF-CBV Relationship during end-tidal CO₂ manipulations in humans and its significance for BOLD fMRI. *Proceedings of the 15th Annual Meeting of the Organization for Human Brain Mapping (OHBM)*, San Francisco, 2009, accepted.
2. Jean J Chen and G. Bruce Pike. Evidence of CMRO₂ invariability during end-tidal CO₂ manipulations in humans. *Proceedings of the 15th Annual Meeting of the OHBM*, San Francisco, 2009, accepted.
3. Claire Cohalan, Jean J Chen and G. Bruce Pike. Neuronal activation-induced cerebral blood volume change in humans measured using VASO and VERVE. *The 17th Annual Scientific Meeting of the International Society for Magnetic Resonance in Medicine (ISMRM)*, Hawaii 2009, p. 13.
4. Jean J Chen and G. Bruce Pike. Does global cerebral oxygen metabolism change during hypocapnia and hypercapnia in awake humans? *The 17th Annual Scientific Meeting of the International Society for Magnetic Resonance in Medicine (ISMRM)*, Hawaii 2009, p. 214.
5. Jean J Chen and G. Bruce Pike. BOLD-specific flow-volume relationship during hypercapnia and hypocapnia in humans. *The 17th Annual Scientific Meeting of the ISMRM*, Hawaii, 2009, p. 1627.
6. Jean J Chen and G. Bruce Pike. Functional changes in cerebral blood flow and venous blood volume: what is the steady-state relationship? *Proceedings of the 14th Annual Meeting of the OHBM*, Melbourne, 2008, poster 309.

7. Jean J Chen and G. Bruce Pike. Measuring hemodynamic contributions to the BOLD post-stimulus undershoot. *Proceedings of the 14th Annual Meeting of the OHBM*, Melbourne, 2008, poster 656.
8. Jean J Chen and G. Bruce Pike. Steady-state relationship between cerebral blood flow and venous blood volume. *Proceedings of the 16th Annual Scientific Meeting of the ISMRM*, Toronto, 2008, p. 1909.
9. Jean J Chen and G. Bruce Pike. Origins of the BOLD post-stimulus undershoot. *Proceedings of the 16th Annual Scientific Meeting of the ISMRM*, Toronto, 2008, p. 216.
10. Jean J Chen and G. Bruce Pike. *Functional measurement of venous cerebral blood volume measurement at 3 Tesla. Proceedings of the 13th Annual Meeting of the OHBM*, Chicago, USA, 2007, p. 48.
11. Jean J Chen, Kamakshi Advani, G. Bruce Pike. Analysis of the biomechanical origin of the BOLD post-stimulus undershoot. *Proceedings of the 13th Annual Meeting of the OHBM*, Chicago, USA, 2007, p. 47.
12. Jean J Chen and G. Bruce Pike. Dynamic measurement of functional changes in venous cerebral blood volume at 3 Tesla. *Proceedings of the 15th Annual Scientific Meeting of the ISMRM*, Berlin, Germany, 2007, p. 2617.
13. Jean J Chen, Kamakshi Advani, G. Bruce Pike. Characterization of the BOLD post-stimulus undershoot. *Proceedings of the 15th Annual Scientific Meeting of the ISMRM*, Berlin, Germany, 2007, p. 2620.

List of Abbreviations and Symbols

ASL	Arterial spin labeling
ATP	Adenosine triphosphate
BASSI	Bandwidth-modulated adiabatic selective saturation and inversion
BBB	Blood-brain barrier
BOLD	Blood-oxygenation level-dependent signal
B_0	Static magnetic field
B_1	Excitation magnetic field
CBF	Cerebral blood flow
CBV	Cerebral blood volume
CMR _{glu}	Cerebral metabolic rate of glucose
CMR _{O₂}	Cerebral metabolic rate of oxygen
CO ₂	Carbon dioxide
CPMG	Carr-Purcell Meiboom-Gill
CPP	Cerebral perfusion pressure
CSF	Cerebral spinal fluid
dHb/oHb/tHb	Deoxyhemoglobin/oxyhemoglobin/total hemoglobin
D	Diffusion coefficient
DSC	Dynamic susceptibility contrast
EPI	Echo planar imaging
FAIR	Flow-sensitive alternating inversion recovery
fMRI	Functional magnetic resonance imaging
GE	Gradient echo
GM	Grey matter
G_0	Magnitude scale of microscopic field inhomogeneities (diffusion model)
HASTE	Half-Fourier Single-shot turbo spin-echo
K_0	Magnitude scale of microscopic field inhomogeneities (exchange model)
MION	Monocrystalline iron oxide nanocolloid
MLEV	M. Levitt composite RF pulse sequence [1]

MOTIVE	Modulation of tissue and vessel
MRI	Magnetic resonance imaging
O ₂	Oxygen
OEF	Oxygen extraction fraction
OGI	Oxygen-to-glucose index
PASL	Pulsed arterial spin labeling
PET	Positron emission tomography
QUIPSS II	Quantitative imaging of perfusion using a single subtraction (version II)
r_c	Characteristic length of microscopic field inhomogeneities (diffusion model)
R_1	Longitudinal relaxation rate
R_2 / R_2^*	Transverse relaxation rate
RF	Radio frequency
ROI	Region-of-interest
$rCBV$	Relative CBV
$rVERVE$	Relative VERVE signal
SAR	Specific absorption rate
SE	Spin echo
SNR	Signal-to-noise ratio
τ_{ex}	Intra-extra-cellular exchange time
τ_{180}	CPMG refocusing interval
T	Tesla
T_1	Longitudinal relaxation time
T_2 / T_2^*	Transverse relaxation time
TE	Echo time
TI	Inversion time
TR	Repetition time
TSE	Turbo spin-echo
VASO	Vascular space occupancy
VERVE	Venous refocusing for volume estimation
WM	White matter
Y	Blood oxygen saturation

Abstract

Changes in cerebral venous blood volume (ΔCBV_v) is a critical component of the BOLD fMRI signal (instead of total ΔCBV), but its role has remained relatively unexplored, predominantly because measuring CBV_v non-invasively is challenging. Motivated by this challenge, this thesis focuses on the development and use of the venous refocusing for volume estimation (VERVE) technique to non-invasively measure ΔCBV_v . Driven by the substantial signal-to-noise (SNR) gain at high field, VERVE was re-designed for 3 T. This technique is strongly field-dependent through its reliance on venous blood transverse relaxation (T_2) variations as a function of the Carr-Purcell Meiboom-Gill (CPMG) refocusing interval and blood oxygenation. To characterize this dependence, human whole blood T_2 relaxometry was performed at 3 T. The results reveal significantly enhanced blood T_2 dependence relative to 1.5 T, one best modelled as a diffusion process. In addition, human grey and white matter T_2 relaxometry results support venous blood T_2 variation being the predominant source of VERVE contrast at 3 T. The subsequent design of VERVE was based on the blood relaxometry results. Also, to minimize signal biases due to gradient-echo BOLD effects, greatly amplified at 3 T, a turbo spin-echo approach was adopted, further boosting SNR. VERVE was then used with arterial spin labeling (ASL) to assess the steady-state venous flow-volume relationship in humans under visual and sensorimotor stimulation. The results demonstrated a spatially-invariant flow-volume relationship characterized by a power-law coefficient (α) of 0.23, significantly lower than Grubb's value of 0.38 (derived using total ΔCBV). The assumption of the latter in calibrated BOLD introduced a significant underestimation in cerebral oxygen metabolism changes (ΔCMRO_2). Finally, the interactions giving rise to the controversial BOLD post-stimulus undershoot were examined with respect to the prevalent biomechanical, metabolic and neuronal theories. CBV_v , CBF and BOLD responses to graded visual and sensorimotor stimulation were acquired using VERVE and ASL in healthy humans. A

slower transition of venous ΔCBV relative to BOLD, CBF as well as total ΔCBV was established, supporting a significant biomechanical contribution to the BOLD undershoot. In addition, CBF exhibited consistent post-stimulus undershoots well-correlated with those of BOLD, supporting a neuronal origin.

Résumé

Les changements du volume sanguin cérébral veineux (ΔCBV_v) est un élément essentiel du signal BOLD (par opposition à l'ensemble de ΔCBV). Pourtant, jusqu'ici le rôle du CBV_v est resté relativement inexploré, et ce du aux difficultés liées aux mesures non-invasives du CBV_v . Motivée par ce défi, cette thèse se rapporte sur le développement et l'utilisation de la méthode VERVE (refocalisation veineuse pour l'estimation du volume), qui permet l'estimation non-invasive de ΔCBV_v . D'abord, l'augmentation importante du rapport signal-sur-bruit (SNR) aux champs magnétiques élevés a mené à réviser VERVE pour 3 T. Le contraste VERVE est basé sur les variations du temps de relaxation transversale (T_2) sanguin veineux en fonction de l'intervalle de refocalisation Carr-Purcell Meiboom-Gill (CPMG) et de l'oxygénation sanguine. Pour caractériser cette dépendance, qui dépend fortement du champ magnétique, une étude relaxométrique du sang humain a été réalisée à 3 T. Les résultats indiquent que la dépendance du T_2 sanguin est amplifiée de façon importante entre 1.5 T et 3 T. Un modèle de diffusion décrit le mieux cette dépendance. D'autre part, une étude relaxométrique de la matière grise et blanche a été réalisée, confirmant la dominance de l'effet T_2 sanguin dans le contraste VERVE. La composition de VERVE se rapporte aux résultats relaxométriques sanguins. En plus, afin de minimiser l'effet de l'écho de gradient, amplifié à 3 T, une approche turbo spin-écho a été adoptée. VERVE est ensuite utilisée avec le marquage des spins artériels (ASL) pour mesurer les changements du CBV_v et du débit sanguin cérébral (CBF) chez les sujets sains lors de stimulations visuelles et sensorimotrices. Les résultats démontrent une relation débit-volume invariante à travers le cortex, caractérisée par $\alpha = 0.23$, inférieure à la valeur de Grubb (0.38, calculée à partir du CBV total). En employant cette dernière, une sous-estimation significative est introduite dans le changement de la consommation cérébrale de l'oxygène (ΔCMRO_2). Finalement, les interactions à l'origine du controversé sous-dépassement post-stimulus de BOLD ont été examinées à l'égard de la théorie

biomécanique, métabolique et neuronale. Les réponses du CBV_v , du CBF et de BOLD ont été obtenues lors de stimulations visuelles et sensorimotrices de durées variables chez des sujets sains en utilisant VERVE et ASL. Un ralentissement de transition de ΔCBV_v par rapport à BOLD, CBF ainsi que ΔCBV total a été démontré, ceci suggérant une importante contribution biomécanique. De plus, le CBF démontre des sous-dépassements post-stimulus qui ont été corrélés avec ceux de BOLD, favorisant une origine neuronale.

Original Contributions

The original scientific contributions made in the course of this Ph. D. project are,

1. Establishing the insensitivity of the T_2 of cortical grey and white matter to changes in the CPMG refocusing interval at 3 T;
2. Discovery of a linear enhancement in the dependence of the whole human blood T_2 on the CPMG refocusing interval and blood oxygen saturation at 3 T relative to 1.5 T;
3. Finding that the weak-field approximation of the bounded diffusion model continues to provide a better description of the blood T_2 dependence than the two-site exchange model at 3 T;
4. A revised design for the venous refocusing for volume estimation (VERVE) fMRI technique which minimizes T_2^* effects, making it suitable for high-field imaging;
5. Discovery that the BOLD-specific steady-state flow-volume relationship during neuronal activation is characterized by a power-law coefficient that is significantly lower than that used by the widely adopted Grubb's relationship;
6. Determination that this flow-volume relationship between visual and sensorimotor regions are similar, and that the overestimation in the assumed contribution of CBV to the BOLD signal leads to $\Delta\text{CMR}_{\text{O}_2}$ underestimation;
7. Finding that the BOLD post-stimulus undershoot is associated with a concurrent undershoot in CBF as well as a delayed venous CBV recovery;
8. Discovery that the BOLD post-stimulus undershot is spatially heterogeneous, larger during visual activation than during sensorimotor stimulation, potentially attributable to metabolic and structural differences.

Chapter 1

Introduction

The brain is as complex as it is important, constituting one of the final frontiers in our understanding of mammalian physiology. It is a highly dynamic and even capricious system that has presented many challenges to human understanding. At the base of a full understanding of cerebral physiology is the knowledge of the metabolic and hemodynamic processes supporting neuronal activity. Building upon cumulative knowledge which led to the consensus that the brain's energy requirements are met by the production of adenosine triphosphate (ATP), current neuroscience research aims to resolve, among many others, the debate regarding the main contributors to this energy expenditure, primarily with respect to synaptic currents, action potentials and glial signaling [2, 3]. In addition, increasing interest is attached to the mechanisms underpinning the initiation of the cerebral hemodynamic response, and the connection of the latter to metabolic requirements [4-6]. While answers to these questions are of immense value to basic neuroscience, they also pave the way for a deeper understanding of neurological diseases such as stroke, multiple sclerosis and Alzheimer's disease, which ravage the lives of millions.

Human cerebral functional physiology has historically been studied using microscopy (Figure 1.1), electroencephalography as well as nuclear imaging [7-9]. However, it is no coincidence that brain research has become dramatically more prolific over recent years, as technological advances have furnished scientists with easier and more powerful ways to probe brain physiology. Functional MRI (fMRI), which has revolutionized neuroimaging with its multimodal capabilities, has made enormous contributions to this field through the blood-oxygenation level-dependent (BOLD) contrast mechanism. The BOLD technique takes advantage of changes in blood

oxygenation accompanying alterations in neuronal activity, producing maps of functional activity at relatively high temporal and spatial resolution. It is prized for its simplicity, accessibility, noninvasiveness and lack of ionizing radiation, and has found fast-growing application in a wide array of areas. Today, BOLD fMRI is the de facto standard for the in vivo investigation of human brain function. However, this simple technique belies a substantial complexity, and the accurate interpretation of BOLD signals is contingent upon a correct understanding of the relationship between oxygenation metabolism and hemodynamic responses, which has yet to be fully achieved. In addition, multi-modal fMRI data, comprising both metabolic and hemodynamic measures, will tremendously benefit the understanding and treatment of various neurological conditions [10].

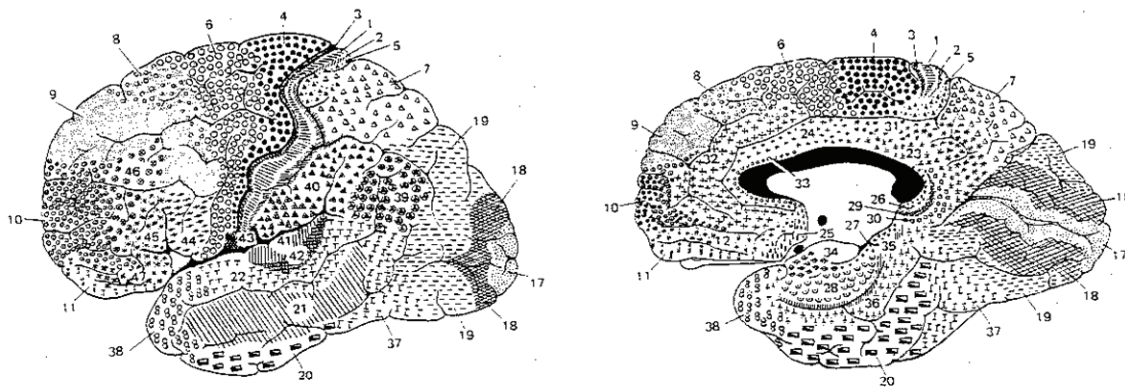


Figure 1.1 Brodmann's cytoarchitonic map of the adult human brain.

The map was obtained through microscopy of Nissl-stained brain slices, and has provided a valuable physiological basis for the classification of functional areas, which are denoted by the various Brodmann's area numbers. (source: [9])

The work contained in this thesis was motivated by the need to better understand the hemodynamic and metabolic responses underlying the BOLD signal. Specifically, it focuses on clarifying the BOLD contrast mechanism with respect to cerebral blood volume (CBV), which accounts for up to 5% of the human cortical tissue volume [11, 12]. Conventionally, CBV has been measured using positron emission tomography and X-ray computed tomography. However, these measures do not reflect venous blood volume changes, which underlie the CBV contribution to the BOLD signal and yet remain largely unexplored. Our particular interest in venous blood has led us to

the exploration of fundamental MR properties of blood, which are at the centre of the BOLD effect, and are strongly dependent on the magnetic field strength at which they are measured. In addition to the valuable contribution to basic fMRI knowledge constituted by these measurements, they are also of paramount importance to the development of novel fMRI methods, such as the venous refocusing for volume estimation (VERVE) technique, designed to monitor changes in venous blood volume in vivo. In this thesis, our development of VERVE for high-field applications is followed by its demonstration at 3 Tesla on cohorts of healthy human subjects. The resulting data has provided important insights regarding cerebral hemodynamic response, in both the steady state and transient state. The transient response, which we studied primarily through the prominent BOLD post-stimulus undershoot, has furnished valuable clues to the mechanisms governing cerebral hemodynamic changes.

The main body of this thesis is based on three manuscripts, and is organized as follows. Chapter 2 contains a review of the background literature on brain physiology and magnetic resonance imaging (MRI) necessary for understanding the work described herein. Chapter 3 is comprised of a manuscript titled “Human whole blood T_2 relaxometry at 3 Tesla”, which documents detailed measurement of human blood T_2 and the associated blood chemistry results, and is in press for publication in *Magnetic Resonance in Medicine*. Complementary results on human cortical grey and white matter T_2 and blood T_1 relaxometry are presented in Chapter 4, along with a technical description of the development of VERVE at 3 Tesla. The second manuscript, titled “BOLD-specific cerebral blood volume and blood flow changes during neuronal activation in humans”, has been submitted to the *NMR in Biomedicine*, and appears in Chapter 5. The final manuscript, titled “Origins of the BOLD post-stimulus undershoot”, has been submitted to *NeuroImage* and is presented in Chapter 6. In Chapter 7, the findings of this work and corresponding implications are summarized, while potential extensions and applications of the current research are enumerated. Lastly, an additional manuscript, based on data acquired prior to this project and titled “Cerebral blood flow measurement using fMRI and PET: a cross-validation study”, is included in the Appendix. This work reports on our findings of the equivalence between PET and fMRI measurements of activation and hypercapnia-induced CBF change, and has been published in the *International Journal of*

Biomedical Imaging. Also included in the Appendix are experimental data pertaining to this thesis but not included in the manuscripts.

Chapter 2

Background

With the development of fMRI [13, 14] during the past decade, most brain mapping studies now employ this modality, and neuroscience research in this area has expanded prodigiously. Functional MRI methods do not image neuronal activity directly; instead, they target the detection of changes in its various physiological correlates. The superior sensitivity and relative technical simplicity of BOLD imaging have resulted in its unequivocal dominance in fMRI. However, the observed BOLD signal has a complex and only partially understood dependence upon cerebral blood flow (CBF), blood volume (CBV), oxygen metabolism ($CMRO_2$), and vascular architecture. The physiological basis of the BOLD signal, as well as the associated technical background of magnetic resonance imaging, will be described in detail in this chapter, assuming a basic understanding of MR physics and imaging principles [15, 16].

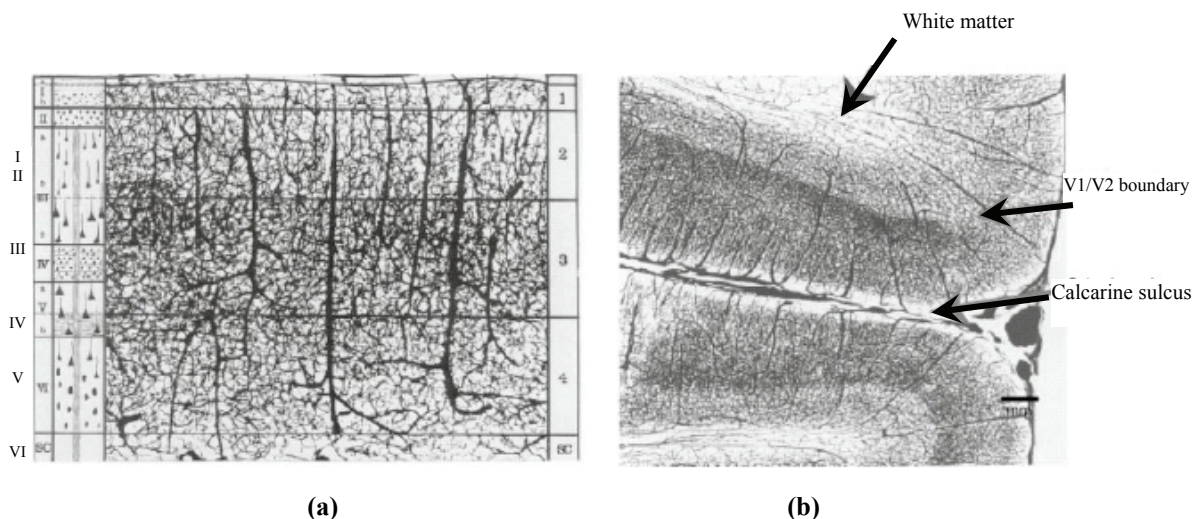


Figure 2.1 Vascularization varies across the cortical layers.

(a) The most densely vascularized region falls near layers III and IV. **(b)** Vascular density can vary significantly across boundaries of functional areas, as exemplified by the drastic difference between the primary (V1) and secondary (V2) visual areas. (adapted from [17, 18])

2.1 Functional Physiology

Cortical grey matter, where the bulk of neuronal processing takes place, can be subdivided into six layers, namely (I) the molecular layer; (II) the external granular layer; (III) the external pyramidal layer; (IV) the internal granular layer; (V) the internal pyramidal layer; and (VI) the multiform layer. Layers II to VI contain the soma (cell bodies) and axons of pyramidal neurons, glia and interneurons, with layer IV receiving input from other cortical and subcortical areas. As seen in Figure 2.1, layers III and IV are generally the most densely vascularized, although their thicknesses are spatially variable. For instance, layer IV in the visual cortex is one of the thickest, but it is the most insubstantial in the motor cortex. Layer VI, the farthest from the cortical surface, is almost entirely composed of dendrite and associated axons, which constitute cerebral white matter. Furthermore, vascularization parallels synaptic activity more than it does soma content.

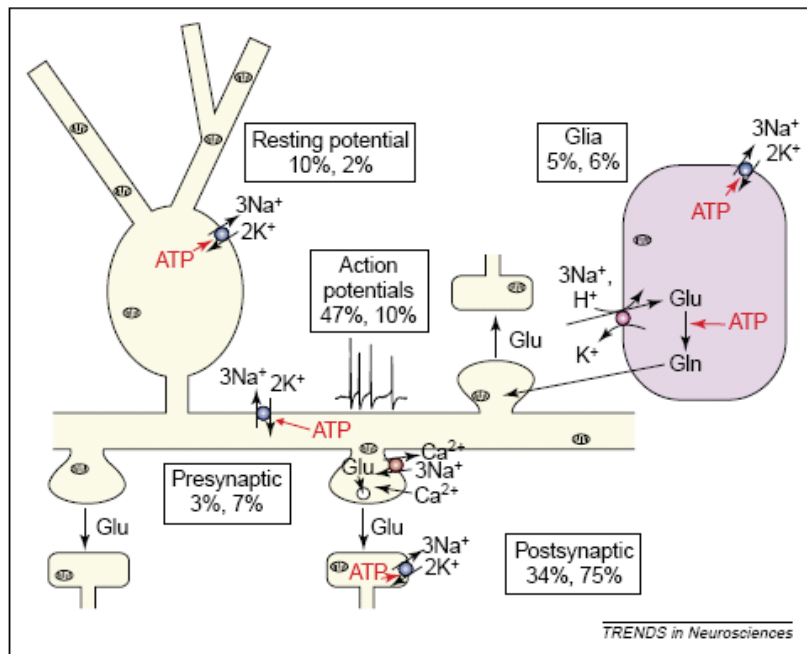


Figure 2.2 Schematic of excitatory process.

Neurons are shown in yellow and glial cells in mauve. The predicted percent energy (ATP) use are given first for rodents and secondly for primates. Nearly all signaling energy is expended on reversing Na^+ and K^+ fluxes across the cell membrane, or on reversing the Ca^{2+} fluxes, which are indirectly powered by the Na^+/K^+ pumps. ATP, the main fuel for brain cells, is produced in the mitochondria by oxidative phosphorylation. The conversion of glutamate (Gln) to glutamate (Glu), a major excitatory neurotransmitter, has been found to take place in the glia. (source: [2])

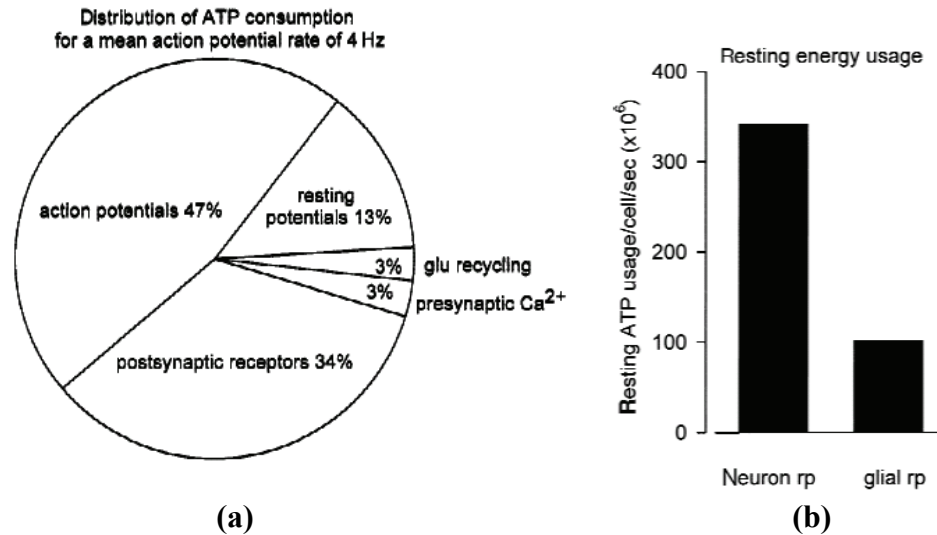


Figure 2.3 Cerebral ATP consumption.

(a) The distribution of signaling-related ATP expenditure corresponding to various cellular activities in a rodent model reveals action potentials and postsynaptic currents to be the primary consumers of energy (glu : glutamine, Ca²⁺: calcium ion channel activity). (b) The ATP required to maintain resting potential (rp) in neurons far exceed that of glia. (adapted from [3])

2.1.1 Neuronal Activation

Action potentials, otherwise referred to as spikes or neuronal firing, trigger the influx of calcium ions (Ca²⁺) and thus the release of neurotransmitter-filled vesicles across the synaptic cleft, which then bind with receptor molecules in the postsynaptic membrane. This binding, also called synapses, engenders small hyperpolarizing currents altering the membrane potential in the postsynaptic neuron, either giving rise to new action potentials (excitatory synapse) or preventing them (inhibitory synapse), thus realizing the extensive propagation of neuronal signaling [19]. The former synapse is frequently mediated by glutamate release, and the latter by the release of gamma-aminobutyric acid (GABA), predominant excitatory and inhibitory neurotransmitters, respectively. In the central nervous system, inhibitory neurons are outnumbered 9:1 by their excitatory counterparts, and are associated with a significantly lower metabolic cost [3].

A neuron's ability to generate synaptic and action potentials depends on the existence of an electrochemical gradient across the cell membrane, arising from intra-extracellular differences in the concentrations of various ions, most notably sodium (Na⁺) and potassium (K⁺). As shown in Figure 2.2 and Figure 2.3a, this ionic charge separation

is maintained by an active transport mechanism (via the Na/K-pump), which requires adenosine triphosphate (ATP) turnover [20]. The rodent-primate differences originate primarily from the longer axonal/dendritic distances as well as higher firing frequency in primates [3]. ATP is the primary energy storage for neurons, and its synthesis is regulated by the rate of its utilization. A main channel of such synthesis is through glycolysis, a series of anaerobic, enzyme-catalyzed reactions resulting in the conversion of glucose into ATP, pyruvate and lactate [21]. Normally, glycolysis followed by the trans-carboxylic acid (TCA) cycle, a more efficient ATP synthesizing process which is associated with oxygen utilization in the mitochondria (oxidative phosphorylation), as well as CO₂ and water as by-products. CO₂ is readily soluble, and combines with water to form bicarbonate (HCO₃⁻) and hydrogen (H⁺) ions. Glycolysis can directly and more quickly supply ATP in the absence of oxygen, but this occurs only under rare circumstances, as the associated efficiency is much lower than that of the TCA cycle. In summary, variations in neuronal activity are generally reflected in changes in cerebral glucose (CMR_{glu}) and oxygen (CMR_{O2}) consumption.

Cerebral energy consumption has often been suggested to be driven directly by metabolic deficits, primarily in the pre-synaptic terminals or glia, but recent neurovascular research has suggested that postsynaptic currents and action potentials dominate energy requirements (Figure 2.3a), and that hemodynamic responses are driven primarily by neurotransmitter-related signaling [2, 3, 22-25]. The glia, subdivided into macro- and microglia, comprise all non-neuronal cells in the nervous system that provide nutrients and support, as well as maintain homeostasis and participate in signaling. In cortical grey matter, there are similar numbers of neurons and glia cells, with astrocytes being the most abundant macroglia. Since the consumption of ATP is higher in neurons, in which electrochemical gradients must be maintained for the firing of action potentials, the resting-state energy usage of neurons exceeds that of glia by more than three-fold (Figure 2.3b). Astrocytes are equipped with abundant glutamate receptors, and are actively involved in the recycling of extracellular glutamate into glutamine, the precursor to neuronal glutamate production [3, 26]. However, due to a ~70% lower oxidative capacity, astrocytic activation is mainly associated with lactate production increase [27].

Finally, although the cerebral oxygen-to-glucose index ($OGI = CMR_{O_2}:CMR_{glu}$) has been found to broadly agree with the stoichiometric ratio of 6:1 [28], stimulus-dependent OGI variations have been repeatedly observed using PET and MR spectroscopy [29-31], which also found the fractional CMR_{glu} change to far exceed that of CMR_{O_2} under an assortment of stimulation conditions, a phenomenon that has yet to be fully explained [29, 32]. It should be noted that the dramatically superior efficiency of aerobic ATP synthesis over its anaerobic counterpart [3] precludes the possibility of a purely anaerobic response to stimulation-driven ATP demand [31]. Thus, relative deficiencies in the sensitivity of previous oxidative metabolism experiments [33] as well as the transient utilization of a tissue glycogen reserve have both been suggested as the cause of the above OGI disparities [29].

2.1.2 Cerebral Vasculature

Blood supply to the brain and much of the spinal cord is derived from the internal carotid arteries (ICAs) and the vertebral arteries (VAs) [19]. These are associated with volumetric flow rates of approximately 600 and 170 mL/min, contributing to 70% and 30% of the total CBF, respectively [34-36]. The major arteries of the brain also include the anterior cerebral artery (ACA), the middle cerebral artery (MCA), the posterior cerebral artery (PCA) and the basilar artery (BA). The ICA bifurcates into the MCA and ACA, which supply the frontal, parietal and limbic lobes, as well as the lateral and anterior parts of the occipital and temporal lobes. The inferior and posterior aspects of the latter lobes are supplied by the PCA, while the cerebellum is mainly irrigated by the BA, which originates from the VA. Major cerebral arteries, with a mean diameter of 4 mm, divide into smaller arteries, which become increasingly muscular with the level of branching [18]. Arterioles, as can be observed in Figure 2.4, are the smallest arteries, with a mean diameter of 30 μ m. The arteriolar wall contains several layers of sphincters (smooth muscle fibres) and can change its tone in response to chemical signals [37].

Venules are the smallest veins, and generally lack smooth muscles. Blood drains via venules into larger veins, which are more numerous than arteries, and have a mean

diameter of 5 mm [18]. Veins hold more than half of the blood in the circulatory system; their tone alters easily with intravascular pressure increase, and are believed to respond to decreased arteriolar resistance through a generally passive vasodilation [28], but can contract as required, due to the presence of venous smooth muscles [38]. The superior superficial cerebral veins (draining the cortex) lead into the superior and inferior sagittal sinuses, while the inferior veins (draining subcortical regions) are collected by the transverse and cavernous sinuses [19]. Inter-subject variability in the superior veins is higher than in the deep veins, notably the internal cerebral vein (ICV). The ICV pair fuses to form the great vein of Galen, which then combines with the inferior sagittal sinus to form the straight sinus. The latter merges with the transverse and cavernous sinuses to form the sigmoid sinus, which leads into the internal jugular vein (IJV). Venous flow in the IJV pair is between 600 and 800 mL/min, and has been found to constitute over 75% of the entire cerebral drainage capacity [39].

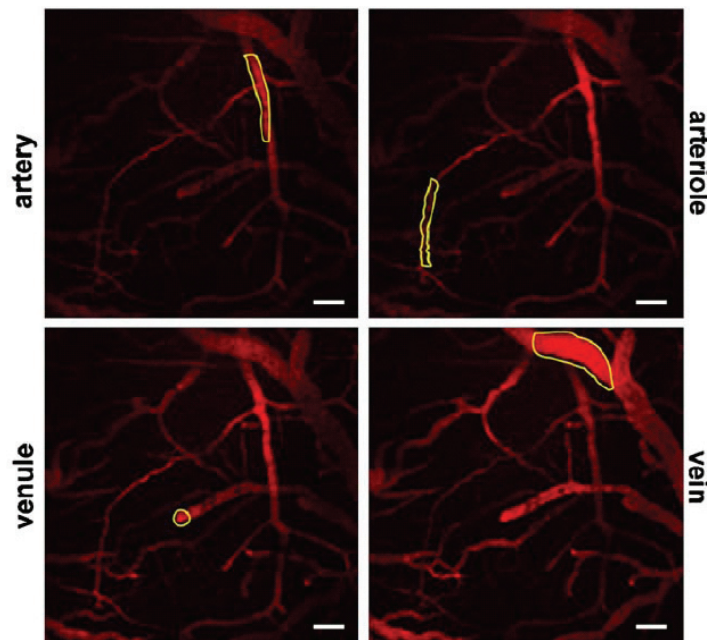


Figure 2.4 The cerebral vasculature.

The propagation of a bolus of dye through the cerebral vasculature in a rat model is shown, as imaged using two-photon microscopy. The bolus enters through the arteries and passes into arterioles. Following transit through the capillaries, the dye passes into the venules, and finally exits through the veins. The scale bar indicates 100 μm . (source: [40])

Flow velocity is lowest in capillaries and highest in major arteries, with arteriolar and venular velocities being comparable. Capillaries are the smallest vessels in the cerebrovascular system, with a mean diameter of 8 μm . They derive from arterioles, and merge into venules. Capillaries and small venules constitute the site of exchange between blood and interstitial fluid. To facilitate this exchange, the capillary wall is lined with a single endothelial layer, and has neither smooth muscles nor elastic tissue enforcement. Despite this lack, the capillary blood volume can readily alter in response to neuronal signaling, due to the extensive pericytic and astrocytic control of capillary tone [22, 25, 41]. In addition, free intra-extravascular exchange is prevented by the blood-brain barrier, a system of anatomical and physiological mechanisms that controls the movement of substances from the blood stream to the brain, effectively separating the nervous system from the rest of the body. Finally, the structure of the cerebral microvasculature can vary according to functionality, typically reflecting local metabolic demands or patterns of growth [42]. Inter-capillary distances were found to correlate with tissue metabolic activity, and the local tissue blood volume fraction can be used to assess the capillary density as well as metabolic rate [42].

2.1.3 Neurovascular Coupling

The propagation of both synaptic and action potentials is mediated by the opening of ion channels. Thus, the cellular ATP requirements are modulated by the rate of synapses and neuronal firing, and increases in the discharge frequency result in a greater need for glucose and oxygen, the basic substrates of ATP production. This surge in need is met via increased tissue perfusion (CBF) [43-45] realized by dilation of the arterioles, which decreases the resistance of the latter to flow and leads to increased blood volume (CBV) [46]. This process is referred to as functional hyperemia, which enhances not only nutrient transport but also waste removal. The hemodynamic response is generally initiated through contractions and relaxations of arterial smooth muscles (regulated globally and locally) and is unlikely to be dictated by oxygen content, given the low vascular reactivity to O_2 . Although this process has traditionally been associated solely with neuronal signaling, hence the term “neurovascular coupling” [43], attention has

lately been shifting towards a model that also includes an indispensable participation of the glia [2, 25].

Strong global CBF responses can be effected by intravascular CO₂ alterations. Notwithstanding the nervous response initiation by the macrovascular CO₂ receptors, the homeostatic blood pH is actively maintained. Thus, acidosis, a direct result of increased CO₂ presence, is known to produce vasodilation and hence flow increases [28], potentially mediated by a global neural network [2]. Hypercapnic challenges, in which the arterial CO₂ content is increased, inducing large CBF increases without a significant concomitant increase in metabolic rate [47], have been widely used to study cerebrovascular coupling. Hypercapnia-triggered increase in baseline CBF has been shown to modulate stimulus-induced CBF change [48, 49], and can be a powerful tool in probing the mechanisms of cerebral hemodynamic response.

Regional flow variations can be triggered not only by localized metabolic CO₂ accumulation (hence acidosis), but also by changes in extracellular K⁺, Ca²⁺ and adenosine concentrations, which are correlates of cellular activity changes [50]. In addition, much importance has been attached to the role of nitric oxide (NO), which is synthesized locally following glutamate receptor activity, and has been implicated in the modulation of vasodilatory effects produced by nearly all the above mediators [28, 51, 52]. The means of the electrochemical control of microcirculation is much debated, and in view of the extensive innervation of the cerebral microvasculature, astrocytes [22, 25], local interneurons [22] as well as subcortical neurons [22] have all been implicated in the fine-scale control and maintenance of arteriolar and capillary tone.

As glucose and oxygen are required in ATP production, ATP usage can be reflected in CMR_{glu} alterations, and changes in CMR_{glu} have been found to be generally comparable to those in CBF. However, CBF changes have often been found to far exceed those in CMR_{O₂}, bringing into question the assumption that functional hyperemia subserves oxidative phosphorylation. Superseding the supposed spatial-scale disparity between CBF and CMR_{O₂} regulation [4], diffusion limitation of oxygen imposed by hemoglobin binding has been suggested as the main cause for the low observed oxygen extraction fraction (OEF) [53]. Brain tissue has low intrinsic oxygen tension, and according to the diffusion-limitation model, blood flow up-regulation in response to

neuronal activity would result in decreased mean transit time and hence OEF, with the consequence that increased oxygen diffusion across the blood-brain barrier requires an enhanced capillary-tissue oxygen pressure gradient produced only by a disproportionately large blood flow increase [6, 54]. However, the validity of this theory has been questioned due to recent observations of continued CBF increase during a significantly hyperperfused baseline state [49, 55].

2.2 Blood Properties and Physiology

Blood is composed mainly of plasma and red blood cells (erythrocytes). Plasma contains proteins, glucose, amino acids, lipids, gases, inorganic ions, and for the most part, water [37]. Erythrocytes, on the other hand, contain hemoglobin, and are responsible for the delivery of oxygen. The ratio of the volume of erythrocytes to whole blood volume is called the hematocrit (Hct). Microvascular Hct is between 45% and 75% of the arterial value [56], due to preferential erythrocytic flow through the macrovascular lumen [57].

Erythrocytes contain hemoglobin (dHb), made up of 4 protein sub-units, each surrounding a heme group embodying a free Fe (II) ferrous ion (Figure 2.5). The heme groups are each capable of reversibly binding with one O₂ molecule, thus endowing the erythrocyte with the capacity for efficient oxygen transport. In the deoxygenated state, each of the heme Fe (II) ions has six outer-shell electrons, four of which are unpaired. This configuration results in the paramagnetism of the deoxyhemoglobin (dHb) --- the state of having a small positive magnetic moment when placed within a magnetic field, causing a susceptibility-induced enhancement in the transverse MR relaxation rate ($R_2 = 1/T_2$). Upon binding with oxygen, however, the Fe (II) ion switches to a low-spin and diamagnetic state, and no longer contributes to R_2 enhancement. The key role of deoxyhemoglobin (dHb) in the detection of neuronal activation has been discussed by Ogawa *et al.* [14]. In this context, blood oxygenation refers to the fraction of total hemoglobin that is oxygenated. At rest, the oxygenation of arterial blood in humans is approximately 98%, while that of venous blood averages close to 60% [58]. In addition to the hematocrit, the amount of paramagnetic dHb in venous blood also heavily depends on

blood oxygenation and varies with the amount of aerobic metabolism (dHb production), blood flow (dHb removal) and volume (dHb storage).

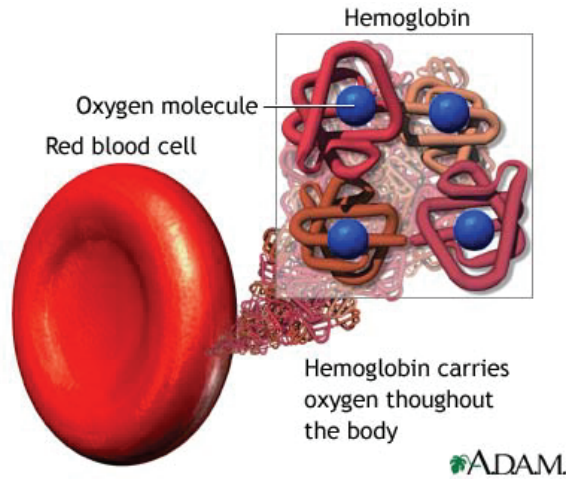


Figure 2.5 Schematic of a red blood cell.

Erythrocytes (red blood cells) contain hemoglobin, each of which is made up of 4 protein sub-units surrounding a heme group. Each heme group contains a free iron ion, capable of binding with an oxygen molecule. When deoxygenated, the heme becomes paramagnetic.

The microscopic local field inhomogeneities induced by the magnetic moment of deoxygenated erythrocytes have been ascribed to the dependence of venous blood transverse relaxation on oxygenation and on the Carr-Purcell Meiboom-Gill (CPMG) refocusing interval (i.e. the interval between consecutive RF refocusing pulses in a multi-echo spin-echo scan [59]). The intravascular dephasing of blood is characterized by interactions between dHb of the erythrocytes and water, which is found both in the plasma and in the erythrocytes. The mechanism of signal loss has been attributed to either dynamic dephasing arising from diffusion of water molecules relative to the paramagnetic centres of the erythrocytes and/or to rapid intra-extra-cellular chemical exchange of water protons [60]. In the weak-field approximation of a diffusion-based R_2 enhancement (T_2 reduction) model proposed by Jensen and Chandra [61], changes in R_2 are specified by

$$R_2 = R_{20} + G_0 \frac{\gamma^2 r_c^2}{2D} F\left(\frac{2D\Delta t}{r_c^2}\right), \quad \text{where } F(x) = \frac{1}{\sqrt{\pi}} \int_0^\infty dy \frac{e^{-y}}{\sqrt{y}} \left[1 - \frac{1}{xy} \tanh(xy)\right] \quad [2.1]$$

where R_{20} is the intrinsic transverse relaxation rate, D is the diffusion coefficient, r_c is the characteristic length of the field inhomogeneity, γ is the gyromagnetic ratio, Δt is the refocusing interval, and G_0 is the mean squared magnitude of field inhomogeneities.

Brooks *et al.* used the Luz-Meiboom two-site chemical exchange model to characterize the same phenomenon [62], in the form of

$$R_2 = R_{20} + \gamma^2 K_0 \tau_{ex} \left(1 - \frac{2\tau_{ex}}{\Delta t} \tanh\left(\frac{\Delta t}{2\tau_{ex}}\right) \right) \quad [2.2]$$

where τ_{ex} is the exchange time, K_0 is the variance of microscopic spatial field inhomogeneities. Stefanovic and Pike showed evidence of the diffusion model better characterizing venous T_2 at 1.5 T [63], while other authors found diffusion to be sufficiently rapid to be well approximated by the exchange model [62, 64, 65]. Nonetheless, parameterization of both models has been high variably across studies for these conclusions to be generalized [66, 67]. Due to its high relevance to fMRI and its strong dependence on field strength, a detailed knowledge of human blood T_2 relaxation at 3 T is of substantial value to numerous MR applications. A comprehensive discussion thereof is presented in Chapter 3.

2.3 BOLD Contrast Mechanisms and Measurement

2.3.1 The BOLD Effect

The blood-oxygenation level-dependent (BOLD) fMRI technique reflects, in essence, the amount of deoxyhemoglobin (dHb). As originally described by Ogawa *et al.* [14], the BOLD effect originates from the paramagnetic nature of dHb, which creates inhomogeneities in the local static magnetic field (B_0), thus susceptibility shifts, resulting in a reduction in T_2 and T_2^* . The BOLD signal has been experimentally established as a surrogate of neuronal activity [68, 69], as shown in Figure 2.6, where BOLD is shown to be correlated, to various degrees, to local field potential (LFP), multi-unit activity (MUA) and spike density function (SDF), which are representative of cortical electrical signaling.

BOLD-related MR signal changes are observed predominantly in regions within or proximal to capillaries, venules and veins. Positive BOLD signals can be measured during increases in oxygenation, which occur during periods of CBF increase accompanying neuronal activity (hence CMRO_2), which contribute to increased local field homogeneity by reducing the paramagnetic dHb population. However, the amount of dHb is also dependent on CBV, and more specifically, on CBV from the partially deoxygenated blood compartments. Although CBF increases bring about improved local field homogeneity, the accumulation of dHb (CBV) in these compartments contributes to the opposite, thus counteracting the effect of CBF in producing the BOLD signal. As previously mentioned, non-functional stimuli such as hypercapnia can cause global CBF increase, which prompts a global increase in oxygenation and hence in BOLD signal, much in the same way that neuronal activation causes local oxygenation increase. The physical mechanisms and quantitative modeling of the BOLD effects will be discussed in the subsequent sections.

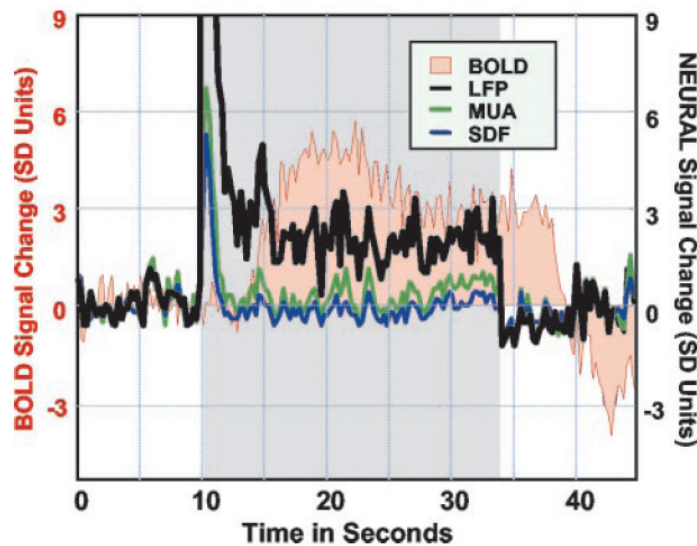


Figure 2.6 BOLD signal and underlying neuronal activity.

The BOLD signal corresponding to primary visual activation (stimulation period as shaded region) is shown with simultaneous time courses of local field potential (LFP), multi-unit activity (MUA) and spike density function (SDF), obtained through intra-cortical electrophysiological recording. MUA and SDF are reflections of action potential firing, correlating well with the spike density function. On the other hand, LFP, more representative of synaptic activity, was found to better correlate with BOLD. (source: [69])

2.3.2 BOLD Contrast Mechanisms

The BOLD effect has both intravascular and extravascular contributions, the relative weightings of which dependent on field strength. Intravascular BOLD contrast results from the dynamic dephasing of water protons around the paramagnetic field perturbations produced by the deoxyhemoglobin and/or from water exchange between the intra- and extracellular compartments [60]. Assuming slow intra-extra-vascular water exchange, the dHb-induced susceptibility difference between erythrocytes and plasma produce MR frequency shifts which result in T_2 reduction, as described earlier. Consequently, a decrease in dHb quantity and concentration, which can result from neuronally mediated CBF increase, results in longer T_2 values, hence a rise in signal intensity.

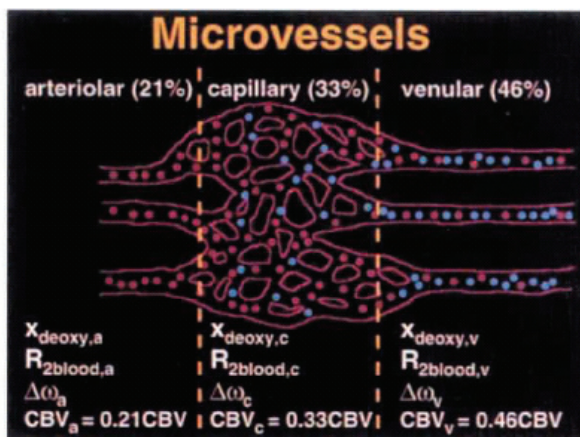


Figure 2.7 The human cerebral microvascular composition.

The deoxy-hemoglobin are shown in blue while oxy-hemoglobin are shown in red. The dHb fraction (X_{deoxy}) will determines the local magnetic susceptibility shift ($\Delta\omega$) and T_2 relaxation rates (R_2) which give rise to the BOLD signal, the microvascular contribution of which is more reflective of neuronal activity. The signal in each voxel is in turn determined by the voxel-wise vascular components, their respective water densities and volumes. (source: [70])

Blood oxygenation changes take place primarily in the venous compartments (i.e. capillaries, venules and veins), each associated with a different hematocrit- and CBV-dependent dHb concentration, with microvascular hematocrit (Hct) being 85% that of macrovessels (Hct = 44%). At rest, the intravascular compartment in human grey matter can be defined by a CBV of approximately 0.047 ml blood/ml tissue [11]. Of this total CBV, microvascular morphometry [71] reveals an arterial/capillary/venous CBV fraction

distribution of 21%/33%/46% (Figure 2.7). Remarkably, despite this diminutive venous CBV, the intravascular BOLD component can constitute up to 70% of the total available BOLD signal at 1.5 T [72], and 50% at 3 T [73].

The field perturbation arising from the presence of dHb may extend significantly beyond the blood vessels in which it is contained (Figure 2.8). The extravascular BOLD signal is modulated by both static and dynamic dephasing. In the static dephasing regime, the bipolar field offset generated by the susceptibility difference between deoxygenated blood and the surrounding tissue induces a position-dependent dephasing in the tissue. Thus, spins have a position-dependent Larmor frequency, and as the transverse signal evolves, spins lose phase coherence. This effect produces T_2^* shortening, and is the dominant extravascular BOLD mechanism surrounding vessels with diameters greater than 20 μm [60]. The dHb-induced extravascular field offset at the surface of a vessel depends on the susceptibility difference between the intravascular and extravascular media [28], whereas the spatial scale of the dHb-induced field distortion scales with vascular volume if water diffusion is negligible. This is in contrast with intravascular BOLD, the amplitude of which depends not on the total quantity, but on the concentration of deoxyhemoglobin. The tissue volume affected by the bipolar field offset increases with $B_0^{2/3}$ [73].

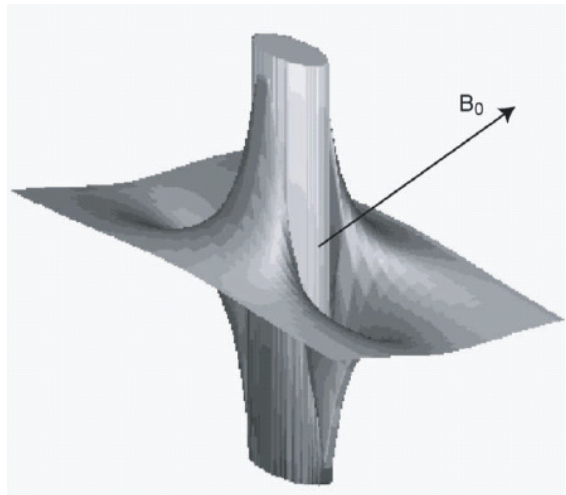


Figure 2.8 The magnetic field disturbance produced by a blood vessel.

A blood vessel, simulated as a cylinder of infinite length and oriented perpendicular to the main magnetic field (B_0), is shown in the centre. The field perturbations due to the presence of paramagnetic material are shown perpendicular to the axis of the vessel. (source: [60])

In dynamic dephasing, the expectation value for spin displacement due to diffusion during each TE is of the same order as the size of the local field distortion surrounding a vessel. The water molecules are therefore not confined to the influence of a single position-dependent field strength during TE, but experience a range of fields depending on their individual trajectory. The averaging effect of diffusive motion may dampen the position-dependent phase dispersion associated with static dephasing, thus potentially attenuating the T_2^* -weighted BOLD effect, particularly around capillaries and small post-capillary vessels. However, the same diffusion effect contributes to increased signal dephasing in T_2 -weighted images, analogous to the intravascular BOLD effect. In the presence of diffusion, radio-frequency (RF) refocusing pulses becomes increasing ineffective around small vessels, thus enhancing T_2 -weighted BOLD contrast near the microvasculature. Thus, extravascular dynamic dephasing contributes to increased spatial specificity of the BOLD signal to neuronal activation.

2.3.3 Measurement of BOLD

As mentioned earlier, static averaging effects are greatest near post-capillary vessels and veins, and are consequently not specific to the site of the activated cortex [73]. On the other hand, intravascular dephasing effects scale with dHb concentration, and are therefore most prominent in the draining veins [70]. Both of these mechanisms of BOLD contrast are expected to contribute to the gradient-echo (GE) BOLD signal, while the static dephasing mechanism makes effectively no contribution to the spin-echo (SE) BOLD signal, which is primarily sensitive to intravascular dephasing [70]. As a result, the activation-induced signal contrast demonstrated by T_2^* sensitive techniques is higher than in T_2 -weighted techniques by about a factor of 2 to 4 [73]. Thus, GE EPI-based BOLD imaging affords superior sensitivity to susceptibility changes and has virtually been the exclusive choice at 1.5 T, where contrast-to-noise (CNR, i.e. SNR of the time series) enhancement is the chief priority.

At 1.5 T, the contribution of the microvasculature to the BOLD signal has been deemed negligible, and the T_2 sensitivity of GE sequences to major vessels as well as capillaries results in inaccuracies in the spatial localization of BOLD-based activation

mapping. While GE BOLD is sensitive to a wide range of vessel sizes (as shown in Figure 2.9), various studies have concluded that intravascular signals from venules and veins are by far the largest contributors to observed GE BOLD changes [72, 74, 75]. Thus, to correctly interpret the T_2^* BOLD effect, it is important to determine the fraction of fMRI changes that is of intravascular origin, and how this fraction behaves as a function of oxygen saturation and hematocrit.

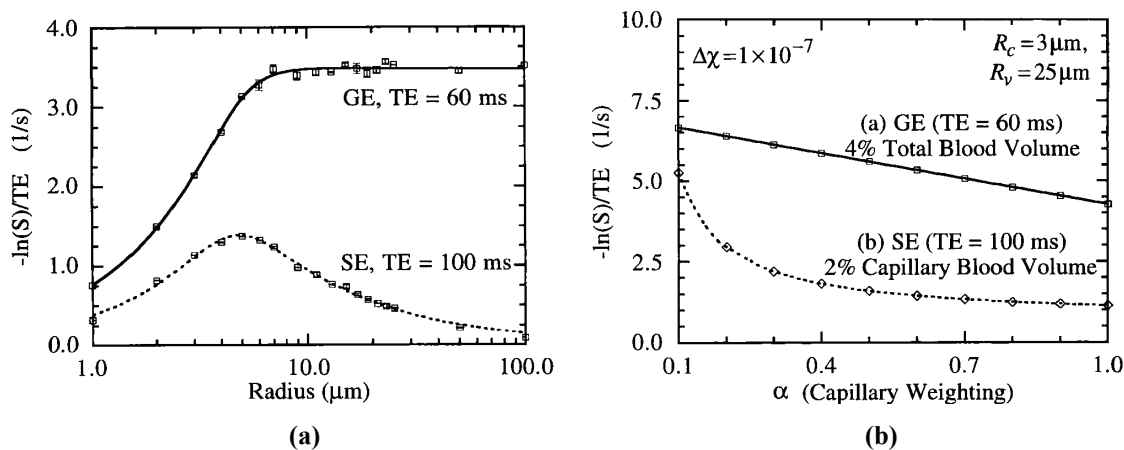


Figure 2.9 Gradient- and spin-echo BOLD contrast.

(a) Simulated data showing the effect of vessel size on extravascular GE (T_2^* -weighted) and SE (T_2 -weighted) BOLD (i.e. $-\ln(S)/TE$) at 1.5 T, in which increasing venous oxygenation during neuronal activation contributes to reduction in both decay rates. However, GE-BOLD contrast is maximal for larger vessels while SE-BOLD contrast is maximal for capillaries (radius $R < 8 \mu\text{m}$). (b) While GE-BOLD contrast (represented by the ordinate) decreases linearly with increasing capillary weighting (α), SE-BOLD is approximately invariant with capillary weighting for the most part, indicating higher intrinsic microvascular sensitivity. $\Delta\chi$ is the susceptibility change. Capillary (R_c) and venular (R_v) radii were assumed to be $3 \mu\text{m}$ and $25 \mu\text{m}$, respectively. (adapted from: [72])

As mentioned earlier, SE BOLD can potentially provide superior microvascular specificity relative to GE BOLD, due to the sensitivity of SE to diffusion (Figure 2.9). However, despite the fallacies of GE BOLD, SE BOLD has not yet found wide-spread use in fMRI studies due to its substantially lower sensitivity. SE BOLD stands to benefit from increased BOLD CNR resulting from high B_0 , which can make it an increasingly viable alternative to GE EPI. Nonetheless, while extravascular dynamic dephasing occurs closest to the site of activation, the bulk of the SE BOLD contrast at 1.5 T still originates from intravascular T_2 effects, which are greatest in the draining veins. To combat this obstacle, the intravascular component can be isolated from the extravascular effect using

diffusion weighting. However, the separation of intravascular signal originating from fast (capillary) and slow (venous) flow remains challenging [75]. In addition, the loss of SNR due to diffusion weighting can be severe, discouraging its use unless highly specific localization of activation is critical [76]. It is noteworthy that at field strengths of 4 T and above, the decrease in venous T_2 begins to produce significant intravascular attenuations, further adding to the appeal of SE BOLD [77]. The optimization of SE and GE BOLD acquisitions will be further discussed in the next section.

Finally, it should be mentioned that the upper limit in fMRI temporal and spatial resolution is not hardware-related. Rather, the maximum spatial resolution of BOLD fMRI relies on the spatial specificity of the BOLD response to the location of neuronal activity, while the temporal resolution is limited by the rate of hemodynamic response of cerebral circulation [78, 79]. As such, improvements in acquisition speed and spatial resolution do not translate directly to improved spatial and temporal resolution of BOLD activation maps.

2.3.4 Detection of BOLD

Although BOLD measurement techniques are simple, the detection of BOLD from the acquired data is not. At 1.5 T, the GE BOLD signal is only 1% for a 50% change in CBF, while the SE BOLD would be significantly lower [28]. The detection of this miniscule signal change is further hampered by noise, consisting primarily of thermal noise and physiological fluctuations. Thermal noise is a stochastic process that is induced in the receiver coil by currents traveling in the body. It can be reasonably approximated as a spatially-uniform, field-independent white Gaussian noise. On the other hand, physiological fluctuations, characterized primarily but not exclusively by cardiac pulsations, respiratory noise and vasomotion, can produce spatially structured signal modulations. Cardiac pulsations ($\cong 1$ Hz) and vasomotion ($\cong 0.1$ Hz) [80] can introduce significant signal change in blood, CSF and the brain parenchyma, while breathing ($\cong 0.3$ Hz) modulates the volume of the lungs, a sizeable source of field non-uniformity. Lastly, in alert subjects, the BOLD signal induced by actual brain activity, but one un-related to the functional task, can also be a substantial source of noise. All these effects can

potentially produce stimulation-correlated signal changes of the same order of magnitude as the activation-induced BOLD signal, confounding the detection of neuronal activation.

The physiological contribution to the noise in BOLD scales with the associated BOLD signal, and becomes increasingly dominant with increasing field strength [81]. As a result, higher fields do not yield a proportional increase in BOLD CNR. The optimization of the BOLD contrast is based on the maximization of the local T_2 and T_2^* differences between oxygenation states. Thus, the optimal GE BOLD echo time (TE) can be approximated by the average cortical tissue T_2^* . Typical TE values are 45 ms at 1.5 T and 30 ms at 3 T [81]. The SE BOLD TE is generally optimized on the same principle, and is typically near 100 ms at 1.5 T [60] and 90 ms at 3 T [82]. As the SE BOLD signal is diffusion-modulated, the TE can be chosen to emphasize diffusion-mediated extravascular dephasing surrounding vessels of a certain caliber. This permits the enhancement of the highly desirable microvascular contribution, and becomes increasingly feasible at higher fields, where the intravascular BOLD signal sees significant reduction.

The relative insignificance of the desired BOLD signal amidst the above potential confounds (i.e. false positives) means that the true activation-induced MR signal is usually not detectable by eye, hence necessitating the use of statistical analysis. One of the most common approaches for a simple block stimulation design is the t -test, based on a linear model of the BOLD signal (which comprises of signal and noise, and incorporates a hemodynamic response model) [83]. The t -statistic is proportional to the ratio between signal change and noise variance, increases with the number of measurements. Voxels exhibiting t -scores above the threshold associated with $p < 0.05$ are deemed to show statistically significant activation. This threshold must, however, incorporate corrections for multiple comparisons, commonly based on Bonferroni's correction or Random Field Theory [83]. These corrections impose the requirement of multiple voxels simultaneously activating, which improves the exclusion of false positives and negatives.

2.4 CBF Measurement

For functional brain mapping, CBF needs to be measured at the microvascular scale (tissue perfusion) since macrovascular flow changes can be remote from the activated region. To this purpose, traditional methods such as transcranial Doppler flowmetry are ill-suited. Since the introduction of the nitrous oxide method [84], H_2^{15}O PET [11, 85], contrast-enhanced X-ray CT [12, 86] and the more recent bolus-tracking based MRI methods [87, 88] have developed into well-established tools for quantitative regional perfusion imaging in humans. However, the relatively long imaging times required per CBF measurement, coupled with the inherent ionizing radiation and exogenous contrast toxicity, limit the application of these techniques to dynamic CBF monitoring. Near-infrared spectroscopy (NIRS) [89, 90] and diffuse optical tomography (DOT) [91] have also been used to provide correlates of perfusion changes in humans and animals, but these methods suffer from limited spatial coverage and regional resolvability.

The most successful class of noninvasive perfusion fMRI techniques is arterial spin labeling (ASL), in which arterial water is magnetically labeled (or tagged) upstream and allowed to flow into the region of interest and exchange with tissue water [92, 93]. By repeating the measurement with and without upstream tagging (to form *tag* and *control* images) and taking the difference, an image with a perfusion dependent intensity is formed. While the earliest ASL experiments employed continuous ASL (CASL) techniques, fMRI studies have normally been performed using pulsed ASL (PASL), which are associated with significantly lower RF energy deposition and magnetization transfer effects, and is therefore better suited for human fMRI applications. The control image is acquired with the exact same parameters as the tagged image, but in the absence of blood inversion, so as to permit the correction of static tissue effects in the tag image, which can be greater than the effects of inflow. Hence, the amplitude of the control-tag signal difference is proportional to CBF. Finally, if the equilibrium magnetization and T_1 of blood is known, then the absolute CBF value can be quantified.

The first application of ASL to detect activation induced CBF changes was by Kwong *et al.* [94], using the pulsed ASL (PASL) technique. Many variants of PASL have since been introduced with recent developments focusing on enhanced multiple slice imaging and quantification capabilities [95-105]. ASL is primarily sensitive to flow in the

arterial and capillary compartments, but is relatively insensitive to the venous compartments due to rapid intra-extravascular water exchange and the decay of the arterial label [102]. This lends support to the argument that ASL-perfusion techniques provide more specific activation localization [102, 106-108]. However, accurate functional mapping using CBF is contingent on resolving the following sources of confounds, to which most PASL techniques are prone: (i) transit-delay related errors, ascribable to T_1 decay during the spatially-variant time period taken for the tagged spins to reach the imaging slice, which can result in varying degrees of CBF underestimation; and (ii) intravascular signal contribution, originating from labeled blood in large arteries passing through the region-of-interest only to perfuse a more distal brain region, which can cause CBF overestimation. Recent developments have enabled a significant reduction in these errors, as will be discussed.

In comparison with BOLD, the primary shortcomings of PASL-based fMRI, are poor signal-to-noise (SNR), limited brain coverage (i.e. due to transit delay artifacts), and reduced temporal resolution (i.e. due to tagging delay). In spite of the potential confounds, successful cross-validation of PASL-based CBF measurements using PET has been performed by various groups [109-113] including ourselves [114] (see Appendix III). In addition, microsphere-based cross-validation has also been achieved [115]. The main advantage of ASL is that it provides a direct measure of CBF – a fundamental physiological quantity, which BOLD does not provide. Furthermore, pseudo-CASL techniques, developed based on the principles of both CASL and PASL, can significantly enhance ASL labeling efficiency, and have the potential to substantially increase ASL SNR for fMRI applications [116].

The ASL technique used in this work is called “quantitative imaging of perfusion using a single subtraction II” (QUIPSS II) [103]. The QUIPSS II technique was designed to minimize the effect of transit delay variations on CBF estimation [102]. In QUIPSS II, a saturation pulse is applied to the imaging region prior to tagging to reduce tissue signal contribution. In addition, a saturation pulse is applied to the tagging region at a delay of T_{I1} after tagging to create a well-defined bolus shape [103]. The remaining incoming tagged blood continues to relax towards equilibrium, and after a delay of T_{I2} (to allow inflowing blood to reach imaged slice), the tag image is acquired. Conveniently, T_{I2} can

be selected to achieve a simultaneous suppression of non-perfusion intravascular signal. The QUIPSS II principle can be applied in conjunction with various PASL labeling schemes to maximize brain coverage and SNR while minimizing CBF bias [117].

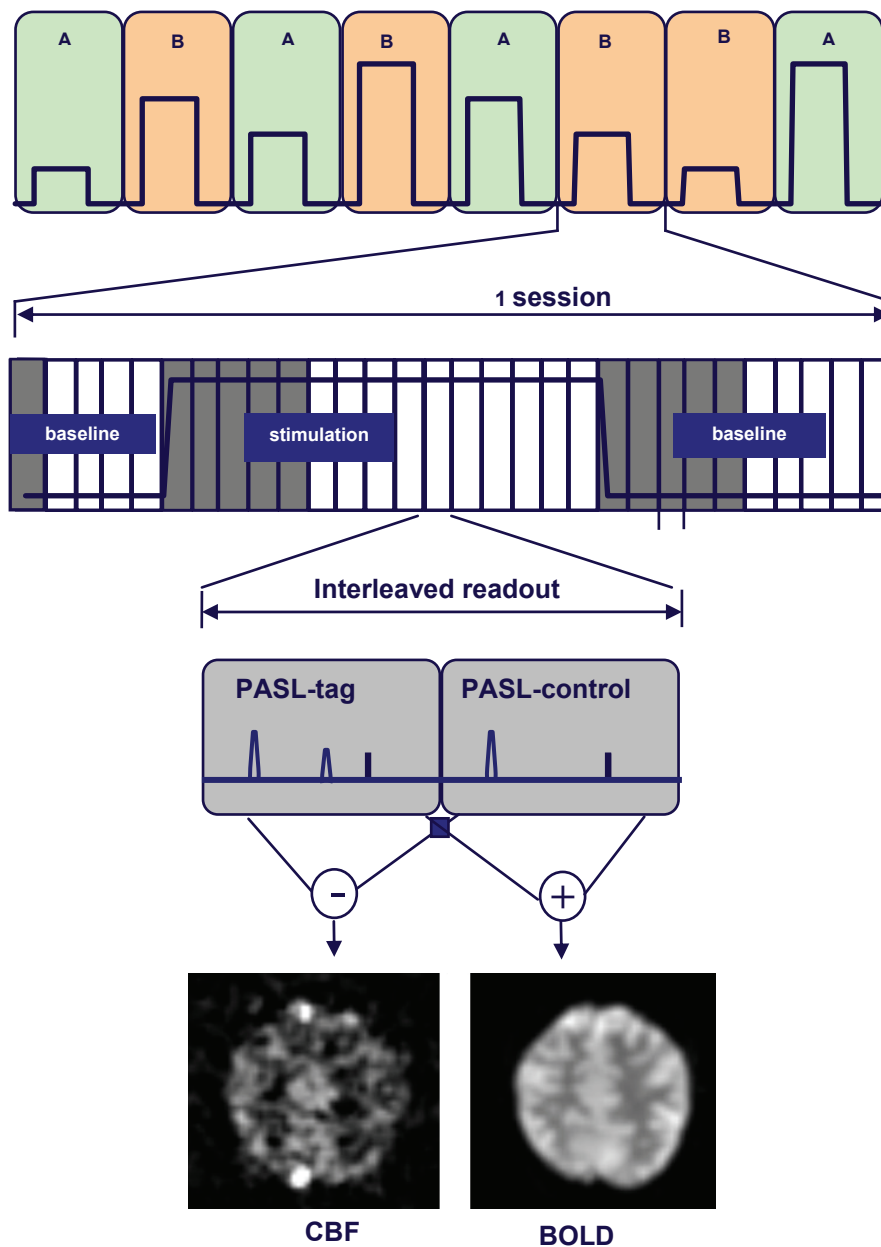


Figure 2.10 Sequence diagram for simultaneous BOLD and CBF acquisition.

A typical fMRI trial with various forms of neuronal stimulation is shown, in which CBF and BOLD are both measured using pulsed ASL (QUIPSS II PASL).

CBF data can be acquired simultaneously with BOLD data by employing an interleaved approach. Alternatively, as shown in Figure 2.10, the average of the control and tag signals is approximately independent of flow (positive and negative blood magnetizations canceling out), and can be used as a BOLD time series, given a sufficiently long TE [102]. At 3 T, the optimal TE for BOLD contrast shortens dramatically [81] relative to its value at 1.5 T, permitting the simultaneous acquisition of CBF and BOLD data using ASL. Finally, profile uniformity and selectivity in the QUIPSSII pre-saturation and labeling pulses contribute significantly to CBF quantification accuracy, and both can be improved using BASSI (bandwidth-modulated adiabatic selective saturation and inversion) RF pulses [118], designed to provide these features at no additional RF power cost. Finally, background suppression has been found to be crucial in CBF quantification, as the limited flow signal can be easily biased and obscured by the dominant static tissue signal [119].

2.5 CBV Measurement

CBV is defined quantitatively as the blood volume in a tissue voxel divided by the mass of that voxel [120, 121]. At normal cerebral perfusion pressure (CPP), the CBV-CBF ratio remains relatively constant over a wide range of CBF values, but when CPP is reduced, a decrease in CBF is compensated by an increase in CBV and OEF, thus achieving autoregulation. This process is integral to the support of neuronal metabolism, especially given the negligible cerebral energy stores. Activation-induced CBV increase has been found to strongly correlate with CBF increase (approximately 0.059 ml/ml-increase-in-CBF [122]), and to respond linearly to neuronal activity [123, 124]. Quantitative and relative CBV have been estimated using radioactive microspheres [125], perfluorocarbon emulsions [126], and very recently, confocal microscopy [41, 127]. These methods are robust but nonetheless highly invasive, with the former two constituting terminal experiments.

Optical imaging techniques (DOT and NIRS) have recently been used in human CBV measurements [90, 91, 128, 129], but finer-scale CBV mapping is prevented limited depth-penetration, low spatial coverage and high modeling complexity for spatial

localization. Spatially-resolved in vivo human CBV estimates can be derived from perfusion PET and CT measurements based on tracer kinetic modeling [85] and the central volume principle [130], although temporal resolution and repeatability are intrinsically limiting factors in these methods, as indicated previously. Most of the current MRI-derived CBV data originate from rapid imaging of a contrast (typically gadolinium-DTPA) bolus followed by analysis using indicator dilution theory [131]. Such was the case in the first human fMRI brain maps, obtained by Belliveau *et al.* [132]. The major shortcomings of this method for functional imaging are poor temporal resolution and the limited repeatability due to the use of exogenous contrast injection.

Steady-state contrast techniques use agents with a long intravascular half-life, which alleviate the requirement for multiple injections and affords monitoring of CBV changes [133]. One such agent, MION (monocrystalline iron oxide nanocolloid), induces susceptibility (R_2/R_2^*) enhancement in proportion to CBV change. MION been used in rats to provide CBV-weighted signals with a five fold increase in CNR over BOLD at 2 T [134] (Figure 2.12), and was shown to provide increased activation detection specificity at 9.4 T (Figure 2.11) [135]. However, while increased field strength augments the sensitivity of MION-based CBV methods, the competing effect of oxygenation change accompanying that of blood volume also becomes increasingly apparent. BOLD effects could potentially obliterate the MION-enhanced CBV-weighted signal at 9.4 T, whether using spin-echo or gradient-echo [136]. Alternative techniques, such as RRST₁ (rapid steady-state T_1) [137], isolate blood by drastically shortening its T_1 using gadolinium-based contrast agents. The RRST₁ technique has been successfully applied to a rat model to yield plausible hypercapnia-induced CBV changes. At this time, dynamic CBV imaging using steady-state contrast enhancement has been limited to animals [138-142], but initial testing of stable blood-pool contrast agents in humans has begun [143]. In general, relative CBV measurements made using contrast-enhanced methods are negligibly affected by partial-volume effects from CSF (although tissue partial-volume effects have yet to be quantified). However, it should be noted that contrast-enhanced methods measure total Δ CBV, while the BOLD signal depends primarily upon venous Δ CBV, and that the relative size and fractional variation in each vascular component of total Δ CBV remains unclear [126, 134, 144, 145]. Furthermore, there is a potential that

hematocrit alterations affect the feasibility of contrast-enhanced methods for transient CBV characterization, and this issue is being actively investigated [146].

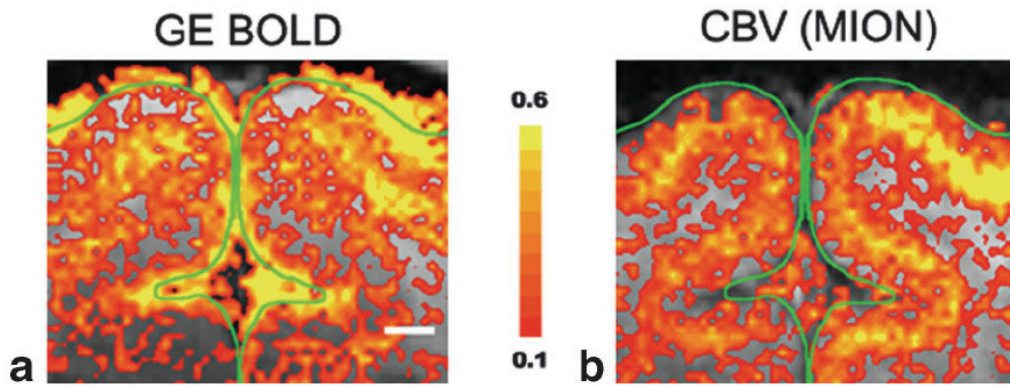


Figure 2.11 Gradient-echo BOLD and MION imaging of activation.

(a) Gradient-echo (GE) BOLD reveals cat visual cortical activation, with the largest BOLD signals observed on the cortical surface (indicated by the green tracing). **(b)** MION-CBV imaging exhibits higher specificity, showing largest changes in the middle cortical layer. (adapted from [147])

To date, three approaches to non-contrast agent-based Δ CBV monitoring for fMRI have been introduced. The simplest, introduced by Lu *et al.*, attempts to isolate blood from tissue based on T_1 differences and has been termed vascular space occupancy (VASO) [148]. This technique consists of a non-selective inversion recovery (IR) sequence with the inversion time (TI) adjusted to null the blood signal. It is assumed that as CBV increases, tissue water moves into the vascular space and is nulled, thereby producing a CBV-proportionate drop in the VASO signal (demonstrated in Figure 2.12). Limitations of the technique include: i) that the assumption of water movement has not been established; ii) that the VASO signal is not directly translatable into CBV; iii) the potential contamination of the VASO signal from multiple sources (*e.g.* changes in blood T_1 , partial volume effects, BOLD contrast, *etc.*); and iv) that VASO is theoretically sensitive to total (not venous) CBV, which is dominated by components that contribute negligibly to BOLD. Due to its heavy reliance on inversion-recovery contrast, the VASO signal can be substantially modulated by partial-volume contributions from stationary tissue and CSF. CSF contamination proved significant [149, 150], especially if the assumption of intravoxel water content conservation (assumption (i)) is violated.

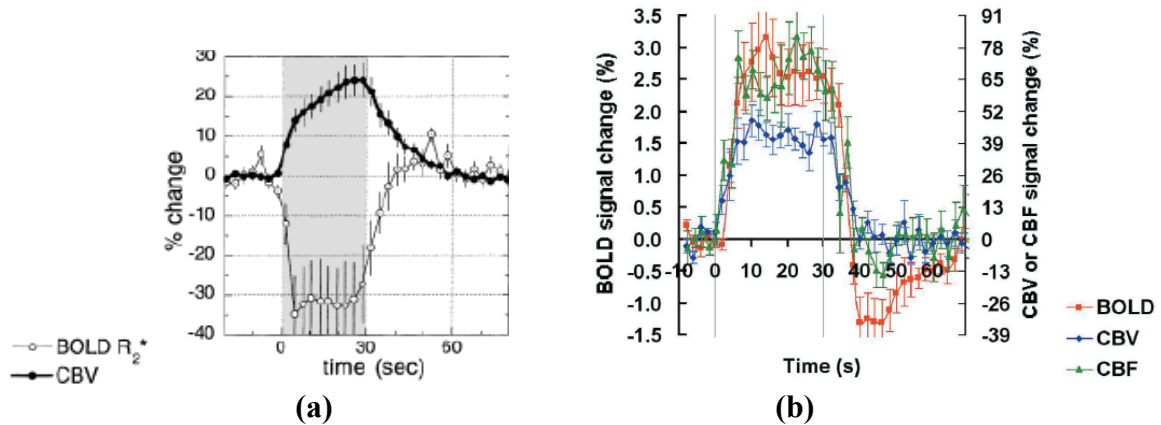


Figure 2.12 CBV measurements by MION and VASO.

The total Δ CBV response: (a) measured using MION imaging in a rat under forepaw stimulation at 2 T [151] and (b) measured using VASO under human visual stimulation at 1.5 T [152]. While MION reveals a lower but less noisy CBV response which recovers slowly, VASO shows a much higher steady-state response accompanied by a quicker recovery. The sources of these differences are yet to be resolved. (adapted from [151, 152])

A second technique, introduced by Kim *et al.*, exploits the magnetization transfer (MT) difference between tissue and blood, and has been termed modulation of tissue and vessel (MOTIVE) [153]. Pulsed MT is used to modulate the tissue signal while ASL or injection of a contrast agent is used to modulate the blood signal. This technique, which the authors indicate is only sensitive to arterial CBV, has been demonstrated in rats at 9.4 T [153, 154]. As MOTIVE relies on the simultaneous use of arterial spin tagging and MT-contrast, it is relatively insensitive to partial-volume effects involving CSF. However, MOTIVE's ability to separate arterial and venous blood contribution at lower field strengths remains ambiguous, resulting in the confinement of MOTIVE to animal studies at ultra-high field [153]. Furthermore, it remains that BOLD is mainly modulated by changes in venous blood volume, and only negligibly influenced by arterial Δ CBV. According to a recent animal study, the fractional change in venous CBV is expected to be far below that of both arterial and total CBV [126]. Therefore, none of the above techniques provides BOLD-specific blood volume characterization.

A third approach, developed in this lab by Stefanovic and Pike [155], sought to isolate venous CBV changes. This is done by exploiting venous blood's unique T_2 relaxation properties, as a function of refocusing interval and oxygen saturation [59, 63, 156, 157]. This method has been named venous refocusing for volume estimation

(VERVE) [155]. The VERVE technique specifically targets venous CBV by taking advantage of the dependence of T_2 in partially deoxygenated blood on oxygenation and the CPMG refocusing interval, alluded to in section 2.2. As a result, the signal intensity measured in venous blood following a train of closely spaced RF refocusing pulses (the fast-refocusing regime) exceeds that resulting from a sparse inversion pulse train (the slow-refocusing regime). The difference between the T_2 -weighted venous blood signals obtained from these two regimes has been shown to be directly proportional to the corresponding venous blood volume change at 1.5 T [155]. The derivation of venous Δ CBV from the VERVE difference signal will be detailed in Chapter 4. The intrinsic dependence of the pair-wise difference VERVE signal on refocusing rate precludes significant impact of partial-volume contamination in VERVE, as partially-deoxygenated blood has been shown to be the only component to significantly exhibit such dependence. As such, VERVE is a particularly powerful and attractive technique for noninvasive functional imaging. However, the T_2 dependence of deoxygenated blood on refocusing rate and oxygen saturation is known to be field-variant, as will be shown in Chapter 3. As blood T_2 behaviour decides the parameterization of VERVE, the transition from 1.5 T to 3 T necessitates a fresh examination of blood relaxometry, which is presented in Chapter 3. In addition, T_2 -weighted imaging at 3 T presents unique challenges due to potential signal biases which were deemed negligible at 1.5 T (as will be discussed in the following subsections). These challenges compel the design of the VERVE sequence to be revised. A detailed description of this development is the chief subject of Chapter 4.

2.6 *CMRO₂ Measurement and BOLD Modeling*

As CMRO₂ is tightly coupled with neuronal activity, it is a highly desirable metric for mapping cerebral function. The baseline steady-state relationship between CBF, CMRO₂ and CMR_{glu} suggests that almost all glucose undergoes oxidative metabolism [158]. Human PET has conventionally been used to assess CMRO₂ (¹⁵O-O₂ PET) [159] as well as CMR_{glu} (¹⁸F-FDG PET) [160]. However, the substantial scan time precludes dynamic metabolic monitoring, while the limited half-lives of the radioisotopes constrain the availability, SNR and spatial resolution of PET measurements. Optical methods have also

been used to measure CMRO_2 owing to their inherent oxygen-sensitivity [161], but are characterized by the same limitations that exist for perfusion measurement. Finally, MR spectroscopy (MRS) can be used for noninvasive macroscopic CMRO_2 (^{13}C , ^{17}O and ^{31}P MRS) and CMR_{glu} (^{19}F MRS) estimation [159, 162, 163] based on similar principles as used in PET. Notwithstanding the powerfulness of hetero-nuclear MRS in studying metabolism, metabolic mapping is inherently precluded. BOLD-based CMRO_2 measurement has flourished in recent years due to the relatively high versatility and spatial resolution of MRI, as well as the dynamic nature and robustness of the BOLD signal. However, as an oxygenation-based technique, BOLD functional mapping hinges on the question of “to what extent are activation-induced increases in ATP demand met through oxidative versus anaerobic metabolism of glucose”, which has been the subject of intense debate [44, 164-167].

In spite of early PET work (based on H_2^{15}O and $^{15}\text{O}_2$ methods [168, 169]) indicating that CMRO_2 was essentially invariant even during episodes of intense neuronal stimulation [168, 170], evidence for substantial CMRO_2 changes has accumulated in subsequent studies using PET [171-173], optical methods [4, 161], MRS [163] and MRI [5, 174-182]. There is now a general consensus that fractional changes in blood flow are normally accompanied by smaller but consistent changes in CMRO_2 , with $\Delta\text{CBF}:\Delta\text{CMRO}_2$ ratios (n) of approximately 2 to 4. As alluded to earlier, the oxygen limitation theory attributes this imbalance between CMRO_2 and CBF to the limited diffusion rate of O_2 from the capillaries to tissue [6, 176, 183-185]. However, results from ourselves [49] and others [55, 186-189], which show decreased BOLD yet preserved CBF activation responses during global CBF increases, do not support this theory.

Various models have been proposed to enable CMRO_2 measurements through fMRI based on simultaneous CBF and BOLD acquisitions, BOLD signal modeling, and hypercapnia calibrations [5, 174, 190]. These models, which primarily address the extravascular BOLD effect due to bulk susceptibility effects and intravascular BOLD contrast due to changes in venous oxygen saturation, form the basis of the calibrated BOLD technique. With the aim of integrating previous models into a unified formalism while facilitating the prediction of BOLD dependence during neuronal stimulation as well as

hypercapnia, this lab has introduced a steady-state deoxyhemoglobin dilution model of the BOLD signal, as detailed in Ref. [5],

$$\frac{\Delta BOLD}{BOLD_0} = M \left(1 - \left(\frac{CMR_{O_2}}{CMR_{O_2}|_0} \right)^\beta \left(\frac{CBV}{CBV_0} \right) \left(\frac{CBF}{CBF_0} \right)^{-\beta} \right) \quad [2.3]$$

where $M \equiv TE \cdot A \cdot CBV_0 \cdot [Hb]_{v0}^\beta$. In this equation, $[Hb]_{v0}$ is the deoxyhemoglobin concentration at baseline CBV, A is a field strength- and sample-specific proportionality constant, and β is a constant in the range $1 < \beta < 2$ [28, 72], accounting for contributions from the intravascular and extravascular BOLD components. The subscript '0' is used here and elsewhere in the text to refer to the baseline value of a variable. The term M , which has been found to be spatially variant [49], is approximately equal to the fractional BOLD signal attenuation that occurs due to deoxyhemoglobin at baseline, and therefore represents the maximum possible BOLD response [174], as illustrated in Figure 2.13. Note that in the interest of minimizing neuronal metabolism modulation and oxyhemoglobin dissociation caused by CO_2 -related acidosis, mild hypercapnia should be used for BOLD calibration [191].

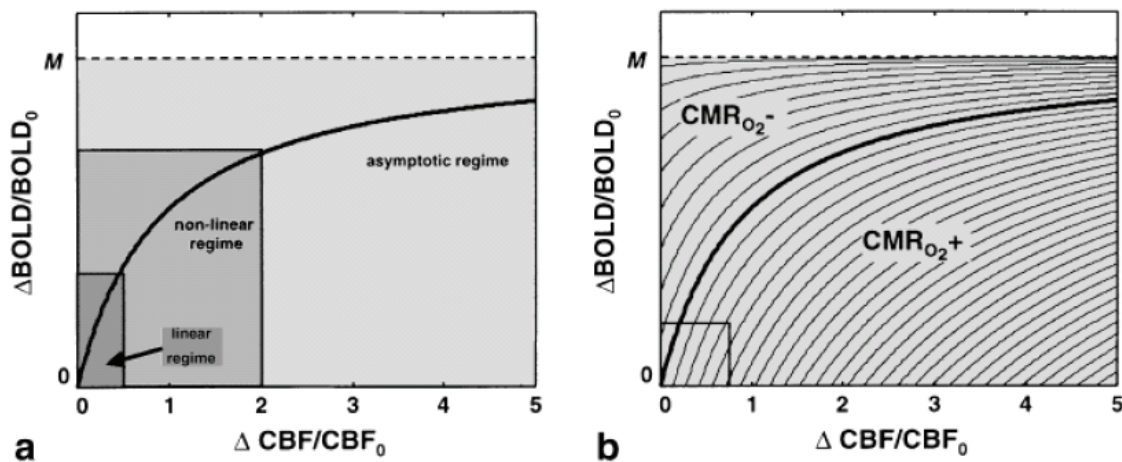


Figure 2.13 The deoxy-hemoglobin dilution model.

The relationship between BOLD, CBF and CMR_{O_2} : (a) the predicted BOLD signal increases linearly with CBF up to a change of 50%. At very high CBF values, the BOLD signal ceases to increase further, but instead shows an asymptotic upper limit. (b) The iso- ΔCMR_{O_2} contours, increases in CMR_{O_2} results in BOLD signal decrease. (source: [192])

Although calibrated BOLD has been applied primarily to steady-state (block-design) $\Delta\text{CMR}_{\text{O}_2}$ quantification [5, 174], the increasing popularity of event-related fMRI paradigms in numerous applications highlights the importance of validating the calibrated BOLD methodology for transient $\Delta\text{CMR}_{\text{O}_2}$ estimation [193]. Recent multi-modal imaging and electrophysiology studies of the rat somatosensory system [123, 124, 194] have suggested a broadly sustained linearity between neuronal activity and each individual hyperemic component of the BOLD model under impulse stimulations at various intensities and frequencies, all within the typical time window of the transient hemodynamic response. However, given the potential temporal mismatch amongst the responses underlying the transient BOLD signal, the extent to which CMR_{O_2} can be accurately quantified dynamically using the current BOLD model is still unclear. Nonetheless, the above findings lay the foundation for the eventual application of the calibrated BOLD method for monitoring cerebral energetics at higher temporal resolution.

Most human fMRI studies probing the basis of the BOLD signal [6, 70, 174, 176, 178-180, 195-198] have, in the past, assumed a consistent functional relationship between steady-state blood flow and volume, independent of the origin or mechanism of the flow change. The most widely used empirical relationship between CBF and CBV is that obtained by Grubb *et al.* [46] in anesthetized rhesus monkeys based on hypercapnia-induced global hemodynamic changes, and is given in the form of

$$\frac{\text{CBV}}{\text{CBV}_0} = \left(\frac{\text{CBF}}{\text{CBF}_0} \right)^\alpha \quad [2.4]$$

where $\alpha = 0.38$. This expression permits ΔCBV to be estimated from MRI measures of ΔCBF . However, while our preliminary VERVE data [155] and the results of others [151, 199, 200] are in general concordance with Grubb's formulation, it remains that BOLD is modulated by venous CBV changes, instead of by total CBV, as is described by Grubb's study. Furthermore, the steady-state flow-volume relationship is not expected to hold during transients [201], and is questionable for neurovascular pathologies. The development of techniques for non-invasive venous CBV measurement is therefore of tremendous general interest.

2.7 BOLD Signal Dynamics

While our understanding of the steady-state relationships between CBF, CBV, CMRO_2 and BOLD has improved substantially in recent years, the transient behaviour of these parameters immediately following the onset and offset of neural stimulation remains unclear and disputed. In addition to being of importance for activation detection in fMRI statistical analysis [202-204], the transients have been implicated as potentially more spatially precise markers of neuronal activation than their steady state counterparts [205-207]. For instance, the ‘initial dip’ in the BOLD response, a small negative response which may occur 2 to 4 s following the stimulus onset, has been observed in several studies [205, 206, 208-212], yet its existence and significance has been contentious [213, 214]. The initial dip has been suggested to reflect a rapid focal increase in CMRO_2 at the site of increased neuronal activity. Support for this postulate has also come from optical imaging studies that measured an immediate surge in deoxyhemoglobin (dHb) in activated ocular dominance columns, followed by a rise in oxygenation in the sub-pial venules overlying the active cortical region 2-3 s after the stimulus onset [4].

A more prominent and robust transient in the BOLD signal is the relatively long (10-30 s) post-stimulus undershoot [215], as conceptualized in Figure 2.14. This phenomenon is widely observed, both using GE BOLD [216-218] and SE BOLD [77, 219]. It is in general more pronounced in the former case, suggesting an intra- as well as an extravascular contribution. The precise origins of this undershoot are uncertain and much debated. To date, three theories of the origin of the BOLD post-stimulus undershoot prevail: i) a CBF undershoot (perhaps associated with an undershoot in neuronal activity) [216]; ii) a delayed and slow return of venous CBV to baseline [134, 215]; and iii) a prolonged elevation in CMRO_2 [152]. Resolving this issue is of considerable importance for assessing the spatial specificity of the response, and for our general understanding of cerebral physiology. Among others, the Balloon Model, which was presented by Buxton *et al.* [215] as an integrated dynamic model of the BOLD response (Figure 2.14), has been used to interpret the BOLD undershoot from a biomechanical perspective, via a slow venous CBV response.

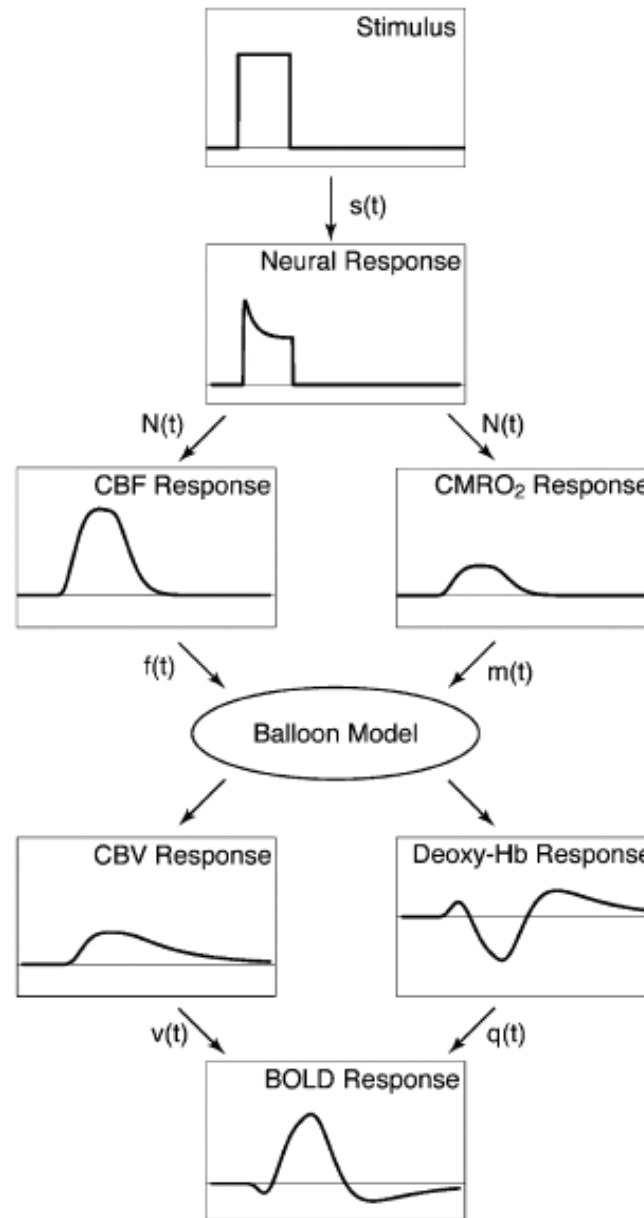


Figure 2.14 Generation of BOLD transient response by the Balloon Model.

The stimulus, $s(t)$, drives the neuronal response, $N(t)$, which in turn drives the CBF response, $f(t)$, and the $CMRO_2$ response, $m(t)$. Both of these drive the Balloon Model, producing the CBV and dHb responses, $v(t)$ and $q(t)$, which produce the BOLD signal. (source: [215])

The Balloon Model includes considerations for: i) the BOLD signal as a function of CBF, CBV and $CMRO_2$; ii) the viscoelastic properties of the cerebral vasculature (*i.e.* the balloon [215, 220]); iii) neurovascular coupling; and iv) the temporal nonlinearity of the neuronal response. While the Balloon Model can reproduce all the transient features

discussed above, experimental validation has yet to be achieved. In addition, recent cortical electrophysiological recordings in primates demonstrate clear post-stimulus undershoots in neuronal activity, which may be the source of the CBF undershoots, and explain a major portion of the BOLD undershoot [221]. This finding, which would link the BOLD undershoot to cortical neuronal behaviour, would provide interesting insights when interpreted in conjunction with the emerging evidence of an intricate spatial dependence of the undershoot [219, 222, 223]. The above observations indicate that the BOLD undershoot is a highly complex phenomenon, the origins of which can only be unraveled by being able to experimentally measure all contributors of the BOLD signal.

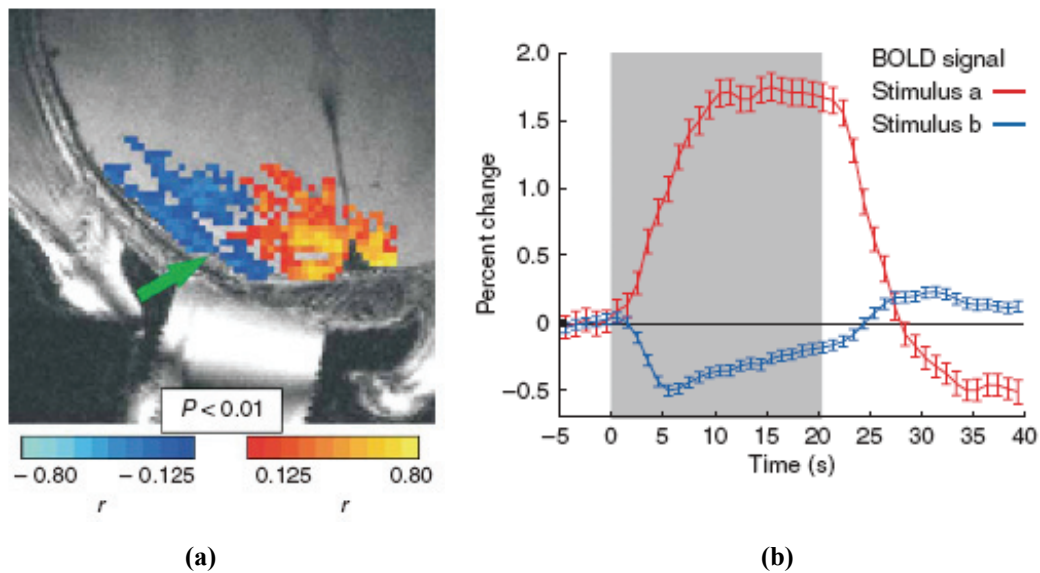


Figure 2.15 Positive and negative BOLD responses in the primate visual cortex.

The ROIs (a) corresponding to the positive and negative BOLD signals (b) do not overlap. Furthermore, temporal characteristics in the positive BOLD signal are mirrored by the negative BOLD time course. (adapted from [221])

Sustained negative BOLD responses accompanying positive BOLD changes have also been widely observed (Figure 2.15), but there has been much debate as to the source. This phenomenon is to be distinguished from the initial-dip and post-stimulus undershoot, as it possesses a steady state analogous to that of the positive BOLD steady-state signal [181, 221]. The magnitude and extent of the negative BOLD response has been found to vary widely with the stimulation condition [224-226]. Sustained negative BOLD has

been attributed to a negative hemodynamic response [227], possibly via blood theft by cortical regions neighbouring an area of activation, as well as to a negative neuronal activity response (relative to the defined baseline condition) [221, 225], possibly due to neuronal inhibition [228]. However, as negative BOLD observed in the hemisphere contralateral to the neuronal activation cannot be explained by arterial blood diversion [181, 229], neuronal inhibition has been explored as the dominant cause. The inhibition may be necessary during tasks requiring a high level of attention or dexterity, in which the baseline activity of certain cortical areas is suppressed to enhance concentration [227, 230], although a contribution of vascular/hemodynamic origin cannot be excluded from consideration [221, 227].

2.8 High-field Imaging

The migration of neuroimaging to higher field strengths has received overwhelming support in recent years, due to the potential for achieving higher SNR, enhanced contrast, increased spatial resolution and shorter acquisition time.

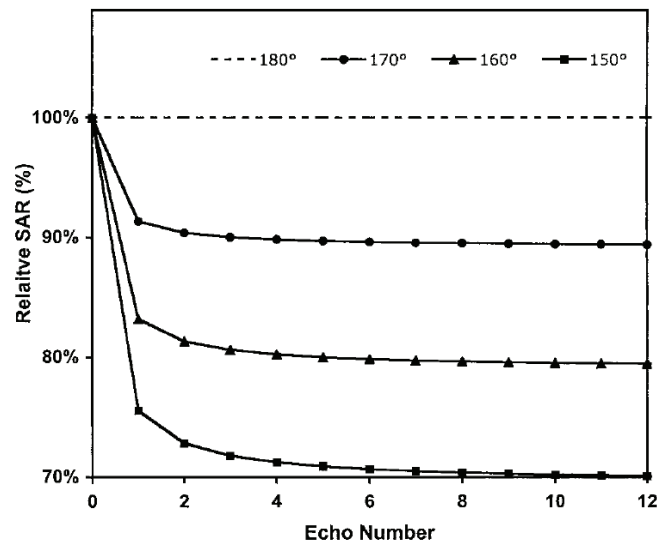


Figure 2.16 The relative specific absorption rate (SAR) for turbo spin-echo.

The average SAR can be substantially reduced by decreasing the refocusing flip angle. However, with 150° refocusing pulse train, the refocusing efficiency is reduced by 30%, hence decreasing SNR. (source: [231])

The term “high-field” has customarily been used to refer to field strengths of 3 T and above [73, 231]. Currently, while 1.5 T is still the clinical standard field strength, the use of 3 T clinical scanners is on the rise. In addition, 7 T human-imaging systems are increasingly used in research, and since 2004, 9.4 T magnets have also been applied to human studies. Needless to say, the definition of “high-field” will continue to evolve with time, as higher field strengths become feasible. While the magnitude of the associated benefits varies with the application, high-field imaging has also introduced new technical challenges and safety considerations. Currently, an overwhelming majority of fMRI research studies are conducted at 3 T, which has become the de facto fMRI standard. Compared to imaging at 1.5 T, 3 T systems offer the benefits of high-field imaging; compared to imaging at higher fields, 3 T imaging steers clear of the majority of the increasingly complex biological interactions [232] while remaining relatively affordable.

2.8.1 Relaxation Characteristics

The most fundamental difference between imaging at 3 T and at 1.5 T is in the relaxation times of various tissues, as T_1 , T_2 and T_2^* can be approximated as functions of B_0 . For instance, GM T_1 has been found to increase from approximately 1000 ms at 1.5 T to 1331 ms at 3 T, while GM T_2 sees smaller variations [233-237]. GM T_2^* , however, decreases drastically due to enhanced local static field inhomogeneities with rising B_0 . This decrease has been cited to be as much as from 65 ms to 28 ms [238]. Generalizing to all tissue types, T_1 at 3 T not only lengthens as predicted by the empirical formula of Fischer *et al.* [239], but also converges for different tissue types, while T_2^* decreases supra-linearly with increasing B_0 . No field dependence was predicted for T_2 by the Purcell-Pound theory of relaxation, and yet, possibilities of cross-relaxation with macromolecules and chemical exchange, as well as dynamic averaging, all exhibit field-dependence and may potentially lead to T_2 shortening at 3 T. Dynamic averaging effects, which result from water diffusion, scale supra-linearly with B_0 [157], and have recently been found to be the dominant T_2 relaxation mechanism for water at 7 T [240]. Overall, the T_2 and T_2^*

shortening can result in increased image blurring and distortions, but also higher fMRI contrast, as will be discussed later.

The changes in relaxation rates have advantages as well as disadvantages. Sequence repetition times can lengthen because of the T_1 increase. In order to maintain acquisition speed, the acquisition bandwidth would have to increase. In addition, good T_1 contrast (i.e. for ASL) becomes more difficult to obtain using sequences with short TR, short TE and high flip angles, and magnetization preparation for contrast-enhancement becomes essential.

2.8.2 SNR and RF Characteristics

Theoretically, the available magnetization, and hence the MR signal, rises linearly with the field strength. In practice, with a B_0 increase from 1.5 T to 3 T, an SNR improvement between 1.3 and 2.1 times in various brain tissues has been reported in practice [231], with the improvement factor proportional to tissue water content. The corresponding implications on functional imaging will be discussed in the subsequent sections.

While SNR increases with increasing B_0 , a concomitant increase in B_1 inhomogeneities makes the signal gain increasingly non-uniform. B_1 inhomogeneities arise from dielectric resonance of the RF field within brain tissue, and as B_0 increases, the corresponding effective wavelength of the B_1 becomes shorter and increasingly comparable with the dimensions of the human head. B_1 inhomogeneities can lead to substantial variations of the phase and amplitude of the B_1 field with position, which implies that the local signal strength may depend on the sample's shape, permittivity and conductivity [73]. B_1 inhomogeneities can result not only in signal attenuation, but also in the production of spurious echoes which contaminate the desired signal. The effect of both sources of error is enhanced at higher fields, further highlighting the need for corrective measures as well as RF cycling schemes [1].

With regard to the dependence of RF power on B_0 , the square-law relationship holds for proton Larmor frequencies of up to 200 MHz. Thus, a pulse sequence when run on a 3 T system (Larmor frequency = 128 MHz) could deposit 4 times as much power into the sample as when run at 1.5 T with the exact same parameters. Consequently,

constraints on the specific absorption rate (SAR) place significantly greater limitations on the design of many pulse sequences, especially those relying on multiple 180° refocusing RF pulses [231], including VERVE. As the average SAR is proportional to the sum of the square of flip angles of all RF pulses in the sequence divided by the sequence duration, lengthening the TR can result in substantial SAR reduction. In addition, schemes for low-SAR refocusing trains have been developed [241, 242], in which refocusing flip angles are reduced to well below 180° while sufficient signal consistency is still achieved.

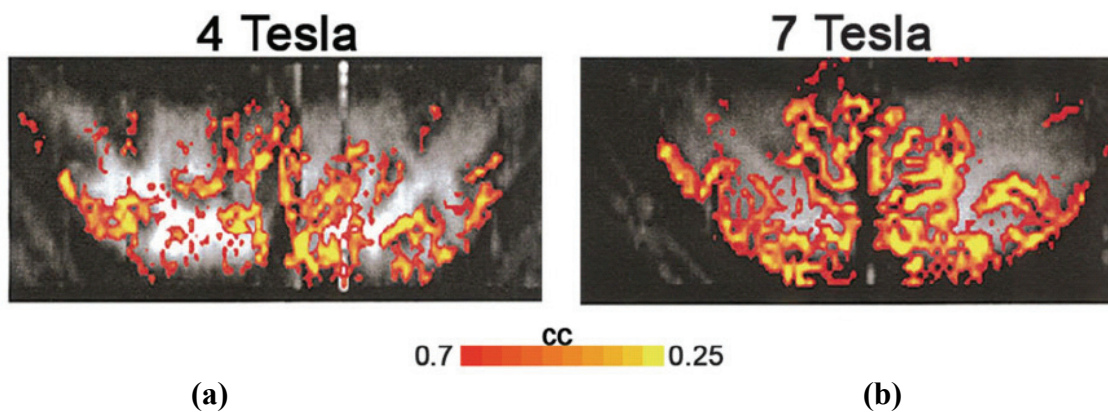


Figure 2.17 Spin-echo BOLD sensitivity variation with field strength.

Due to an increase in SNR, SE BOLD sensitivity is significantly enhanced at high field, demonstrated via activation maps thresholded at the same statistic significance at 4 T and 7 T. The increased SNR also permits the use of higher spatial resolutions, in this case voxels of $1 \times 1 \times 3 \text{ mm}^3$. (adapted from [77])

2.8.3 Functional MRI

The oxygenation dependences of the BOLD effect in the physiological oxygenation range at low and high field are similar. In pure parenchyma, the intravascular BOLD signal originates predominantly from venules for all TEs at low field, and for short TEs at high field. In GE BOLD, the intravascular contribution from draining veins has been shown to dominate intravascular signal change at 1.5 T [243, 244], contributing up to two thirds of the total BOLD signal. Intravascular contribution continues to be significant at high field, amounting to 50% of BOLD contrast [75] at 3 T and 4 T [74].

One of the main driving forces behind a shift to higher fields has been the belief that BOLD contrast would increase significantly with increasing B_0 [73]. It has been

experimentally determined that BOLD sensitivity to microvascular susceptibility alterations improves substantially at high field [231], as illustrated in Figure 2.17. However, the dependence of BOLD contrast on B_0 is complex, as several mechanisms contribute to the total BOLD contrast (see section 2.3). Irrespective of the mechanism, the optimal gradient-echo TE for detecting activation decreases with increasing B_0 , which increases the strength of static dephasing and hence decreases GM T_2^* .

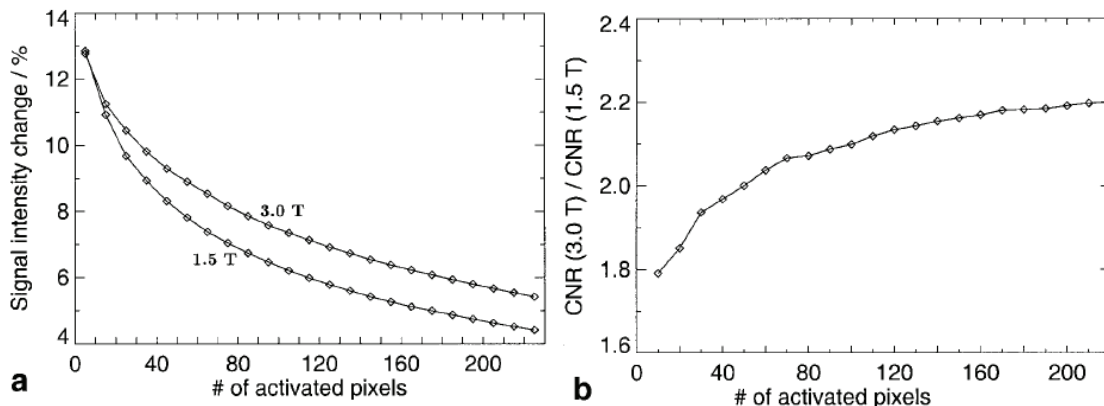


Figure 2.18 BOLD contrast variation with field strength.

The average percent BOLD signal change is higher at 3 T than at 1.5 T (a), while the signal change in the smallest ROI is similar at both fields. Furthermore, the contrast-to-noise (CNR) at 3 T greatly exceeds that at 1.5 T (b), and increases with area of activation. (adapted from [238])

As briefly stated previously, at a given TE, the intravascular BOLD contribution becomes progressively weaker with increasing B_0 as a result of venous T_2^* and apparent T_2 reduction [77, 238]. Thus, the contribution of large vessels to GE BOLD is expected to decrease relative to that of the microvasculature at higher fields [77], resulting in higher microvascular specificity in BOLD maps [73]. Therefore, while one third of GE BOLD at 1.5 T originates from the extravascular dephasing associated with draining veins [72], the relative contribution from capillaries has shown a two-fold increase at 3 T by virtue of enhanced dynamic averaging effects [238]. However, as B_0 increases further, the influence of dynamic averaging at the level of the microvasculature will decrease relative to that of static averaging. Once static averaging becomes the dominant signal source from the capillary bed, further increases in B_0 will not lead to increases in capillary contribution to the total GE BOLD signal relative to large vessels [73].

The quantification of BOLD T_2^* effects becomes more difficult at high field due to susceptibility increase and the resultant signal drop-out, making SE BOLD increasingly viable. While the SE BOLD signal is restricted to intravascular contribution from large vessels at 1.5 T, microvascular signal contributes 50% to the SE BOLD signal at 3 T. Due to the supra-linear field dependence of the BOLD effect size on venous blood oxygenation, dynamic averaging effects, which pertain to the microvasculature, will increase significantly, making SE BOLD more feasible at field strengths above 3 T, as illustrated in Figure 2.17. At very high fields, the SE BOLD signal will arise exclusively from the tissue microvasculature [73].

While a substantial signal increase is expected with B_0 , this increase is not translated directly to the BOLD contrast-to-noise characteristics, as the strongest source of noise in BOLD is physiological noise, the amplitude of which scales with the BOLD signal [81]. Specifically, respiratory and cardiac noise can significantly modulate the local magnetic field, creating additional susceptibility gradients. As described earlier, both of these effects will increase with field strength, potentially undermining the B_0 -related contrast gain (see Figure 2.18), and highlighting the importance of optimal imaging parameter selection. Lastly, increased susceptibility effects, which result in drastic T_2^* reduction with increasing B_0 , can result in heightened ghosting and geometric distortions in GE echo-planar imaging (EPI) acquisition, which is most commonly used in fMRI. Thus, the importance of correcting for image distortions is heightened at higher fields [231], especially in areas proximal to air-tissue interfaces.

Finally, perfusion-based fMRI has potentially superior localization compared to BOLD. CBF is measured directly with ASL instead of with BOLD, which depends on a complex interplay of multiple physiological parameters including CBF [73]. However, as perfusion images have substantially lower SNR than those of BOLD, the latter has had an unchallenged dominance in fMRI. Nonetheless, Wang *et al.* [117] provided evidence that due to a field-dependent T_1 prolongation, ASL sensitivity increases directly with B_0 . Of course, this can only happen through optimization of imaging sequence parameters, taking into account T_2/T_2^* shortening. Similar concerns pertain to CBV measurement, and the development of techniques for VERVE venous CBV measurement at 3 T which accounts for the above concerns will be discussed in detail in Chapter 4.

Chapter 3

Deoxygenation-Induced Transverse Relaxation Effects in Blood at 3 Tesla

3.1 Preface

A major premise of the venous refocusing for volume estimation (VERVE) technique, the continued development of which is a main target of this thesis, is that the T_2 of partially deoxygenated blood varies with the CPMG refocusing interval (τ_{180}) and oxygen saturation (Y) in a predictable fashion. While this has been established at 1.5 T, with the conclusion that blood T_2 behaviour can be more accurately characterized by the diffusion model proposed by Jensen and Chandra [61] than using the Luz-Meiboom two-site exchange model [245], the substantial variability of T_2 relaxation properties with magnetic field strength makes the quantification and parameterization of blood T_2 at 3 T a necessary and important step in the development of the VERVE technique for high-field applications. In addition, an accurate knowledge of blood T_2 variation with field strength, which influences the relative intra- and extra-vascular BOLD contributions, underlies a correct understanding of the BOLD signal [77, 246].

In this chapter, detailed *ex vivo* whole human blood T_2 relaxometry experiments at 3 T are documented. A wide range of venous blood oxygenation levels was achieved using *in vivo* oxygenation modulation, and a comprehensive set of CPMG refocusing intervals was employed to probe the T_2 dependence of whole venous blood samples on Y and τ_{180} . The results indicate that the diffusion model remains superior to the exchange model in representing whole blood T_2 behaviour at 3 T. In addition, for the benefit of BOLD functional imaging, T_2 dependence on oxygenation at 3 T was found to be enhanced relative to 1.5 T, increasing the microvascular signal contribution and hence

specificity in activation localization [247]. However, this increase will likely be smaller than previously predicted, as the blood T_2 enhancement with B_0 was found to be linear, rather quadratic, as previously suggested in the literature. Supplementary results pertaining to these experiments but not included in the manuscript can be found in Appendix II.

Human Whole Blood T_2 Relaxometry at 3 Tesla

Jean J. Chen and G. Bruce Pike

McConnell Brain Imaging Centre
Montreal Neurological Institute
McGill University

Magnetic Resonance in Medicine 2009; 61: 249-254

3.2 *Abstract*

A precise understanding of human blood spin-spin relaxation is of key importance for numerous applications, particularly functional MRI, which is increasingly performed at 3 Tesla. It is well known that T_2 measured from partially deoxygenated blood depends on the Carr-Purcell Meiboom-Gill (CPMG) refocusing interval (τ_{180}) and on blood oxygenation (Y), yet debate remains over the quantification of this phenomenon, primarily with respect to the accuracy of its characterization by the diffusion and fast two-site exchange models. In this study, a detailed characterization of the deoxygenation-induced T_2 reduction in human whole blood, as well as a comprehensive assessment of the role of τ_{180} , were performed at 3 T. The diffusion model was found to better fit the observed T_2 behaviour than does the exchange model. The estimated diffusion-model parameters suggest the T_2 decay enhancement at 3 T is due to a linear increase in the magnitude of deoxygenation-induced field inhomogeneities with field strength. These findings also confirm the potential of τ_{180} -manipulation in measuring changes in venous blood volume.

Key words: blood relaxometry; deoxyhemoglobin; T_2 ; diffusion; two-site exchange; CPMG refocusing interval; oxygenation

3.3 Introduction

T_2 relaxation enhancement in partially-deoxygenated blood has been widely observed [66, 247-251] and underpins the BOLD fMRI technique. Blood T_2 changes have also been employed to monitor blood oxygenation in vivo [250] and made use of by the venous refocusing for volume estimation (VERVE) technique to measure changes in venous cerebral blood volume [155] at 1.5 T. However, as blood T_2 behaviour is B_0 -dependent, the intra- and extra-vascular BOLD contributions and hence the interpretation of the BOLD signal will vary significantly with B_0 . As the role of high-field imaging continues to grow, so does the necessity for detailed knowledge of whole human blood T_2 behaviour at 3 T.

The unique dependence of blood T_2 on oxygenation, hematocrit, and the Carr-Purcell Meiboom-Gill (CPMG) refocusing interval (τ_{180}) has been explored in simulation as well as in ex vivo MR studies [59, 61-63, 66, 247, 250-253]. However, these studies were largely focused on $B_0 \leq 1.5$ T [59, 63, 66, 251, 253], and many used red blood cell suspensions [62, 66, 248, 249] and stored animal blood [247, 253]. Furthermore, the literature lacks in simultaneous evaluations of the effect of oxygenation [248, 253] and τ_{180} [254] at 3 T. At 1.5 T, Stefanovic and Pike [63] found human blood T_2 relaxation enhancement to be best described by the diffusion model proposed by Jensen and Chandra [61]. These results do not, however, exclude a contribution from concurrent two-site exchange [62, 245]. Moreover, interpretations at 1.5 T cannot be directly extrapolated to 3 T, since the contributions of diffusion and exchange mechanisms to T_2 decay, as well as the respective limitations of these models, vary with B_0 . For instance, at field strengths greater than 1.5 T, Matwiyoff *et al.* predicted that the contribution of diffusion to whole blood T_2 reduction would scale with B_0^2 , but that of exchange would be relatively constant [248]. On the other hand, using the Luz-Meiboom model, Wright *et al.* predicted that the effect of exchange would increase with B_0^2 [59]. Thus, in view of the rapidly expanding use of high-field fMRI, there is great need for a detailed characterization of whole blood T_2 with respect to Y and τ_{180} at 3 T. In this paper, we address the limitations of previous studies by assessing the accuracy of the exchange and diffusion models in describing whole human blood T_2 over a wide range of oxygenation

levels at 3 T using a comprehensive set of τ_{180} values. We also probe the dependence of blood T_2 on both the hematocrit and pH over physiologically relevant ranges.

3.4 Theory

The dependence of apparent blood T_2 on oxygenation (Y) and the CPMG refocusing interval (τ_{180}) [59] is embodied in the term ΔT_2 ,

$$\frac{1}{T_2} = \frac{1}{T_{2,0}} + \frac{1}{\Delta T_2}, \quad [3.1]$$

where $T_{2,0}$ is the intrinsic blood T_2 . The intravascular dephasing of the blood spins is characterized by interactions between deoxyhemoglobin and water, which has been attributed to dynamic dephasing arising from the random diffusive walk of water molecules in the vicinity of the paramagnetic centres of the erythrocytes. Using the weak-field-inhomogeneities approximation of the diffusion model proposed by Jensen and Chandra [61],

$$\frac{1}{\Delta T_2} = G_0 \frac{\gamma^2 r_c^2}{2D} F \left(\frac{2D\tau_{180}}{r_c^2} \right), \quad [3.2]$$

where D is the blood water diffusion coefficient, r_c is the characteristic length of the field inhomogeneities, γ is the gyromagnetic ratio, G_0 is the mean-squared magnitude of field inhomogeneities, and F is defined as found in Ref. [63]. In contrast, assuming rapid intra-extra-cellular exchange of water protons across the cellular membrane, Brooks *et al.* [62, 245] investigated the use of the Luz-Meiboom two-site exchange model for ΔT_2 characterization,

$$\frac{1}{\Delta T_2} = \gamma^2 K_0 \tau_{ex} \left(1 - \frac{2\tau_{ex}}{\tau_{180}} \tanh \left(\frac{\tau_{180}}{2\tau_{ex}} \right) \right), \quad [3.3]$$

where τ_{ex} is the exchange time (i.e. the time constant in the exponential correlation function $K(t)$), and K_0 is the amplitude variance of spatial field inhomogeneities (i.e. $K(t=0)$). Stefanovic and Pike proved the diffusion model to better characterize whole human blood T_2 at 1.5 T [63], although other authors found T_2 behaviour to be well approximated by the exchange model [62, 245]. The predicted accuracy of the exchange model was limited in the intermediate-echo regime [245], in which most fMRI interest lies. Furthermore, the paucity of knowledge on the T_2 behaviour of whole human blood at high field coupled with the potential B_0 -dependence in the relative accuracy of these models necessitate a detailed examination at 3 T.

3.5 Methods

Whole blood specimens were obtained by forearm venipuncture from 10 healthy human subjects (5 males/females, age mean \pm SD = 29.2 \pm 7.6 years), all with informed consent (Research Ethics Board, Montreal Neurological Institute). In vivo oxygenation modulation was performed per Ref. [63]. Four blood samples were obtained per subject -- sample 1: at rest; samples 2 and 3: after 2 and 4 minutes of arm exercise, respectively; sample 4: 15 seconds after pressure cuff removal. The samples were sealed in 3 mL blood-gas syringes (diameter = 9 mm, with balanced 25U heparin, Westmed, Tucson, AZ, USA,) immediately after air bubble removal. The scans began within 5 minutes of the final blood draw, such that the effects of residual metabolism were minimized.

All MR experiments were performed on a Siemens Trio 3 T system (Siemens, Erlangen, Germany) with a quadrature transmit-receive head coil and using $MnCl_2$ -doped fluid phantoms with physiologically relevant T_2 's. A magnetization-prepared segmented EPI sequence [63], which had been shown to provide consistent T_2 estimates, was chosen due to its ability to achieve very short τ_{180} . Nonetheless, experimental verification was repeated against a conventional multi-echo SE CPMG technique [255] as the gold standard, at $\tau_{180} = 8, 10, 12, 17.5, 20, 24$ and 37.5 ms; both sequences used nonselective composite 180° pulses. The number of acquired echoes in the CPMG sequence was adjusted such that the same range of the T_2 decay curve was sampled. The T_2 fitting procedure is described under Data Processing. The segmented EPI and the CPMG

techniques were found to produce statistically indistinguishable T_2 estimates over all τ_{180} 's and T_2 's (data not shown). However, segmented EPI, which acquired fewer echoes than the standard CPMG technique at short τ_{180} 's, resulted in higher uncertainty.

The blood-gas syringes were placed in a custom-built MR-compatible apparatus to be rotated on their long axis at approximately 20 rpm during scan dead times to prevent erythrocyte sedimentation while motion artifacts are minimized. T_2 decay was measured using 13 τ_{180} 's --- 2, 2.5, 3, 3.5, 4, 5, 6, 8, 10, 12.5, 17.5, 27.5 and 37.5 ms. The TR was 3 s and the FID was sampled using segmented EPI echo-trains with a length of 3 and a readout bandwidth of 616 Hz/pixel. The imaging slice had 64 x 64 voxels (size = 1.56 x 1.56 x 5 mm³), and ran through the centre of the 50 mm long blood-filled sections of the syringes (parallel to the static field), positioned at the isocentre of the magnet. Each scan session lasted approximately 90 minutes, over which the sample temperature was measured at 20.1 ± 2.2 °C (mean ± SD). Immediately after the scans, blood gas analysis was performed (Bayer, Leverkusen, Germany) to assess the oxygenation (Y), hematocrit (Hct) and pH, calibrated for ex vivo temperature.

T_2 was calculated using unconstrained least-square mono-exponential fitting to the average signal measured in manually demarcated regions-of-interest. Data falling within 2 SD's of the average noise magnitude were excluded, and the T_2 estimated from the remaining data were fitted to the diffusion (Eqs. [3.1-3.2]) and exchange (Eq. [3.3]) models using nonlinear least-square minimization (LSQ). The uncertainty (SD) in each T_2 measurement was calculated as the standard error of the nonlinear fit, and later used in the weighted diffusion and exchange model fits, in the constrained and unconstrained mode. In the constrained mode, $T_{2,0}$ was calculated for the resting-state oxygenation for each subject and applied to all remaining oxygenation levels, whereas in the unconstrained mode, $T_{2,0}$ was free to vary with oxygenation and obtained from individual best fits. Weighted and unweighted LSQ fits were both evaluated, with the residuals tested to ensure a normal distribution. Model accuracies were assessed using the sums of squared-residual (SSR) and chi-squared (χ^2) values. The relationship between oxygenation and the magnitude scale of the field inhomogeneities (K_0 in the exchange model and G_0 in the diffusion model) was quantified through weighted LSQ fitting, evaluated using the SSR and the normalized mean-squared error (NME = mean-squared-error/SD). Furthermore,

correlations between $T_{2,0}$ and oxygenation, hematocrit and pH, as well as the interaction between oxygenation, hematocrit and pH, were assessed using linear regression.

3.6 Results

A 2% oxygenation (Y) decrease was expected from scan-related delays. The blood oxygenation (Y) averaged 72 ± 26 % at rest (sample 1) and 82 ± 18 % post-exercise (sample 4), ranging overall from 20% to 98%. The group-average pH was 7.540 ± 0.060 (mean \pm SD), ranging from 7.372 to 7.613. The group hematocrit was 42 ± 4 % (group mean \pm SD), ranging from 35% to 53%. Oxygenation and pH were positively correlated ($P < 0.05$), but no relationship was observed between pH and hematocrit ($P = 0.55$) or hematocrit and oxygenation ($P = 0.12$).

The average estimation uncertainty associated with the T_2 values was 30.4 ms, as calculated across all oxygenation levels and refocusing intervals. Since the weighted fits demonstrated lower stability and did not always converge, unweighted fitting was used. The T_2 estimates and corresponding fits to both the constrained and unconstrained exchange and diffusion models are shown in Fig. 1. The unconstrained diffusion model produced a lower SSR than the constrained version (0.0031 s² vs. 0.0038 s², $P < 0.05$) as well as a lower NME (1.25×10^{-4} vs. 1.45×10^{-4}) and χ^2 -statistic (5.56 vs. 6.63). On the other hand, constrained exchange model fits (SSR = 0.0053 s², NME = 1.69×10^{-4} , $\chi^2 = 8.31$) were better ($P < 0.05$) than unconstrained (SSR = 0.0069 s², NME = 2.02×10^{-4} , $\chi^2 = 10.09$). The value of ΔT_2^{-1} was estimated for the unconstrained diffusion (Fig. 2a) and constrained exchange (Fig. 2b) models based on the T_2 fits and their respective $T_{2,0}$ estimates. Differences between the models are visually evident particularly at short τ_{180} and high Y levels.

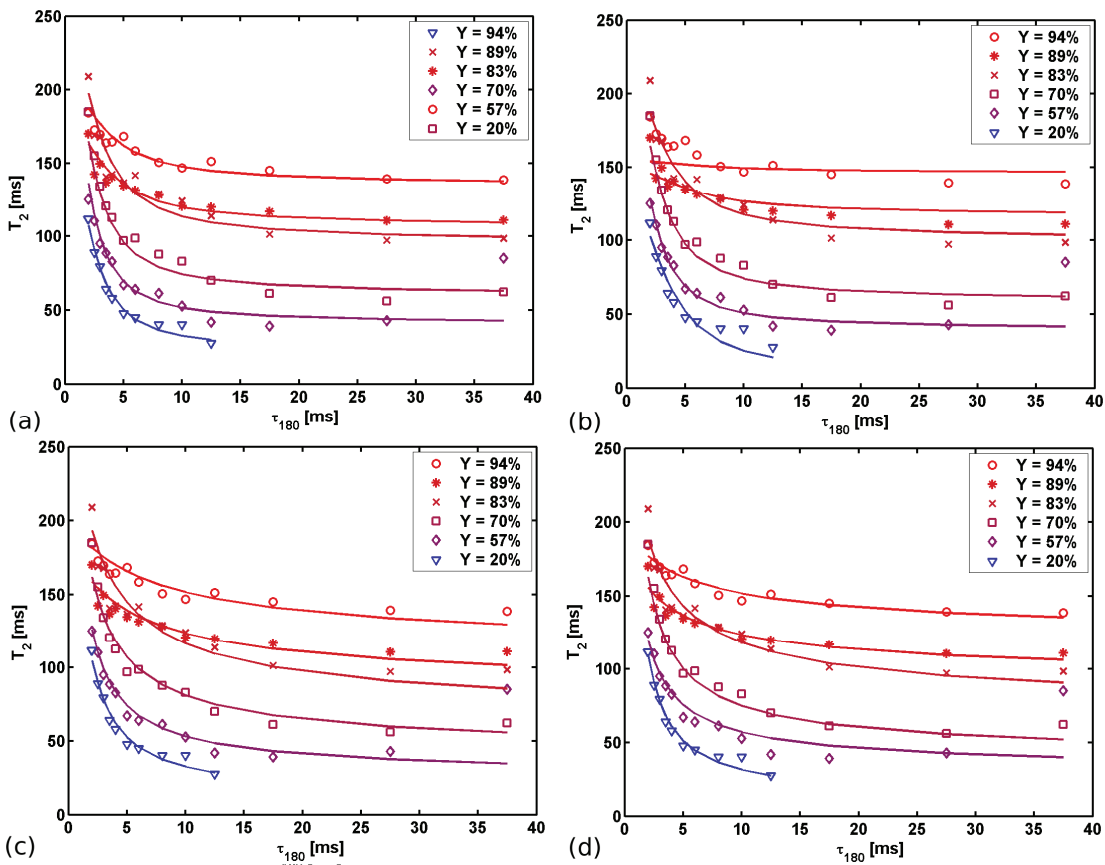


Figure 3.1

Whole human blood ex vivo T_2 relaxometry data from select subjects collected at 3 T (open symbols), shown with the fit (solid line, with oxygenation level colour-coded) to the constrained (a) and unconstrained (b) exchange model, as well as the constrained (c) and unconstrained (d) diffusion model. The estimated venous blood T_2 values, obtained using a T_2 -prepared segmented EPI sequence, demonstrate a strong dependence on blood oxygenation (Y) and refocusing interval (τ_{180}), and are better described by the diffusion model. Venous blood oxygenation was modulated *in vivo* using an exercise protocol.

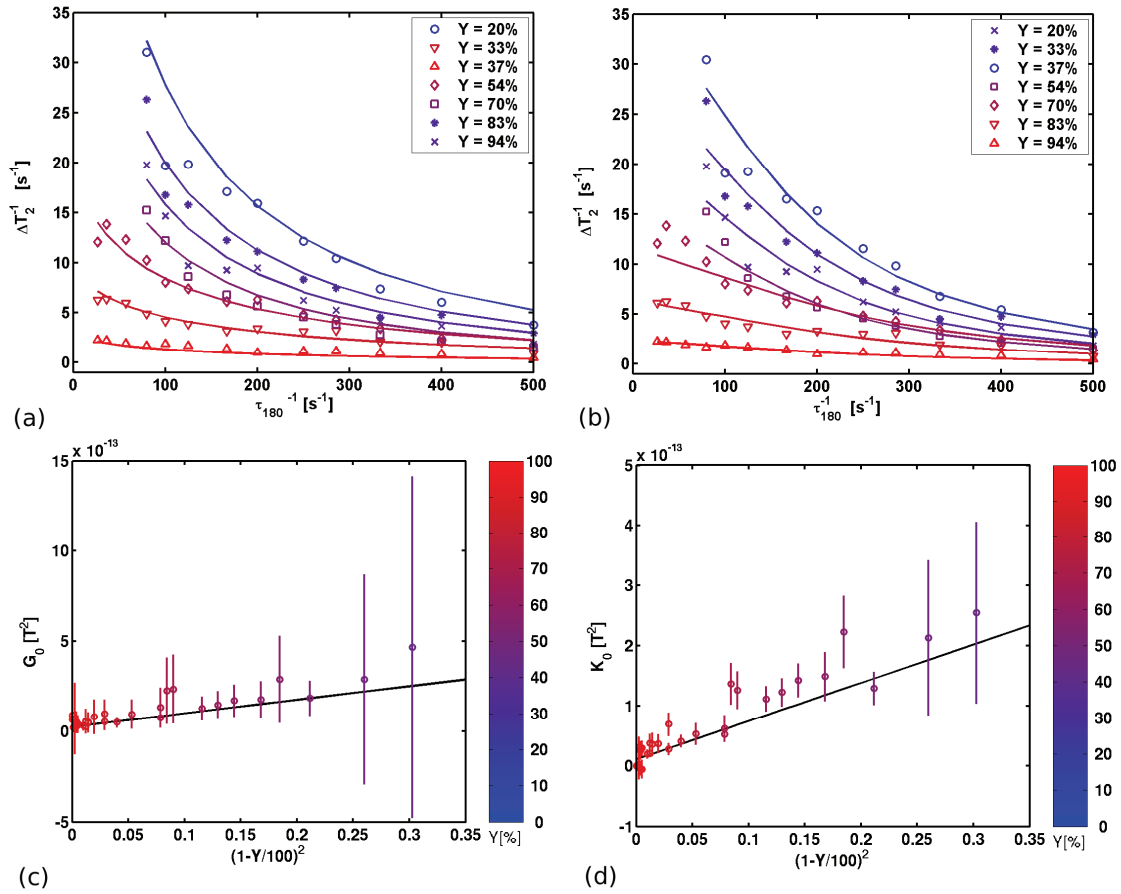


Figure 3.2

No significant relationship was revealed between $T_{2,0}$ and oxygenation ($P = 0.22$), or between $T_{2,0}$ and pH (Table 3). However, $T_{2,0}$ correlated negatively with the hematocrit ($P = 0.004$). Lastly, the constrained exchange model resulted in a group-mean $T_{2,0}$ of 174.5 ± 15.4 ms, which was not correlated with the hematocrit ($P = 0.14$) or pH ($P = 0.07$).

Using the unconstrained diffusion model, a quadratic relationship was established between G_0 and Y ($P < 0.05$) using weighted linear LSQ fitting (Fig. 2c),

$$G_0 = \left\{ (7.52 \pm 1.26) \times 10^{-13} (1 - Y[\% / 100\%])^2 + (2.60 \pm 2.71) \times 10^{-14} \right\} [\text{T}^2]. \quad [3.4]$$

with $SSR = 1.78 \times 10^{-25} \text{ T}^4$, $NME = 3.32 \times 10^{-14} \text{ T}^2$, $r = 0.89$, $P < 0.05$. G_0 significantly correlated with the hematocrit ($P < 0.05$) and pH ($P < 0.05$). The blood water diffusion coefficient (D) at $20 \text{ }^\circ\text{C}$ was calculated to be $1.4 \times 10^{-9} \text{ m}^2 \text{ s}^{-1}$ [61, 249], as an average of $D_{\text{intracellular}}$ and $D_{\text{extracellular}}$ weighted by $\text{Hct} = 42\%$. The group-average r_c was $(2.73 \pm 0.03) \times 10^{-6} \text{ m}$, and r_c was positively correlated with pH ($P = 0.002$) (Table 2).

Table 3.1

The parameter estimates for the unconstrained diffusion and constrained exchange models obtained at 3 T using the formulation in Ref. (11), and compared to their equivalents at 1.5 T, obtained using the same experimental protocol (c.f. Ref. [63]).

Model / Field	3 T			1.5 T		
Unconstrained Diffusion	r_c [μm]	G_0 [10^{-13} T^2]	$T_{2,0}$ [ms]	r_c [μm]	G_0 [10^{-13} T^2]	$T_{2,0}$ [ms]
	2.73 ± 0.03	9.60 ± 0.60	186.1 ± 27.0	4.30 ± 0.20	4.50 ± 0.51	203.0 ± 3.0
Constrained Exchange	τ_{ex} [ms]	K_0 [10^{-13} T^2]	$T_{2,0}$ [ms]	τ_{ex} [ms]	K_0 [10^{-13} T^2]	$T_{2,0}$ [ms]
	1.67 ± 0.01	7.26 ± 0.74	174.5 ± 15.4	3.00 ± 0.20	3.01 ± 0.15	157.0 ± 6.0

A quadratic relationship between K_0 and Y was derived using the constrained exchange model ($r = 0.94$, $P < 0.05$), with a slope and intercept of $(6.36 \pm 0.75) \times 10^{-13} \text{ T}^2$ and $(1.01 \pm 1.62) \times 10^{-14} \text{ T}^2$, respectively, $SSR = 6.35 \times 10^{-26} \text{ T}^4$, and $NME = 1.50 \times 10^{-14} \text{ T}^2$ (Fig. 2d). K_0 was also found to significantly correlate with pH ($P < 0.05$), but the effect of hematocrit on K_0 was just below significance (Table 2). In addition, the weighted mean exchange time was $1.67 \pm 0.01 \text{ ms}$. τ_{ex} was also negatively correlated with the pH ($P < 0.05$), although the dependence was slight. Finally, the relationship between τ_{ex} and oxygenation was not significant, but a trend was observed ($P = 0.07$).

To facilitate comparison with the results at 1.5 T, G_0 and K_0 were also fitted using the formulation found in Ref. [63], as summarized in Table 1. Overall, the diffusion model, both constrained and unconstrained, resulted in higher accuracy, with the unconstrained diffusion model returning the lowest SSR, and yielding a group average $T_{2,0}$ of 186.1 ± 27.0 ms (mean \pm SD). No significant relationship was revealed between $T_{2,0}$ and oxygenation ($P = 0.22$), or between $T_{2,0}$ and pH (Table 3). However, $T_{2,0}$ correlated negatively with the hematocrit ($P = 0.004$). Lastly, the constrained exchange model resulted in a group-mean $T_{2,0}$ of 174.5 ± 15.4 ms, which was not correlated with the hematocrit ($P = 0.14$) or pH ($P = 0.07$).

Table 3.2

Significance levels (P -values) of the interaction between key diffusion/exchange model parameters and physiological measures are listed below. G_0 was found to be significantly correlated with the hematocrit ($P < 0.05$) and pH ($P < 0.05$). A positive correlation was detected between r_c and pH ($P < 0.05$), as well as between r_c and oxygenation ($P = 0.007$). K_0 was also found to be significantly correlated with pH ($P < 0.05$). The effect of hematocrit on K_0 was just below statistical significance. τ_{ex} was found to be negatively correlated with the pH ($P < 0.05$), although the dependence was negligible. Finally, a positive oxygenation dependence in τ_{ex} was found to approach significance ($P = 0.07$).

Parameters	Unconstrained Diffusion Model		Constrained Exchange Model	
	r_c	G_0	τ_{ex}	K_0
Y	0.007	< 0.001	0.07	< 0.001
Hct	0.54	0.01	0.41	0.07
pH	0.002	< 0.001	0.02	< 0.001

Table 3.3

Based on $T_{2,0}$ estimates obtained using the unconstrained diffusion model, linear regression revealed no significant correlation between $T_{2,0}$ and oxygenation ($P = 0.22$), nor between $T_{2,0}$ and pH. However, $T_{2,0}$ was found to correlate negatively with hematocrit ($P < 0.05$). A positive correlation was also found between pH and oxygenation ($P < 0.05$), but no relationship was observed between pH and hematocrit ($P = 0.55$) or between hematocrit and oxygenation ($P = 0.12$).

Parameter	r	P
Y	0.22	0.22
Hct	0.40	0.004
pH	0.23	0.16
Y x Hct	$r = 0.26; P = 0.12$	
Y x pH	$r = 0.65; P < 0.001$	
Hct x pH	$r = 0.05; P = 0.55$	

3.7 Discussion

In this study, a comprehensive analysis of whole human blood T_2 as a function of Y and τ_{180} was performed. The concomitant decrease in oxygenation and pH ($P < 0.05$) can be explained through the Bohr shift. Both diffusion and two-site exchange processes likely contribute to T_2 reduction with oxygenation, but the relative magnitude of these effects depends on τ_{180} and B_0 . In both cases, the quadratic relationship between ΔT_2^{-1} (Fig. 2a and 2b) and oxygenation corroborates previous findings [63, 249, 256]. The constrained exchange model outperformed the unconstrained model, as was the case at 1.5 T [63], likely due to the lower sensitivity of the constrained exchange model to noise. As seen in Table 1, the slope of K_0 increased significantly at 3 T compared to 1.5 T. K_0 was also negatively correlated with pH ($P < 0.05$), pointing to amplified T_2 relaxation enhancement with decreasing pH, supported by the strong correlation ($P < 0.001$) between pH and oxygenation (Table 3). The exchange time ($\tau_{ex} = 1.67 \pm 0.01$ ms) is consistent with literature values [59, 61, 63, 66, 245, 251], and agrees well with findings by Gillis *et*

al.[249], but is shorter than observed at 1.5 T ($P < 0.05$) (Table 1), which may be a further reflection of limitations in the exchange model. Finally, the negative correlation between τ_{ex} and pH echoes results from Morariu *et al.* [257].

The diffusion model of Jensen and Chandra [61] best described our T_2 data at 3 T, as was the case at 1.5 T [63]. Our results reflect the limitations in the exchange model in addressing the intermediate- τ_{180} range under the weak-field-inhomogeneity assumption, as was suggested by Brooks *et al.* [245] to result from the simplification of the temporal-correlation function. The slope of G_0 predicted by the unconstrained diffusion model showed an approximately linear increase ($P < 0.05$) at 3 T compared to 1.5 T, as was also observed with the exchange model, implying substantial growth in the susceptibility difference between plasma and deoxygenated erythrocytes with B_0 . G_0 correlated negatively with the hematocrit ($P < 0.05$), reflecting the hematocrit's effect on the relative contributions of intra- and extra-cellular water resonance in deoxygenation-induced dephasing described by Matwiyoff *et al.* [248]. The r_c estimate (2.73×10^{-6} m) was within the range of red blood cell diameters measured in previous human and canine studies [61, 245], but lower than observed at 1.5 T (Table 1). K_0 and G_0 are not equal as postulated by Jensen and Chandra, chiefly as it was impossible to use infinitely narrow refocusing RF pulses. Finally, no significant relationship was found between r_c and τ_{ex} ($P = 0.12$).

Our T_2 estimates are in close agreement with values reported in the literature [59, 63, 247], and the dynamic range of T_2 's for the same group of τ_{180} values is larger at 3 T than at 1.5 T [63]. The $T_{2,0}$ derived from the unconstrained diffusion model (186.1 ± 27.0 ms) was not significantly different from that observed at 1.5 T ($P = 0.21$) [63], and is well within the range determined by other methods [59, 258] in human blood. While $T_{2,0}$ did not vary with oxygenation or pH, it correlated negatively with the hematocrit, as suggested by previous studies [247, 249], and justified by the fact that the variance in the local resonance frequency is proportional to the inhomogeneity volume fraction. Interestingly, the $T_{2,0}$ derived using the constrained exchange model did not vary with Hct or pH, unlike predicted by Gillis *et al.*[249].

Our data demonstrates an approximately linear dependence of G_0 and K_0 on B_0 , in apparent contradiction with certain previous studies reporting more substantial T_2 decay

enhancement [247, 254], which we ascribe to methodological differences. Notably, the exclusive use of long τ_{180} values in certain previous experiments [254] likely increased T_2 estimation uncertainty. Comparison was also drawn between the T_2 decay enhancement as a linear function of B_0 demonstrated by our data and the putative quadratic relaxation rate shift increase with B_0 derived from the diffusion and exchange models, in which red blood cells are assumed to be microscopic spheres (only true for hypotonic cell suspensions). However normal erythrocytes are disk-shaped, likely biasing the orientation of diffusion as well as intra- and extracellular field inhomogeneities [259]. Moreover, the effect of erythrocyte alignment with the field [260] and of the Curie spin [253] can both increase dramatically with B_0 . Thus, our results may reflect intrinsic limitations in the models. We believe the underlying physical phenomenon to be too complex to be fully described by either model, but our data show that the current parameterization of the diffusion model provides the best simplification at 3 T.

The findings of this study further validate the use of τ_{180} modulations to isolate deoxygenated blood, as employed by the venous-refocusing for volume-estimation (VERVE) technique [155]. The enhanced T_2 dependence on oxygenation at 3 T translates to an increase in the VERVE contrast-to-noise ratio by approximately 150%. The increases in microvascular contribution to BOLD at 3 T is likely to be smaller than previous predicted, as we observed a linear rather than quadratic blood T_2 enhancement with B_0 . In summary, we observed high accuracy of the diffusion model as formulated by Jensen and Chandra [61] in approximating T_2 reduction in partially deoxygenated human whole blood at 3 T, and confirm the validity of the weak-field-inhomogeneity assumption. The significantly enhanced T_2 sensitivity to oxygenation and τ_{180} at 3 T is explained by a linear increase in the magnitude of deoxygenation-induced field inhomogeneities from 1.5 T to 3 T.

3.8 Acknowledgments

The authors thank Mr. André Cormier for his assistance in the blood collection process. This research was supported by the Natural Sciences and Engineering Research Council of Canada (J. J. C.) and the Canadian Institutes of Health Research (G. B. P.).

Chapter 4

Development of VERVE at 3 Tesla

The transition from 1.5 T to 3 T implies not only higher potential signal-to-noise ratio (SNR), but also changing relaxation rates and increased levels of field inhomogeneities, as outlined in Chapter 2. The development of VERVE at 3 T therefore requires a re-evaluation of the MR relaxation properties of brain tissue in the presence of these increased inhomogeneities. This chapter also describes blood longitudinal relaxation behaviour in relation to deoxygenation at 3 T, complementing the study of venous blood transverse relaxation that was presented in Chapter 3. Finally, the increase in Larmor frequency translates to a drastic increase in RF power deposition, which must be addressed concurrently with VERVE contrast optimization. These various aspects of the development process will be described in the following.

4.1 Tissue T_2 Relaxometry at 3 T

4.1.1 Background

As mentioned previously, the most fundamental difference between imaging at 3 T and at 1.5 T is the relaxation times of various tissue types. No field dependency was predicted for T_2 by the Purcell Pound theory of relaxation, but cross-relaxation with macromolecules, intra-extra-cellular exchange and dynamic averaging can all potentially lead to T_2 shortening. The quantification of brain tissue T_2 is important not only for the optimization of VERVE acquisition parameters, but also for measuring hemodynamic and metabolic parameters fundamental to brain function investigations [70].

At field strengths up to 3 T, it is well-established that transverse relaxation in grey matter (GM) takes place at a slower rate than in white matter (WM) in the healthy adult brain [235, 236, 261]. The shorter white matter T_2 is thought to be caused primarily by the abundance of myelin sheaths [262]. However, a significant amount of regional heterogeneity within each tissue has been documented [262, 263]. A shortening of GM T_2 has been observed in the deep grey matter [61, 264], as well as in the cerebral cortices [265]. This has been postulated to result from the accumulation of ferritin with age, but previous quantitative relaxometry studies have shown no correlation with tissue iron concentration [266, 267]. Shorter apparent T_2 in GM than in WM of the occipital lobe has also been reported at both 4 T and 7 T [268].

In addition to T_2 shortening, the presence of an agent of high magnetic susceptibility may give rise to a dependence of T_2 on the interval between the refocusing pulses (τ_{180}) in a Carr-Purcell Meiboom-Gill (CPMG) experiment. T_2 is expected to decrease with refocusing interval elongation due to an increasing extent to which water molecules sample the magnetically inhomogeneous environment surrounding the agent within an inter-echo interval [269]. This phenomenon has been extensively studied both in iron-rich GM [264, 270] and in blood, where partial deoxygenation leads to the production of paramagnetic deoxyhemoglobin (dHb). Stefanovic and Pike have shown experimentally through detailed whole blood and tissue T_2 relaxometry that only the T_2 of blood (vs. those of pure parenchyma) changes with the refocusing interval [271]. However, a recent study reported very pronounced occipital grey and white matter T_2 dependencies on the refocusing rate at both 4 T and 7 T, the estimated T_2 decreasing by 30%–40% between a short (6–7 ms) and a set of long (more than 10 ms) refocusing interval acquisitions [268]. While a greater decrease in blood T_2 with refocusing interval elongation is expected at higher fields, the overall shortening of blood T_2 in combination with low tissue blood content makes it unlikely that the blood T_2 dependence on the refocusing interval alone fully explains these ultra-high field findings.

In view of the above suggestions of an extravascular source of brain tissue T_2 dependency at 4 T and 7 T, we sought to evaluate brain tissue T_2 behaviour at 3 T. We investigated the refocusing rate dependence of T_2 in cortical GM and WM in a cohort of healthy human volunteers at 3 T. Our hypothesis is that the variation of the refocusing

intervals in the range of interest produces no effect on the extravascular brain tissue T_2 . We adopted methodology previous proven to minimize partial volume effects in tissue T_2 relaxometry and to maximize the robustness of T_2 estimates [271]. Our results clearly demonstrate that cortical brain tissue continues to be associated with negligible dependence on the CPMG refocusing interval, as detailed in the following sections.

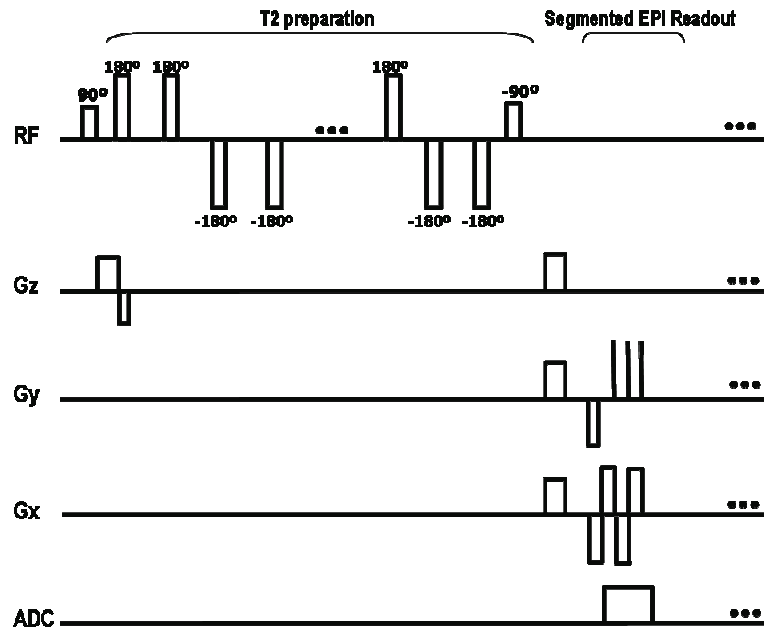


Figure 4.1 The segmented EPI sequence diagram.

MR sequence diagram for one repetition of the segmented spin-echo EPI technique: the refocusing train with interval τ_{180} is followed by segmented EPI readout, the duration of which is set to minimize flow sensitivity.

4.1.2 Methods

4.1.2.1 MR Acquisition

Five healthy adult volunteers were studied (3 females and 2 males), with ages ranging from 23 to 35 years. All subjects were scanned using a Siemens 3 T Trio system with a circularly-polarized transmit-receive head coil. Informed consent was obtained before each session. A high resolution T_1 -weighted gradient-echo sequence with a 256-mm field of view (FOV), 256 x 256 matrix size (1 mm isotropic resolution), TR/TE of 23/10 ms, and nonselective 30° RF-spoiled excitation, was

used as anatomical reference and for tissue segmentation. This was followed by four single-slice T_2 relaxometry scans using T_2 -prepared segmented echo-planar imaging (EPI) (Figure 4.1) and a multi-echo single-slice CPMG relaxometry sequence (both at $1 \times 1 \times 5 \text{ mm}^3$) (Figure 4.2), prescribed axially at the midline of the occipital lobe. The head of the subject was immobilized using a vacuum bag, and all acquisitions were obtained in a single scan session, which persisted for approximately 40 minutes per subject.

The single-slice T_2 -prepared segmented EPI sequence, which allowed for very short refocusing intervals to be explored, contained a slice non-selective T_2 -weighted magnetization preparation with a nonselective 90° excitation followed by a train of hard refocusing pulses with subsequent nonselective tip-up, as well as a slice-selective excitation and segmented EPI readout (Figure 4.1). Given the increased presence of B_1 inhomogeneities at 3 T, nonselective composite 90°_x - 180°_y - 90°_x pulses were used for refocusing, arranged in a pattern following a 16-term MLEV phase cycle [1]. Finally, a large spoiling gradient was applied following the slice-selective tip-up to dephase any remaining transverse magnetization. Six different T_2 preparation durations were run with an inter-refocusing interval of 4 ms, providing six effective echo times (TE), equally spaced over the sampling window, extending from 24 to 144 ms. Three k -space lines were acquired per excitation with a readout bandwidth of 616 Hz/pixel and a TR of 4 sec.

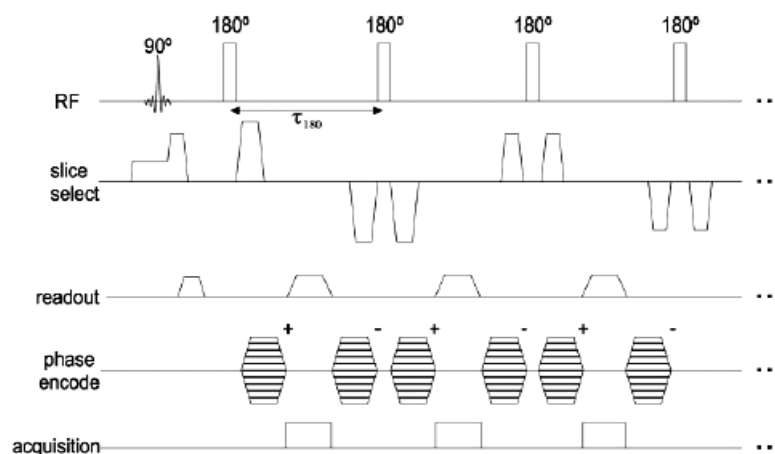


Figure 4.2 The schematic diagram of the multi-echo CPMG sequence.

The refocusing pulses are flanked by matching spoiler gradients, the magnitude of which descends with increasing echo number to minimize spurious echoes while maximizing image SNR. (source: [255])

In the multi-echo CPMG sequence, slice non-selective composite 90°_x - 180°_y - 90°_x pulses were used for refocusing once again to minimize the effects of B_1 inhomogeneities. All refocusing pulses were flanked by spoiling gradients, alternating in sign and decreasing in magnitude in order to maximally suppress stimulated echoes, flow effects and signal contributions outside of the slice of interest [272]. The sequence parameters were optimized to provide robust T_2 measurements with the shortest achievable inter-echo intervals, given the primary motivation of investigating the T_2 dependence on a wide range of refocusing intervals. The inter-echo intervals probed were 8, 12, and 24 ms. This choice was motivated by the range of T_2 values relevant for functional acquisitions at 3 T, as well as by power deposition considerations. The three CPMG refocusing intervals were applied in randomized order, and the number of measurements in each case was set such that comparable temporal sampling windows were used for all relaxometry data, as shown in Figure 4.3. Finally, B_0 and B_1 field mapping [255] were performed, and their effect on T_2 estimates examined.

4.1.2.2 Data Analysis

Brain masks were determined from the high-resolution T_1 -weighted scans based on the MNI 305 brain atlas (Montreal Neurological Institute, Montreal, Canada). Tissue segmentation within these masks was then performed using a parametric Bayesian approach that assumes the voxel intensities are drawn from a mixed population of three statistical distributions (GM, WM, and CSF) [273]. The conditional probability distributions of all tissue classes were assumed to be Gaussian, with equal class prior probabilities. For each subject, three sets of 50 manually selected voxels for each of GM, WM, or CSF were used to compute mean intensity and standard deviation for each class. This training data set allowed an explicit calculation of the parametric estimates of the *a posteriori* probabilities as scaled likelihoods of voxel intensity value given that the voxel belongs to a class, as stipulated by Bayes's theorem [274]. The Bayesian classification produced three normalized *a posteriori* probability maps specifying the probabilities of voxels belonging to GM, WM, or CSF, respectively. From each of these probability

maps, the axial slab corresponding to the 5-mm transverse slice of the relaxometry acquisitions was sampled. Careful visual inspection was performed to verify alignment. The threshold for inclusion was a 95% average of normalized a posteriori probabilities.

For each echo time, the relaxometry data from all voxels within each ROI were averaged. Nonlinear least squares were used to fit the resulting decay curves to a mono-exponential decay model. Since multi-exponential fitting was found to provide no additional information in regards to T_2 dependence on the CPMG refocusing interval [271], only mono-exponential fits were attempted. Finally, two-way analysis of variance (ANOVA) and linear regression was used to investigate the effects of refocusing interval and inter-subject variability on the estimated T_2 values.

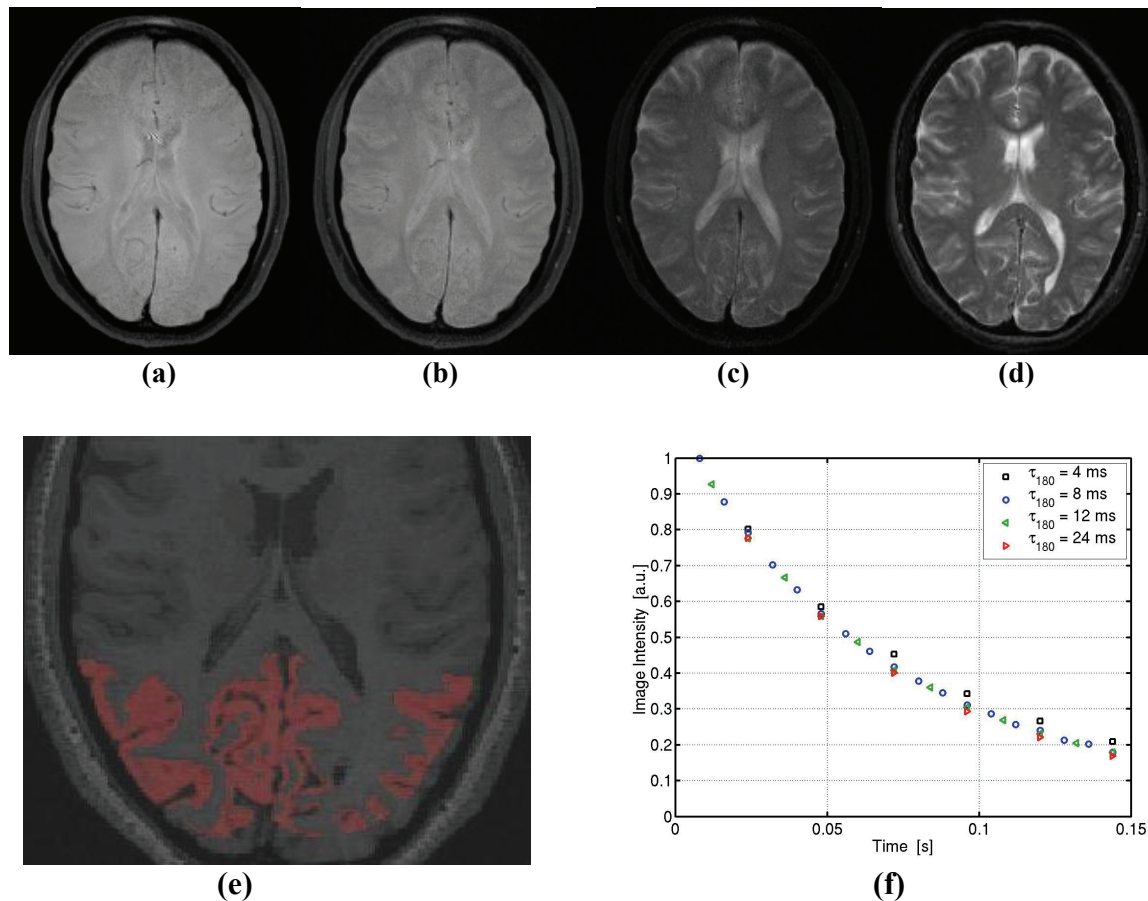


Figure 4.3 Sample brain relaxometry data from a single subject.

Images of the third echo are shown for multi-echo spin-echo acquisitions with refocusing intervals of 4 ms (a), 8 ms (b), 12 ms (c), and 24 ms (d). The cortical grey matter ROI for the subject, obtained using Bayesian classification of the 3D T_1 -weighted data with a *posteriori* probability > 95%, is shown

in (e) for the occipital lobe. The corresponding average T_2 -decay curves for the 4 different refocusing intervals (f) were used in least-square fitting to obtain T_2 estimates.

4.1.3 Results

The per-subject GM and WM T_2 estimates are summarized in Table 4.1 and Table 4.2, respectively, with the standard deviation (SD) representing T_2 estimate variability within the ROIs. Specifically, in grey matter (GM), T_2 dropped by 1.1 ± 0.9 ms between the 8 ms and 12 ms acquisitions, and by 1.2 ± 0.6 ms between the 12 ms and 24 ms acquisitions. In white matter (WM), T_2 dropped by 0.8 ± 1.5 ms between the 8 ms and 12 ms acquisitions, and by 1.0 ± 0.7 ms between the 12 ms and 24 ms acquisitions. The T_2 drops were statistically significant in both grey ($p = 6.7 \times 10^{-8}$) and white matter ($p = 7.5 \times 10^{-11}$). However, overall, there was no statistically significant T_2 trend with τ_{180} , as assessed by linear regression.

Table 4.1 Cortical grey matter T_2 variation with refocusing interval.

The T_2 estimates and the associated propagated uncertainties (SD) are listed for cortical grey matter over all refocusing intervals (τ_{180}). The results for $\tau_{180} = 4$ ms were obtained using segmented EPI, whereas the remaining three datasets were acquired using multi-echo CPMG.

Subject	τ_{180} (ms)			
	4	8	12	24
1	80.7 ± 12.8	75.8 ± 9.9	74.9 ± 10.3	73.8 ± 11.2
2	84.6 ± 10.8	79.5 ± 8.4	78.8 ± 8.1	77.2 ± 9.6
3	88.2 ± 10.4	82.8 ± 9.8	82.4 ± 10.0	80.9 ± 11.0
4	82.1 ± 11.6	78.0 ± 10.7	77.2 ± 11.3	75.5 ± 12.3
5	85.3 ± 9.5	77.8 ± 8.3	75.1 ± 9.2	74.8 ± 11.1
Mean ± SD	84.2 ± 11.5	78.8 ± 9.8	77.7 ± 10.3	76.5 ± 11.4

Overall, the estimated T_2 decreased by an average of 7.7 ± 1.6 ms in GM between the 4 ms and 24 ms acquisitions, equivalent to a shortening of approximately 9%. The same metric for white matter was found to be 10.9 ± 0.9 ms, also translating to a 9% T_2 shortening. Finally, both grey and white matter T_2 was subject-dependent ($p = 1.2 \times 10^{-6}$).

and 8.2×10^{-7} , respectively). The use of B_0 and B_1 correction did not alter the results of the statistical analysis, but introduced additional sources of variance.

Table 4.2 Cortical white matter T_2 variation with refocusing interval.

The T_2 estimates and the corresponding propagated uncertainties are shown for cortical white matter over all refocusing intervals.

Subject	τ_{180} (ms)			
	4	8	12	24
1	81.5 ± 9.7	72.5 ± 6.3	71.8 ± 7.3	70.7 ± 7.7
2	84.1 ± 8.5	74.9 ± 5.5	75.0 ± 5.7	73.8 ± 6.6
3	86.8 ± 9.6	78.0 ± 8.4	78.3 ± 8.8	76.6 ± 9.1
4	82.9 ± 9.1	72.4 ± 6.5	72.0 ± 5.7	70.6 ± 6.1
5	83.3 ± 8.6	75.3 ± 6.0	71.8 ± 5.9	72.0 ± 6.9
Mean ± SD	83.7 ± 9.3	74.6 ± 7.0	73.8 ± 7.4	72.8 ± 7.8

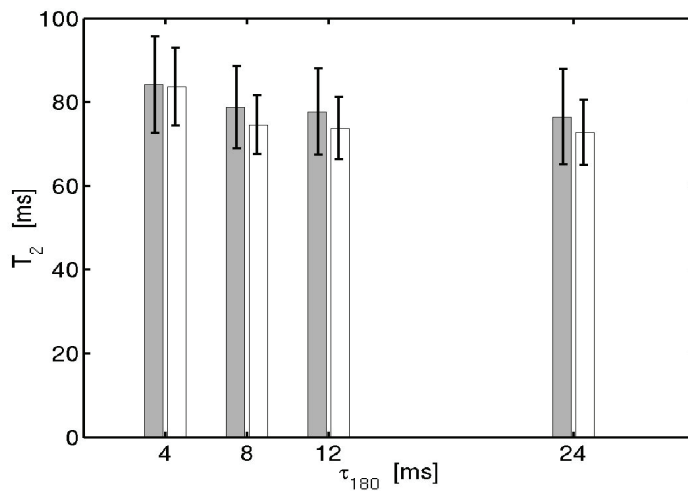


Figure 4.4 GM and WM dependence on CPMG refocusing interval.

Grey and white represent GM and WM, respectively. The error bars representing the spatial variability of the T_2 values over the ROI.

4.1.4 Discussion

The grey and white matter T_2 measurements are in general agreement with the literature. Whereas GM T_2 was found to be higher than WM T_2 , as was found at 1.5 T using the same technique [271], their respective values begin to approach each other at 3 T. This observation remained unchanged whether B_0 and B_1 correction were applied. It is interesting to draw a trend based on these results and earlier studies [268, 275], and postulate that GM and WM T_2 contrast could reverse at field strengths higher than 3 T.

Both grey and white matter exhibited T_2 variations with the CPMG refocusing interval (τ_{180}) at 3 T (Figure 4.4). However, the overall T_2 dependence on τ_{180} can be considered negligible in view of the variation in blood T_2 over the same τ_{180} range, as described in Chapter 3. Furthermore, it is likely that the slight tissue T_2 dependence on τ_{180} is of intravascular origin, attributable to the small content of deoxygenated blood in GM, occupying approximately 4-5% of the resting-state tissue volume [70]. This observation is consistent with the previous observation that brain tissue T_2 variability is primarily dependent on blood volume [276].

The above theory was verified experimentally. Using the calculated intrinsic GM and WM T_2 , the corresponding GM and WM blood volume were estimated by adopting the blood T_2 dependence on τ_{180} (see Chapter 3) and assuming no T_2 variation in pure parenchyma. The resting-state blood oxygenation level was assumed to be 60%, as was commonly observed in existing studies [277, 278] as well as in our own experiments. The resulting average grey matter blood volume was estimated to be 5.5%, in close agreement with values found in the literature [279-282]. Using a similar approach, the white matter blood volume was estimated to be 3.2%, also in agreement with previous reports [280, 281, 283]. These results, in combination with the blood T_1 relaxometry data presented in the next section, as well as blood T_2 relaxometry results (Chapter 3), confirm the feasibility of the VERVE concept for isolating deoxygenated blood at 3 T.

4.2 Blood T_1 Relaxometry

4.2.1 Background

Blood T_1 has been suggested to be variable with physiological condition [122, 157], although the optimization of VERVE contrast assumes minimal T_1 variability. In addition, a constant blood T_1 is fundamental to arterial spin labeling [284] and the vascular space occupancy (VASO) technique as described in the previous chapter [285]. High-field T_1 properties of blood have been previously investigated by Silvennoinen et al [122] at 4.7 T and by Lu et al [286] at 3 T using bovine blood. Both studies reported linear T_1 increase with Y and T_1 decrease with increasing hematocrit (Hct), coinciding with findings by Stefanovic and Pike at 1.5 T [63]. Notwithstanding the similarities between the magnetic properties of bovine and human blood, a detailed examination of whole human blood T_1 at 3 T would directly establish the validity of the above results for high field human studies, as well as the feasibility of VERVE development at 3 T.

4.2.2 Methods

4.2.2.1 MRI Acquisition

Whole blood specimens were obtained by forearm venipuncture from 10 healthy human subjects (age = 29.2 ± 7.6 years). An equal number of males and females were chosen to avoid gender bias in the data. Informed consent was obtained from all subjects prior to the phlebotomy. A blood pressure cuff was placed approximately 4 cm above the olechreon process and inflated to approximately 50% above the subject's systolic pressure in order to create partial arterial and venous occlusion and achieve a local accumulation of deoxyhemoglobin. Blood oxygenation was modulated via exercise during the occlusion, which consisted of elbow flexion and extension while holding a 2.3 kg weight in the non-dominant hand. Four blood samples were obtained from each subject. The first sample was collected at rest, the second and third samples after 2 and 4 minutes of arm exercise, respectively, and 15 seconds after the removal of the pressure cuff, the final sample was collected to capture the ensuing hyper-oxygenation. The

samples were sealed, post air-bubble removal, in 3 mL blood-gas syringes (diameter = 9 mm) containing balanced 25U heparin to prevent coagulation (Westmed, Tucson, AZ, USA). The scans began within 5 minutes of the final blood draw in order to minimize the effects of residual metabolism. To the same end, the interval between the scan session and the blood gas analysis, during which the syringes were immersed in ice baths, was minimized.

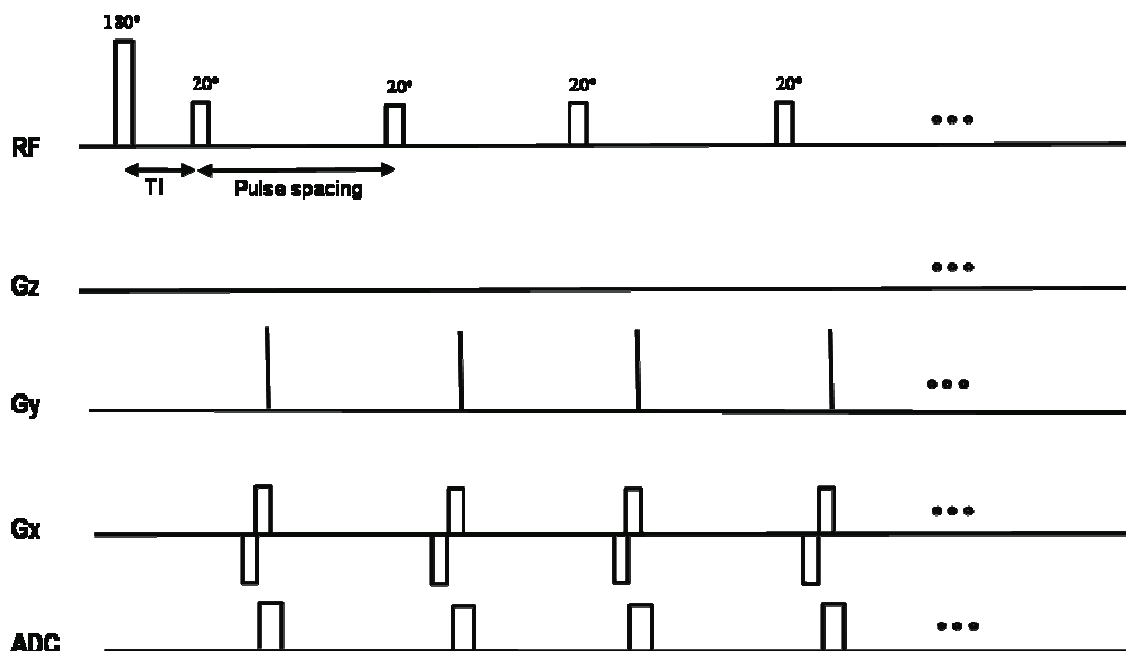


Figure 4.5 The Look-Locker sequence diagram.

The Look-Locker sequence [287] enables robust T_1 relaxometry measurements to be obtained in a span of seconds.

Blood T_1 was measured using a segmented-EPI Look-Locker sequence (Figure 4.5) [287] in which 90°_x - 180°_y - 90°_x composite non-selective inversion pulses were used with an inversion time of 15 ms. The flip angle was 20° , with a pulse spacing of 495 ms, an echo time of 10 ms, a repetition time of 4 s, a readout bandwidth of 140 Hz/pixel and an echo-train length of 1. For both T_1 and T_2 scans, the matrix size was 64×64 , covering a field of view (FOV) of 100 mm, achieving $1.56 \times 1.56 \times 5 \text{ mm}^3$ voxels. The imaged slice was positioned through the centre of the 50 mm long blood-filled sections of the syringes (placed in parallel with the static field), located at the isocentre of the magnet

field. Our protocol ensured minimal oxygenation change during the scan, as confirmed by pre- and post-scan blood gas analysis which revealed a Y decrease of approximately 2% due to scan-induced delays.

4.2.2.2 Data Processing

T_1 was obtained from fits to the Look-Locker data [287] using unweighted least-square minimization. Furthermore, correlations between T_1 and oxygenation, hematocrit (Hct) and pH, in addition to the interaction between oxygen, hematocrit and pH, was assessed using linear regression.

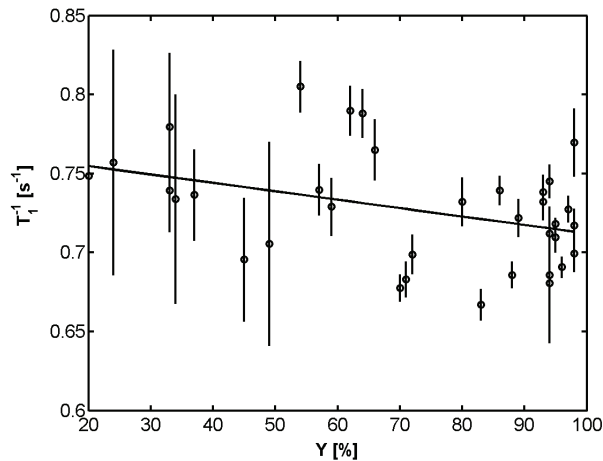


Figure 4.6 The blood R_1 (T_1^{-1}) variation with oxygenation.

Whole blood T_1 was found to have a modest linear dependence ($r = 0.39$, $P < 0.05$) on oxygenation (Y), with a slope of $(-5.32 \pm 2.40) \times 10^{-4}$ s and a y-intercept of $(7.65 \pm 1.71) \times 10^{-1}$ [288]. The vertical bars represent uncertainties in the R_1 estimates.

4.2.3 Results

Across all oxygenation states, the group-average pH from the blood gas analysis was 7.54 ± 0.06 , and the average hematocrit was $42.3 \pm 4.0\%$. The group-average T_1 for the resting-state condition ($Y = 72.0 \pm 25.5\%$) and the post-exercise hyperoxygenation phase ($Y = 81.7 \pm 17.6\%$) was 1359.1 ± 31.9 ms and 1393.7 ± 84.8 ms, respectively. The average uncertainty in T_1 estimates across all samples was 39.9 ms. Linear [63] and quadratic [157] relationships between T_1 and oxygenation were investigated, with linear dependence better describing the T_1 relaxation rate decrease with increasing Y ($P = 0.02$

vs. $p = 0.15$). Weighted linear fitting resulted in a slope of $(-5.32 \pm 2.40) \times 10^{-4}$ and a y-intercept of $(7.65 \pm 1.71) \times 10^{-1} [\text{s}^{-1}]$. To enable comparison with results at 1.5 T [63], this relationship was reformulated to

$$R_1 = (1286.10 \pm 29.70 [\text{ms}])^{-1} - (0.53 \pm 0.24)10^{-6}[\text{ms}^{-1} / \%] \cdot Y[\%], \quad [4.1]$$

with $\text{NME} = 0.0542 \text{ s}$ and $\text{SSR} = 0.125 \text{ s}^2$. The corresponding T_1^{-1} estimates are plotted against Y in Figure 4.6. A correlation of $r = 0.39$ reflects the low SNR in the estimated T_1 dataset. The regression did not reveal a significant dependence of T_1 on the hematocrit ($p = 0.16$), as seen in Table 2, but did show a correlation between T_1 and pH approaching significance ($p = 0.06$).

Across all oxygenation states, the group-average pH from the blood gas analysis was 7.54 ± 0.06 , and the average hematocrit was $42.3 \pm 4.0\%$. A positive correlation was found between pH and oxygenation ($p < 0.05$), but no relationship was observed between pH and hematocrit ($p = 0.55$) or between hematocrit and oxygenation ($p = 0.12$).

4.2.4 Discussion

As expected, blood T_1 was substantially longer at 3 T (mean \pm SD = $1382.3 \pm 61.8 \text{ ms}$) than at 1.5 T ($1079.9 \pm 46.5 \text{ ms}$). T_1 was found to increase linearly with oxygenation at 3 T, in line with recent observations by Stefanovic and Pike at 1.5 T [63] and by Silvennoinen *et al.* at 4.7 T [122]. This dependence, postulated to arise from proton-deoxyhemoglobin interactions [122, 289], was found to be quadratic by Thulborn et al [157]. However, in the latter study, the variations in T_1 with Y were very slight, as is also seen here, thus increasing the difficulty in characterizing the trend. In this study, the relationship between T_1 and Y was statistically better described by a linear than a quadratic fit; but given the small range of T_1 variation with Y , these results do not disprove the existence of quadratic relationships, especially if presented with a wider range of Y and Hct values. In addition, although theoretically an increasing hematocrit can act to reduce blood T_1 through macromolecular magnetization transfer, as was seen in certain previous studies [122, 256, 286], the current data did not reveal a T_1 dependence on the hematocrit. This could be caused by the relatively uniform set of Hct values

available in this blood sample pool, and does not exclude T_1 dependence on Hct. Keeping in mind that microvascular cerebral hematocrit values are expected to be only 85% those of macrovascular Hct [122], an additional verification could be made by diluting the blood samples. In summary, the observed low T_1 variation with blood oxygenation, hematocrit and pH fulfills requirements by VERVE, since oxygenation-induced signal change will continue to be T_2 -dominated at 3 T. In addition, the VERVE model will exhibit minimal T_1 -sensitivity, as the subtraction between fast- and slow-refocused images in the same state (activation or baseline) cancels T_1 weighting, which is not modulated by refocusing rate.

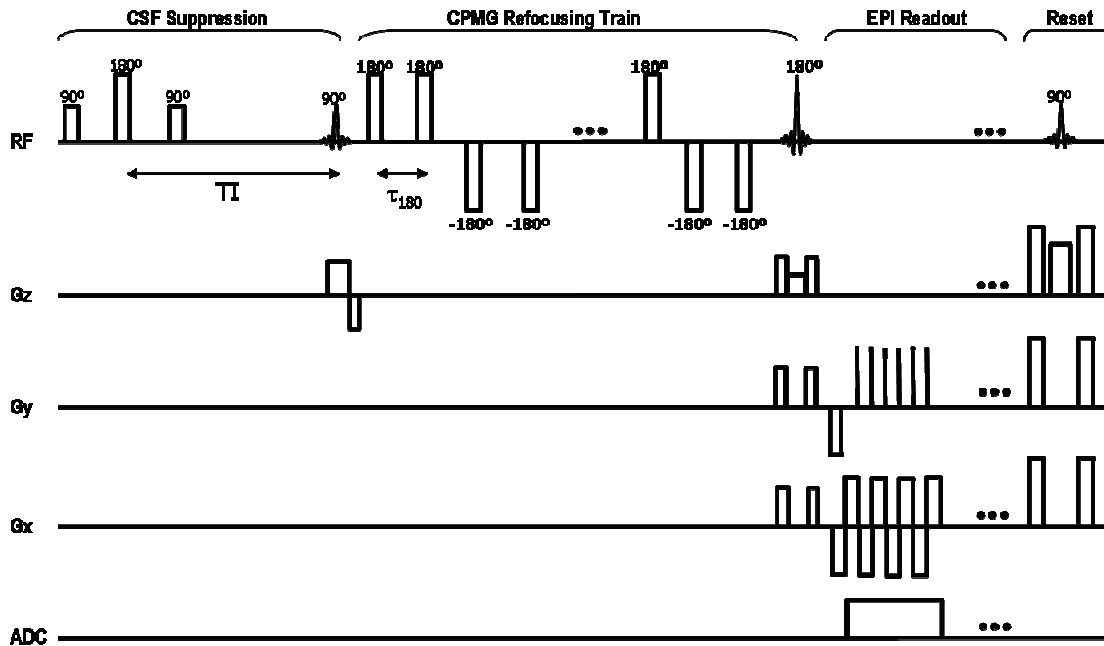


Figure 4.7 VERVE [155] sequence diagram with EPI readout.

The 90°_x - 180°_y - 90°_x -TI preparation is used to null the CSF signal efficiently [290]. The interval between the refocusing pulses (τ_{180}) is varied in alternate measurements, while keeping the echo time constant.

4.3 Gradient-Echo BOLD Effects in VERVE

4.3.1 Background

The venous refocusing for volume estimation (VERVE) technique was first presented by Stefanovic and Pike at 1.5 T [155]. Their implementation is shown in Figure 4.7. The sequence employs a T_1/T_2 selective $90_x-\tau-180_y-\tau-90_x$ inversion (TI) preparation for T_2 -selective and SNR-enhanced nulling of the CSF, with EPI readout following a train of either tightly or sparsely spaced hard refocusing pulses, arranged according to the CPMG refocusing interval (τ_{180}) for fast- and slow-refocusing, respectively. The lower limit of the fast-refocusing τ_{180} is constrained by the minimum possible spacing between RF pulses; the fast and slow trains, which feature 64 and 8 pulses, respectively, result in matching effective echo times. Composite rectangular $90^\circ_x-180^\circ_y-90^\circ_x$ refocusing pulses were used to minimize the sensitivity to B_1 inhomogeneities. As described in the original reference [155], the VERVE signal is given by,

$$rVERVE = \frac{\Delta S_{b,A}}{\Delta S_{b,B}} = \frac{f_{b,A}}{f_{b,B}} \cdot \frac{e^{-TE/T_{2,b}(Y_A, \tau_{180}^F)} - e^{-TE/T_{2,b}(Y_A, \tau_{180}^S)}}{e^{-TE/T_{2,b}(Y_B, \tau_{180}^F)} - e^{-TE/T_{2,b}(Y_B, \tau_{180}^S)}} \quad [4.2]$$

where $T_{2,b}$ is the blood T_2 , Y_A and Y_B are the blood oxygenation at activation and baseline, τ_{180}^F and τ_{180}^S are the fast- and slow-refocusing intervals, and $f_{b,A}$ and $f_{b,B}$ are the blood water volume fractions at activation and baseline, respectively. The ability of the VERVE technique to accurately estimate venous blood volume is contingent upon the distinct detection of blood T_2 dependence on τ_{180} and on Y . While the ratio $f_{b,A}/f_{b,B}$ can be interpreted as the relative venous CBV ($rCBV_v$), the oxygenation dependence, termed the intravascular spin-echo BOLD (IV SE BOLD) effect, must be corrected through a calibration step before $rCBV_v$ can be derived from $rVERVE$ [155].

An obvious confound in the original VERVE is the introduction of gradient-echo (GE) BOLD (T_2^* weighting) by the EPI readout. Although reasonable ΔCBV_v values were obtained at 1.5 T, the EPI design becomes increasingly impractical at higher fields, as T_2^* effects become significantly enhanced, introducing detrimental decreases in the VERVE signal-to-noise ratio (SNR). Even with the fastest EPI readout, GE-BOLD effects can introduce signal losses in excess of those resulting from oxygenation change.

Therefore, in the event of blood oxygenation rise during focal flow increase, the use of EPI leads to ΔCBV_v estimation bias. While it is possible to predict and correct for GE BOLD effects in the steady state based on simulations, it is difficult to assess the error in the transient period, where concurrent and unknown changes in blood volume and oxygenation could combine to give rise to T_2^* -induced bias in the VERVE signal.

As described in Eq. [4.2], the VERVE signal is based on venous blood T_2 , which should only originate from either an alteration in blood oxygenation or in the actual venous blood volume. However, T_2^* -weighting introduces an additional source of signal change, through deoxyhemoglobin related field inhomogeneity effects. As venous blood volume increases, so too does the amount of deoxyhemoglobin, which would result in signal loss irrespective of whether blood oxygenation decreases. Keeping that in mind, three scenarios of VERVE signal change in the presence of T_2^* decay were simulated, namely (1) a change in venous CBV without a concurrent change in blood oxygenation; (2) a change in blood oxygenation without a concurrent change in venous CBV; (3) simultaneous changes in venous CBV and blood oxygenation. Ideally, a single-shot turbo spin-echo (TSE) readout with minimal TE, which is purely T_2 -weighted, would make the VERVE technique immune to GE-BOLD-related artifacts. Thus, in the subsequent discussion, signals simulated based on a TSE readout will serve in lieu of the reference.

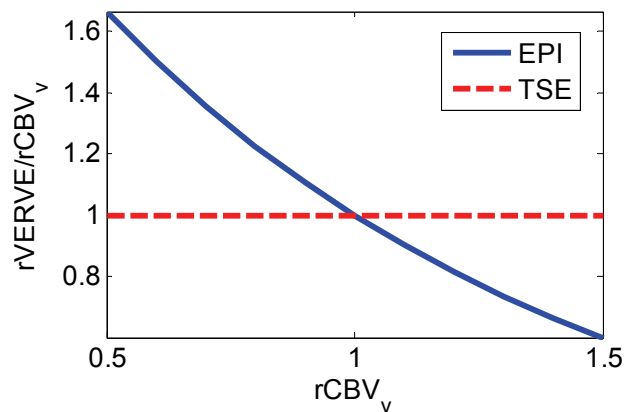


Figure 4.8 VERVE gradient-echo BOLD effect (I).

During venous CBV (CBV_v) change in the absence of blood oxygenation variations, the EPI-based VERVE signal (solid line) can overestimate the relative venous CBV ($r\text{CBV}_v$) during CBV decreases, and underestimate it during CBV increases. The TSE-based VERVE is shown to better represent venous CBV change, as shown by the line along unity.

4.3.2 Results

VERVE signal as measured using both TSE- and EPI-readout were simulated for 3 T conditions, using a baseline parenchymal CBV_v (CBV_0) of 5 ml/(100 g tissue). The simulated τ_{180}^F and τ_{180}^S were 3.7 ms and 30 ms [155], respectively, for a linearly encoded ascending readout with a 100-ms duration and an effective echo time (TE) of 50 ms. A baseline blood oxygenation of 60% was assumed in this case, as is typical in healthy humans [291, 292]. As observed in Figure 4.8, when VERVE is purely T_2 -weighted, as in the case when a TSE readout is used, and when no intravascular oxygenation change applies, the activation-induced VERVE signal ($rVERVE$) increases linearly with venous CBV change ($rCBV_v = CBV_v/CBV_0$). However, with the additional T_2^* weighting, $rVERVE$ is overestimated during CBV decreases, and underestimated during CBV increases.

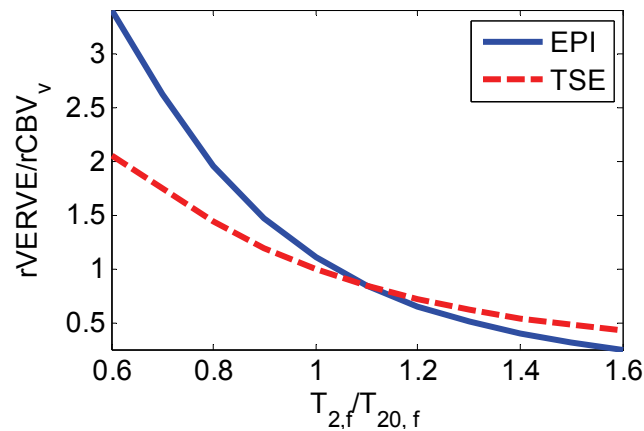


Figure 4.9 VERVE gradient-echo BOLD effect (II).

Even in the absence of CBV_v change, the IV-SE BOLD effect can introduce $rVERVE$ changes during blood oxygenation variations ($T_{2,f} \neq T_{20,f}$). While the VERVE calibration can correct for the T_2 -weighted IV-SE BOLD effect (dashed), the EPI-based VERVE signal (solid line) can introduce further overestimation $rCBV_v$ during oxygenation (Y) decreases (as represented by T_2 decrease) as well as underestimate $rCBV_v$ during Y increases. These effects would remain uncorrected by the VERVE calibration.

This scenario, when applied to the transient CBV response, is the same as outlined in the Balloon Model, proposed by Buxton *et al.* [293] to describe a purely biomechanical reaction in venous volume post-stimulation, when oxygen consumption, and hence blood oxygenation, has returned to pre-stimulation (baseline) levels. Under this assumption,

simulations suggest that it is possible for T_2^* weighting to introduce substantial biases in venous CBV (CBV_v) measurement, to the extent that a low-level CBV_v elevation can be viewed as a CBV_v undershoot.

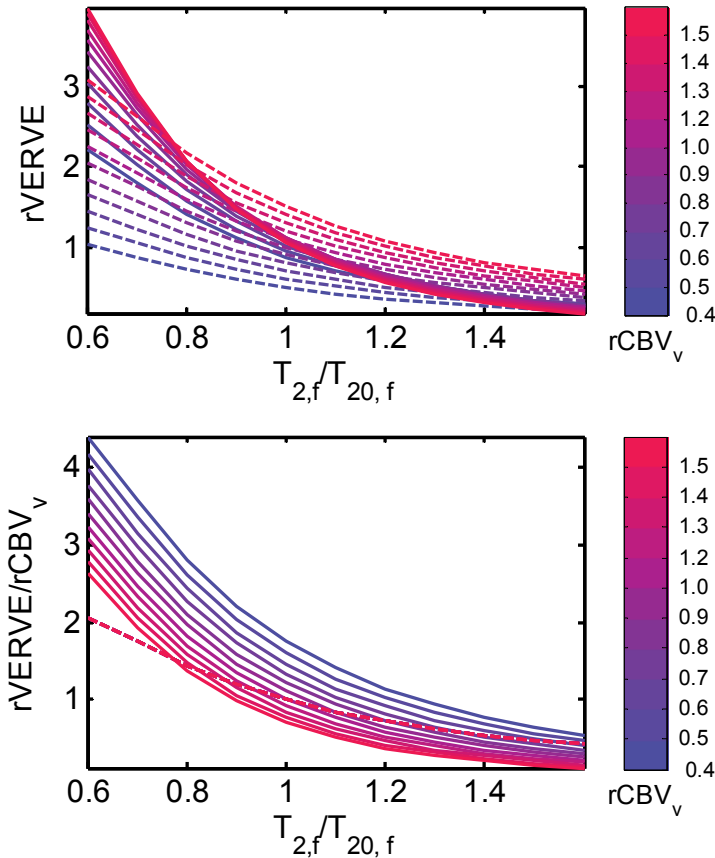


Figure 4.10 VERVE gradient-echo effect (I & II combined).

As expected, in the presence of blood oxygenation change (represented by variations in $T_{2f}/T_{20,f}$), $rVERVE$ underestimates $rCBV_v$, as shown with both T_2 (dashed) and T_2^* -weighted (solid) readout. However, the presence of T_2^* decay results in additional biases. While decreases in ΔCBV_v are over-estimated relative to the T_2 -weighted signal, increases in $rCBV_v$ are underestimated, the degree of the underestimation increasing with $rCBV_v$ and blood oxygenation.

On the other hand, when the venous blood oxygenation changes during activation relative to baseline, T_2^* -weighting can create artificial VERVE signal changes even when venous CBV has not changed relative to baseline. In this simulation, we use the apparent blood T_2 in the fast-refocused regime, which is a surrogate of blood oxygenation, to probe VERVE signal dependence, with $T_{2,0}$ representing the baseline blood T_2 . Venous oxygenation was allowed to vary between 25% and 75%. As seen in Figure 4.9,

compared to the TSE case, the VERVE signal obtained using a T_2^* -weighted (EPI) readout is under-estimated during venous oxygenation (T_2) decrease ($T_{2f}/T_{20,f} < 1$), and over-estimated during oxygenation increases ($T_{2f}/T_{20,f} > 1$).

This scenario in the transient state resembles that which was described by Lu *et al.* [152], in which although CBV has returned to its pre-stimulation (baseline) level following neuronal activation, oxygen consumption and hence blood oxygenation remain elevated and attenuated, respectively. Under these conditions, the simulations suggest that it is possible for T_2^* weighting to introduce substantial CBV underestimation when venous ΔCBV is already low, and overestimation in the opposite case.

When venous CBV and oxygenation change simultaneously, a more complex interplay is spawned, as shown in Figure 4.10. Referencing against the dashed lines (T_2 -weighted readout), it is apparent that using EPI, the BOLD effect associated with the use of EPI results in overestimated venous CBV increases and decreases. Also, greater $r\text{CBV}_v$ lead to greater biases. As outlined above, these errors could lead to seriously flawed interpretations of venous hemodynamics. The substantially enhanced T_2^* decay at 3 T relative to 1.5 T further presses the importance of imposing a purely T_2 -weighted VERVE signal.

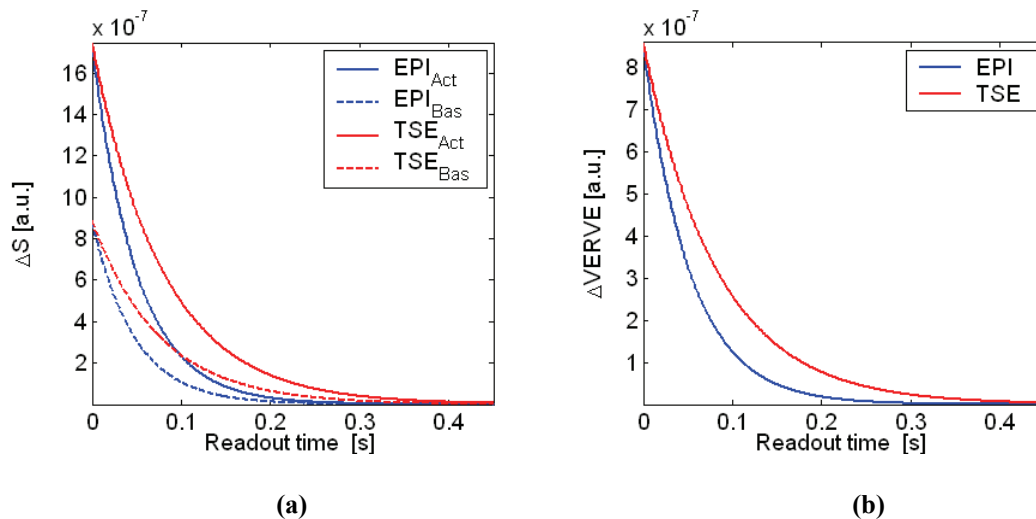


Figure 4.11 T_2 -weighted vs. T_2^* -weighted VERVE readout.

The expected fast-slow signal difference is shown for a T_2 -weighted (TSE) and T_2^* -weighted (EPI) acquisition, both using a readout bandwidth of 700 Hz/voxel (a). The simulated blood T_2 was obtained from relaxometry measurements at 3 T, with τ_{180}^F and τ_{180}^S being 4 and 30 ms, respectively. Theoretically, based on these parameters, the resultant VERVE contrast is up to 200% superior in TSE-VERVE, and the signal strength is maintained over a longer readout time, as expected (b).

It was recognized that techniques other than TSE can also help minimize the GE-BOLD weighting. Both partial-Fourier and parallel imaging acceleration were evaluated experimentally as potential options for reducing the effective TE of EPI acquisitions. However, these methods were found to introduce biases in the phase measurements and tremendously reduce the effectiveness of the correction for phase errors accumulated in the VERVE refocusing trains. As a result, full k -space TSE acquisitions proved the most viable option.

Simulations of EPI- and TSE-VERVE signals were performed assuming a noiseless medium. As shown in Figure 4.11, the VERVE contrast obtained using a T_2 weighted acquisition is consistently superior to that obtained using an EPI acquisition. This enables substantial potential improvement in VERVE CNR at 3 T (relative to 1.5 T), in addition to that stemming from the enhanced venous blood T_2 dependence on CPMG refocusing and oxygen saturation (discussed in Chapter 3). The precise contrast gain associated with the transition from an EPI to a TSE acquisition is specific to the given readout bandwidth and field uniformity (as will be discussed in section 4.5). At 3 T, using τ_{180}^F and τ_{180}^S of 3.7 and 30 ms, respectively, the gain in Δ VERVE obtained using TSE relative to EPI can exceed 100%. Furthermore, given a fixed matrix size, SNR is generally maximized at a low readout bandwidth, corresponding to a long readout time. However, the absolute VERVE contrast also decreases as readout time increases, prompting considerations to optimize both SNR and contrast (discussed in section 4.5).

4.4 Spin-Echo BOLD Effects in VERVE

As described previously, the sensitivity of the VERVE signal to blood oxygenation is both its strength and its weakness, given that blood oxygenation changes during neuronal activation is highly focal and difficult to measure. These oxygenation changes result in the IV SE BOLD effect. However, we have the capability to approximate this change based on other, more easily attainable measurements.

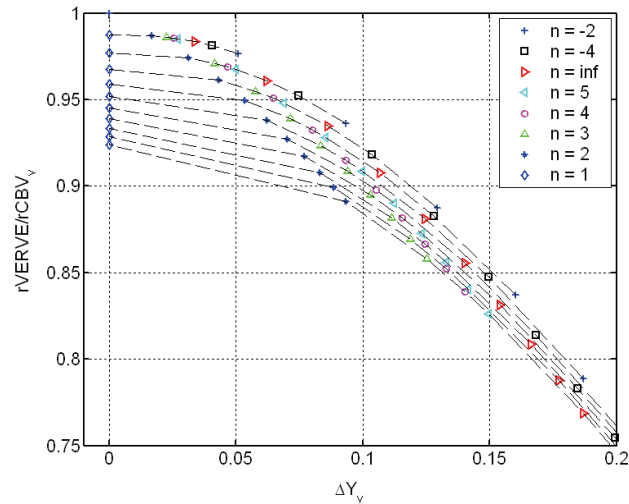


Figure 4.12 The VERVE calibration factor vs. ΔY_v at 3 T.

The ratio between $r\text{VERVE}$ and $r\text{CBV}_v$ at 3 T is plotted for various values of oxygenation change (ΔY_v), modulated by the neurovascular coupling ratio (n) and ΔCBF . Even at $n = 1$, $r\text{CBV}_v$ underestimation can be expected, as a consequence of the oxygenation disparity between the various deoxygenated compartments contributing to volume change. The underestimation is aggravated by increasing ΔY_v as well by increasing flow, as indicated by the dotted lines representing the iso- ΔCBF contours.

4.4.1 Sensitivity to the ΔCBF - $\Delta\text{CMR}_{\text{O}_2}$ Ratio

The degree of IV SE BOLD-induced venous ΔCBV underestimation exhibited by the VERVE signal is dependent on the degree of the associated CBF and venous oxygenation change in addition to the value of the neurovascular coupling ratio (n) applicable to the observed CBV change, as shown in Figure 4.12. In this case, the baseline venous oxygen saturation is assumed to be 60%, with fractional baseline venous CBV ($f\text{CBV}_{v,0}$) assumed to be 43% of total CBV, contributing to 62% ($f\Delta\text{CBV}_v$) of hyperemia-related total CBV change [155]. When n equals to 1, ΔCBF and $\Delta\text{CMR}_{\text{O}_2}$ are precisely matched, thus incurring no venous oxygenation change (ΔY_v) relative to baseline. This is the ideal case for VERVE, where the only remaining source of ΔCBV_v underestimation is the difference between the oxygenation of the capillary and venous compartments. However, neuronal activation has been widely associated with n values largely between 2 and 4 [5, 49, 174, 178, 180]. While further deviations of n from this range results in increasingly nonlinear calibration curves, rendering linearization increasingly difficult, the $r\text{CBV}$ values residing

in the “linear” calibration regime are approximately linearly related to $r\text{VERVE}$ and invariant over a large range of n values.

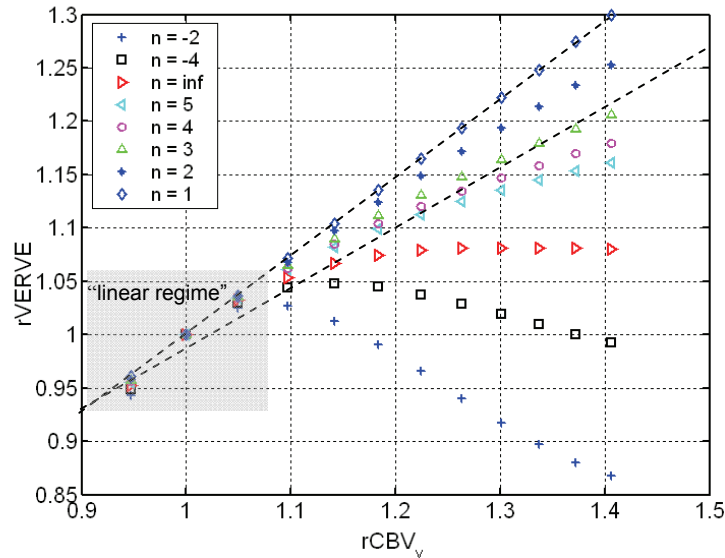


Figure 4.13 VERVE calibration variation with n .

As stated earlier, the IV SE BOLD effect can result in venous CBV underestimation, the degree of which varies with n . A n value of 3 has been found to well represent neuronal activation conditions, for which a linear approximation can be derived for the relationship between $r\text{VERVE}$ and $r\text{CBV}_v$ over a wide range of CBV changes, given a measurement of the baseline venous oxygenation ($Y_{v,0}$). The dotted lines delimit the range linearized calibrations for normal physiological conditions, and the shaded area demarcates the regime where the $r\text{VERVE}$ - $r\text{CBV}$ is approximately linear and invariant over a large range of n values. This group of calibration curves was simulated for $Y_{v,0} = 60\%$.

Given baseline global cerebral venous oxygenation ($Y_{v,0}$) measurements as well as the estimated n value, it is possible to predict the steady-state Y_v corresponding to activation, and hence the expected VERVE underestimation of ΔCBV_v due to activation-induced oxygenation changes. Within the range of $n = 2 \sim 4$ [5, 49, 174, 178, 180], a linear approximation to the relationship between steady-state $r\text{VERVE}$ and $r\text{CBV}$ can be derived across a wide range of flow values, with a correlation coefficient > 0.95 (Figure 4.13). This linear approximation enables an effective elimination of the VERVE estimation biases, and thus corrects for the IV SE BOLD effect. Furthermore, within the typical range of venous blood oxygenation seen in healthy humans, the variation in the calibration factor induced by changing n from 2 and 4 is no more than 20% (see Figure 4.13), well within the cross-sectional standard deviation in the time courses.

Successful calibration of the VERVE signal in the transient state necessitates additional considerations. First, the neurovascular coupling ratio during transient BOLD remains uncertain [194, 215]. In addition, the transient flow-volume relationship has been found to potentially deviate significantly from its steady-state counterpart [294]. Fortunately, the VERVE signal is intrinsically modulated by changes in venous blood volume, and VERVE calibration is therefore unbiased by assumptions regarding the precise flow-volume relationship. Furthermore, as seen in Figure 4.13, the IV SE BOLD calibration factor is effectively invariant over an extremely wide range of neurovascular coupling states at low levels of volume change, which lie within the “linear regime”, and are characteristic of the transient hemodynamic response. Therefore, uncertainties regarding the neurovascular coupling ratio during transitory IV SE BOLD effects do not prevent the characterization of venous CBV transients using VERVE, when calibrated within the normal physiological range.

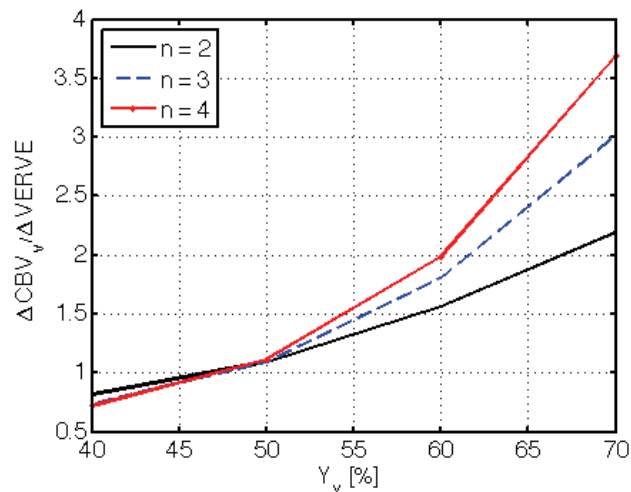


Figure 4.14 The influence of baseline Y_v on VERVE calibration.

The ΔCBV_v underestimation induced by the IV SE BOLD effect increases with baseline venous oxygenation (Y_v). The variability in the calibration factor ($\Delta CBV_v / \Delta VERVE$) also increases with Y_v .

4.4.2 Sensitivity to Baseline Venous Oxygenation

The VERVE calibration process is, however, very sensitive to the baseline venous oxygenation level, as illustrated in Figure 4.14. The degree of ΔCBV_v underestimation

due to the IV SE BOLD effect increases with increasing baseline oxygenation. Assuming $n = 3$, the VERVE calibration factor at $Y_v = 70\%$ is twice as high as at $Y_v = 55\%$. This behaviour is expected, since the level of deoxyhemoglobin-induced T_2 decay enhancement decreases nonlinearly with increasing Y_v . In addition, the variability in the calibration factor increases with Y_v .

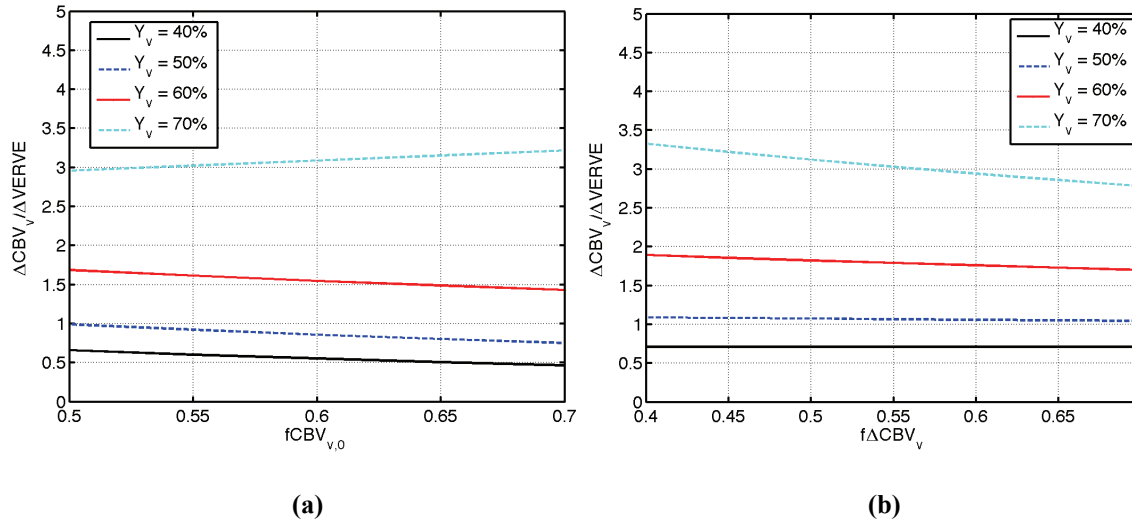


Figure 4.15 VERVE calibration sensitivity to venous blood fraction.

(a) Adopting an underlying $fCBV_{v,0}$ that varied between 0.5 (i.e. 30% capillary CBV_0 contribution) to 0.8 (i.e. no capillary CBV_0 contribution), an approximate 17% variation in the calibration factor can be expected based on a VERVE calibration calculation assuming $fCBV_{v,0} = 0.46$. (b) Assuming a varying $f\Delta CBV_v$ of between 0.4 (i.e. 33% capillary ΔCBV_v contribution) and 0.73 (i.e. no capillary ΔCBV_v contribution) results in a VERVE calibration error of 11%.

4.4.3 Sensitivity to the Resting State CBV_v and ΔCBV_v Fractions

Finally, as the VERVE calibration procedure makes assumptions on the baseline venous CBV fraction ($fCBV_{v,0}$) and activation venous CBV contribution ($f\Delta CBV_v$), the sensitivity of the calibration process to these assumptions was examined. The aforementioned VERVE calibration assumed $fCBV_{v,0} = 46\%$, assigning 21% and 33% of baseline CBV to the arterial and capillary compartments, respectively, as was indicated by cortical morphometry results [70]. Furthermore, $f\Delta CBV_v$ was assumed to be 62%, attributing 27% and 11% of total ΔCBV to arterial and capillary contribution, establishing venous dominance in hyperemic CBV change. Given the small overall contribution of arterial CBV and the fact that it does not contribute to the VERVE signal, the sensitivity

of VERVE calibration based on the compartmental CBV distribution was evaluated by varying the relative sizes of only the “actual” capillary and venous contributions. Such variations encompass the effect of potential mixing of the two compartments, especially in the transient state. Furthermore, we tested the dependence of VERVE calibration on the definition of “capillary” and “venous” compartments, which is relatively ambiguous, not aided by vast differences amongst existing works measuring compartmental contributions to CBV change [126, 127, 295].

In Figure 4.15a, the tissue model underlying the VERVE signal was simulated assuming a $fCBV_{v,0}$ that varied between 0.5 (i.e. 30% capillary CBV_0 contribution) to 0.8 (i.e. no capillary CBV_0 contribution). When assuming $n = 3$ and $Y_v = 60\%$, such a $fCBV_{v,0}$ variation translates to an approximate 17% variation in the calibration factor. This finding was echoed at other values of Y_v , albeit a capillary contribution of 0% is unrealistic and an extreme test case. On the other hand, as shown in Figure 4.15b, assuming a fixed $fCBV_{v,0}$ of 46% while varying $f\Delta CBV_v$ from 0.4 (i.e. 33% capillary ΔCBV contribution) to 0.73 (i.e. no capillary ΔCBV contribution) in simulating the VERVE signal, the corresponding calibration factor for the $Y_v = 60\%$ case showed an 11% variation. The calibration bias introduced by assuming the venous baseline CBV fraction or the venous ΔCBV contribution would not influence the VERVE ΔCBV_v estimates beyond its intrinsic standard deviation. These simulations demonstrate that while the VERVE calibration procedure is based on a number of assumptions with regards to physiological parameters that cannot be measured in vivo, it is robust against deviations from these assumptions in the physiologically relevant range.

In the presence of vasodilative agents such as CO_2 , a CBV increase can occur without a significant concomitant change in oxygen consumption, resulting in $n = \infty$. In fact, in certain studies, a decrease in $CMRO_2$ has been reported, in which case n would be negative [191, 296]. Under these conditions, given the highly nonlinear nature of the $rVERVE$ - $rCBV_v$ relationship, instead of deriving a linear calibration formula for all flow conditions, each ΔCBF level, and hence $\Delta VERVE$ value, must be associated with its own calibration factor.

4.5 VERVE Parameter Optimizations

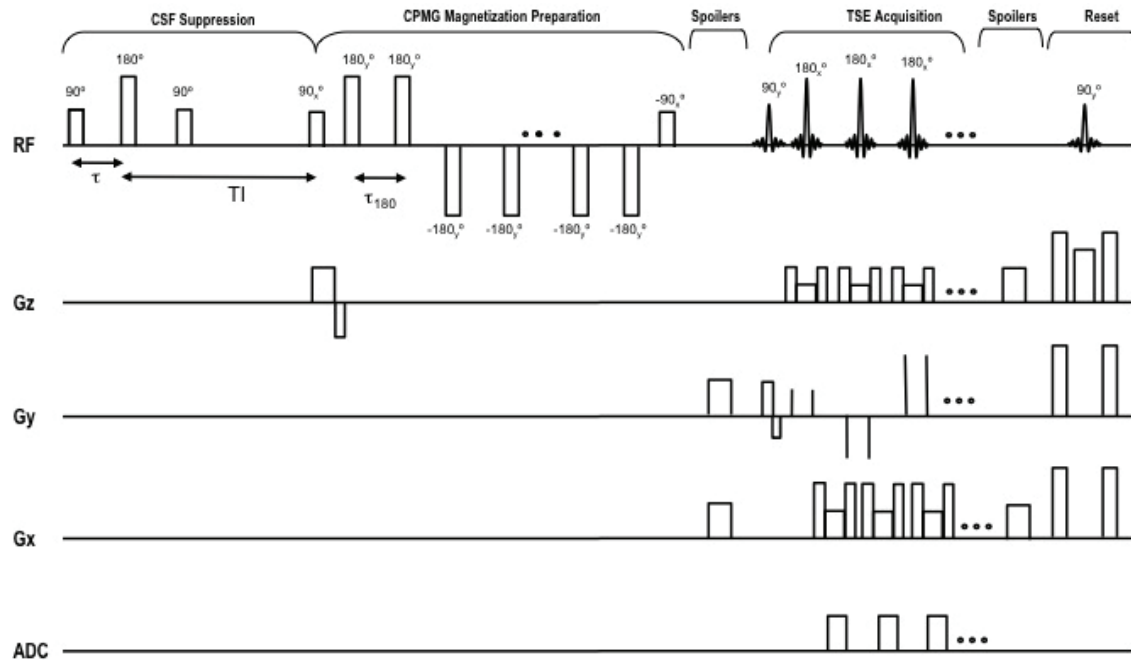


Figure 4.16 The TSE-VERVE sequence diagram.

In TSE-VERVE, each TSE acquisition is flanked by a pair of spoiler gradients to dephase any spurious echo induced by the long train of selective 180° refocusing pulses. The TSE readout is preceded and followed by strong spoiler gradients to eliminate remnant off-resonant magnetization from the refocusing trains. In addition, two sets of strong crushing gradients, intercepted by a 90° excitation pulse, follow the TSE readout to dephase the residual transverse and longitudinal magnetization.

4.5.1 Field Inhomogeneities

VERVE, with long refocusing trains at its core, is ideally dependent strictly on T_2 contrast. As such, systematic errors caused by B_0 and B_1 field inhomogeneities are a much graver concern at 3 T than at 1.5 T. Both B_0 and B_1 related errors can create flip-angle offsets and hence off-resonance (spurious) echoes which would engender T_2 underestimation. This effect is potentially worst with the fast-refocusing VERVE refocusing trains of closely spaced RF pulses, which can potentially create a correspondingly closely spaced train of spurious echoes, interfering destructively with the VERVE signal. In order to maximize VERVE signal robustness in the presence of these potential confounds, the Carr-Purcell Meiboom-Gill (CPMG) RF configuration, which is

a more robust extension of the CP sequence, was employed. The CPMG trains consisted of $90^\circ_x-180^\circ_y-90^\circ_x$ composite pulses, which are the most common choice for reducing the effect of B_1 variations, and the minimum durations of which fulfilled the requirements of fast-refocusing. These pulses were slice non-selective in order to preclude problems associated to with incomplete inversion of spins at the edge of the slice profile, which could also result in spurious echoes. Finally, the minimization of the remaining effects of residual refocusing imperfections was attempted using inter-refocusing spoiling gradients [272] and MLEV phase-cycling [1].

Inter-refocusing spoiling gradients were evaluated as one of the new VERVE design alternatives. This approach has been reported to provide the highest immunity to field inhomogeneities [272]. Furthermore, the spoiled VERVE trains would not impose the stringent limitations on refocusing train lengths, as did do phase-cycling methods, and can therefore substantially increase the flexibility in the VERVE refocusing-train design. We experimented with spoiler-gradient trains in which the spoiler amplitudes were modulated to be alternating and descending, as previously noted to afford optimal SNR and spoiling efficiency [255]. However, notwithstanding the many optimizations that were applied, limitations on gradient slew rate and amplitude unwittingly lengthened the minimum realizable inter-refocusing interval. Experimentally, the subsequent reduction of the fast-refocusing rate proved counterproductive to maximizing VERVE contrast. As such, despite the potential benefits of using spoiler gradients, the phase-cycling method was opted for.

A fundamental requirement of MLEV phase-cycling schemes [1] is that the refocusing train be composed of an even number of pulses (l), with $l \geq 4$, with the best results obtained when $l = 2^k$, where $k = 2, 3, 4, 5 \dots$. The 16-element super-cycle, consisting of four 4-element cycles, was deemed optimal [1], with linear combinations thereof further enhancing the power of the phase-cycle. In the VERVE sequence, we employed variants of a “ $\check{R}\check{R}\check{R}\check{R} R\check{R}\check{R}\check{R} R\check{R}\check{R}\check{R} \check{R}\check{R}\check{R}\check{R}$ ” phase pattern, with \check{R} and R indicating 180° and -180° pulses, respectively. The number of repetitions of this train, as well as the corresponding echo time (TE), was chosen based to optimize image SNR and the VERVE contrast-to-noise ratio (CNR), to be discussed next.

4.5.2 Contrast and Noise

In a noise-free environment, VERVE contrast ($\Delta S_{b,A}/\Delta S_{b,B}$) increases linearly with TE. However, in practice, the optimal VERVE refocusing train combinations do not necessarily correspond to those that theoretically provide the maximum contrast, but rather those that maximize the contrast-to-noise ratio (CNR). Also, given the general shortening of T_2 at 3 T, especially in venous blood, the optimal TE at 3 T is expected to be shorter than that at 1.5 T. The pulse train length constraints imposed by the MLEV phase patterns further condense our options to the following: (1) 8 slow-refocusing pulses ($n^S = 8$); (2) 4 slow-refocusing pulses ($n^S = 4$).

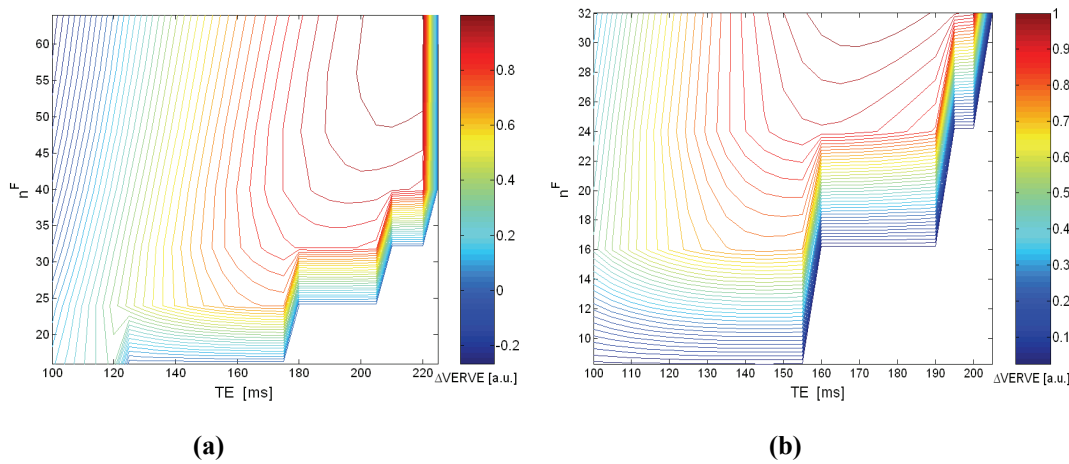


Figure 4.17 VERVE parameter optimization contour plots.

(a) Using the n^F -fast-/8-slow-refocusing RF pulse configuration at a baseline venous oxygenation of 60%, the VERVE signal difference (ΔVERVE , normalized to 1) is maximized at approximately 210 ms (c), with maximum n^F (i. e. equal to 64). **(b)** Alternatively, using the n^F -fast-/4-slow-refocusing RF pulse configuration at the same SNR, ΔVERVE optimized at a TE of 170 ms, with $n^F = 32$. At long TEs accompanied by wide fast-refocusing intervals, contrast is abolished due to noise.

The simulated VERVE signal is based on a venous blood SNR of 45 (estimated from phantom and venous blood images), a conservative estimate corresponding to a baseline venous oxygenation ($Y_{v,0}$) of 60%, assessed empirically from a healthy human cohort ($Y_{v,0}$ typically ranges between 50% and 70% within the normal physiological range). In Figure 4.17, a venous CBV increase corresponding to a blood flow increase of 50% (with $\Delta\text{CBF}:\Delta\text{CMR}_{\text{O}_2} = 3$ and $\text{TR} = 4$ s) was simulated to probe the TE dependency of an n^F -fast/ n^S -slow refocusing train, where n^F and n^S are the number of fast- and slow-

refocusing pulses, respectively. For the n^F -fast/8-slow combination, the amplitude of ΔVERVE , namely the difference between the activation ($\Delta S_{b,A}$) and baseline ($\Delta S_{b,B}$) VERVE signals, is maximized at a TE of approximately 210 ms, at the centre of a wide optimization peak, as shown in Figure 4.17a. Note that although the optimization point is relatively forgiving, should the SNR drop below the average value estimated by the simulations, contrast can quickly become abolished due to noise contamination. This implies that the TE should be chosen below the simulated optimal TE. As the signal strength originating from venous blood is dependent on $Y_{v,0}$, the sensitivity of the optimal TE to baseline oxygenation was also assessed. Based on simulations with $Y_{v,0}$ of 50%, the optimal TE is $\cong 185$ ms, whereas at $Y_{v,0} = 70\%$, the optimal TE is $\cong 235$ ms. The choice of optimal TE for this configuration should therefore be between 185 and 235 ms. Within this range, the most physically realistic parameters are $n^F = 64$, $\tau_{180}^F = 3.02$ ms, $\tau_{180}^S = 24$ ms, producing MLEV phase-cycled refocusing trains with an effective TE of 192 ms.

The simulated optimization contour plot for an n^F -fast/4-slow combination is shown in Figure 4.17b. For a $Y_{v,0}$ of 60%, the value of ΔVERVE is maximized at a TE near 170 ms. Furthermore, at a $Y_{v,0}$ of 50%, the optimal TE is 135 ms, whereas at $Y_{v,0} = 70\%$, the optimal TE is approximately 185 ms. Based on the above information, the final choice of TE for this configuration should be between 135 and 185 ms. Within this range, the most practical parameters are $n^F = 32$, $\tau_{180}^F = 5$ ms, $\tau_{180}^S = 40$ ms, respectively, corresponding to an MLEV phase-cycled refocusing train with an effective TE of 160 ms. It should be noted that while both TE's can provide optimized VERVE contrast, the adoption of a longer TE better suppress extravascular dynamic averaging effects.

The above two designs were both evaluated experimentally. Functional ΔCBV_v data proved that activation maps obtained using the 64-fast/8-slow combination were more robust and exhibited less noise-induced bias. By way of explanation, it is likely that the drastic blood signal decrease from $\tau_{180} = 3$ ms to 5 ms compromised the VERVE contrast, while a slow-refocusing τ_{180} of 40 ms did not provide sufficient SNR for the resultant difference between $\Delta S_{b,A}$ and $\Delta S_{b,B}$ to be meaningful.

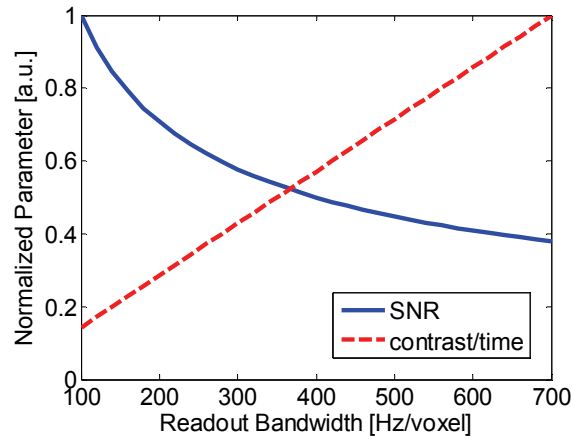


Figure 4.18 VERVE SNR vs. readout bandwidth.

The SNR of images acquired using TSE readout decays supra-linearly with readout bandwidth (solid line), while the contrast-per-unit-time (contrast/time) increases steadily with readout time (dashed line). The most feasible readout bandwidth is found between 300 and 600 Hz/voxel.

Finally, in general, the use of a lower readout bandwidth, hence a longer readout, increases the contrast-per-unit-time of VERVE, though at the cost of the image SNR. According to simulations (Figure 4.18), the gain in contrast follows an approximately linear growth, while the loss in SNR exhibits an asymptotic decrease with increasing bandwidth. Beyond a bandwidth of approximately 350 Hz/voxel, the loss in SNR seems to be outweighed by the gain in contrast, suggesting the use of the fastest-possible TSE readout, namely at 800 Hz/pixel. However, in practice, the use of an 800 Hz/voxel readout bandwidth resulted in a 25% reduction in CNR relative to data acquired with a bandwidth of 350 Hz/voxel. Therefore, while using a long readout undermines the VERVE contrast as seen immediately after the non-selective refocusing train, it is also inadvisable to acquire too quickly. The ideal readout bandwidth should be between 300 and 600 Hz/voxel.

4.5.3 Power Deposition and SNR

Composite pulses consist of RF sub-pulses which can be arranged in an arbitrary complexity, with their ability to reduce sensitivity to field variations increasing with pulse complexity. However, higher order composite pulses quickly become too long to fulfill the fast-refocusing requirements of VERVE. Furthermore, the associated power

deposition also escalates, as predicted by the specific power absorption (SAR) formulation,

$$SAR = \sigma \cdot \frac{\pi^2 r^2 f^2 B_1^2 D}{2\rho} \quad [4.3]$$

where r is the sample radius, f is the Larmor frequency, D is the RF duty cycle and ρ is the tissue density. The SAR limit for the human head, as established by both the Food and Drugs Administration (FDA) and the International Electrotechnical Commission (IEC), is 3 W/kg over 10 minutes. Also, previous studies have indicated that the largest temperature increase in the head is on the skin surface of the face and neck [297, 298]. The heat capacity is greater in samples with larger masses (the denominator), but a larger sample volume is associated with a lower ability for heat dissipation, making larger heads more difficult to image with VERVE. This difficulty is aggravated at 3 T, when where the power deposition is quadrupled due to doubling of the Larmor frequency.

With respect to the VERVE sequence with 64-fast/8-slow refocusing pulses and a TE of 192 ms, the human head SAR limit imposed a minimum TR of 4 s. Although the refocusing pulses in the TSE readout contribute notably to the SAR, the bulk of the SAR originates from the VERVE composite refocusing trains, with the fast-refocusing train depositing more than three times as much power as the TSE readout. The shortest refocusing pulses are the most efficient in eliminating the effects of field inhomogeneities, but also imply high RF amplitudes, hence higher SAR. The simplest way to lower the average SAR is to increase the TR. However, in the interest of designing the VERVE technique with a temporal resolution suitable for functional imaging, it is of considerable interest to reduce power deposition without increasing TR. While maintaining the use of the optimal fast- and slow-refocusing RF configurations, the simplest and most effective way to lower the SAR is to prolong the refocusing pulses, so long as the duration does not exceed the minimal τ_{180} of 3.02 ms. The resulting VERVE sequence enabled a 30% reduction in the minimum TR. However, depending on the amount of field inhomogeneities in the imaged medium, such as air pockets, the effectiveness of these “low-SAR” refocusing trains may vary. Experimentally, lengthening the refocusing pulses by 100% resulted in a reduction in the amplitude of

Δ VERVE by approximately 20%. It is therefore advisable to use the shortest refocusing pulses permitted by the SAR limit whenever possible.

4.5.4. Cerebral Spinal Fluid Suppression

The enormous signal contribution from CSF is a potentially substantial source of confound in venous CBV measurements using VERVE. With blood volume increases there can be displacement of brain tissue and therefore of CSF, and the resulting decrease in CSF signal can far outweigh the increase in blood volume signal. Therefore, it is imperative that the CSF signal be minimized for any given TR. The voxel-wise longitudinal magnetization, consisting of contributions from grey matter (GM), white matter (WM), blood and CSF, is given by

$$M_z = \sum_i M_{0,i} \cdot [1 - 2 \cdot e^{-TI_{CSF}/T_{1,i}} + e^{-TR/T_{1,i}}], \quad i = GM, WM, blood, CSF \quad [4.4]$$

where M_0 is the equilibrium magnetization, TR is the sequence repetition time, and TI_{CSF} is the CSF inversion time. The CSF nulling procedure employed in VERVE was described by Wong *et al.* [290], and designed to selectively maximize the SNR of selected tissue species based on their T_2 values, foregoing the need to employ long TRs in order to restore tissue magnetization. In this approach, a $90^\circ_x - \tau - 180^\circ_y - \tau - 90^\circ_x$ composite pulse is used in the role of the inversion pulse, and the magnetization available for imaging is given by

$$M_z = M_0 \cdot \{1 - [1 + (1 - e^{-(TR - TI_{CSF} - 2\tau)}) \cdot e^{2\tau/T_2} \cdot e^{-TI_{CSF}/T_1}]\} \quad [4.5]$$

where TI_{CSF} is the time between the 180_y pulse and the image excitation pulse. The initial 90°_x pulse eliminates all available magnetization in the z-direction, and the longitudinal magnetization generated during the 2τ period is absent since it is destroyed by the second 90°_x pulse. Under the condition of τ being much less than the T_2 of CSF, the composite pulse will act as a CSF inversion pulse, with the second 90°_x pulse achieving inversion of any magnetization created by the first two pulses. Based on experimental data which illustrate an intrinsic venous blood T_2 of 186 ms (see Chapter 3), a τ of 90 ms was deemed optimal for venous blood T_2 contrast at 3 T. Relative to conventional CSF suppression,

the T_2 -selective CSF suppression technique will allow the augmentation of VERVE SNR even at short TRs.

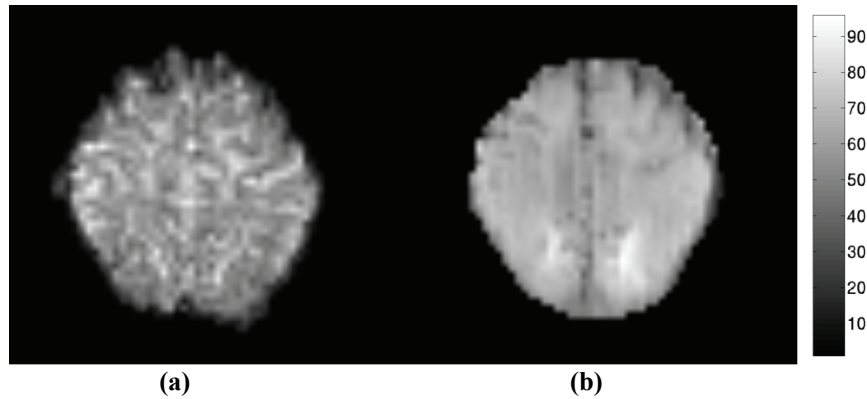


Figure 4.19 Comparison of EPI- and TSE-VERVE SNR images.

Masked SNR maps were calculated from the average of fast- and slow-refocused images for EPI-VERVE (a) and TSE-VERVE (b), both acquired using the 8-channel head-coil at 3 T. SNR was defined as the average signal strength divided by the average standard deviation, and indicated by the scale bar. Compared to the EPI-VERVE, TSE-VERVE exhibits significantly higher SNR.

4.5.5 Summary

Shown in Figure 4.19 are SNR maps for one subject computed from the fast-slow difference images for both EPI-VERVE and TSE-VERVE sequence at 3 T, the latter exhibiting superior SNR. The TSE-VERVE design incorporated all above considerations, as illustrated in Figure 4.16. The VERVE magnetization preparation was composed of a set of non-selective 90°_x tip-down and tip-up pulses flanking an MLEV phase-cycled CPMG train made up of non-selective composite 90°_x - 180°_y - 90°_x refocusing pulses for either fast or slow refocusing. The corresponding τ_{180}^F and τ_{180}^S were 3 ms and 24 ms, respectively, forming a refocusing train with duration of 192 ms. The 90°_y excitation, which was phase-chopped to further reduce signal bias induced by B_0 and B_1 inhomogeneities, was followed by a centrally-encoded spin-echo CPMG readout, which further maximizes SNR. Finally, each acquisition was terminated by a slice-selective 90°_y resetting pulse to accelerate signal recovery. Empirically, at 3 T, the CNR gained over the previous design is reflected by a group-average increase of 50% in activation t -score (in response to identical stimulation paradigms). Results from functional studies employing this technique will be presented in Chapters 5 and 6.

Chapter 5

BOLD-Specific Flow-Volume Relationship during Neuronal Activation

5.1 Preface

The development of the VERVE technique at 3 Tesla, which was detailed in Chapter 4, has provided us with the ability to dynamically and non-invasively monitor venous ΔCBV (ΔCBV_v) at 3 T, established by reasonable and reproducible VERVE ΔCBV_v measurements. This development has made it possible to address some pressing questions regarding the role of venous CBV in fMRI. Given the predominance of venous CBV effects on the BOLD signal, it is of immediate importance to quantify ΔCBV_v corresponding to a given BOLD. Such knowledge is also key to the accurate estimation of the underlying oxygen metabolism (CMRO_2) change using calibrated BOLD [5, 174]. Thus far, Grubb's power-law relationship [46], which predicts $r\text{CBV}$ as $r\text{CBF}^\alpha$, with α assumed to be 0.38, has been predominantly used for this purpose. However, this relationship, which has its origin in non-human primate measurements under hypercapnic challenges, is not accurate for most functional applications, as it reflects total rather than venous CBV changes, the latter being the primary CBV component in modulating the BOLD signal. Nonetheless, robust and non-invasive in vivo venous CBV measurement is non-trivial, and was not possible prior to the development of VERVE.

This chapter documents the study of steady-state ΔCBV_v and ΔCBF responses to graded visual and sensorimotor stimulation measured simultaneously using VERVE and QUIPSS II arterial-spin labeling (ASL), respectively, in healthy human volunteers. The results quantify the expected difference between the flow-volume relationships derived using total and venous ΔCBV . The power-law coefficient (α) found using ΔCBV_v was

0.23 ± 0.05 , largely invariant across the cortex, and substantially lower than Grubb's value of 0.38. Furthermore, the assumption of the latter is shown to produce an overestimation in the contribution of ΔCBV , introducing significant $\Delta\text{CMR}_{\text{O}_2}$ underestimation when using calibrated BOLD.

BOLD-Specific Cerebral Blood Volume and
Blood Flow Changes during Neuronal
Activation in Humans

Jean J. Chen and G. Bruce Pike

McConnell Brain Imaging Centre
Montreal Neurological Institute
McGill University

Submitted to NMR in Biomedicine

Under review

5.2 Abstract

To understand and predict the blood-oxygenation level-dependent (BOLD) fMRI signal, an accurate knowledge of the relationship between cerebral blood flow (ΔCBF) and volume (ΔCBV) changes is critical. Currently, this relationship is widely assumed to be characterized by Grubb's power-law, derived from primate data, where the power coefficient (α) was found to be 0.38. The validity of this general formulation has been examined previously, and α of 0.38 has been frequently cited when calculating oxygen metabolism change ($\Delta\text{CMR}_{\text{O}_2}$) using calibrated BOLD. However, the direct use of this relationship has been the subject of some debate, since it is well established that the BOLD signal is primarily modulated by changes in "venous" CBV (ΔCBV_v , comprising deoxygenated blood in arteriolar, capillary, venular compartments) instead of total CBV, and yet ΔCBV_v measurements in humans have been extremely scarce. In this work, we demonstrate reproducible ΔCBV_v measurements at 3 T using the venous refocusing for volume estimation (VERVE) technique, and report on steady-state ΔCBV_v and ΔCBF measurements in human subjects undergoing graded visual and sensorimotor stimulation. We found that: (1) a BOLD-specific flow-volume power-law relationship is described by $\alpha = 0.23 \pm 0.05$, significantly lower than Grubb's constant of 0.38 for total CBV, (2) this power-law constant was not found to vary significantly between the visual and motor areas, and (3) the use of Grubb's value of 0.38 in gradient-echo BOLD modelling results in a significant $\Delta\text{CMR}_{\text{O}_2}$ underestimation.

Key words: cerebral blood volume, cerebral blood flow, venous CBV, Grubb's relationship, power-law, BOLD, VERVE

5.3 Introduction

To understand and predict the blood-oxygenation level-dependent (BOLD) fMRI signal, an accurate knowledge of the relationship between changes in cerebral blood flow (CBF) and cerebral blood volume (CBV) is critical [5, 174]. Grubb *et al.* first performed a quantitative investigation of this relationship using hypercapnia-based CBF modulation in phencyclidine-anesthetized rhesus monkeys, and obtained CBV from mean transit time data obtained using H_2^{15}O and C^{15}O -hemoglobin tracers. They found a power-law relationship between CBV and CBF which was characterized by the equation, $\text{CBV} = 0.80\text{CBF}^{0.38}$ [46]. This equation has since been used extensively in fMRI signal modeling, and the power-law coefficient of 0.38 has been widely assumed when estimating oxygen metabolism change ($\Delta\text{CMR}_{\text{O}_2}$) using calibrated BOLD [5, 178, 299]. At the same time, the general validity of Grubb's power-law relationship has been supported by data from other imaging modalities in animal and human studies [126, 140, 155, 200]. However, as much as it is widely assumed, the value of α has remained a subject of investigation and debate. Using MRI at 9.4 T, Lee *et al.* found the relationship between relative CBF ($r\text{CBF}$) and total relative CBV ($r\text{CBV}$) during hypercapnia to be $r\text{CBV}(\text{total}) = r\text{CBF}^{0.40}$, consistent with Grubb's measurements of absolute CBF-CBV variations [126]. Using H_2^{15}O and ^{11}CO PET, Ito *et al.* [200] found the relation between CBF and CBV values in healthy human subjects during rest and visual stimulation to be $\text{CBV} = 0.88\text{CBF}^{0.3}$. They went on to perform similar measurements under hyper- and hypocapnic perturbation, and found a similar CBF-CBV relationship [199]. Rostrup *et al.* also performed human PET studies under hyper-/hypocapnic challenges, and found reasonable representation of the CBF-CBV relationship in a power-law format. However, they found significantly different values for α , as summarized by $\text{CBV} = 0.72\text{CBF}^{0.64}$ and $\text{CBV} = 1.10\text{CBF}^{0.46}$ in cortical and sub-cortical grey matter, respectively. Finally, using monocystalline iron-oxide nanocolloid (MION) enhanced MRI on urethane-anesthetized rats undergoing graded hypercapnia, Wu *et al.* found α to be within the above range, but spatially variant [140].

While existing data has established a sound basis for the CBF-CBV coupling within the functionally relevant physiological range, the role of CBV in modulating the

BOLD signal must be considered in more detail. Physiologically, the mechanisms involved in the hyperemic response due to neuronal activation and hypercapnia differ. A purely vascular hyperemic response (i.e. during hypercapnia) is related to CO₂-induced acidosis [300], while neuronally-modulated hyperemia is firstly associated with neurotransmitter-mediated release of nitric oxide [51]. More importantly, since the BOLD signal originates from oxygenation change in partially deoxygenated blood, blood from arteries is not expected to significantly contribute, since it is almost always fully oxygenated under normal physiological conditions. Therefore, the BOLD signal is primarily modulated by changes in venous CBV (ΔCBV_v) rather than in total CBV [5, 126]. The term “venous blood” is a simplified reference to all partially deoxygenated blood, specifically, from a collective of weighted sub-compartments encompassing arterioles [301], capillaries and venules. Ances *et al.* [302] noted that the value of α directly impacts the estimation of oxygenation metabolism from the BOLD signal. Lee *et al.* used perfluorocarbon-enhanced double-echo spectroscopy to separate arterial and venous contribution to hypercapnia-induced CBV increase in rodents [126], and found that absolute venous ΔCBV contributes approximately 36% to the total blood volume increase. Nonetheless, there is a paucity of direct ΔCBV_v measurements in awake animals, and an absence of human data.

Venous refocusing for volume estimation (VERVE) is a recently proposed fMRI technique that targets volumes changes in partially deoxygenated blood. The technique is based on the unique T_2 dependence of deoxygenated blood on oxygen saturation and the Carr-Purcell Meiboom-Gill (CPMG) refocusing interval. Preliminary ΔCBV_v estimates using this technique at 1.5 T [155] and 3 T [303] have been presented. However, in order to minimize T_2^* (gradient-echo BOLD) effects, which increasingly competes with the VERVE effect at higher magnetic field strengths, we revised the design of the VERVE technique. In this work, we use the improved VERVE method in conjunction with arterial spin labelling to study the steady-state relationship between activation-induced changes in CBF and venous CBV in response to graded visual and sensorimotor stimulation in healthy humans.

5.4 Materials and Methods

5.4.1 MRI Acquisition

Sixteen healthy adults (14 females and 2 males, ages ranging from 22 to 31 years) participated in the study, each having given informed consent prior to the scanning session (Research Ethics Board, Montreal Neurological Institute). Subjects were immobilized using a head holder assembly. An RF body coil was used for transmission and an 8-channel phased-array head coil for signal reception. All examinations were performed on a Siemens 3 T Magnetom Trio system (Siemens, Erlangen, Germany). The scanning protocol included a 3D RF-spoiled gradient-echo scan with 1 mm isotropic resolution that served as anatomical reference. The basic functional imaging parameters were: FOV/matrix/slice-thickness/TR = 200 mm/64x64/5 mm/4000 ms. The fMRI acquisitions were single-slice, with a voxel size of 3.1 x 3.1 x 5 mm³, and oriented as oblique-axial to include the primary motor and visual cortices, guided by an 80 s multi-slice BOLD visual and sensorimotor functional scout. During the functional scout, subjects were presented with the visual stimulus while performing the high-frequency motor task described in the next section. Functional localizer *t*-maps were produced using the scanner console software (Siemens, Erlangen, Germany), and the coordinates of the regions with the most significant activation in both the visual and sensorimotor regions were used in placing the imaging slice.

5.4.1.1 Venous CBV Measurement

As first described by Stefanovic and Pike [155], relative venous CBV ($rCBV_v = CBV_{v,A}/CBV_{v,B} \times 100\%$) is directly proportionally to the relative VERVE signal ($rVERVE_s = 100\% + \Delta VERVE$ [304]), which is determined by the ratio between VERVE signals acquired during activation and baseline conditions, $\Delta S_{b,A}$ and $\Delta S_{b,B}$, respectively. These signals are in turn determined by the respective apparent blood T_2 , which depends on the level of blood oxygenation (Y) at activation and baseline, Y_A and Y_B , as well as on the Carr-Purcell Meiboom-Gill (CPMG) refocusing interval (τ_{180}) in the fast- and slow-refocusing regime, τ_{180}^F and τ_{180}^S . $rVERVE$ is therefore summarized by,

$$rVERVE = \frac{\Delta S_{b,A}}{\Delta S_{b,B}} = \frac{f_{b,A}}{f_{b,B}} \cdot \frac{e^{-TE/T2_b(Y_A, \tau_{180}^F)} - e^{-TE/T2_b(Y_A, \tau_{180}^S)}}{e^{-TE/T2_b(Y_B, \tau_{180}^F)} - e^{-TE/T2_b(Y_B, \tau_{180}^S)}} \quad [5.1]$$

where $f_{b,A}$ and $f_{b,B}$ are the blood water volume fractions at activation and baseline, respectively. While the ratio $f_{b,A}/f_{b,B}$ can be interpreted as $rCBV_v$, the oxygenation dependence, termed the intravascular spin-echo BOLD (IV-SE-BOLD) effect, introduces a BOLD effect into the VERVE signal during local oxygenation changes such as those associated with neuronal activation. However, by using venous oxygenation-based calibration, it is possible to estimate and correct this BOLD effect, thus permitting $rCBV_v$ to be derived from $rVERVE$. The theoretical basis of this process has been extensively described by Stefanovic and Pike [155], who demonstrated robust $rCBV_v$ measurements using VERVE at 1.5 T. Given the subject-variability of venous oxygenation, this calibration was based on per-subject baseline venous oxygenation measurements.

The dependence of the apparent blood T_2 on Y and τ_{180} is the foundation of VERVE contrast, and widely known to be highly field-dependent. We obtained this relationship at 3 T through detailed whole human blood relaxometry [305], and found it to be best described by the constrained diffusion model of Jensen and Chandra [61],

$$\frac{1}{\Delta T_2} = G_0 \frac{\gamma^2 r_c^2}{2D} F\left(\frac{2D\tau_{180}}{r_c^2}\right) \quad [5.2]$$

where G_0 is the spatial magnitude of the deoxygenation-induced field inhomogeneities, D is the diffusion coefficient, and γ is the gyromagnetic ratio. Eq. [2] is used to estimate baseline blood oxygenation ($Y_{v,0}$) through venous blood T_2 measurements obtained by in vivo relaxometry, which in turn allows the derivation of subject-specific VERVE calibration factors to compensate for the IV-SE-BOLD effect.

In the original VERVE study [155], an echo-planar imaging (EPI) readout was employed. Although reasonable ΔCBV_v values were obtained at 1.5 T, this design becomes increasingly impractical at higher fields as T_2^* decay during readout is significantly enhanced, introducing gradient-echo BOLD weighting in ΔCBV_v measurements, as well as detrimental decreases in the VERVE signal-to-noise ratio (SNR). At 3 T, a centrically-encoded single-shot turbo spin-echo (TSE) design was

chosen to help minimize this problem while maintaining the acquisition speed of VERVE, and increasing the VERVE contrast-to-noise ratio (CNR) by a minimum of 100%. Moreover, to adapt to the relatively high field non-uniformity at 3 T, the VERVE refocusing train was implemented as magnetization preparation with non-selective tip-down and tip-up pulses, allowing the separation of in-phase and out-of-phase (undesired) signals, the latter being suppressed using pre-readout spoiler gradients following the tip-up. To further minimize undesired signal contribution, each refocusing pulse in the readout is flanked by matched spoiler gradients.

The VERVE magnetization preparation consisted of a refocusing train, as mentioned above, which was composed of a pair of non-selective 90°_x tip-down and tip-up pulses flanking an MLEV phase-cycled CPMG train made up of non-selective composite $90^\circ_x-180^\circ_y-90^\circ_x$ refocusing pulses for either fast or slow refocusing. The corresponding τ^F_{180} and τ^S_{180} were 3 ms and 24 ms, respectively, forming a refocusing train with a duration of 192 ms. This, combined with the echo-spacing of 6.8 ms for the TSE readout, resulted in an effective VERVE echo time (TE) of 198.8 ms. In addition, in the current implementation of VERVE, T_2 -selective cerebral-spinal fluid (CSF) suppression was performed using a $90_x-\tau-180_y-\tau-90_x$ composite inversion pulse [290] with a τ of 90 ms, applied at an inversion time (TI) of 1100 ms for a total repetition time (TR) of 4 seconds. A single-shot TSE readout bandwidth of 350 Hz/pixel was chosen after optimization of the image SNR and T_2 contrast. Lastly, the excitation was phase-chopped, and each acquisition was terminated by a slice-selective 90_{-y}° resetting pulse to accelerate signal recovery. Venous blood oxygenation values, which are necessary for VERVE calibration, were obtained for each subject *in vivo* based on internal jugular oximetry using a magnetization-prepared segmented EPI sequence [278], cardiac-gated using a finger oxymeter.

5.4.1.2 CBF Measurement

The CBF data were acquired using a QUIPSS II ASL sequence [102] with background suppression [119]. Two pre-saturation asymmetric BASSI pulses [100, 118] in the imaging region were followed by an adiabatic BASSI inversion pulse in the labeling region. The QUIPSS II inversion times were $TI_1 = 600$ ms, $TI_2 = 1300$ ms, and the

labeling slab was 100 mm thick, placed 5 mm from the imaged plane. The TE was 25 ms, and EPI readout was used, with a bandwidth of 2170 Hz/pixel.

5.4.2 Stimulation Paradigm

The subjects performed bilateral, sequential finger-to-thumb apposition at low (1.73 Hz) and high (3.46 Hz) frequency (cued by a metronome) while being presented with a radial yellow/blue checkerboard at low (25%) and high (100%) luminance contrast, reversing contrast at 8 Hz. The low finger apposition frequency was accompanied by the low visual-contrast checkerboard presentation and the high apposition frequency by the high contrast checkerboard presentation. The radial checkerboard, consisting of 30 spokes, 6 rings, with min/max radii of 15 and 215 pixels, was implemented using locally developed software (GLStim) based on the OpenGL graphics library (Silicon Graphics, Mountain View, CA), and delivered via a back-projection mirror and screen using a LCD projector with a resolution of 1024 x 768 pixels and a refresh rate of 75 Hz. The visual stimulus occupied between 40° to 45° of the subjects' visual field. The stimulation conditions were alternated with a uniform grey baseline (with luminance level matching that in the presence of the checkerboard) in 16 s off/96 s on/120 s off blocks. During the resting condition, subjects were requested to fixate upon a white triangular point at the centre of the screen to maintain attention. An additional 32 s resting state was inserted at the beginning of the paradigm to permit more robust initial baseline estimation.

5.4.3 Data Processing

Motion correction of the CBF and CBV_v datasets was performed across all runs. Frames with estimated translation exceeding 1 mm or rotation greater than 1° were identified and excluded from the analysis. Mutual alignment of all functional data was then achieved using MincTools (Montreal Neurological Institute, Montreal, Canada). In order to exclude potential extra-cerebral artifacts, brain masks were created manually based on the anatomical reference for each functional dataset. Subsequently, the VERVE and ASL data were spatially smoothed using a two-dimensional Gaussian filter with a full-width at half-maximum (FWHM) of 6 mm. Drift was estimated and removed by subtracting from

each voxel's time course the low-frequency components of its discrete cosine transform, with a cutoff frequency at half of the stimulation paradigm frequency.

The difference between the slow- and the fast-refocused images was calculated at activation and baseline, and the VERVE calibration factor [155], computed from the venous oxygenation measurement, was used to convert ΔVERVE to ΔCBV_v on a per-subject basis. This computation assumed a flow-metabolism coupling ratio ($n = \Delta\text{CBF}/\Delta\text{CMRO}_2$) of 3, which is representative of the average value reported by numerous studies and is reasonably invariant across cortical regions [5, 49, 174, 178, 180]. Notwithstanding the solid basis of this assumption, an error analysis was performed on the VERVE calibration factor while varying n from 2 to 4, which revealed a maximum variation of no more than $\pm 20\%$ in the resulting ΔCBV_v estimate, well within the inter-session variability of VERVE measurements. As customary, ΔCBF was calculated from the difference between the control and tag ASL images. Finally, sinc interpolation was performed to correct the timing differences between the control and tag images in the CBF data, as well as between the fast- and slow-refocused images in the VERVE data. This also permitted the correction of BOLD contamination in ASL data due to this timing difference.

The areas of statistically significant task correlation were identified based on the generalized linear model. The CBF and CBV_v ROIs were defined for each subject by thresholding the t -maps (at the t -value corresponding to a significance level of $p < 0.05$ after correction for multiple comparisons). Furthermore, the motor and visual cortex ROIs were differentiated based on anatomical considerations, with sensorimotor ROIs constrained to the banks of the Rolandic fissure, and the visual ROI in close proximity to the calcarine sulcus. Only the voxels that were significantly activated in both the CBF and CBV_v t -maps were included in the ROI (i.e. the CBF- CBV_v t -map overlap). Furthermore, the ROI obtained from the functional run with the most robust activation (the highest t scores) was used for all remaining functional runs. Restricting the ROI to those activated in both the CBV_v and CBF t -map would enhance specificity to the microvasculature, as the ASL technique is more sensitive to microvasculature changes [102]. In addition, this set of ROIs would shed light on the biomechanical relationship between flow and volume increase in the same vascular compartment.

For each ROI, signal time courses were extracted, from which the steady-state ΔCBF and ΔCBV_v were calculated. Based on literature and our empirical observations, steady-state was defined to commence 52 s after transitions between stimulation and baseline. The power-law coefficient, α , was estimated using unconstrained non-linear least-square curve-fitting weighted by the inverse standard deviation (SD) of ΔCBF and ΔCBV_v data points. One data point was obtained for each subject for the activation and baseline steady-states. The significance of the fit was assessed using regression analysis of the linearized fit.

5.4.4 Simulations

We also investigated the impact of the flow-volume relationship on BOLD, specifically, the gradient-echo BOLD signal (which is overwhelmingly preferred in fMRI studies), based on the deoxyhemoglobin dilution model [5],

$$\frac{\Delta\text{BOLD}}{\text{BOLD}_0} = M \cdot \left[1 - \left(\frac{\Delta\text{CMR}_{\text{O}_2}}{\text{CMR}_{\text{O}_2,0}} \right)^\beta \cdot \left(\frac{\Delta\text{CBF}}{\text{CBF}_0} \right)^{\alpha-\beta} \right] \quad [5.3]$$

where α represents the venous CBV contribution to the BOLD signal, β is a constant linking blood oxygenation to relaxivity, which is estimated to be 1.2 for extravascular BOLD at 3 T [28], and M is the BOLD calibration factor measured as the maximum possible BOLD signal. In the calibrated BOLD technique, M is typically calculated as the slope of the ΔBOLD vs. ΔCBF plot obtained from hypercapnic challenges, assuming negligible $\Delta\text{CMR}_{\text{O}_2}$ (i.e. $1/n = 0$). Furthermore, once M is defined, $\Delta\text{CMR}_{\text{O}_2}$, as well as the neurovascular coupling ratio (i.e. $n = \Delta\text{CBF}/\Delta\text{CMR}_{\text{O}_2}$) can be calculated from the measured ΔBOLD and ΔCBF . In the simulations, we varied the value of α , and studied the effect of this variation on the corresponding $\Delta\text{CMR}_{\text{O}_2}$. The simulation accounted for various values of ΔCBF , assuming $M = 0.05$ [306] and $n = 3$ [5, 49, 178, 180].

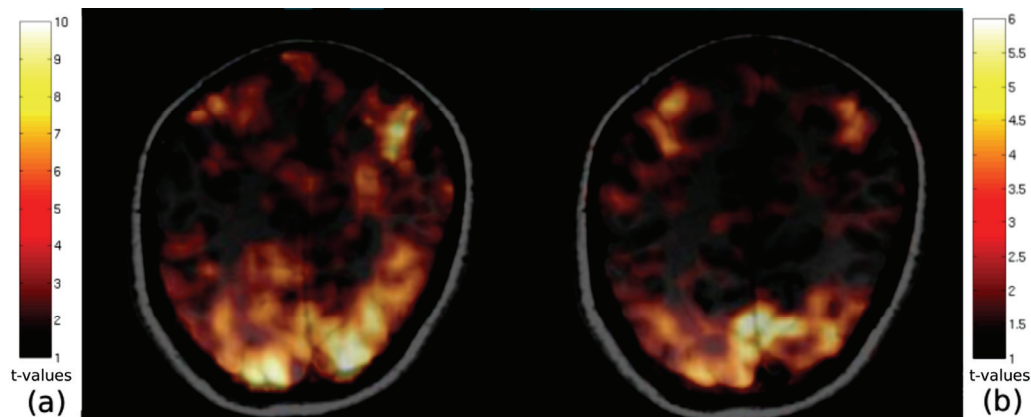


Figure 5.1

The CBV_v (a) and CBF (b) activation t -maps for one subject at 100% visual contrast stimulation and 3.46 Hz bilateral sequential finger tapping. The difference in the sensitivities of the various techniques is reflected by these t -maps.

5.5 Results

The group-average baseline venous oxygenation was measured to be $68.7 \pm 6.7\%$ (mean \pm SD), with a range extending from 48.6% to 76.1%. Sample CBF and CBV_v activation maps for one subject are shown in Figure 5.1 with the corresponding t -value scales. Visual activation was generally more extensive than sensorimotor activation, and produced higher t -values. Also, the differences between the locations of the significantly activated visual cortex voxels in the CBF and CBV_v maps are visually apparent.

Group-averaged time courses for CBV and CBF based on CBF- CBV_v t -map overlap ROIs are shown in Figure 5.2. As detailed in Table 1, ΔCBV_v was higher for high-intensity visual and sensorimotor stimulation ($8.14 \pm 1.31\%$ at low-intensity vs. $10.60 \pm 1.40\%$ at high-intensity). The same was true for ΔCBF , with a smaller differentiation seen in the visual cortex ($45.78 \pm 4.56\%$ at low-intensity vs. 62.08 ± 6.22 at high-intensity) than in the sensorimotor region ($26.14 \pm 4.71\%$ vs. $50.20 \pm 4.27\%$).

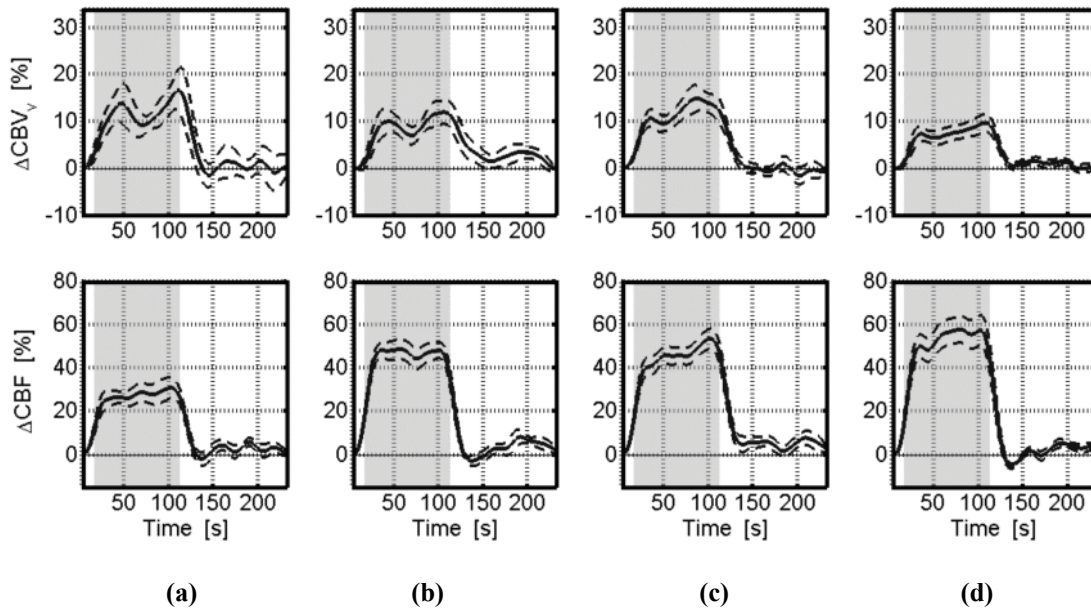


Figure 5.2

The group average CBF and CBV_v time courses obtained from CBF- CBV_v t -map overlap ROIs – (a) low-intensity sensorimotor; (b) low-intensity visual; (c) high-intensity sensorimotor; (d) high-intensity visual. The grey shaded region represents the stimulus-“on” period, and the standard error is shown in dashed lines.

The activation-induced steady-state ΔCBF and ΔCBV_v calculated from the CBV_v -CBF t -map overlap are summarized in Table 1, and the corresponding scatter plots of $rCBV_v$ vs. $rCBF$ obtained from the visual and sensorimotor ROIs are shown in Fig. 3a and Fig 3b, respectively. Fits for the individual regions resulted in $\alpha = 0.19 \pm 0.05$ ($R = 0.53$) and 0.31 ± 0.10 ($R = 0.60$) for the visual and sensorimotor regions, respectively (Figure 5.3). The values of α from these power-law fits were not significantly different ($P = 0.67$), therefore the visual and sensorimotor data were combined to produce the final weighted fit. The resulting power-law coefficient was 0.23 ± 0.05 , with $P < 0.001$. Linearization of the fit yielded $R = 0.52$.

Finally, given the above estimates of α , the core question of how these results affect CMR_{O_2} estimation using calibrated BOLD was addressed through simulations based on the deoxyhemoglobin dilution model, as described by Eq. [5.3]. As stated earlier, the BOLD signal is primarily modulated by venous CBV changes instead of total CBV change, the latter being the objective of Grubb’s original work. As shown in Figure 5.4, the adaptation of a different value for α is expected to have a notable impact on

BOLD signal modeling and prediction. Firstly, an overestimation of α ($\alpha_{\text{assumed}}/\alpha_{\text{true}} > 1$) produces an overestimation of M (the maximum achievable BOLD signal) as determined using calibrated BOLD [5]. Assuming an α of 0.38 in this case, while 0.23 was taken as the nominal “true α ” (to reflect the potential implication of our findings), an M overestimation of approximately 20% could be expected (Figure 5.4a) at a ΔCBF of 20%. Furthermore, this M overestimation decreases sub-linearly with increasing ΔCBF to approximately 20% at $\Delta\text{CBF} = 120\%$. On the other hand, this level of α overestimation translates to a $\Delta\text{CMR}_{\text{O}_2}$ underestimation of 30%, with a minimal dependence on ΔCBF , as shown in Figure 5.4b. Finally, as the flow-volume relationship is nonlinear, the severity of these errors depends strongly on the value of α_{true} , and the effect of an incorrect α on the accuracy of $\Delta\text{CMR}_{\text{O}_2}$ is amplified at higher $\alpha_{\text{assumed}}/\alpha_{\text{true}}$ ratios.

Table 5.1

The group averaged ΔCBF and ΔCBV_v (mean \pm standard error) are summarized for high and low intensity visual and sensorimotor stimulation. The power-law coefficients (α) for these two brain regions (0.19 and 0.31) were not statistically different, and the combined fit yielded $\alpha = 0.23 \pm 0.05$. The values of the coefficient of determination (r^2) reflect the fact that the data is not uniquely explained by the power-law model, but that other models may have provided reasonable fits as well.

	visual		Sensorimotor		Low intensity	High intensity	All
	Low intensity (25% contrast)	High intensity (100% contrast)	Low intensity (1.73 Hz)	High intensity (3.46 Hz)	Visual and sensorimotor	Visual and sensorimotor	
ΔCBF	47.56 \pm 4.86	56.55 \pm 6.43	25.29 \pm 6.11	47.39 \pm 5.26	38.02 \pm 4.21	52.88 \pm 4.17	N/A
ΔCBV_v	10.29 \pm 2.15	9.73 \pm 1.70	10.53 \pm 2.28	13.48 \pm 2.77	10.09 \pm 1.42	10.83 \pm 1.46	N/A
n	13	12	11	13	24	25	49
α	0.19 \pm 0.05		0.31 \pm 0.10		N/A	N/A	0.23 \pm 0.05
p	5.41x10 ⁻⁴		8.19x10 ⁻⁵		N/A	N/A	6.24x10 ⁻⁷
F	14.01		22.53		N/A	N/A	27.68
R	0.53		0.60		N/A	N/A	0.52
r^2	0.22		0.36		N/A	N/A	0.24

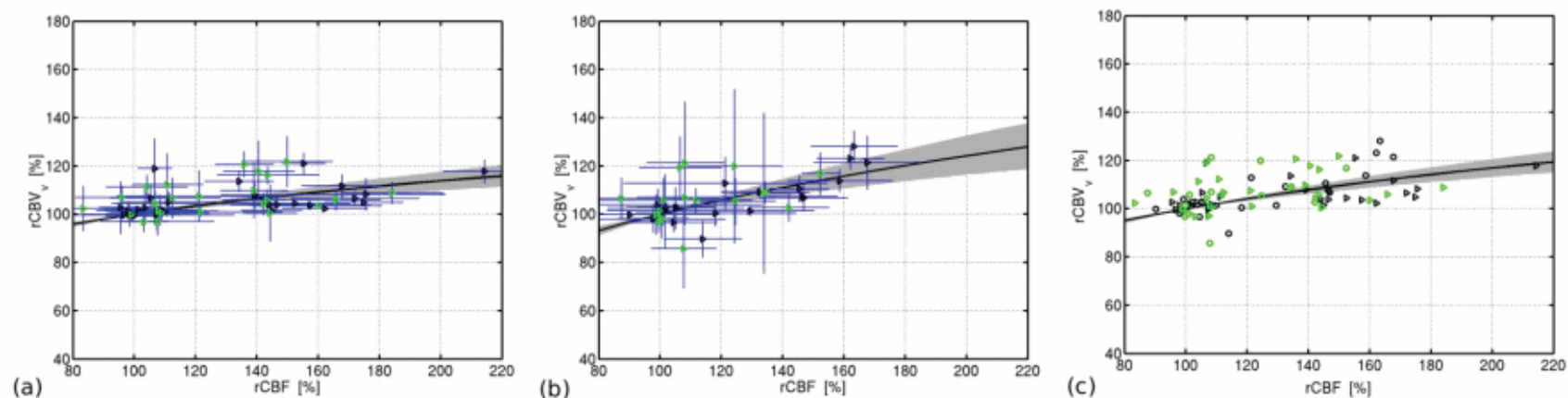


Figure 5.3

The $rCBF$ and $rCBV_v$ measurements obtained from $CBF-CBV_v$ t -map ROI overlaps and the resulting fit to the power-law (dark line) are shown for the visual (a, $\alpha = 0.19 \pm 0.05$) and sensorimotor (b, $\alpha = 0.31 \pm 0.10$) regions, where each symbol representing the steady-state average from one subject. The error bars represent the standard deviation in steady-state. The fit obtained from the combined dataset is shown in (c), where $\alpha = 0.23 \pm 0.05$ (green = low intensity stimulation, black = high intensity stimulation, triangles = visual, circles = sensorimotor). The shaded region represents the 95% confidence interval of the fit in all cases.

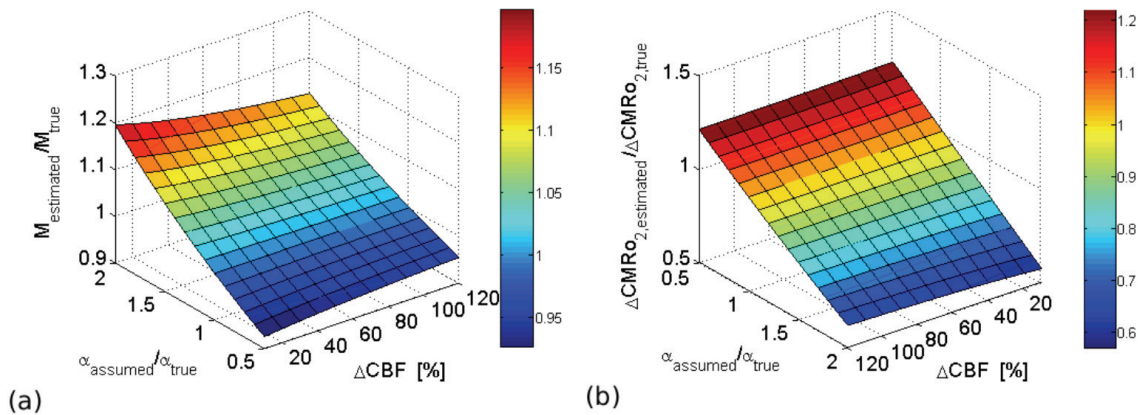


Figure 5.4

Simulated effect of the overestimation of α on the values of M and ΔCMRO_2 calculated a wide range of ΔCBF corresponding to neuronal activation. In this case, the BOLD signal was simulated using a power-law flow-volume relationship on the basis of $\alpha_{\text{true}} = 0.23$ as α_{assumed} is varied from 0.1 to 0.4. M and n were each estimated independently.

5.6 Discussion

The result of our in vivo MR venous oximetry at baseline revealed jugular oxygenation levels between 48.6% and 76.1%, in general agreement with literature estimates made using both MRI and optical methods [307, 308]. We also found the significantly activated region by visual stimulation to be in general more extensive than that of sensorimotor stimulation, as exemplified in Figure 5.1.

It is evident that as we specifically target venous CBV change, we cannot make a direct comparison between our measurements and the myriad of existing literature on total CBV changes in humans. However, it is tempting to validate our measurements through an extrapolation from total to venous ΔCBV . MRI measurements in rodents by Kida *et al.* [294] and Lee *et al.* [126] measured total ΔCBV of 31% and $11 \pm 4\%$, respectively, in response to hypercapnia and somatosensory stimulation. Lee *et al.* further reported a corresponding 15% venous ΔCBV . Using human PET, Ito *et al.* reported a total ΔCBV of $21 \pm 5\%$ in the primary visual cortex using an 8 Hz visual stimulus [200], and ΔCBV of $14 \pm 25\%$ in the primary motor cortex during 2 Hz finger-tapping. Furthermore, recent human visual activation MR studies produced ΔCBV

estimates of $18.2 \pm 2.8\%$ by Li *et al.*[309], $32.4 \pm 11.9\%$ by Gu *et al.* [310] and $27 \pm 4\%$ by Francis *et al.*[311]. A recent VASO study by Lu *et al.* placed ΔCBV at $56 \pm 0.1\%$ for visual stimulation, significantly higher than all previously recorded values. Our venous ΔCBV measurements ranged from 9.7% to 13.5% in the CBF- CBV_v overlap ROIs (Table 1). Microvascular morphometry has found baseline cerebral blood volume to be approximately partitioned as 21% arterial, 33% capillary, and 46% venous [70], comparable with more recent results using perfluorocarbon-enhanced magnetic resonance spectroscopy [126]. Mandeville *et al.* further derived the distribution of CBV changes as approximately 27% arterial, 11% capillary and 62% venous [295]. However, Lee *et al.* report only 36% venous contribution to total ΔCBV , attributing the largest response to arterial CBV [126], a claim supported by two very recent studies [312, 313]. The above estimates place percent ΔCBV_v at approximately 45.6% of the value of total percent ΔCBV , based on which our lowest and highest ΔCBV_v values translate to 16.2% and 41.4% total ΔCBV , respectively, consistent with the literature.

Overall, our average ΔCBF measurements, with a minimum of 26.1% and a maximum of 63.2% (from low to high-intensity stimulation), are in good agreement with previous studies [178, 200, 216, 306], despite the methodological differences. The steady-state ΔCBF significantly exceeded ΔCBV_v for both visual and sensorimotor activation in all subjects, consistent with previous findings of steady-state total ΔCBV in a substantial collection of neuronal activation studies [200, 294, 314, 315]. However, while ΔCBF greatly exceeded ΔCBV_v over the physiological range examined in this work, Ito *et al.* observed comparable ΔCBF and (total) ΔCBV at a visual stimulation frequency of 2 Hz using PET. Finally, ΔCBV_v saturated earlier than did ΔCBF , echoing previous findings based on total ΔCBV measured using MRI and PET under both neuronal stimulation and CO_2 challenges [178, 199, 200, 315];.

Despite the widespread use of Grubb's relationship, its initial adoption by Grubb *et al.* was based on empirical rather than theoretical foundations. The primary assumption of the power-law model is that blood is a Newtonian fluid governed by Poiseuille's law, which predicts a much higher increase in CBF than in CBV. It is further assumed that CBF increases by homogeneous dilation of all vascular segments, without concomitant

changes in perfusion pressure, path length or effective blood viscosity [315]. However, the power function is forced to pass through the origin, potentially imposing a bias on the evaluation of lower flow and volume fractions. Hence, other forms of the flow-volume relationship have been explored since. Wu *et al.* provided a simple linear model relating ΔCBF and ΔCBV [140], whereas Rostrup *et al.* explored both a power-law and an exponential model under graded hypercapnic challenge, with the exponential model yielding a lower sum of squared residuals [315]. Others [295, 314] have investigated multi-compartmental models of greater complexity to represent the vascular bed. However, as is true in most cases, the limited SNR of the data and the intrinsic inter-subject variability makes it difficult to conclusively distinguish the various linear or nonlinear models, and a number of the abovementioned models would have afforded reasonable fits to our data. The power-law relationship, which is prized for its simplicity, has been revealed to be an empirically sound approximation for the CBF-CBV interaction that has plausible physiological basis. Likely for these reasons, the power law model currently holds widespread consensus [199, 200, 299]. Thus, given the extensive use of the power-law model in the fMRI literature, the adoption of this model enables us to directly compare our measurements of venous CBV change to those of total CBV change.

It is likely that ASL-CBF and VERVE-CBV_v would have distinct sensitivities and specificities. The difference between the locations of the highest t -values in the CBF and the CBV_v t -maps from the same subject in Figure 5.1 is potentially an indication of this difference in sensitivity. Specifically, ASL has been associated with higher sensitivity to arteries, arterioles and capillaries [102], while VERVE is more sensitive to the capillaries, venules, veins, and to a lesser extent arterioles, in which diffusion-mediated deoxygenation to neighbouring capillaries has been observed [316]. Therefore, it can be derived that the overlap of the two t -maps would reduce the emphasis given to voxels with primarily macrovascular contribution, including those representing pial vessels, which manifest an evidently different volume response from deeper cortical vessels [219]. Thus, by using the overlap between the CBF and CBV_v t -maps, we increase the weighting of the microvasculature, consisting primarily of arterioles, capillaries and venules. Our choice of ROI, in addition to our exclusive targeting of deoxygenated blood volume, is

likely to account for the differences between our observations and those made by others, as detailed below.

The power-law coefficient we estimated ($\alpha = 0.23$) is substantially lower than the commonly adopted value of 0.38, likely a direct result of using ΔCBV_v measurements, which reflects the weighted average of CBV changes from exclusively the capillary, venular and arteriolar compartments, and is lower than total ΔCBV . This is to be expected from the observation that volume change in arteries is the primary contributor to total percent ΔCBV [126, 312], despite the fact that the capillary and venous compartment occupies largest volumes at rest. However, this difference in α cannot be accounted for by a simple linear scaling of ΔCBV_v . Instead, our results demonstrate an earlier saturation of ΔCBV_v which may reflect the lack of elastic tissue and smooth muscles in the capillaries, which constitute the main contributor to ΔCBV_v . Indeed, recent cortical two-photon microscopy studies [127, 317] have made robust observations attesting to the passive but significant role of capillaries in contributing to local CBV increase during neuronal activation and hypercapnia. An alternative explanation is that larger veins, which are equipped with smooth muscles, participate in homogenizing the CBV distribution across the capillary bed [127], constricting the extent of CBV increase in any given post-arterial vessel.

Using the CBF- CBV_v t -map overlap ROIs, our data did not reveal spatial variability in the flow-volume relationship, as the visual and sensorimotor power-law coefficients were not significantly different. This observation echoes PET findings by Rostrup *et al.* [315]. However, our results do not exclude the possibility of finer-scale spatial heterogeneity in α (as observed by Wu *et al.* and Jin *et al.* across cortical layers using animal MION imaging) which is highly sensitive to vascular content, and may underlie α variation with BOLD response amplitude [140, 222]. Thus, while we could not detect variations at the level of cortical layers, the low α estimate relative to those obtained using total ΔCBV supports the argument that the use of CBF- CBV_v overlap ROIs enhances weighting on the microvasculature [140, 222]. It should be noted, however, that the caveat of using t -maps as a guide to ROI placement is that due to the use of thresholding, a bias towards voxels with the higher flow and volume changes

occurs. Given limited SNR, t -value thresholding is a common practice. However, this practice can prejudice measurements towards blood flow and volume saturation, and conceivably narrows the range of ΔCBF and ΔCBV_v values investigated, thus introducing bias in the estimated power-law. We sought to minimize this effect by using the same ROI for all functional runs.

There is a wealth of data on global hemodynamic change induced by end-tidal CO_2 modulation. While we have drawn comparison between findings in these studies and in our own, we do not exclude the possibility of subtle differences that may exist between CO_2 -induced global changes and focal functional hyperemia, as the venous responses to focal and global (CO_2 -mediated) flow change are governed by partially different mechanisms [318]. The main mechanisms for local control are biomechanical aspects, humoral agents, metabolic aspects and neural response. Systemic global control, on the other hand, is exerted through either neuronal reflexes or hormonal control. Nonetheless, it is widely believed that biomechanical principles govern the interaction between flow and volume [295, 315, 319], which leads us to expect no dramatic differences between focal and global hemodynamic relationships.

Since the BOLD signal is dependent primarily upon deoxygenated, instead of total, blood volume change, the relevant ΔCBV in the context of BOLD modeling may be overestimated using Grubb's coefficient of 0.38, leading to the potential underestimation of $\Delta\text{CMR}_{\text{O}_2}$ for a given ΔCBF and ΔBOLD . The effect of alpha on the estimation of M and $\Delta\text{CMR}_{\text{O}_2}$ using calibrated BOLD was first probed by Davis *et al.* [174] and Hoge *et al.* [5], and more recently by Ances *et al.* [302]. Simulation shows the overestimation of α to cause a substantial overestimation of M . However, the $\Delta\text{CMR}_{\text{O}_2}$ estimation error due to the adoption of an incorrect M was found to be small [180]. On the other hand, given the correct estimate of M , an overestimation of α can result in an underestimation of $\Delta\text{CMR}_{\text{O}_2}$. As our results show, if an α of 0.38 was assumed when the true value was 0.23, the corresponding underestimation of $\Delta\text{CMR}_{\text{O}_2}$ may reach beyond 30%, translating to a mirroring overestimation of n . These effects increase with the level of CBF increase. In the light of these findings, the assumed value of α for steady-state BOLD modeling should be carefully chosen.

Finally, the remarkable SNR in animal hemodynamic studies make them appealing targets for comparison with human data, as we and numerous others have attempted. However, while we have made favourable comparisons between our measurements and those reported in animal studies, we do not preclude the possibility of discrepancies due to the effects of anesthesia. It is known that not only can anesthesia bias hemodynamic response, but the bias is dependent on the anesthetic agent. For instance, urethane has been known to reduce baseline CBF and half the rate of action potentials, while isoflurane has been shown to produce a baseline perfusion increase and prolong activation due to its inhibitive effect on potassium channels [320]. These modifications of baseline conditions, which have been reproduced in human subjects [321], are expected to account for significant ΔCBV and ΔCBF fluctuations, and must be considered before major conclusions regarding human hemodynamics are drawn based solely on evidence from animal studies.

In this work, we performed simultaneous measurements of activation-induced steady-state CBF and venous CBV change in the healthy awake humans. We document, for the first time, in vivo human venous ΔCBV measurements in response to graded visual and sensorimotor stimulation. A power-law relationship linking activation-induced ΔCBF and venous ΔCBV was fitted to our data, showing that the Grubb's constant of 0.38 significantly overestimates the BOLD-specific steady-state CBV response, which is associated with venous, rather than total volume change. Finally, the adoption of Grubb's constant in BOLD signal modeling is shown to lead to underestimation of $\Delta\text{CMR}_{\text{O}_2}$, an effect that should be accounted for in calibrated BOLD.

5.7 Acknowledgments

This research was supported by the Natural Sciences and Engineering Research Council of Canada (J. J. C.) and the Canadian Institutes of Health Research (G. B. P.).

Chapter 6

Contributions to the Post-Stimulus BOLD Undershoot

6.1 Preface

While measuring the steady-state $\Delta\text{CBV}_v\text{-}\Delta\text{CBF}$ relationship has a significant effect on improving the accuracy of $\Delta\text{CMR}_{\text{O}_2}$ estimation using the BOLD signal, a more in depth understanding of the origins of the BOLD transients can also shed invaluable light on the mechanism underlying the neurovascular response to neuronal activation. The most prominent and widely observed BOLD transient is the post-stimulus undershoot, the origin of which has been a subject of active interest since the debut of fMRI [216, 295, 319, 322, 323]. Notably, the BOLD undershoot has been attributed entirely to a transient CBF- CMR_{O_2} decoupling which leaves the post-stimulus CMR_{O_2} elevated without a corresponding elevation in CBF [322, 323]. Recent measurements of total CBV dynamics, provided by the VASO technique, were in support of this theory [152, 324], which implies that there may be a transient disconnection between oxygen metabolism changes and the hemodynamic response.

However, there is strong evidence supporting two other possible scenarios. There is the possibility of a delayed return of venous CBV to baseline, arguing for a biomechanical contribution to the BOLD undershoot [319]. Direct verification of this transient mismatch between the CBF and CBV dynamics has been derived from MION-based measurements in animals [151, 295], but its reproduction in humans has thus far been hampered by the tremendous difficulty in measuring venous CBV dynamics non-invasively. An additional contribution of CBF post-stimulus undershoot [216], which has been unequivocally observed, also has a potential role in causing the transient BOLD

decrease. As the CBF undershoots have been found to be stimulus-dependent [216], they could conceivably be induced by undershoots in the neuronal response [221].

Given its capacity for enabling dynamic imaging of venous CBV, VERVE is a powerful tool for probing the dynamic hemodynamic interactions giving rise to the post-stimulus BOLD undershoot. In the work reported in this chapter, CBV_v , CBF and BOLD data in response to graded visual and sensorimotor stimulation of varying durations were acquired using VERVE and ASL within the same session in healthy human volunteers. The resultant signal time course were modelled, and subsequently analyzed for the time-to-fall and normalized undershoot size (i.e. amplitude and duration). The first key finding was the slow post-stimulus transition of venous CBV relative to both BOLD and CBF, favouring a biomechanical contribution. In addition, the CBF time courses exhibited undershoots which were correlated with those of BOLD, supporting a neuronal contribution. Finally, the BOLD post-stimulus undershoot size was independent of stimulus intensity or duration, and the normalized undershoot parameters were not modulated by stimulus duration, arguing against a purely metabolic origin. These results illustrate experimentally, for the first time, a comprehensive picture of the venous hemodynamic interactions giving rise to the BOLD transients.

Origins of the BOLD Post-Stimulus Undershoot

Jean J. Chen and G. Bruce Pike

McConnell Brain Imaging Centre
Montreal Neurological Institute
McGill University

Submitted to NeuroImage

In Press

6.2 Abstract

The interpretation of the blood-oxygenation level-dependent (BOLD) post-stimulus undershoot has been a topic of considerable interest, as the mechanisms behind this prominent BOLD transient may provide valuable clues on the neurovascular response process and energy supply routes of the brain. Biomechanical theories explain the origin of the BOLD undershoot through the passive ballooning of post-capillary vessels which leads to an increase in venous blood volume (CBV_v , comprising deoxygenated blood in capillary, venular and arteriolar compartments), resulting in susceptibility-induced signal decrease. While there has been substantial evidence supporting a role for venous ballooning, there have also been reports arguing for a prolonged post-stimulus elevation in cerebral oxygenation consumption (CMR_{O_2}) as the primary cause. Furthermore, a contribution of post-stimulus cerebral blood flow (CBF) undershoots has also been demonstrated. To clarify the role of the venous compartment in causing the BOLD undershoot, we performed *in vivo* fMRI measurements of the transient ΔCBV_v , ΔCBF and $\Delta BOLD$ responses in healthy humans. We observed a slow post-stimulus return to baseline in venous CBV which supports the existence of a passive “balloon” effect, implying that previous observations of a quicker recovery of the total CBV response may be dominated by arterial CBV change. Our findings also support a significant contribution from the CBF undershoots, which, combined with a slow venous CBV response, would account for much of the BOLD undershoot.

Key words: BOLD post-stimulus undershoot, cerebral oxygen metabolism, neurovascular coupling, cerebral blood flow, venous cerebral blood volume, fMRI, VERVE

6.3 Introduction

Interpretation of the post-stimulus undershoot in the blood-oxygenation level-dependent (BOLD) signal has been a topic of considerable interest. This BOLD undershoot typically starts between 10 and 20 seconds after stimulus cessation [325], and is observed for up to 60 seconds [78, 151]. This transient feature is present in both the gradient-echo and spin-echo BOLD signal [77, 326]. Insignificant inter-subject variation was found in the duration of the undershoot for a given stimulus, but there is significant variation in its magnitude [327]. The mechanisms behind this prominent BOLD transient may provide valuable clues on the neurovascular response process and energy supply routes of the brain. In addition, the spatial specificity of the undershoot has been suggested to reflect spatial variability in neuronal activity [219, 328]. This discussion, however, is complicated by reports of contradictory observations as to the most likely origin of the undershoot, and there is great interest in reconciling these differences by gaining access to more direct measures of hemodynamics and metabolic processes that govern the BOLD response.

The BOLD post-stimulus undershoot reflects a transient increase in the local deoxy-hemoglobin (dHb) count, which could result from a number of possible scenarios. Biomechanical models, which attribute the local dHb accumulation to the temporal mismatch between the Δ CBF and venous Δ CBV responses, include the Balloon Model, proposed by Buxton *et al.* [319], as well as the Windkessel Model, proposed by Mandeville *et al.* [329]. This biomechanical interpretation is supported by a number of human and animal imaging and modeling studies [151, 329-334]. Notably, using monocrySTALLINE iron-oxide nanocolloid (MION) enhanced CBV imaging (measuring total CBV change) simultaneously with BOLD and laser Doppler flowmetry measurements, Mandeville *et al.* obtained robust, high signal-to-noise measurements which demonstrated a delayed compliance in CBV in a rat model at 2 T and 4.7 T in response to both focal and global hyperemia [151, 330]. Furthermore, there is accumulating evidence that the CBV post-stimulus response is in fact composed of a fast and a slow response, attributed to the elastic arterial recovery from stress and the more passive venous recovery, respectively [329, 335, 336].

Alternatively, a transient post-stimulus decoupling between CBF and CMRO_2 can also create a post-stimulus accumulation of deoxyhemoglobin, producing a BOLD undershoot [337-339]. In support of this theory, a number of studies have shown evidence of speedy post-stimulus recovery in total CBV, as measured using vascular space occupancy (VASO) as well as contrast-enhanced imaging, which, combined with a fast CBF recovery, suggests a post-stimulus CMRO_2 elevation that is decoupled with the hemodynamic response [152, 322, 323, 340].

In an effort to reconcile these alternate observations, more recent studies [218, 219, 222] have examined the spatial variability of post-stimulus CBF, CBV and BOLD behaviours by imaging at high spatial resolution. Using MION at 9.4 T, Yacoub *et al.* showed that CBV changes in anesthetized cat cortical tissue persist after stimulus-cessation while CBV changes in the surface vessels quickly return to baseline levels, despite a concurrent undershoot in the BOLD signal in both the tissue and surface vessel areas [219]. This was confirmed by later findings from Zhao *et al.* and Jin *et al.*, who found the most prolonged post-stimulus CBV elevation to be the middle layer, corresponding to the location of the largest BOLD undershoot.

Interestingly, the main debate has not substantially involved another important theory, one that regards the role of CBF. A post-stimulus undershoot in CBF [69, 180, 221, 334, 341-346], which would also result in local dHb accumulation, is a potentially significant contributor. Hoge *et al.* observed post-stimulus CBF undershoots using human primary visual cortex stimulation at 1.5 T [341], a finding reproduced by Shmuel *et al.* in visual stimulation of anesthetized monkeys, and suggested to be associated with a post-stimulus decrease in neuronal activity as revealed in cortical electrophysiological recordings [221]

Numerous optical studies found the post-stimulus period to be characterized by an undershoot in the concentration of oxy-hemoglobin [Hb] and/or an overshoot in [dHb] [55, 347-349]. In particular, using arterial spin labeling (ASL) and BOLD in conjunction with near-infrared spectroscopy (NIRS), an elevation was found in post-stimulus [dHb], mirroring the undershoot in the BOLD and CBF data, with the timing of the post-stimulus elevation in total hemoglobin concentration coinciding with the overshoot in [Hb] [347, 349]. In addition, using optical imaging and laser Doppler flowmetry (LDF) to estimate

CBV and CBF changes, respectively, Jones *et al.* [350] found delayed post-stimulus [dHb] recovery. However, this was contradicted by an immediate recovery in [Hb] observed by Schroeter *et al.* [348]. Notwithstanding the abundance of optical data, optical studies are intrinsically limited by penetration depth, spatial resolution and the fundamental differences in the measured parameters compared to MRI. Therefore, the above data, while adding valuable perspective, have not unequivocally resolved the debate.

To the present, there has not been data to address the simultaneous contribution of CBF and venous CBV directly measured in humans. In the context of BOLD contrast, as is addressed in this work, the term “venous blood” refers to all partially deoxygenated blood, specifically, blood from a collective compartment encompassing capillaries and venules, as well as, to a lesser extent, arterioles [316, 317]. In this study, we sought to clarify these contributions to the BOLD undershoot by performing human fMRI measurements of in vivo transient responses in ΔCBV_v , ΔCBF and ΔBOLD evoked by graded visual and sensorimotor stimulation.

6.4 Materials and Methods

6.4.1 Stimulation Paradigm

Sixteen healthy adults (14/2 females/males, ages ranging from 22 to 31 years) participated in the study, and gave informed consent prior to the scanning session. The subjects performed bilateral, sequential finger-to-thumb apposition at low (1.83 Hz) and high (3.46 Hz) frequency (cued by a metronome) while being presented with a radial yellow/blue checkerboard at low (25%) and high (100%) contrast, reversing contrast at 8 Hz. The low apposition frequency was accompanied by the low contrast checkerboard, the high apposition frequency by the high contrast checkerboard. The radial checkerboard stimulus was implemented using locally developed software (GLStim) based on the OpenGL graphics library (Silicon Graphics, Mountain View, CA), and was delivered via a back-projection mirror and using a LCD projector with a resolution of 1024 x 768 pixels and a refresh rate of 75 Hz. The visual stimulus occupied between 40° and 45° of the subjects’ visual field. The stimulation conditions were alternated with a uniform grey

baseline (with luminance level matching that in the presence of the checkerboard). During the resting condition, subjects were requested to look at a white triangular fixation point to maintain attention. Two stimulation-“on” durations were used, namely 24 s and 96 s, each flanked by 16 s and 120 s of pre- and post-stimulus baseline blocks, respectively. By varying the stimulation duration, we expect to modulate the neuronal activity-induced metabolic deficit, thereby making it possible to test the theory that the BOLD undershoot is caused mainly by a post-stimulus elevation in $CMRO_2$, which was suggested to occur mainly to restore this deficit [152]. Each off/on/off block was repeated twice, and jittered [351] to achieve an effective temporal resolution of 2 s. An additional 32 s resting state was inserted at the beginning of the paradigm to permit more robust baseline estimation.

6.4.2 MRI Acquisition

All examinations were performed on a Siemens 3 T Magnetom Trio system (Siemens, Erlangen, Germany). Subjects were immobilized using a head holder assembly. An RF body coil was used for transmission and an 8-channel phased array head coil for signal reception. The scanning protocol included a 3D RF-spoiled gradient-echo scan with 1 mm³ isotropic resolution which served as anatomical reference. An 80 s multi-slice BOLD visual and sensorimotor functional scout was acquired to guide slice positioning. During the functional scout, subjects were presented with the high-contrast visual stimulus while performing the high-frequency motor task described in the previous section. Activation *t*-maps were produced using scanner console software, and the coordinates of the regions with the most significant activation in both the visual and sensorimotor regions were used in placing the imaging slice.

The common functional imaging parameters were: FOV/matrix/slice-thickness/TR = 200x200 mm²/64x64/5 mm/4 s. The fMRI acquisitions were all single-slice, with a voxel size of 3.1x3.1x5 mm³. The VERVE technique was used to measure changes in venous CBV (ΔCBV_v). Cerebral-spinal fluid (CSF) suppression was performed at an inversion time of 1100 ms for a repetition time of 4 s. This was followed by the VERVE magnetization preparation, composed of a pair of non-selective 90° tip-down and tip-up pulses flanking an MLEV phase-cycled CPMG train made up of non-selective composite

90°_x - 180°_y - 90°_x refocusing pulses for either fast or slow refocusing. The corresponding τ_{180}^F and τ_{180}^S were 3 ms and 24 ms, respectively, forming a refocusing train with duration of 192 ms; this duration, combined with the echo-spacing of 6.8 ms for the TSE readout resulted in an effective VERVE echo time (TE) of 198.8 ms. One cycle of phase-chopping was used in the slice-selective excitation pulse. Venous blood oxygenation, which is necessary for VERVE calibration, was obtained for each subject *in vivo* based on internal jugular oximetry using a magnetization-prepared segmented EPI sequence [278], cardiac-gated using a finger oxymeter.

CBF and BOLD data were simultaneously acquired using pulsed ASL, which was previously shown to provide BOLD measurements equivalent to those acquired with standard BOLD [352]. The QUIPSS II ASL technique [102] was used, with ASSIST background suppression [353]. The protocol contained the following parameters: $TI_1/TI_2/TE/\text{labeling thickness}/\text{gap} = 700 \text{ ms}/1300 \text{ ms}/25 \text{ ms}/100 \text{ mm}/5 \text{ mm}$. Two asymmetric BASSI pre-saturation pulses [100, 118] in the imaging region were followed by an adiabatic BASSI inversion pulse in the labeling region (gap of 5 mm). EPI readout (bandwidth = 2170 Hz/pixel) was used.

6.4.3 Data Analysis

Motion correction of the CBF, CBV_v and BOLD datasets was performed across all runs using AFNI's *2dimreg* software [354]. The frames with estimated translation exceeding 1 mm or rotation greater than 1° were excluded from the analysis. The CBF and CBV_v data were then aligned to each other using MincTools (Montreal Neurological Institute, Canada), such that all functional data were mutually aligned. The functional data were spatially smoothed using a two-dimensional Gaussian filter with a full-width at half-maximum (FWHM) of 6 mm. Drift was removed by subtracting from each voxel's time course the low-frequency components of its discrete cosine transform, with a cutoff frequency at half of the stimulation paradigm frequency.

The difference between the slow- and the fast-refocused images was calculated, and a calibration factor computed from the venous oxygenation was used to convert ΔVERVE to ΔCBV_v on a per-subject basis [155]. As customary, ΔCBF was calculated from the difference between the control and tag ASL images, while ΔBOLD was obtained

as the average between tag and control. Finally, sinc interpolation was performed to correct the timing differences between the control and tag images in the CBF and BOLD data, as well as between the fast- and slow-refocused images in the VERVE data. This also permitted the correction of potential BOLD contamination in ASL data due to this timing difference [355].

We used *fMRIstat* [83] to identify areas of statistically significant task correlation based on the generalized linear model, with corrections for multiple comparisons. The gamma-variate hemodynamic response function, which has been found to provide robust activation correlation for all modalities, was used for the analysis. The BOLD, CBF and CBV_v ROIs were defined for each subject by thresholding the t -maps (at the t -value corresponding to a significance level of $p < 0.05$ after correction for multiple comparisons). Visual and sensorimotor cortex ROIs were differentiated based on anatomical considerations, with sensorimotor ROIs constrained to the banks of the Rolandic fissure, and the visual ROI in close proximity to the calcarine sulcus. The time-course analysis was based on the overlap between the significantly activated voxels in the CBF, CBV_v and BOLD t -maps obtained from the functional run with the highest activation t values. Theoretically, ASL is more sensitive to arterioles and capillaries [102], whereas VERVE is more sensitive to intravascular changes in the capillaries and the post-capillary compartment (i.e. venules and veins), and BOLD is sensitive to both intra- and extra-vascular contributions, stemming from oxygenation changes in capillaries, venules and veins. Therefore, although each voxel is likely to contain all compartments, it is likely that restricting the ROI to those activated in the CBV_v , CBF and BOLD t -maps would reduce emphasis of the arterial and venous macrovasculature. In addition, the use of the overlapping ROIs targets the interaction of CBF and CBV_v in the exactly the same location as the corresponding BOLD undershoot. Finally, to minimize overall bias towards the highest t -scores, the CBF- CBV_v -BOLD overlapped ROI from the functional run with the most robust activation (the highest t -scores) was applied to all other functional runs.

The CBF, CBV_v and BOLD time courses derived from each ROI were temporally low-pass-filtered (Hanning filter, FWHM = 6 s). Piece-wise fitting of the time courses to a double-gamma hemodynamic response function [202] was performed using the

unconstrained nonlinear least-square method, i.e. the onset and offset transient portions of the time courses were fit separately, such that neither is biased by the temporal features of the other. The time-to-fall (T_f) of the time courses (the time taken to fall to the half-maximum) was estimated from the modeled time courses, as illustrated in Figure 6.3. The statistically significant undershoots (at the $p < 0.05$ level) were identified, and their durations quantified via their respective full-width at half-maximum ($FWHM_{US}$). Both T_f and $FWHM_{US}$ were corrected for the low-pass filter FWHM. Finally, the normalized post-stimulus response amplitude (A_{PS}) for each time course was calculated as the measured post-stimulus response amplitude within the BOLD $FWHM_{US}$ time frame divided by the corresponding positive response amplitude. Thus, A_{PS} enabled us to assess the behaviours of all measurements precisely when the BOLD post-stimulus undershoot occurs. The dependence of T_f , $FWHM_{US}$ and A_{PS} on stimulus type, stimulation intensity and the stimulation-“on” duration was assessed using 3-way ANOVA, while inter-modality differences were evaluated using Student’s t -test. Finally, the correlation between undershoot parameters in matching sets of time courses was assessed using linear regression.

6.4 Results and Discussion

6.5.1 Results

CBV_v, CBF and BOLD t -maps for one subject under high-intensity visual and sensorimotor stimulation are shown in Figure 6.1 for 96 s stimulus-“on” duration, overlaid with the corresponding anatomical reference image. VERVE-CBV, ASL-CBF and BOLD have distinct sensitivities and specificities, as can be seen from the peaks in the t -maps. Although each voxel is likely to contain multiple vascular compartments, it is likely that using the overlap between all three sets of t -maps would increase the probability of including voxels with high capillary and venular weighting.

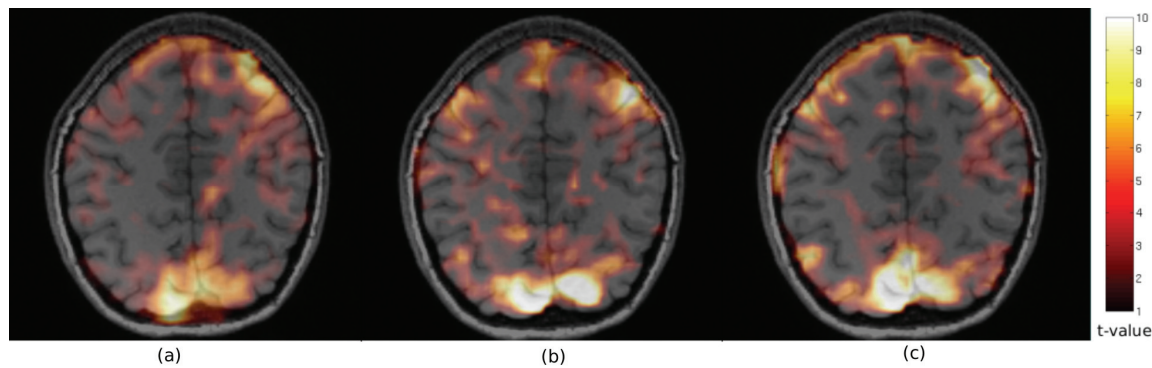


Figure 6.1

Sample CBV_v (a), CBF (b) and BOLD (c) activation t -maps from one subject during 100% contrast visual stimulus accompanied by 3.46 Hz bilateral finger tapping. Only voxels presenting significant activation in all three maps were used in the time course analysis.

The group-averages of the measured time courses for ΔCBV_v , ΔCBF and BOLD are shown in Figure 6.2 for the 96 s stimulation condition in the visual and sensorimotor regions. The post-stimulus dynamics can be clearly seen in these measured time courses, particularly the slow recovery of ΔCBV_v , as well as the well-defined undershoots in the visual ΔCBF and all BOLD responses. However, to enable the quantitative assessment of these features, modeling was performed on these time courses. The positive response amplitude is defined as the average time course amplitude above the FWHM of the positive response, and is therefore unbiased by stimulation duration. The post-stimulus response amplitude was normalized by the positive response amplitude to compare the transient responses between data acquired using different modalities.

A sample set of the measured CBV_v , CBF and BOLD time courses obtained under visual stimulation is shown in blue in Figure 6.3, for short (Figure 6.3a, c, e) and long (Figure 6.3b, d, f) stimulation duration, along with their least-square fits to the double-gamma variate model. As shown in Figure 6.3g, all transient parameters were normalized to enable cross-modality and cross-subject comparison and categorization.

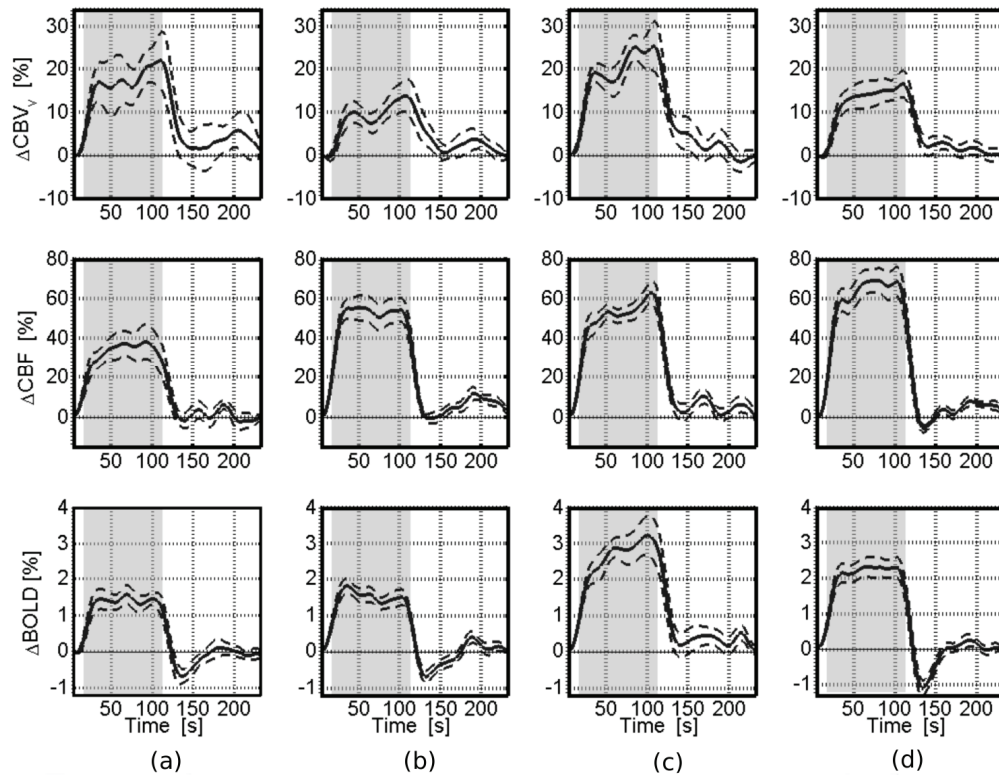


Figure 6.2

Group-averages of measured time courses for 96 s stimulation duration: (a) low-intensity sensorimotor stimulation ($n = 11$); (b) low-intensity visual stimulation ($n = 13$); (c) high-intensity sensorimotor stimulation ($n = 12$); (d) high-intensity visual stimulation ($n = 14$). The dashed lines indicate the standard error, and the stimulation-on period is indicated by the shaded region. In order to enable better visualization of the general transient dynamics, these time courses were smoothed using a low-pass Hanning filter with a 13 s FWHM.

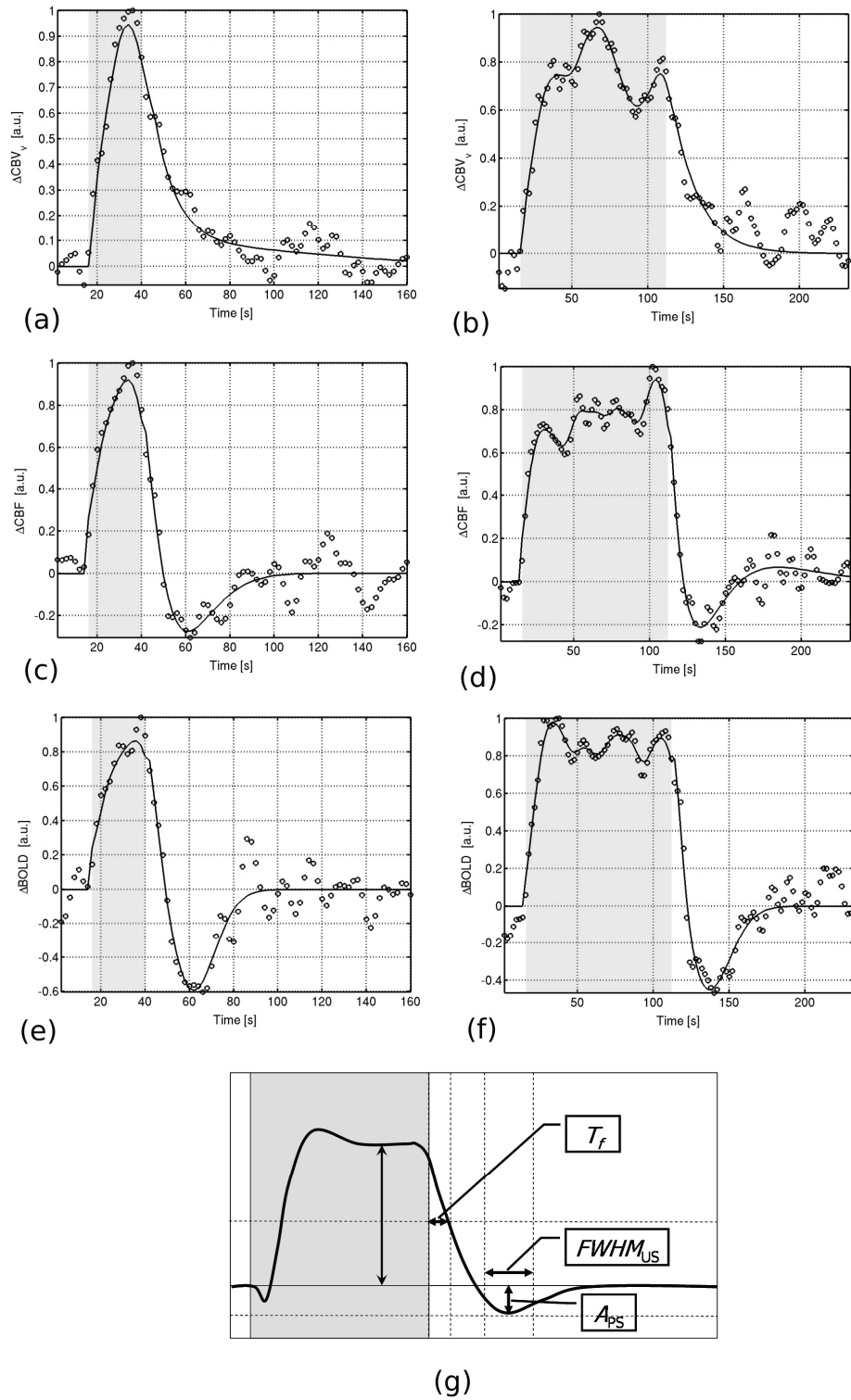


Figure 6.3

Sample measured (dotted line) and fitted (solid line) CBV_v (a-b), CBF (c-d) and $BOLD$ (e-f) time courses (normalized), for the high-intensity visual stimulation in one subject. The transient parameters measured from the modeled time courses are illustrated in (g).

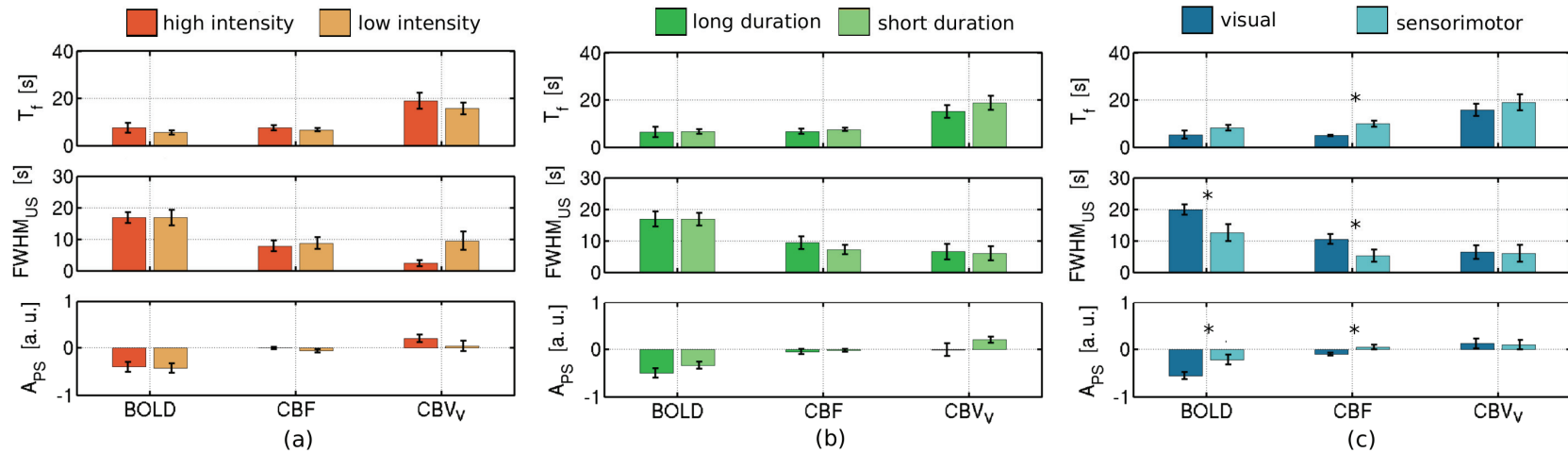


Figure 6.4

The group-average post-stimulus transient parameters, time-to-fall (T_f), normalized post-stimulus response amplitude (A_{ps}) and undershoot full-width-half-maximum ($FWHM_{US}$) are shown for CBV_v , CBF and BOLD responses, classified by stimulus intensity (a), duration (b) and type (c). Only the CBF and BOLD data showed statistically significant undershoots, with CBV_v being characterized by the longest T_f . No stimulation intensity or duration dependence was found in any of the parameters (a-b), but both the BOLD and CBF undershoots (A_{ps} and $FWHM_{US}$) were significantly larger in the visual than the sensorimotor case. In addition, the CBF T_f were both significantly longer in the visual than the sensorimotor region. Asterisks indicate significant difference ($p < 0.05$).

All transient parameter estimates were categorized as shown in Figure 6.4, and assessed for their dependence on stimulation intensity, duration and type. The rate of post-stimulus recovery was judged based on T_f , while the undershoot size was assessed based on $FWHM_{US}$ and A_{PS} . The BOLD recovery and undershoot size were found to be independent of stimulation intensity (Figure 6.4a) and duration (Figure 6.4b). However, the BOLD A_{PS} and $FWHM_{US}$ were both significantly influenced by the type of stimulation (i.e. visual vs. sensorimotor), with $p = 0.01$ for both cases (Figure 6.4c). The CBF undershoot was also independent of stimulation intensity and duration, but as in the BOLD case, both A_{PS} and $FWHM_{US}$ were significantly different between the visual and sensorimotor cases ($p = 0.01$ and 0.03 , respectively), as shown in Figure 6.4c. Lastly, no dependence on stimulation intensity, duration or type was observed in any of the CBV_v transient parameters.

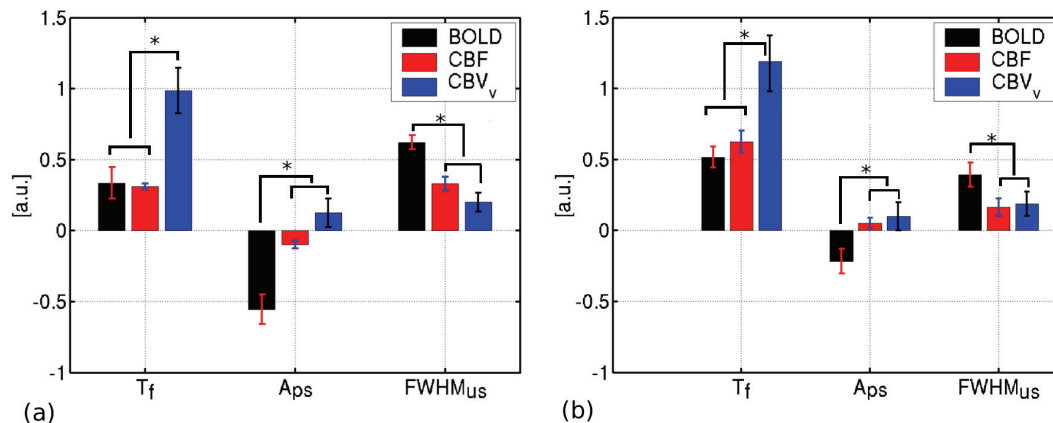


Figure 6.5

All post-stimulus transient parameters were summarized under the visual (a) and sensorimotor (b) categories. T_f , A_{PS} and $FWHM_{US}$ were rescaled differently for better ensemble visualization. The CBV_v data was characterized by a T_f that was significantly longer than that of either CBF or BOLD for both visual ($p < 0.01$) and sensorimotor stimulation ($p < 0.05$), as well as post-stimulus elevation. The CBF and BOLD T_f were mutually indistinguishable. Furthermore, the BOLD response exhibited more prominent and consistent undershoot features than both CBF and CBV_v , with the longest $FWHM_{US}$ in all categories and the most negative A_{PS} . This was also common to both visual ($p < 0.001$ for both $FWHM_{US}$ and A_{PS}) and sensorimotor stimulation ($p < 0.05$ for both $FWHM_{US}$ and A_{PS} for CBF, A_{PS} for CBV_v). The CBF and CBV_v undershoot sizes did not differ significantly. Asterisks indicate significant difference ($p < 0.05$).

The transient parameters were compared according to data type (i.e. BOLD, CBF or CBV_v). As significant differences were found between the transient responses to visual and sensorimotor stimulation, the data were further divided according to the stimulation type, shown in Figure 6.5. The first main observation is that T_f for CBV_v (visual: 16.4 ± 2.6 s, sensorimotor: 19.1 ± 3.4 s) was longer than either that of CBF (visual: 5.0 ± 0.3 s, sensorimotor: 10.0 ± 1.2 s) or BOLD (visual: 5.4 ± 1.8 s, sensorimotor: 8.3 ± 1.2 s). The CBF and BOLD T_f were statistically indistinguishable. This was the case for both visual ($p < 0.01$) and sensorimotor stimulation ($p < 0.05$). The BOLD response exhibited more prominent and consistent undershoot features than both CBF and CBV_v , with the longest $FWHM_{US}$ in all categories and the largest A_{PS} . This was also common to both visual ($p < 0.001$ for both $FWHM_{US}$ and A_{PS}) and sensorimotor stimulation ($p < 0.05$ for both $FWHM_{US}$ and A_{PS} for CBF, A_{PS} for CBV_v). The CBF and CBV_v undershoot sizes did not differ significantly. Another notable observation is that undershoots were consistently observed in the visual CBF responses, reflected by the negative average CBF response (Figure 6.5a). In the sensorimotor case, the CBF response did not show significant undershooting, and the average CBF A_{PS} was statistically indistinguishable from zero, reflecting an early return of CBF to baseline (Figure 6.5b). However, under both groupings, the average A_{PS} for CBV_v was consistently above zero, characteristic of an elevated venous CBV over the course of the BOLD undershoots.

6.5.2 Discussion

In this study, we sought to shed light on the possible mechanisms underlying the BOLD post-stimulus undershoot by directly measuring venous CBV changes, as well as ΔCBF and BOLD, in healthy human subjects during graded visual and sensorimotor stimulation of varying durations. At 3 T, the VERVE technique provided robust measures [356] which are in agreement with contrast-enhanced measurements of venous volume change in animals [126]. The CBF and BOLD response amplitudes to graded stimulation were in excellent agreement with the literature [178, 200, 341]. Both the positive BOLD and CBF responses increased with stimulation intensity (Figure 6.2). However, this was not

the case for CBV_v , likely because the CBF- CBV_v relationship is characterized by a shallow trend, with CBF variations far exceeding those in CBV_v [126, 356]. Our focus is, nonetheless, on the physiological and biomechanical mechanism underlying the transient response. We have developed a set of measures, namely the time-to-fall (T_f), the normalized post-stimulus response (A_{PS}) and the FWHM of the post-stimulus undershoots ($FWHM_{US}$), which characterize multi-modal post-stimulus transient response without being biased by the vastly different response amplitudes.

6.5.2.1 CBF Post-Stimulus Undershoot

The first important finding of this study is that the CBF response, as measured using QUIPSS II ASL, exhibited post-stimulus undershoots, the amplitude of which was correlated with the BOLD undershoot amplitude. The use of surround subtraction [355] minimized the potential of the CBF transients being biased by oxygenation effects, and hence precluded the possibility of the CBF undershoots being solely the result of BOLD contamination. CBF undershoots have been observed in both MRI and optical imaging literature [180, 221, 341, 349, 357]. However, a number of studies reported the absence of CBF undershoots under stimulation conditions similar to those studied here and using similar analysis techniques [152, 337]. While the exact origin of this difference is unclear, it has been suggested that the precise type of stimulus or paradigm influence the occurrence of the CBF transients [216]. Although the positive CBF change has been found to be independent of the stimulus type, delayed and stimulus-dependent finer-scaled flow adjustments [337] may contribute to diverging post-stimulus responses.

The CBF undershoot has been suggested to be the result of an autoregulatory CBF feedback mechanism of neuronal origin [180, 334]. Using cortical electrophysiological recordings, Shmuel *et al.* demonstrated post-stimulus undershoots in neuronal activity following visual stimulation, providing further support for a neuronal origin to the CBF undershoot [22, 25, 41, 221], which is also in concordance with predictions based on the “arteriolar compliance model”, in which neural activity modulates the compliance of arteriolar smooth muscle, and hence the initiation of the CBF response [343]. In our study, the dependence of the CBF post-stimulus response (in terms of T_f , $FWHM_{US}$ and A_{PS}) on stimulation type may be a reflection of the differences in the neuronal activities elicited by visual and sensorimotor activation. However, we do not preclude regional

variability in vascular structure and hemodynamic response, which could have also contributed to the visual-sensorimotor CBF response difference.

6.5.2.2 Venous Compliance

Another important finding of this study is that the CBV_v post-stimulus responses were clearly characterized by a slower return to baseline relative to either CBF or BOLD. This observation is thus in support of a passive and lagging dilatory component to the CBV response as described by Buxton *et al.* [319] and observed by Mandeville *et al.* [151, 329]. However, in this case, the definition of “venous blood” encompasses all deoxygenated vascular compartments, and our measurement of ΔCBV_v is a weighted average of the CBV response in all these vascular compartments, expected to include capillaries and venules [127, 317], and to a lesser extent, arterioles and veins. The nature of the venous blood volume response was also reflected by previous observations of a passive dilatory component of CBV decrease [134, 223]. Furthermore, as the ΔCBV_v transient parameters were uninfluenced by the intensity, duration or type of the stimulation, our findings support a primarily biomechanical response in venous blood volume to neuronal activation, hence a response modulated largely by changes in blood flow.

CBV_v manifested significantly longer T_f than both CBF and BOLD, as was also observed in previous fMRI studies [151, 358]. Having reduced the contribution of draining veins from the analysis (by using the CBF- CBV_v -BOLD t -map overlap), our findings likely reflect primarily venular response, and support biomechanical theories regarding the contribution of the venous CBV to the BOLD undershoot [319, 329, 359]. Furthermore, in Mandeville’s modified Windkessel Model, the temporal evolution of total CBV was described as a rapid elastic response of the postarteriolar compartment, approximately synchronized with the CBF response, followed by slow venous relaxation of stress [329], the latter being the chief cause of the BOLD undershoot. This bi-phasic CBV behaviour was experimentally confirmed by Silva *et al.* [335] and Shen *et al.* [223]. The close agreement between our CBV_v T_f measurements and the characteristics of the slow component [295] is evidence that the fast component is likely more arterially weighted. Indeed, this was postulated by the arteriolar compliance model, in which

baseline vascular state affects the dynamic response by changing the relative contributions of the active smooth muscle component and the passive connective tissue component to the overall vessel compliance. When coupled with the passive Balloon Model, the arterial compliance model was able to predict the observed CBF and BOLD response at various baseline conditions [343].

Our findings of delayed venous compliance are in agreement with optical imaging spectroscopy studies [360-362]. Malonek *et al.* noted an increase in [dHb] accompanied by a simultaneous increase in total hemoglobin concentration [tHb], presumably reflecting an early total blood volume increase. Their observation of a CBF change lagging [tHb] changes by 1 to 2 sec supports the notion of active neurovascular regulation of blood volume in the capillary bed and the existence of a delayed, passive process of capillary filling [363]. A post-stimulus elevation in [tHb] and overshoot in [dHb] was also observed by Hoge *et al.* using diffuse optical tomography [362], in line with a prolonged CBV recovery observed by Martindale *et al.* [360]. The relative timings of these parameters were found to be consistent between the sensorimotor and the visual systems [364], in line with our observations.

The current results differ from findings of a more instantaneous CBV recovery observed in studies measuring total Δ CBV using the vascular space occupancy (VASO) and gadolinium-enhanced bolus tracking techniques [152, 340, 365]. Notably, VASO measured a CBV response that decreased earlier than BOLD or CBF, but lagged behind that of BOLD by 5 to 10 s in its eventual return to baseline [152, 285]. This is in contrast with our finding of a slower initial CBV_v drop-off relative to BOLD and CBF. Also in contrast with these earlier findings, our data show that venous CBV remains elevated over the whole duration of the BOLD undershoot, as indicated by positive $CBV_v A_{PS}$, and is likely to play a role in inducing the BOLD undershoot. These observations likely reflect dynamic differences between venous and total CBV change.

As described earlier, total Δ CBV transitions, involving both the arterial and venous compartments, have on several occasions been found to be biphasic. Venous blood volume change has been shown to contribute to only $\cong 40\%$ to total Δ CBV [126], implying that arterial dilation is likely to contribute most to total percent CBV change, as was reported by various groups [126, 218, 366]. Thus, arterial CBV is expected to

contribute substantially to the “fast” phase of total CBV response described above, and total ΔCBV , being the weighted average of its arterial and venous components, is likely to exhibit a faster initial post-stimulus recovery reflective of CBF recovery. As we observed a decidedly slower post-stimulus response in CBV_v , we can attribute the slow component in total CBV change to primarily capillary and venular contribution, as was observed in recent cortical two-photon microscopy studies [127, 317]

Variations in the spatial specificity of the CBV measurements could also result in different observation of the CBV transient. Using MION imaging at high spatial resolution, Yacoub *et al.* showed that the post-stimulus CBV response was distinctly slower in the deeper parenchyma than near the cortical surface [219]. Their findings are consistent with a CBV response with primarily capillary and venular weighting, and are in remarkable agreement with our observations, derived from ROIs with high microvascular weighting. As the BOLD signal is modulated by partially-deoxygenated volume instead of total CBV, the quantification of CBV contributions to the BOLD undershoot should be based primarily upon CBV_v measurements. The fractional CBV changes associated with neuronal activation are expected to be weighted more towards deeper cortical layers, while the BOLD response is generally greater in the draining pial veins on the cortical surface, as reflected by the spatial profile analysis in previous works [218, 223]. Nonetheless, given the spatial resolution employed in most *in vivo* human fMRI studies, including the current study, it is not possible to spatially resolve the various vascular compartments or cortical layers reliably. Thus, the BOLD and CBV_v responses observed in this study are both weighted averages of the contributions from capillaries, venules and veins (pial and intra-cortical) across multiple cortical layers.

6.5.2.3 BOLD Post-Stimulus Response

BOLD showed significant and pronounced undershoots, as expected. The BOLD A_{PS} estimates were significantly larger than those of CBF in all cases ($p < 0.05$), showing that the undershoot figures most prominently in the BOLD time course. The BOLD undershoot amplitude did not vary significantly with the positive ΔCBF , in agreement with previous observations [341].

Significant correlation was found between the BOLD and CBF A_{PS} , strengthening support for the existence of a non-negligible CBF contribution to the BOLD undershoot. In addition, the BOLD undershoot amplitude was significantly larger in the visual region, in agreement with recent studies [299, 367]. The same was true for $FWHM_{US}$, and both the undershoot amplitude and duration dependency coincide with findings with the CBF transients, while no such dependency was observed with CBV_v . Given that the CBF response is likely to have a significant neuronal correlation [22, 32], which is likely to vary with stimulus type, this visual-sensorimotor difference in the BOLD undershoot not only adds support for a strong contribution of the CBF undershoot to the BOLD undershoot, but further implicates the role of a neuronal contribution in producing the BOLD undershoots. However, the BOLD T_f was not significantly different between the visual and sensorimotor categories, while that of CBF was (Figure 6.4c). This observation may be attributed to the concurrent and significant CBV_v contribution, as the $CBV_v T_f$ was also found to be independent of stimulus type. This finding further indicates that neuronally mediated factors such as CBF and biomechanical factors such as CBV_v both contribute to the formation of the BOLD undershoots, though in different fashions.

Differences in visual and sensorimotor neuronal activity are likely to result from fundamental differences in the stimuli, as well as from the neural and glial heterogeneity that characterizes the cerebral cortex [368]. The cortex is also characterized by heterogeneity in vascular density [369]. It was found that surface layers of the cortex (layers I to III), which are associated with the highest level of vascularization, are also the locations of the largest BOLD changes and undershoots [223, 335]. In addition, the occipital lobe surface is more vascularized than the surface of the sensorimotor areas [370]. These facts may also attribute the BOLD undershoot difference between visual and sensorimotor stimulation to the regionally specific capillary density. However, given that no significant distinction was made between the visual and sensorimotor transient CBV_v responses hints that this regional difference in hemodynamics is not solely the result of local vascular construct, but may have a neuronal contributor that is determined by the nature of the stimuli themselves. Indeed, Hoge *et al.* extensively studied the visual stimulus-dependence in the BOLD and CBF dynamic responses, and found that certain visual patterns, such as the polychromatic radial checkerboard used in this study,

produced more robust and pronounced BOLD undershoots than others [337, 341]. Further along this theme, Fox *et al.* studied the BOLD transients across a wider variety of tasks, and reported that while the occurrence of undershoot is brain region-dependent, the amplitudes of the undershoots depends on the type of task, and hence on the underlying neuronal activity [371]. It is therefore reasonable to postulate that the BOLD undershoot also stems from stimulation-specific metabolic triggers, which are likely to be reflected in the corresponding CBF response. Boden *et al.* found that changes in [Hb] lead those in [dHb] in the sensorimotor system but not in the visual system, an effect shown to result from a systemic response accompanying sensorimotor activity, but otherwise found no fundamental physiological difference between cortical hemodynamic regulation in motor and visual cortex [364]. This systemic response was explored earlier by Vafae *et al.*, who attributed the difference mainly to a difference in attention requirements [372]. Unlike during visual stimulation, where the subject's attention is required both during activation and baseline, the sensorimotor system is required to be at rest between stimulation blocks. This motor task paradigm is likely to emphasize the subjects' level of anticipation, hence elevating baseline CBF in spite of the subjects being at rest. The ensuing elevation in baseline oxygenation may give rise to a smaller BOLD undershoot. The BOLD post-stimulus undershoot is strongly influenced by baseline hemodynamic and metabolic conditions. Cohen *et al.* observed that the post-stimulus undershoot resolved more quickly with hypocapnia and appeared to be abolished with hypercapnia [187], a behaviour that was reproduced by Behzadi *et al.* using the arterial compliance model [343]. This was further confirmed by Lindauer *et al.*, who observed no undershoot during hyperoxia, and more pronounced undershoots during hypoxia [373].

The existence of a non-hemodynamic basis for the undershoot was supported by simulations by Jones *et al.* [326], giving occasion to theories in which metabolic factors are the sole origin [152, 340]. It has been postulated that the BOLD undershoot is incurred by elevated post-stimulus oxygen metabolism ($CMRO_2$), which is needed to restore the ion gradients depleted by action potential generation [152]. Derived from measurements of total ΔCBV , this $CMRO_2$ elevation was further suggested to occur in the absence of prolonged CBF or CBV elevation, resulting in a transient dissociation between $CMRO_2$ and CBF. Notwithstanding the obviously slower response in post-stimulus

ΔCBV_v , which is one of our main arguments in favour of a biomechanical contribution, as well as the potential caveats of inferring CBV dynamics from a plasma-based technique, our analysis of the BOLD undershoot sensitivities also argue against a post-stimulus ΔCMRO_2 elevation being the main cause of the BOLD undershoot. Evidently, the level of oxygen consumption, which modulates dHb content, would depend on the type of stimulus and the level of activation elicited, as the latter contributes directly to the degree of depletion experienced in the ion gradients, and hence the level of metabolic deficit. Thus, should the sustained CMRO_2 (the existence of which was to eliminate this deficit) be the only cause of the BOLD undershoot, the amplitude and duration of the latter would be expected to correlate with the intensity and/or duration of the stimulus. However, in this study, neither the normalized BOLD post-stimulus undershoot amplitude nor duration was influenced by stimulation duration or intensity over the range studied by the above authors. This echoes our previous finding of BOLD undershoot independence on stimulus duration over a wider range [346]. It is therefore evident that sustained metabolism cannot be the sole cause of the BOLD undershoots.

Finally, certain animal studies have reported small BOLD undershoots [335] during motor stimulation while others show the contrary [151, 374]. However, the necessity of using anesthetic agents in these studies could have substantially modified functional and hemodynamic transients. Urethane has been known to reduce baseline CBF [375] and halve the rate of action potentials [376], while isofluorane has been shown to increase baseline perfusion and prolong activation due to its inhibitive effect on potassium channels [320]. Huttunen *et al.* found that urethane-anesthetized rodents exhibited BOLD responses over a much wider range of stimulus frequencies than alpha-chloralose-anesthetized rats, which only responded to low-frequency stimuli. Although tight neural–hemodynamic coupling was observed in both cases [374], the varying baseline conditions are expected to seriously influence the BOLD undershoot, and as described earlier, baseline CBF elevation undermines BOLD undershoots. Furthermore, Palmer *et al.* reported fluctuations in partial carbon dioxide pressure and pH in alpha-chloralose anesthetized rats [377]. These parameters can affect the hemodynamic response to neuronal activation and could conceivably lead to variation in one or more

aspects of the response within and between animals as physiological condition changes over time.

We have shown clear evidence for the contribution of prolonged venous CBV elevation to the BOLD post-stimulus undershoot, as proposed by the Balloon and Windkessel models. However, this biomechanical factor is likely not the only contributor to the undershoot, the occurrence of which is dependent on the stimulus [341] and baseline [371]. The BOLD undershoot has previously been suggested to result solely from ongoing metabolism and flow-metabolism uncoupling [152, 340], and was supported by a faster post-stimulus drop-off in total Δ CBV. However, such observations may reflect a predominance of arterial CBV in their measurements, which is not the main modulator of the BOLD signal. Our results also support CBF undershoots as a significant contributor to the BOLD post-stimulus undershoot, whether engendered through biomechanical or neuronal means.

6.6 Acknowledgments

This research was supported by the Natural Sciences and Engineering Research Council of Canada (J. J. C.) and the Canadian Institutes of Health Research (G. B. P.).

Chapter 7

Conclusions

7.1 Summary

In this thesis, the venous refocusing for volume estimation (VERVE) fMRI technique was re-designed to fulfill the requirements of imaging at 3 Tesla and to optimize its performance. Underpinning these developments was a series of blood and brain tissue relaxometry experiments which were performed to confirm the validity of the theoretical basis for VERVE imaging and to enable its optimization. In addition, VERVE was used to investigate the steady-state as well as the dynamic flow-volume relationship underlying neuronal activation in healthy humans.

In Chapter 3, detailed whole human blood T_2 MR relaxometry experiments at 3 T are documented, in which we used a comprehensive set of CPMG refocusing intervals in conjunction with a wide range of blood oxygen saturation levels. For this purpose, we established the equivalence between T_2 values measured using a standard multi-echo spin-echo CPMG method and T_2 -prepared segmented EPI, the latter finding application for in vivo venous oximetry. Our MR results were complemented by rigorous blood gas analysis. These results constitute the most complete investigation of whole human blood relaxometry at 3 T to-date. Based on the results, we conclude that whole human blood T_2 dependence on the CPMG refocusing interval and oxygenation at 3 T is compatible with the weak field-inhomogeneity assumption, and is better characterized by the diffusion model [61] than the two-site exchange model [245]. The results shed light on the field-dependence of various mechanisms contributing to the above dependence of apparent whole blood T_2 . Furthermore, they unequivocally establish not only the validity, but also the advantage of VERVE imaging at high field.

Chapter 4 contains experimental data which complement those in Chapter 3 in laying the groundwork for the development of VERVE at 3 T, the de facto standard field strength for fMRI. Whole blood T_1 relaxometry results, performed over a blood oxygenation range corresponding to those used for T_2 relaxometry, revealed a statistically significant but small T_1 dependence on blood oxygen content at 3 T. While this finding reaffirms the negligibility of T_1 effects in the T_2 -weighted VERVE technique, it highlights the need for oxygenation effects to be considered in predominantly T_1 -weighted fMRI techniques such as arterial spin labeling. In addition, cortical T_2 relaxometry at 3 T was performed, with the main observations continuing to support the independence of grey and white matter T_2 from changes in the CPMG refocusing interval. These results demonstrate a consistency in parenchymal T_2 behaviour between 1.5 T [271] and 3 T, and lay the final foundation for the development of VERVE at 3 T. The remainder of this chapter details this development, describing the significant expected improvements and addressing several important technical aspects, specifically in relation to field inhomogeneities, parameter optimization and power deposition. This documentation not only facilitates future developments of VERVE for other field strengths, but also reveals directions for potential improvement in the technique which could not be accommodated in this project, due either to hardware or to software limitations.

In Chapter 5, the functionality of the VERVE technique developed for 3 T is demonstrated for robust venous ΔCBV (ΔCBV_v) measurement. In conjunction with arterial spin labeling (ASL) ΔCBF imaging, VERVE was used in the study of cortical hemodynamic changes during graded visual and sensorimotor stimulation in healthy human subjects. Cardiac-gated T_2 -prepared segmented EPI was successfully used for in vivo venous oximetry, which was required for subject-specific VERVE calibration. Based on these experiments, we report, for the first time, on in vivo human ΔCBV_v and ΔCBF measurements, which were fit to a power-law formulation. The results were compared to previous results by Grubb *et al.* [46], which have found wide application in BOLD modeling. Our analysis resulted in a spatially-invariant power-law coefficient of $\alpha = 0.23 \pm 0.05$, and indicates that the BOLD-relevant flow-volume may be substantially overestimated by the adoption of Grubb's value ($\alpha = 0.38$), as the BOLD signal is primarily modulated by venous, instead of total, CBV changes. The effect of this

overestimation on calibrated BOLD was probed through simulations using the Deoxyhemoglobin Dilution Model, revealing a substantial underestimation of $\Delta\text{CMR}_{\text{O}_2}$.

An investigation of the BOLD post-stimulus undershoot is presented in Chapter 6. Cortical ΔCBV_v , ΔCBF and BOLD signals were measured concurrently in healthy human subjects under visual and sensorimotor stimulation using VERVE and ASL. The corresponding multi-modal time courses were extracted from the activation ROI common to all three. Notably, the existence of a delayed post-stimulus venous CBV evolution was confirmed, supporting a contribution of venous ballooning to the BOLD undershoot. In addition, our finding of the significant contribution by post-stimulus CBF undershoots is conclusive evidence that the BOLD undershoots are not caused solely by delayed venous compliance [319] or by a post-stimulus flow-metabolism uncoupling [152, 323]. This well-defined CBF undershoot, which has been linked, in one study, to a concurrent decrease in neuronal activity [221], is likely to have a neuronal origin. This argument is further bolstered by our observation of a distinct difference between BOLD undershoot characteristics found under visual and sensorimotor stimulation. In summary, our results have provided critical insights into the mechanisms underlying functional hyperemia, and advanced our understanding of neurovascular interactions.

7.2 Future Work

The VERVE method is a promising new technique for noninvasive and dynamic venous ΔCBV monitoring, and provides results in agreement with steady-state venous-extrapolations based on total CBV measurements found in the literature. As demonstrated in this thesis, VERVE has been invaluable in determining the BOLD-specific steady-state flow-volume relationship during neuronal activation, and has provided a means to verify the existence of venous volume contribution to the BOLD post-stimulus undershoot. A natural extension of the reported research is to investigate the hemodynamic process underlying sustained negative BOLD signals [225, 378, 379]. Sustained negative BOLD changes have been associated with decreased total CBV in anesthetized animals, but it is unclear whether this decreased perfusion is due to a local reallocation of blood [378] or to systematic neuronal suppression of inflow [380]. As

venous CBV strongly modulates the BOLD signal amplitude, knowledge of its role in producing the negative BOLD signal is critical to the debate. In particular, a study of the neurovascular interaction that contributes to the negative BOLD transients may effectively complement the information gleaned from the positive BOLD transients, and substantially supplement the existing knowledge of brain physiology.

Another obvious extension of the flow-volume experiments is the measurement of the hemodynamic response induced by means other than neuronal activity, such as CO₂ manipulation. A graded paradigm, involving both hyper- and hypocapnia, would permit the investigation of such a relationship during both increased and decreased perfusion. Conventional methods of CO₂ manipulation include hyperventilation [381] and the breathing of pre-determined gas mixtures [49]. However, these methods do not provide stable CO₂ targeting. This inability of maintaining a steady state makes these methods difficult to adopt for steady-state hemodynamic studies [382]. The recent development in computerized targeting and delivery methods is expected to significantly improve the accuracy of CO₂ and perfusion targeting. The sequential gas delivery method, proposed by Slessarev *et al.* [383], permits accurate targeting of end-tidal CO₂ while maintaining a constant O₂ pressure (and vice versa) through a feed-forward approach, which also allows more rapid transitions than feed-back based methods [384]. This technique has been successfully applied in fMRI studies [385], and is expected to greatly facilitate our investigation of steady-state hemodynamics by reducing end-tidal fluctuations introduced by physiological instability and human error.

Closely preceding the introduction of VERVE, another dynamic and noninvasive CBV monitoring technique, namely the vascular space occupancy (VASO) method [285], received much attention. VASO assumes the nulling of blood (arterial and venous) based on a non-selective inversion recovery sequence, with subsequent signal decreases interpreted as resulting from blood volume increase. Theoretically, VASO targets total CBV instead of venous CBV. This was confirmed by the experimental observation that the CBV behaviour measured by VASO decidedly differs from those measured by VERVE in both the steady and transient states. Certain differences are to be expected, of course, given that the two techniques target different blood compartments. However, the situation is also complicated by recent reports of contaminating signals that may

substantially affect the accuracy of VASO [150, 386, 387]. It is therefore of unique interest to analyze the similarities and differences between VERVE and VASO, and to reconcile any difference based on physiological or experimental justifications. In addition, with the currently wide interest in VASO as an easily implemented technique, a VASO-VERVE comparison study could potentially help establish whether VASO is a reliable technique for functional CBV mapping, given its drawbacks.

In addition to the post-stimulus undershoot, an early transient BOLD signal drop termed the “initial dip” has also been a contentious phenomenon. The initial dip was first noted by Frostig *et al.* using optical imaging [45], and was more recently seen by Yacoub *et al.* using MRI [328]. The general interest in this transient feature is prompted by the argument that its location may be more proximal to the site of neuronal activity than that of the steady-state BOLD signal [213]. In addition, the initial dip may be evidence of transient flow-metabolism uncoupling. The investigation of the BOLD post-stimulus undershoot in this thesis produced no evidence of CBF-CMR_{O₂} uncoupling, however, and instead highlighted the important role of venous CBV in contributing to a transient negative BOLD signal, a contribution which has hitherto not been explored. The capability of the VERVE technique to measure changes in venous CBV make it the best candidate so far in helping to resolve the flow-metabolism coupling debate. However, the temporal resolution of the current implementation of VERVE is 4 s, whereas the initial dip only lasts up to 3 s [388]. The VERVE temporal resolution is primarily limited by the restrictions on the specific absorption rate (SAR), imposing long repetition times, thus not providing sufficient sampling of the dip. To improve the temporal resolution of VERVE measurements and make it a more powerful technique, an important consideration is reducing the SAR, and several potential approaches may be taken to that end.

While the choice of single-shot turbo spin-echo has greatly improved VERVE SNR and spatial integrity, its read-out refocusing pulses add substantially to the overall power deposition. The most obvious SAR-reducing alternative is to use parallel imaging to reduce the number of refocusing pulses involved in the readout. With our recently updated scanner hardware, which now includes a 32-channel receiving head coil, RF power reduction is undoubtedly possible with reduced sacrifice of image quality. It should be noted that as acceleration reduces SNR, an optimization between SNR and

SAR would be required. However, the fact remains that the bulk of the SAR originates from the VERVE magnetization preparation instead of the readout, which calls for modification of the non-selective refocusing trains. One possibility that has been tentatively explored is low-flip-angle refocusing schemes, such as the pseudo steady-state concept [241, 242, 389], which could retain T_2 contrast while allowing flip angle reductions of up to 30%, translating to a 50% reduction in average power deposition. The greatest challenge in adopting reduced flip-angle approaches is overcoming the sensitivity of VERVE to alternate echo pathways, which could annihilate the desired fast-slow signal difference, a small one, given the low parenchymal venous blood content. Furthermore, although our current employment of nonselective composite refocusing pulses in conjunction with phase-cycling is highly effective against spurious echo production from field inhomogeneities, further increases to B_1 -inhomogeneity immunity are always welcome, and would potentially boost the feasibility of using reduced flip angles. There are few options that exceed adiabatic pulses in B_1 -insensitivity. However, conventional adiabatic pulses are characterized by long durations and high RF power, neither of which lends itself to improving the temporal resolution of VERVE. In addition, the effectiveness of conventional adiabatic pulses in a spin-echo configuration is low compared to pulsed RF [390]. Therefore, reduced SAR and ΔB_1 sensitivity being the goal, low-power and short-duration adiabatic pulses would have to be developed.

Finally, in the interest of whole-brain functional mapping using venous ΔCBV_v , VERVE should be further revised for multi-slice or three-dimensional imaging. Given the importance of continuous non-selective refocusing and the coexistent need to reduce power deposition, the acquisition of the refocused signal must be accelerated yet further. Parallel three-dimensional imaging, for example, can be customized for this purpose.

Appendix I

Ethics Approval for Human Studies

All human studies included in this thesis were approved by the Montreal Neurological Institute and Hospital Research Ethics Board (REB, MNI/H, Montreal, Canada). The confirmations of ethics approval are included in the following pages.



Centre universitaire de santé McGill
McGill University Health Centre

Les meilleurs soins pour la vie
The Best Care for Life

8

April 18, 2006

Dr Bruce Pike

Magnetic Resonance Imaging, brain Imaging Centre
MNI

Re: 6.a. NEU-05-059

Human whole blood MRI relaxometry at 1.5T and 3T

PI: Dr. Bruce Pike

- Consent form Submission letter dated 4/12/2006
- Application for Initial Review version 2004.11.26/2002.10.31 signed March 21, 2006;
- English Consent Form version March 21, 2006;
- French Consent Form version le 21 mars 2006;
- MR Committee approval letter dated February 7, 2006;
- Certificate of translation validation for written informed consent to research dated 06/04/2006;

Dear Dr. Pike,

Thank you for submitting your **Application for Initial Review** for the above-cited research protocol.

The above submission, reviewed by the full REB at the March 6, 2006 meeting # 6.a., was found to be *acceptable* for continuation at the McGill University Health Centre (MUHC). This was entered accordingly into the minutes of the REB meeting.

The approval of the study is valid until April 18, 2007

All research involving human subjects requires review at recurring intervals. To comply with the regulation for continuing review of "at least once per year," it is the responsibility of the investigator to submit an Application for Continuing Review to the REB prior to expiry. However, should the research conclude for any reason prior to approval expiry, you are required to submit a Termination Report to the board once the data analysis is complete to give an account of the study findings and publication status.


The Research Ethics Boards (REBs) of the McGill University Health Centre are registered REBs working under the published guidelines of the Tri-Council Policy Statement, in compliance with the "Plan d'action ministériel en éthique de la recherche et en intégrité scientifique" (MSSS, 1998) and the Food and Drugs Act (2001.06.07), acting in conformity with standards set forth in the (US) Code of

Federal Regulations governing human subjects research and functioning in a manner consistent with internationally accepted principles of good clinical practice.

Should any revision to the study or other development occur prior to the next required review, you must advise the REB without delay. Regulation does not permit initiation of a proposed study modification prior to REB approval of the amendment.

We trust this will prove satisfactory to you. Thank you for your consideration in this matter.

Yours very truly,

A handwritten signature in black ink, appearing to read 'E. Bereza', with a stylized flourish at the end.

Eugene Bereza, MD CM, CCFP
Chair, MNH/I Research Ethics Board
EB/lz

Meeting of March 6, 2006 # 6.a.



Centre universitaire de santé McGill
McGill University Health Centre

Les meilleurs soins pour la vie
The Best Care for Life

August 27, 2008

Recd. Sept. 2/08

Dr. Bruce Pike
Magnetic Resonance Imaging
Room WB3, MNI

Re: 5.f. PIKB 2002/1
Functional MRI of Brain Physiology (CIHR Grant MOP 15630)
PI: Dr. Bruce Pike

- Application for Continuing Review signed August 11, 2008
- Consent Form – English, version August 7, 2008
- Consent Form – French, version 7 aout 2008

Dear Dr. Pike,

Thank you for submitting your **Application for Continuing Review** for the above-cited research protocol.

The above submission, reviewed by the full REB at the August 26, 2008 meeting #5.f., was found to be acceptable for continuation at the McGill University Health Centre (MUHC). This was entered accordingly into the minutes of the REB meeting.

The re-approval of the study is valid until October 27, 2009

All research involving human subjects requires review at recurring intervals. To comply with the regulation for continuing review of "at least once per year," it is the responsibility of the investigator to submit an Application for Continuing Review to the REB prior to expiry. However, should the research conclude for any reason prior to approval expiry, you are required to submit a Termination Report to the board once the data analysis is complete to give an account of the study findings and publication status.

The Research Ethics Boards (REBs) of the McGill University Health Centre are registered REBs working under the published guidelines of the Tri-Council Policy Statement, in compliance with the "Plan d'action ministériel en éthique de la recherche et en intégrité scientifique" (MSSS, 1998) and the Food and Drugs Act (2001.06.07), acting in conformity with standards set forth in the (US) Code of Federal Regulations governing human subjects research and functioning in a manner consistent with internationally accepted principles of good clinical practice.

Should any revision to the study or other development occur prior to the next required review, you must advise the REB without delay. Regulation does not permit initiation of a proposed study modification prior to REB approval of the amendment.

We trust this will prove satisfactory to you. Thank you for your consideration in this matter.

Yours very truly,

Eugene Bereza, MD CM, CCFP
Chair, MNH/I Research Ethics Board
EB/ah

Meeting of August 26, 2008 #5.f.

Appendix II

Whole Human Blood T_2 Relaxometry --- Supplementary Material

As part of the experiments involved in obtaining the blood relaxometry data documented in Chapter 3, a series of experiments were conducted to validate the experimental protocol and to assess additional physical and chemical properties of whole human blood. The corresponding results bear significant interest for future studies of a similar nature, and to the knowledge of human brain physiology at large. As they were not included in the manuscript, they are summarized in the following sections.

A2.1 Blood T_2 Variations with Elapsed Time

As mentioned in Chapter 3, the blood gas analysis (Bayer, Leverkusen, Germany) for assessing the oxygenation (Y), hematocrit (Hct) and pH was performed immediately after the MR relaxometry scans. In order to ensure minimal blood oxygenation change as a result of scan-induced delay, we performed pre- and post-scan blood gas analysis on one subject, which revealed a small Y decrease of approximately 2% post-scan relative to pre-scan levels. Thus, minimal oxygenation change during the scan was established.

In the course of the scan session, RF power deposition by the relaxometry pulse sequences, which could potentially cause sample temperature increase, depended on the refocusing interval. To preclude RF heating-induced T_2 biases, the sequence of refocusing intervals used in the T_2 relaxometry acquisition was randomized. In addition, the stability of blood sample temperature during the 90-minute scan period was assessed through an extra blood sample kept in the scanner room and monitored for temperature changes every 2 minutes using a digital temperature probe (Maverick, Edison NJ, USA).

The sample temperature was found to increase from 11.1 °C to 21.2 °C within 30 minutes from being removed from the ice bath, at which temperature it remained for the rest of the 90-minute scan duration (mean \pm SD = 20.1 \pm 2.2 °C). Stability in the corresponding T_2 was evaluated through repeated T_2 relaxometry using a constant τ_{180} over a 90 minute period. A τ_{180} of 8 ms was chosen to match the average delivered RF power to that of the full set of refocusing intervals. The resulting T_2 estimates (136.4 \pm 6.1 ms) showed no significant correlation with elapsed time or with temperature.

A2.2 Cross-Validation of T_2 Relaxometry Methodology

The single-slice T_2 -prepared segmented EPI T_2 relaxometry technique (Figure 4.1), which allowed for very short refocusing intervals to be explored, has previously been shown to provide consistent T_2 estimates at both short and long τ_{180} [63, 278]. Nonetheless, experimental verification was repeated at 3 T using the conventional multi-echo spin-echo (SE) Carr-Purcell Meiboom-Gill (CPMG) technique [255] as the “gold standard” (Figure 4.2). Both the segmented EPI and the SE CPMG sequences employed nonselective composite 180° pulses to maximize refocusing uniformity.

The τ_{180} values used for verification were 8, 10, 12, 17.5, 20, 24 and 37.5 ms, and the number of acquired data points (echoes) in the CPMG sequence was adjusted such that for each τ_{180} , the same range of the T_2 decay curve was sampled, as to match the sampling window of the segmented EPI sequence. The scans were performed on MnCl₂-doped fluid-filled phantoms with a range of physiologically relevant nominal T_2 values. The T_2 fitting procedure is described in section 3.5. As shown in

Table A2.1, the segmented EPI and the CPMG methods were found to produce statistically indistinguishable T_2 estimates over all τ_{180} 's and T_2 's, thus validating the segmented EPI technique for comprehensive blood T_2 relaxometry.

Table A2.1 Comparison of T_2 measured by CPMG and segmented EPI.

MnCl_2 phantom T_2 estimates were obtained using the segmented EPI technique and the multi-echo spin-echo CPMG (SE CPMG) technique (mean \pm SD) over a range of inter-refocusing intervals (τ_{180}). No statistically significant difference was observed.

τ_{180} (ms)	Phantom	SE CPMG		Segmented EPI	
		Data points	T_2 (ms)	Data points	T_2 (ms)
8	1	32	18.3 \pm 3.0	6	21.0 \pm 20.7
	2	32	49.2 \pm 1.9	6	52.0 \pm 20.2
	3	32	124.3 \pm 1.2	6	121.3 \pm 23.4
10	1	26	18.2 \pm 4.7	6	19.3 \pm 12.5
	2	26	48.7 \pm 2.7	6	51.4 \pm 13.2
	3	26	123.0 \pm 2.0	6	119.5 \pm 17.9
12	1	20	18.2 \pm 6.3	6	19.7 \pm 15.1
	2	20	49.1 \pm 3.8	6	51.5 \pm 15.4
	3	20	122.4 \pm 3.3	6	119.7 \pm 19.7
17.5	1	14	18.1 \pm 12.2	6	21.7 \pm 22.9
	2	14	48.7 \pm 6.8	6	52.1 \pm 22.0
	3	14	120.8 \pm 6.7	6	120.6 \pm 24.9
20	1	12	18.1 \pm 14.0	6	23.6 \pm 26.5
	2	12	49.0 \pm 8.4	6	52.3 \pm 25.0
	3	12	120.2 \pm 8.6	6	120.9 \pm 27.4
24	1	10	*	6	*
	2	10	58.8 \pm 11.2	6	52.9 \pm 30.0
	3	10	143.7 \pm 12.2	6	120.5 \pm 31.6
37.5	1	8	*	6	*
	2	8	49.4 \pm 21.4	6	54.4 \pm 47.7
	3	8	118.4 \pm 20.5	6	121.2 \pm 47.2

* data SNR insufficient for accurate T_2 estimation.

A2.3 In Vivo Blood Water Diffusion Coefficient

As reported in Chapter 3, we found the whole blood T_2 variation with oxygenation and the CPMG refocusing interval to be best described by the diffusion model [270]. However, given the fact that our blood relaxometry experiments were conducted ex vivo at room temperature ($\cong 20$ °C), at which temperature the water diffusion rate is likely to differ from that found at the average human in vivo temperature of 37 °C, it was of interest to assess potential bias introduced by applying our results to in vivo conditions. We are encouraged by well-documented evidence of very slight T_2 variation within this temperature range [157, 261, 391, 392], a point further confirmed by our experimental data in section A2.1, which showed an average blood T_2 shortening of merely 5.1% over a 10 °C temperature increase, well within the T_2 estimation uncertainty. Moreover, in the above temperature range, the oxy-hemoglobin dissociation curve is minimally affected [37], and the variability in water diffusion permeability across the erythrocyte membrane has also been shown to be negligible [393]. Finally, the temperature dependence of the apparent diffusion coefficient (ADC) of whole blood was assessed experimentally.

Whole human blood samples were drawn at resting state through forearm venipuncture and immediately immersed in $MnCl_2$ -doped water baths with temperatures of 7 °C, 24 °C and 37 °C, chosen to represent near-freezing, room-temperature and in vivo conditions. The samples were sealed in 3 mL blood-gas syringes (diameter = 9 mm, with balanced 25U heparin, Westmed, Tucson, AZ, USA), and placed vertically into the water bathes, which were contained in an MR-compatible insulated set-up. This ensemble was immediately imaged using a Siemens Trio 3 T system (Erlangen, Germany), with body-coil transmission and quadrature head-coil reception. The following parameters were used in the diffusion-weighted imaging protocol: TR = 3 s, TE = 72 ms, $b = 700$, slice thickness = 5 mm, readout bandwidth = 1392 Hz/voxel. The scan session lasted 25 minutes, which introduced minimal change in the sample temperatures, as verified by pre- and post-experimental temperature measurements using a digital temperature probe (Maverick, Edison NJ, USA).

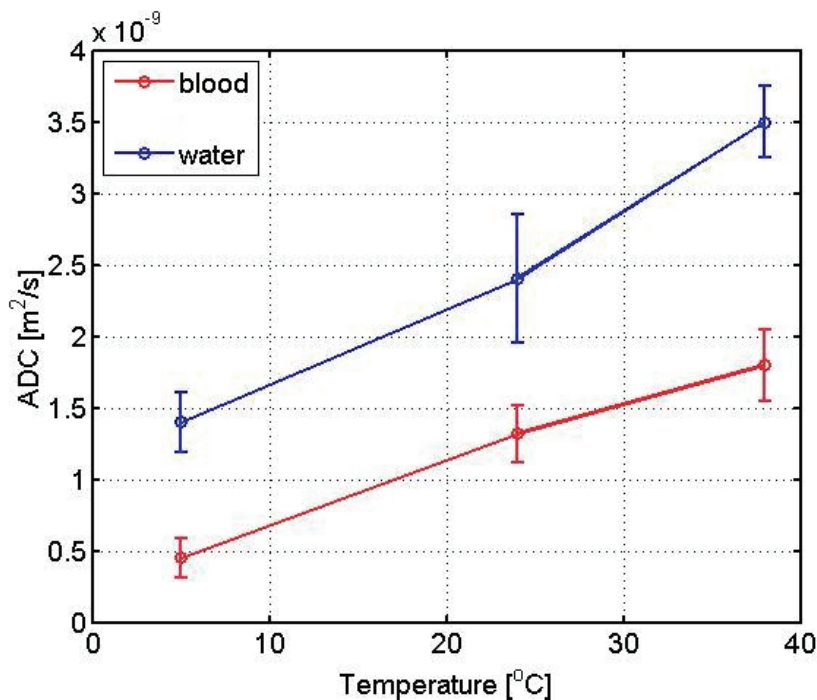


Figure A2.1 Diffusion measurements in blood and water.

Anisotropic diffusion coefficient (ADC) measurements in whole human blood and MnCl_2 -doped water are shown for temperatures of 7, 24 and 37 °C.

The average blood oxygenation was measured to be 50.7%. In the blood samples, the ADC was measured as an average of values measured at the top and bottom halves of the syringes in order to account for sedimentation effects. At temperatures of 7, 24 and 37 °C, the average ADC estimates for whole blood were 0.5 ± 0.1 , 1.3 ± 0.2 and 1.7 ± 0.3 m^2/s . The corresponding ADC values for the MnCl_2 -doped water were used as reference, and found to be 1.4 ± 0.2 , 2.4 ± 0.4 and 3.5 ± 0.3 m^2/s , respectively. As seen in Figure A2.1, blood and water ADC values increased with temperature at similar rates up to approximately room temperature, after which water ADC rose supra-linearly with temperature whereas blood ADC rose sub-linearly.

The water ADC measurements were in excellent agreement with literature reports on the temperature dependence of water diffusion [394-396]. The water diffusion rate in whole blood was lower than that found in pure water, likely due to the higher viscosity and hence diffusion restrictions. The apparent reduction in the rate of ADC increase with temperature in blood may arise from the existence of erythrocytic membranes.

Specifically, the expected diffusion distance experienced by the average water molecule over a TE of 74 ms is comparable to the average diameter of the human red blood cell, lending strength to our argument that the limiting effect of the cellular membranes on water diffusion strengthens as the water molecules move faster (at higher temperatures).

Finally, based on the above measurements, the temperature-dependence of the water-diffusion rate can be addressed by varying the diffusion coefficient ($D = \text{ADC}$) in the diffusion T_2 model. Correspondingly, the average ADC change corresponding to a temperature change from 20 to 37 °C was found to be approximately 30%. Nonetheless, given the minimal variation of whole blood T_2 over this temperature range, the increase in D will merely result in a 14% increase in the estimated characteristic length of the field inhomogeneities (i.e. r_c rising from 2.7×10^{-6} m to 3.1×10^{-6} m), otherwise bearing no impact on the interpretation of our T_2 relaxometry results.

Appendix III

ASL and PET Cross-Validation of Cerebral Blood Flow Measurement

A3.1 Preface

Cerebral blood flow (CBF) is one of the primary modulators of the BOLD fMRI signal, and the measurement of CBF changes (Δ CBF) is therefore of immense value to the understanding and modeling of BOLD. Non-invasive pulsed arterial spin labeling (PASL) techniques offer the opportunity for monitoring CBF dynamically without incurring the ionizing radiation that undermines the repeatability of traditional methods such as positron emission tomography (PET). In addition, PASL and BOLD can be interleaved to provide simultaneous flow and metabolism-correlated measurements. These aspects of PASL make it extremely attractive for fMRI, but as the use of PASL becomes increasingly ubiquitous, so has the need to verify the equivalence of CBF measurements made using PASL and the more well-established PET technique. Such a cross-validation would not only reinforce the feasibility of PASL measurements for BOLD modeling, but would also provide a more complete picture of the feasibility of PASL and PET for fMRI applications.

In the following section, the flow-sensitive alternating inversion recovery (FAIR) PASL technique, which has been extensively used in fMRI, is compared with H_2^{15}O PET, in terms of Δ CBF measurements during graded neuronal stimulation and hypercapnia in healthy humans. The FAIR PASL technique, although affected by certain technical limitations, was chosen for its extensive involvement in BOLD quantification in previous and current fMRI literature, and was found to provide Δ CBF measurements equivalent to those obtained using PET under all experimental conditions. These results represent the most comprehensive and direct comparison to-date of CBF measurements obtained using

fMRI and PET, and establish the feasibility of using FAIR, and PASL in general, for functional CBF imaging and BOLD modeling.

Cerebral Blood Flow Measurement using fMRI and PET: A Cross-Validation Study

**Jean J. Chen, Marguerite Wieckowska, Ernst Meyer
and G. Bruce Pike**

McConnell Brain Imaging Centre
Montreal Neurological Institute
McGill University

International Journal of Biomedical Imaging; 2008: 516359.

A3.2 *Abstract*

An important aspect of functional magnetic resonance imaging (fMRI) is the study of brain hemodynamics, and MR arterial spin labeling (ASL) perfusion imaging has gained wide acceptance as a robust and non-invasive technique. However, the cerebral blood flow (CBF) measurements obtained with ASL fMRI have not been fully validated, particularly during global CBF modulations. We present a comparison of cerebral blood flow changes (Δ CBF) measured using a flow-sensitive alternating inversion recovery (FAIR) ASL perfusion method, to those obtained using H_2^{15}O PET, which is the current gold standard for *in vivo* imaging of CBF. To study regional and global CBF changes, a group of 10 healthy volunteers were imaged under identical experimental conditions during presentation of 5 levels of visual stimulation and one level of hypercapnia. The CBF changes were compared using 3 types of region-of-interest (ROI) masks. FAIR measurements of CBF changes were found to be slightly lower than those measured with PET (average Δ CBF of $21.5 \pm 8.2\%$ for FAIR vs. $28.2 \pm 12.8\%$ for PET at maximum stimulation intensity). Nonetheless, there was a strong correlation between measurements of the two modalities. Finally, a *t*-test comparison of the slopes of the linear fits of PET vs. ASL Δ CBF for all 3 ROI types indicated no significant difference from unity ($p > 0.05$).

Keywords: positron emission tomography (PET), functional magnetic resonance imaging (fMRI), arterial spin labeling (ASL), flow-sensitive alternating inversion recovery (FAIR), cerebral blood flow (CBF), blood-oxygenation level dependent (BOLD), visual cortex (VC), neuronal activation, hypercapnia.

A3.3 Introduction

Neuronal activity results in focal changes in hemodynamics, metabolism and blood oxygenation of associated brain areas. Functional maps of cerebral blood flow (CBF) can be used to monitor hemodynamic changes in the healthy brain as well as alterations associated with cerebrovascular disease. Positron emission tomography (PET) is capable of providing *in vivo* quantitative measures of CBF, and has evolved to be considered the gold-standard for studying cerebral hemodynamics. However, PET imaging involves the injection of radioactive tracers, which limits its repeatability and application in healthy volunteers. Among other limitations are low temporal and spatial resolution, low signal-to-noise ratio (SNR), as well as the requirement for a cyclotron. Thus, magnetic resonance (MR) perfusion imaging, being widely available, and having relatively high spatial and temporal resolution, is increasingly seen as an attractive alternative to PET.

MR perfusion imaging is performed using dynamic susceptibility contrast (DSC) techniques or arterial spin labeling (ASL) [121, 397]. DSC imaging has not been widely applied in human functional research due to the requirement of an exogenous contrast agent and limited temporal resolution. ASL is based on the detection of magnetically labeled arterial blood-water spins and has therefore been used with more success in functional MRI (fMRI) studies. Pulsed ASL methods such as PICORE (proximal inversion with control for off-resonance effects), FAIR (flow-sensitive alternating inversion recovery), QUIPSS I/II (quantitative imaging of perfusion using a single subtraction) and Q2TIPS (QUIPSS II with thin-slice T1 and periodic saturation) have greatly facilitated perfusion-based fMRI [103, 121, 341, 357, 398-400].

The validation of MR perfusion measurements using various invasive and non-invasive methods has been a topic of considerable interest. Walsh *et al.* compared CBF measured using continuous ASL and radioactive microspheres using a rat model, and found ASL to underestimate CBF under high flow [401]. On the other hand, based on radiotracer-enhanced quantitative autoradiography flow measurements in rats, Ewing *et al.* concluded that CBF were overestimated by ASL under ischemia [402]. In healthy humans, Østergaard *et al.* [403] found a highly linear relationship between PET and DSC MR CBF measurements (using Gd-DTPA), consistent with the values reported in the

literature. Similar findings were reported by Carroll *et al.* [112], Lin *et al.* [404] and Grandin *et al.* [111] in healthy human subjects. Quantitative CBF values of 68.1 ± 9.5 and 26.7 ± 5.0 mL/100 g/min were measured for grey matter (GM) and white matter (WM), respectively [404]. In addition, Grandin *et al.* reported a high correlation between DSC and PET CBF measurements under the effect of vasodilative pharmacological agents, with PET results having higher reproducibility [111]. However, Carroll and Grandin found that GM CBF values were overestimated with DSC MR, possibly due to sensitivity to the presence of large blood vessels [111, 112].

Ye *et al.* reported a comparison of resting CBF using steady-state ASL and PET, and measured GM CBF of 64.12 and 67.13 mL/100 g/min, respectively. The PET and ASL measurements were not statistically different from one another, and were both in good agreement with literature values [109]. However, the WM ASL CBF (23.8 mL/100 g/min) was 30% lower compared to PET (33.7 mL/100 g/min), the discrepancy being attributed to the arterial tagging time difference between GM and WM, specific to the quantitative model employed in this study. In epilepsy patients, Liu *et al.* studied perfusion in the temporal lobe using the FAIR-prepared half-Fourier single-shot turbo spin-echo (HASTE) technique [405], and also found a statistically significant correlation between ASL and PET data. A functional comparison involving PET and ASL was first performed by Zaini *et al.* using a simple finger-tapping task [406]. However, the matching of spatial resolution and noise was not possible for PET and ASL data. In a more recent study by Feng *et al.* [101], another comparison of PET and FAIR fMRI measurements of CBF changes was reported, using a single level of visual stimulation in healthy subjects. Once again, results obtained by the two methods were very similar, with the PET CBF percent change being slightly higher than that of FAIR (Δ CBF of 38.79% vs. 36.95%).

Notwithstanding the contributions of the above studies, several factors limit the scope and applicability of the existing studies. First, an accurate comparison of PET and fMRI perfusion is challenging due to methodological differences. In particular, spatial resolution disparities lead to difficulties in accurate region-of-interest (ROI) registration and partial-volume matching, which are critical for direct comparisons. Second, both techniques are inherently sensitive to physiological variations, which reduce measurement reproducibility. Carroll *et al.* measured inter-exam ASL CBF variation in a single subject

to be as high as 20 mL/100 g/min in GM and 15 mL/100 g/min in WM, while those observed with PET were 4-5 mL/100 g/min [112]. Grandin *et al.* observed variations of up to 13% for PET and 16% for MR CBF measurements at rest in the same individual [111]. As a result, high inter-subject and inter-exam variability between PET and MR are expected, particularly in inexperienced volunteers scanned over several days. Thirdly, past comparisons of CBF measurements were largely performed without functional stimulation, and for those within the fMRI context, the impact of graded stimulus intensity [341] has not been explored. Finally, previous ASL and PET CBF data were not always collected in similar environments.

We were interested in evaluating the relative accuracy of the FAIR ASL method for Δ CBF measurements in comparison with PET. Previous ASL research [284, 407] has shown the accuracy of FAIR in determining CBF to be dependent on the transit delay and label width, which can be variable across subjects and experimental conditions. This has led to the introduction of techniques less sensitive to transit delay and bolus width, such as QUIPSS II [103], and their adoption by our group [49, 100, 306] and others. However, the FAIR technique [408] has been, and continues to be used extensively in the literature as a well-established method for the investigation of functional hemodynamics [341, 357, 399, 400]. Notably, some widely adopted and investigated biophysical models of the BOLD signal have been developed and validated based on CBF data using FAIR [101, 174, 178, 357, 409]. Thus, a dedicated assessment of the validity of FAIR for CBF measurement would be a highly valuable addition to our knowledge.

In this study, we compare FAIR fMRI measurements of CBF with those made using PET during graded levels of visual stimulation. In addition, we measured CBF changes induced by hypercapnia, which has been employed to explore global, activation-independent, perfusion increases, and applied to cross-subject calibrations of the BOLD response [174]. Also, over the course of our experiments, the conditions for ASL and PET data collection were also closely matched and monitored.

A3.4 *Methods and Materials*

A3.4.1 *Experimental design*

Visual stimuli were generated using locally developed software (GLStim) based on the OpenGL graphics library (Silicon Graphics, Mountain View, CA). The baseline condition consisted of a uniform grey field, while the activation pattern was a yellow-blue radial checkerboard with 30 spokes and 6.5 rings of equal radial thickness, reversing contrast at 4 Hz. The checkerboard contains both colour and luminance contrast designed to produce robust local CBF increase in the primary visual cortex (V1) [341, 357]. In an effort to maintain the subjects' attention, a fixation task (a small arrow randomly changing directions) was present at the centre of the field-of-view (FOV) throughout the scans. Subjects were requested to continuously report the arrow direction by means of an MR-compatible mouse.

The graded visual stimulation and hypercapnia schemes were matched to those previously employed in calibrated fMRI studies of flow-metabolism coupling [357]. In addition to the uniform grey-field reference condition, the subjects were presented with 4 graded levels of visual stimulation, ranging from 25% to 100% intensity, while inhaling atmospheric composition medical air supplied at 16 L/min. Furthermore, mild hypercapnia (induced using air mixture of 5:21:74% CO₂:O₂:N₂) was used to study global CBF changes. Both PET and ASL scans included 6 sessions of 3 minutes, each consisting of one visual-respiratory condition played out continuously. Each stimulation session was preceded and followed by a baseline condition (Figures 1 and 2) of 1 and 2 minutes, respectively.

A total of 10 healthy human subjects (8 male, 2 female), aged 23.9 ± 3.3 years, were imaged under the above six experimental conditions. Informed consent was obtained from every subject prior to each PET and MRI scanning session, with the experimental protocol being approved by the Research Ethics Board of the Montreal Neurological Institute (MNI, Montreal, Canada). In order to achieve maximal similarity between the PET and fMRI experimental conditions, the sizes of the projected checkerboards were matched, as well as the lighting intensity at the two imaging locations. During the scans,

subjects were asked to breathe through a non-rebreathing face mask, allowing control of the incoming air composition.

A3.4.2 Magnetic resonance imaging

Subjects were immobilized with a foam headrest and head restraints. A nasal cannula connected to a capnometer was used to monitor end-tidal carbon dioxide (ETCO₂) and the respiratory rate, whereas the arterial oxygen saturation (O₂Sat) and the pulse rate were measured with a finger pulse-oximeter. The pulse and respiratory rates are indicators of blood CO₂ tension. The stimulus was presented by an adjustable back-projection mirror mounted on the head coil.

The MR scans were performed on a 1.5 T Siemens Magnetom Vision system (Siemens, Erlangen, Germany). To optimize the SNR of the functional data in the visual cortex, a transmit-receive surface coil placed near the occipital lobe was used to acquire all functional images. Thus, prior to the functional scans, a surface-coil T1-weighted (T1W) anatomical scan, acquired at a resolution of 1x1x2 mm³, was used in slice-selection and alignment of all functional data. However, as the surface-coil anatomical data has highly non-uniform intensity, registration to PET data using our local software was difficult. Therefore, an additional high-resolution 1x1x1 mm³ T1W anatomical scan with a head-coil was also acquired to facilitate the registration of PET and surface-coil MR data. We use the interleaved FAIR-BOLD echo-planar imaging sequence as implemented by Hoge *et al.* [357] in order to directly evaluate their measurements, as well as to achieve simultaneous BOLD monitoring. Furthermore, we selected imaging parameters to best enable replication of experimental conditions in previous fMRI flow-metabolism studies [175, 357]. The FAIR inversion time and echo time (TE) were 900 ms and 20 ms, respectively, while the BOLD TE was 50 ms. A 7-mm thick single oblique slice parallel to the calcarine sulcus was acquired on a 64x64 matrix with a 5x5 mm² inplane voxel size. As seen in Figure A3.1, the repetition time of the sequence was 12 s, allowing acquisition of a total of 60 frames per 6 minutes run, 30 FAIR and 30 BOLD frames. Of these 30 frames, 11 were excluded (1 min post-onset and post-cessation of stimulation plus the first scan in the run) to ensure that only data corresponding to the physiological steady-state response was examined. The chosen FAIR implementation

minimizes errors related to the tagging slab arrival time and width through the use of a single-slice acquisition and a body coil inversion [341]. In order to obtain an accurate masking location of V1 (primary visual cortex), BOLD-based retinotopic mapping was performed in a separate session, using a visual stimulus composed of a thick black-and-white expanding ring, also designed using GLStim [175, 357]. A total of 16 slices of 4 mm parallel to the calcarine sulcus were acquired using a BOLD sequence during 6 randomly ordered runs of 6 minute visual stimulation.

A3.4.3 Positron emission tomography

The protocol for the PET experiments was adapted from previous PET studies aimed at reproducing MRI results [410]. The subjects were immobilized using a self-inflating foam headrest, which minimized motion during scans. The stimulus was presented through an adjustable mirror mounted on the patient table. As previously described, the O₂Sat level and pulse rate were monitored using a finger pulse-oxymeter, while a capnometer connected via a nasal cannula monitored the ET_{CO}₂ and the respiratory rate. In addition, a short indwelling catheter was placed by an anesthetist into the left radial artery for blood sampling and a more precise examination of blood gases. A three-way stop cock allowed for simultaneous automatic (using a locally-developed sampling system for blood activity measurement) and manual (for blood gases examination) blood sample withdrawal. Automatic blood sampling was performed at 0.5-second intervals throughout the data collection period. A fine needle-catheter was placed into the antecubital vein of the right arm for injection of the isotope.

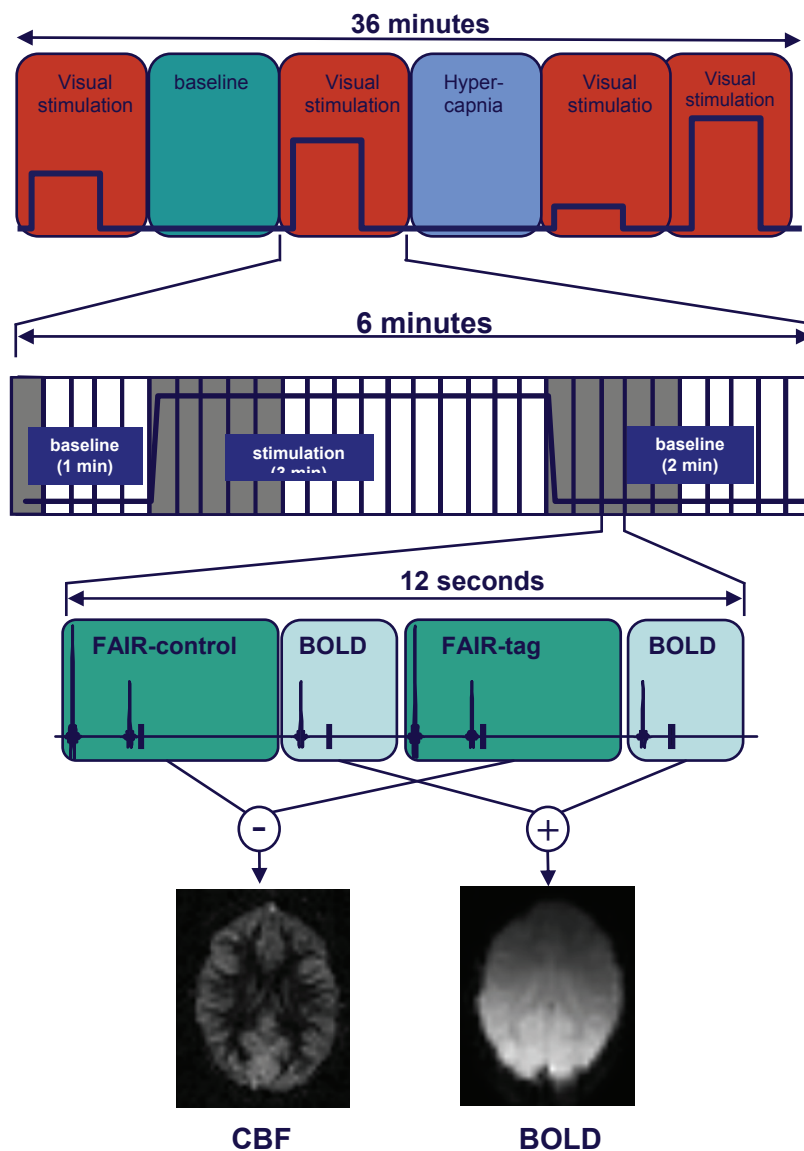


Figure A3.1

(A) The fMRI experimental protocol consisted of 6 randomly presented sessions (baseline, hypercapnia and 4 levels of visual stimulation). (B) The interleaved BOLD-FAIR sequence was repeated 30 times during each run of 6 minutes, composed of a 1-minute baseline, 3-minute stimulation and 2-minute baseline period. Scans shaded in grey (1 min post onset and cessation of stimulation plus first scan in the run) were excluded in percent change calculations to ensure that time-averaged data included only physiological changes in steady-state. (C) The basic structure of the BOLD-FAIR sequence consists of 2 BOLD acquisitions (averaged to form 1 BOLD-contrast image) interleaved with 1 slice-selective and 1 non-selective ASL acquisition. (D) These 4 acquisitions produce a flow-weighted FAIR image through subtraction, and a BOLD image through addition.

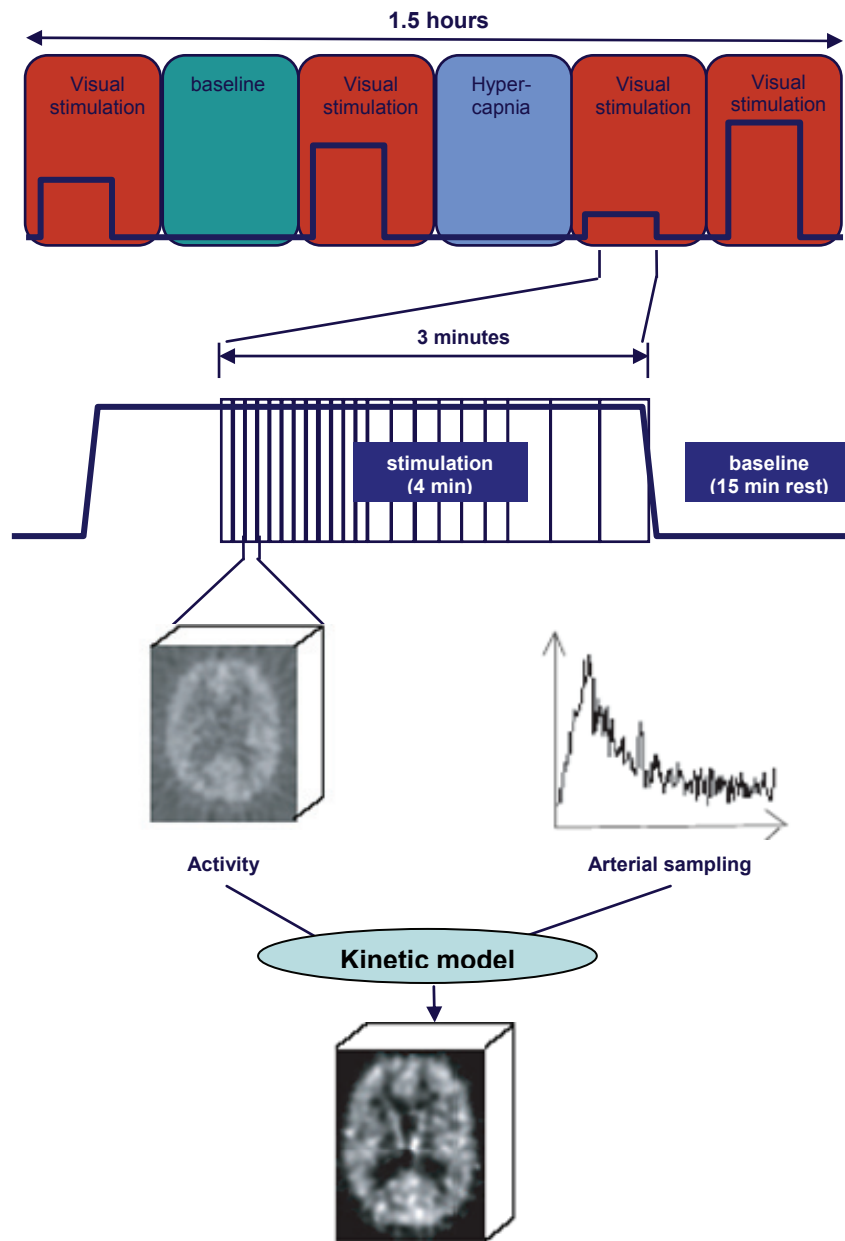


Figure A3.2

(A) The PET experimental protocol consisted of 6 randomly presented sessions (baseline, hypercapnia and 4 levels of visual stimulation). A tracer bolus injection was given at the start of each block. (B) Each run has a 3-minute acquisition period divided in 12 5-second, 6 10-second and 3 20-second frames, followed by 15 minutes of rest. (C) A volume of activity distribution was acquired during each frame. (D) This series of distribution images and the blood activity curve were fit into a kinetic model, resulting in a CBF map.

PET images were acquired on an ECAT EXACT HR⁺ (CTI/Siemens, Knoxville, TN) whole-body tomography system operating in three-dimensional (3D) mode. The volumetric images were reconstructed on 128x128 matrices of 2x2 mm² pixels using filtered back-projection with an 8-mm Hanning filter. For each of the 6 sessions, 10 mCi of H₂¹⁵O were injected. The H₂¹⁵O isotopes were prepared in a Cyclone 18/9 cyclotron (IBA, Belgium) adjacent to the scanner. The reconstructed images were automatically corrected for random and scattered events, detector efficiency variation and dead time [411, 412]. Also, a transmission scan was collected for each subject before the experiments for estimating attenuation of the 511 keV gamma rays as a function of tissue density [413]. A normalization scan was acquired for eliminating effects due to ring geometry and crystal sensitivity [414]. The stimulation conditions were presented in random order. As shown in Figure A3.2, during each 3-minute scan, the subjects were presented with only one type of stimulation, which started 1 minute before the start of the scan. This delay was designed to enable condition matching with fMRI. Arterial blood sampling and dynamic imaging started at injection time, and each scan was followed by a 15 minutes resting period, allowing the radioisotope to decay before a new injection. Due to the short half-life of H₂¹⁵O (2 minutes) and its kinetic behaviour, the observed H₂¹⁵O activity changes are very fast immediately after injection, requiring the acquisition of more frames at the beginning of the scan. Thus, each 3-minute scan consists of 21 frames acquired in 12 5-second intervals, followed by 6 frames at 10-second and 3 frames at 20-second intervals. Finally, due to the tracer kinetic model fitting required for PET data, only one volumetric CBF image was obtained for each experimental condition and no time evolution was measured.

A3.4.4 Data analysis

Flow-sensitive MR perfusion images were obtained by subtraction of the slice-selective and non-selective FAIR acquisitions. Subject motion, assessed by examining the temporal standard deviation images, was deemed negligible. Quantitative analysis of PET images was performed using the two-compartment weighted integration method [415]. No motion correction was performed given the longer acquisition time, due to which the effects of motion are greatly reduced. Three different methods of selecting the ROI were

examined. The ROIs were defined on an individual basis due to inter-subject slice placement variability. In addition, for group analysis, PET (volume) and fMRI data (single-slice) data were resampled into the same reference frame, accounting for PET's lower image resolution.

- *V1-based ROI*: The first ROI selection criterion involved choosing only voxels within the primary visual cortex (V1), since this region should contain the most reliable activation for the stimulus used. V1 was defined using fMRI-based retinotopic mapping with an eccentricity range of 5-10°, as described previously [341, 357, 416], and resampled onto the slice corresponding to the fMRI data for each subject. However, retinotopic V1 regions meeting these criteria can be small, rendering the masking process highly sensitive to misregistration between MRI and PET. Also, a small ROI mask might produce variable results, with activation data outside V1 ignored. Hence, other ROIs types were considered in the analysis.
- *t-map-based ROI*: The second type of ROI was obtained based on activation *t*-maps for both PET and fMRI CBF images. For fMRI, individual *t*-maps were calculated using *fMRIstat* [83]. PET *t*-maps were automatically generated with the locally developed software used for PET analysis, *DOT* (version 1.8.0, S Milot, MNI) [417]. Both fMRI and PET *t*-maps were thresholded at the 0.05 significance level to obtain the mask, accounting for multiple comparisons for each subject. The overlap between fMRI and PET masks was taken to be the ROI.
- *GM-based ROI*: Since the CBF changes occur mostly in GM, a third set of ROIs, consisting of a GM map in the fMRI occipital lobe slice, was defined for each subject. The GM ROIs were obtained using Bayesian fuzzy classification [273] on the high resolution anatomical MR images. This is well suited for hypercapnia studies, which are best analyzed via the global demarcation of GM. The occipital GM ROIs include activated visual cortical areas.

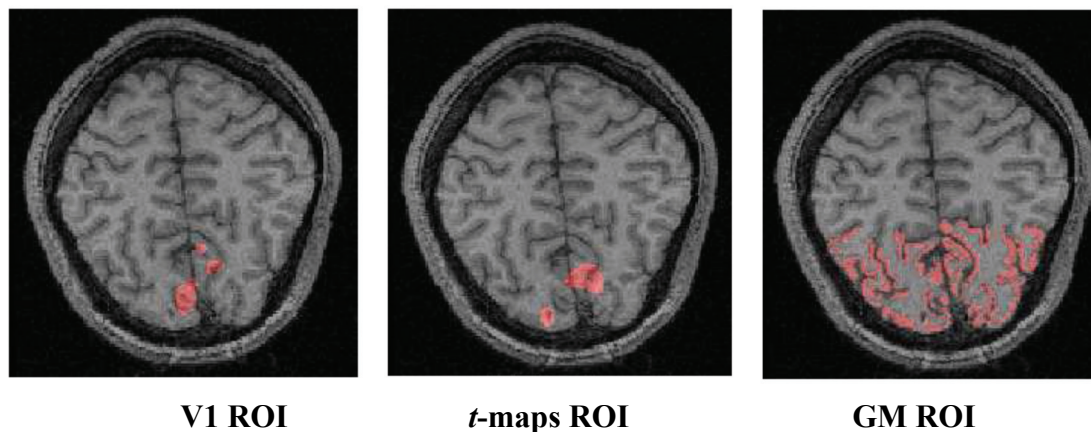


Figure A3.3

Sample ROIs (shown in red) defined for one subject. The V1 ROI was obtained by retinotopic mapping, the t -map ROI included common voxels from thresholded and resampled FAIR and PET t -maps, and the grey matter (GM) ROI was defined by Bayesian classification of the anatomical structures.

In this study, the raw FAIR fMRI images have a higher spatial resolution than PET images. To maximize the degree of matching between the MR and PET data, the surface-coil MR anatomical scans were first manually registered to the head-coil images using *Register* (D MacDonald, MNI) [418], then transformed into Talairach space. Prior to the subsequent resampling the surface-coil fMRI data into the head-coil and stereotaxic coordinates, the images were blurred using a $12 \times 12 \text{ mm}^2$ FWHM (full-width-at-half-maximum) Gaussian kernel, resulting in a resolution approximately equal to that of PET data. The post-blurring MR data was then resampled into a $1 \times 1 \text{ mm}^2$ grid using trilinear interpolation. Since FAIR data is single-slice, PET data was transformed into the FAIR slice space [406]. Individual PET scans were registered to the first PET scan for each subject using an in-house implementation of the variance-of-ratios algorithm [419]. Following this, an average PET scan was calculated for registration of PET onto the MR anatomical space. *DOT* was then used to transform the registered PET images into Talairach space. These images were subsequently resampled onto the same slice from the fMRI data in Talairach space, and the final sampling of the PET CBF slices corresponds to that of fMRI for each subject. All ROI masks were also resampled into Tailarach space, with a resolution of $1 \times 1 \times 1 \text{ mm}^3$.

To characterize the relationship between CBF changes measured using PET and FAIR, a correlation analysis was performed. The initial analysis was at the level of individual CBF changes for each subject, averaged across all voxels in the subject's ROIs, while the subsequent analysis was performed on the CBF data averaged across all subjects in the individually defined ROIs.

A3.5 Results

A3.5.1 Physiological monitoring

Overall, the pulse rate was not influenced by the air composition. It ranged from 55.6 to 58.3 beats/minute (subject average) throughout the experiment. The subjects also maintained a reasonably constant respiratory rate, between 15.7 and 17.9 breaths/minute. While ETCO_2 was stable at 40.2-42.1 mmHg during the five normocapnia conditions, a small ETCO_2 increase of about 4 to 6 mmHg was observed during hypercapnia, in agreement with rise in pressure introduced by CO_2 . Finally, arterial saturation of O_2 remained constant at 98-99% throughout all the sessions.

A3.5.2 Regions of interest (ROI)

The three ROIs used for the ΔCBF comparisons were defined on a subject-basis, as described in Methods and Materials, and an example is shown in Figure A3.3. For all subjects, the V1 ROIs were the smallest, containing only between 0.101cc and 0.187cc, due to the stringent retinotopic mapping criteria. V1 was correctly identified by the ROIs, but due to the small mask size, the corresponding ΔCBF measurements are prone to variations introduced by misregistration and motion. On the other hand, the t -map ROIs contained between 0.202cc and 0.407cc. To obtain the t -map ROI's at $p=0.05$, the fMRI t -maps were thresholded at 5.42, and the PET maps at 4.45. A lower standard deviation was seen in the responses detected in these ROIs, and the FAIR t -maps contained no statistically significant voxels for 2 of the 10 subjects. The largest were the GM ROIs, covering 1.489-0.625 cc for the same group of subjects. Some automatically classified GM voxels were excluded by the certainty-level threshold, but the final GM ROIs were still significantly larger than the V1 ROIs. As previously mentioned, larger ROI masks

may include non-activated voxels, leading to reduced levels of measured ΔCBF . Nonetheless, the GM masks provide an effective means of comparing CBF measurement across modalities, especially for the hypercapnia condition.

A3.5.3 Activation time-course

Time-series CBF data were obtained only from fMRI data as PET measurements were not available as separate frames. The BOLD and FAIR time courses were obtained by averaging all voxels in the ROI, and shown in Figure A3.4 in the V1 ROI of one subject (activation paradigm from left to right: baseline, checkerboards from 25% to 100% intensity and hypercapnia). We observed an increase in the level of signal change with increasing checkerboard intensity for both BOLD and FAIR. As expected, the activation SNR, defined as the ratio of the ROI mean over the standard deviation during activation, was lower for FAIR than for BOLD.

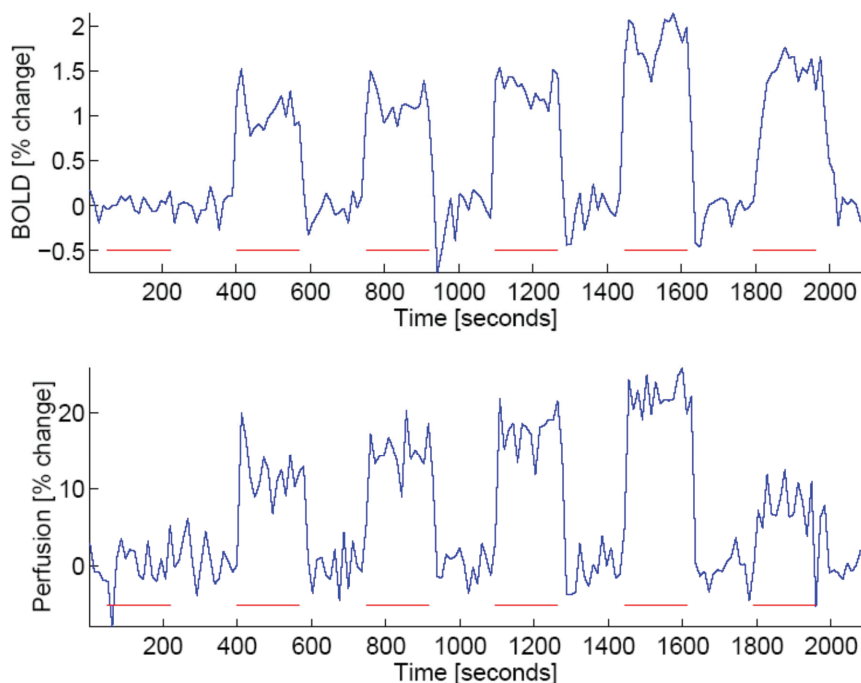


Figure A3.4

BOLD (top) and FAIR (bottom) time courses of the CBF percent change in the V1 ROI averaged over 10 subjects are shown, from left to right, corresponding to baseline, 25%, 50%, 75% and 100% intensity checkerboards, and 5% hypercapnia. The horizontal bars represent the 3-minute periods during which the stimulus was on. An increase in signal change can be observed with increasing checkerboard intensity for BOLD and FAIR perfusion, ranging between 1.0%-1.9% and 11.4%-22.5%, respectively.

In the averaged time courses, FAIR Δ CBF ranged between 11.4% and 22.5% for the various stimulation intensities, and BOLD changes between 1.0% and 1.9%. These are in the range of percent changes previously reported by Hoge *et al.* using the same stimulation and acquisition design (between 1.1% and 2.2% for BOLD, and between 23% and 48% for FAIR) [175, 357]. The measured percent changes in small ROIs such as the V1 were expected to decrease with the application of image blurring. This was true for average FAIR Δ CBF in V1, where lower values (between 16.4% and 30.4%) were measured compared to the study by Hoge *et al.* (where no blurring was applied). Comparatively lower signal changes were also measured during hypercapnia (1.5% and 7.2% for BOLD and FAIR, respectively, compared to 2.5% and 21%, respectively, in previous studies [341, 357]), despite similarity in observed ETCO_2 changes. However, our post-blurring BOLD percent changes in the V1 ROI (between 1.1% and 2.1%) were still similar to those obtained by Hoge *et al.*.

Table A3.1

CBF measured with PET in 10 subjects under 6 experimental conditions (baseline, 4 levels of graded visual checkerboard (CHB) stimulation as well as hypercapnia (HC)) in the V1 ROI, followed by the CBF measurements averaged over the 10 subjects in all 3 ROIs --- V1, t -map and GM ROIs. The PET Δ CBF measurements have a high standard deviation, largely attributable to the abnormally high CBF measured in subject 8.

Subject	Baseline	25% CHB	50% CHB	75% CHB	100% CHB	5% HC
CBF [ml/100g/min]						
1	47.7	62.5	50.5	49.0	61.3	46.8
2	34.6	54.4	53.4	43.1	52.4	38.1
3	32.6	58.3	42.6	48.6	55.9	39.8
4	42.4	50.4	55.3	45.1	52.0	60.2
5	36.8	51.6	63.0	39.6	43.4	38.4
6	39.5	46.4	74.7	59.6	62.6	50.7
7	62.5	72.5	62.9	64.3	68.6	65.0
8	114.3	139.5	137.8	164.3	148.7	115.9
9	66.1	80.2	53.6	66.65	76.4	66.6
10	50.0	36.6	45.4	37.1	31.8	35.1
Average mean\pmstd CBF in V1 ROI:						
	52.6 \pm 24.4	65.2 \pm 28.9	63.9 \pm 27.6	61.7 \pm 37.4	65.3 \pm 31.9	55.6 \pm 24.1
Average mean\pmstd CBF in t-map ROI:						
	53.6 \pm 24.5	70.6 \pm 27.9	71.3 \pm 27.0	68.9 \pm 37.6	73.8 \pm 30.2	60.0 \pm 23.2
Average mean\pmstd CBF in GM ROI:						
	47.0 \pm 22.3	52.8 \pm 23.2	51.7 \pm 20.4	50.3 \pm 26.8	52.8 \pm 23.9	49.8 \pm 21.0

A3.5.4 FAIR vs. PET

Relative PET CBF changes were calculated from absolute PET CBF values, and compared with relative FAIR Δ CBF changes. PET CBF values in the V1 ROIs for all 10 subjects, as well as averaged Δ CBF over all subjects in the 3 ROI types, are presented in Table A3.1. The results are in the range of published CBF values [357]. However, the PET CBF measurements have a high standard deviation, largely attributable to the abnormally high CBF measured in subject 8. As previously mentioned, Δ CBF time-courses could not be obtained for PET data; instead, time-averaged Δ CBF in the PET ROIs were compared to individual and group-averaged FAIR results. The PET Δ CBF maps were found to have significantly lower SNR than FAIR (<1.0 for V1 and GM ROIs, and <2.27 for t -map ROIs) for all the experimental conditions, as seen in Table A3.1, and demonstrated considerable inter-subject variability under each condition. We further noted that Δ CBF for subject 10 in the V1 and GM ROIs were negative for PET (possibly due to a relatively high PET CBF measured at baseline) and only very slightly positive for fMRI (the subject having no significant voxels in the t -maps ROI). Data from this subject is likely to account for much of the standard deviation seen in both techniques.

The Δ CBF values measured with FAIR and PET in all the ROIs during baseline and 4 graded levels of visual stimulation are presented in Figure A3.5. PET data is shown as having much higher standard deviation than FAIR measurements, even when the GM ROIs were used. The group-averaged results seem to provide a better indication of the CBF changes.

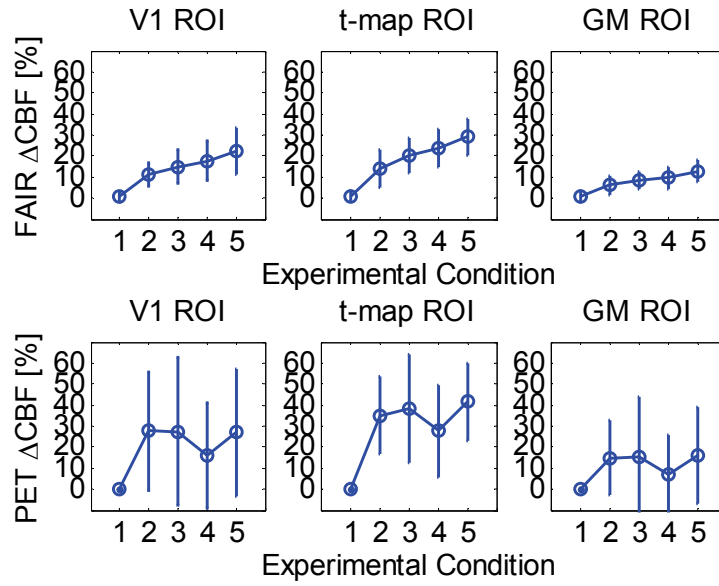


Figure A3.5

fMRI (top) and PET (bottom) CBF percent changes during visual stimulation in the V1, *t*-map and GM ROIs. Error bars represent the standard deviation in the data. Experimental conditions 1 to 5: baseline, 25%, 50%, 75% and 100% intensity checkerboard visual stimulation. The FAIR CBF maps have considerably higher SNRs than PET maps, and there was a consistent monotonic increase in the CBF percent change (Δ CBF) with stimulus intensity in the FAIR data which could not be discerned distinctively in PET given the limited SNR.

Table A3.2

FAIR and PET CBF percent changes averaged over all subjects (mean \pm std), for all conditions (baseline, 4 levels of visual checkerboard (CHB) stimulation, and hypercapnia (HC)), in the V1, *t*-map and GM ROIs. For PET, the baseline percent change was fixed at 0%, since only one baseline volume was acquired.

	Baseline	25% CHB	50% CHB	75% CHB	100% CHB	5% HC
	ΔCBF [%]					
ROI: retinotopically defined VI (mean\pmstd):						
FAIR	0.6 \pm 2.6	11.3 \pm 5.7	15.0 \pm 8.1	17.5 \pm 9.4	22.5 \pm 11.2	8.3 \pm 6.2
PET	0.0 \pm 0.0	27.6 \pm 27.9	27.5 \pm 35.3	16.3 \pm 25.0	26.9 \pm 30.0	8.1 \pm 19.6
ROI: PET and FAIR <i>t</i>-map overlap (mean\pmstd):						
FAIR	1.1 \pm 2.7	14.0 \pm 8.7	20.1 \pm 8.3	23.5 \pm 9.1	29.1 \pm 8.8	10.5 \pm 7.1
PET	0.0 \pm 0.0	35.2 \pm 18.2	38.4 \pm 25.5	27.7 \pm 22.1	41.6 \pm 18.3	15.7 \pm 18.0
ROI: occipital lobe grey matter (mean\pmstd):						
FAIR	0.9 \pm 3.0	6.1 \pm 4.4	8.6 \pm 4.0	9.5 \pm 4.9	12.8 \pm 5.1	7.9 \pm 6.2
PET	0.0 \pm 0.0	15.0 \pm 17.8	15.7 \pm 28.2	7.3 \pm 18.3	16.0 \pm 23.2	9.7 \pm 23.0

Table A3.2 summarizes the FAIR and PET Δ CBF group averages. The FAIR baseline signal value was obtained from the 6-minute baseline data, whereas in PET, since only one baseline volume was obtained, the baseline percent change was fixed at 0%. The regions of activation-induced Δ CBF in both the V1 and t -map ROIs were localized to the expected site of activation. However, as seen in Figure A3.6, the Δ CBF in the GM ROIs are lower, since many less-than-maximally-activated voxels are likely to have been included in the mask. In addition, a post-blurring data resolution of $14 \times 14 \text{ mm}^2$ implies that both GM and WM contribution can be expected in the same voxel, the GM signal intensity thus diminished in both PET and FAIR [357]. We further observed that for all ROIs, increases of FAIR Δ CBF appear to correspond well with increases in visual stimulation intensity, in agreement with previous observations [341]. This was not the case for PET data. Finally, for the hypercapnic condition, Δ CBF in all three ROIs were similar for FAIR and PET.

A3.5.5 Correlation analysis

In Figure A3.6, group-averaged Δ CBF values for baseline and the 4 visual stimulation conditions are shown as dots, while the hypercapnic Δ CBF is represented by a triangle.

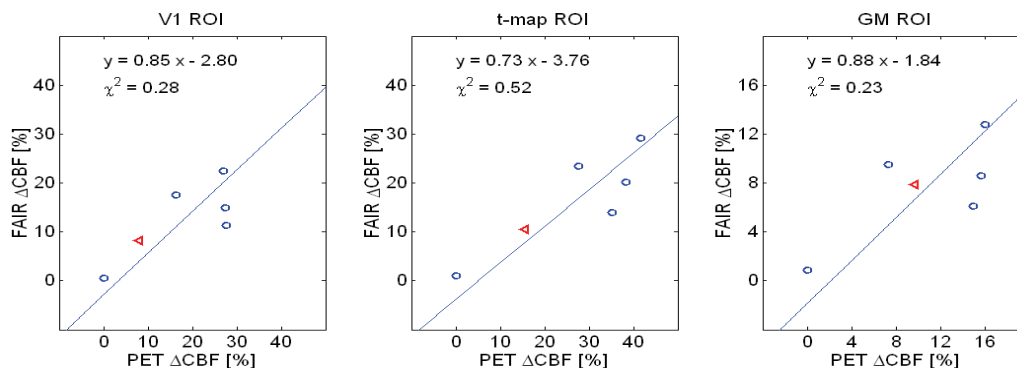


Figure A3.6

Correlation plots of group-average fMRI CBF percent changes with respect to PET CBF changes in the V1, t -map and GM ROIs. The dots represent results from baseline and 4 levels of visual stimulation, and the triangles represent the results for the 5% hypercapnia condition. The equations resulted from the linear fitting of the data, represented by the dotted lines. The hypercapnic Δ CBF measured using PET and MR are similar. In all 3 cases, the χ^2 values have probabilities well within the range of acceptance, and t -test results indicate the slope of the linear fit is not significantly different from unity

The hypercapnic ΔCBF values were quite consistent between PET and MR measurements. Note that for all experimental conditions, higher correlation was seen when comparing the PET and MR group averages (Figure A3.6) than when comparing the two sets of individual subject values (0.76, 0.87, 0.73 vs. 0.45, 0.29, 0.57 for the V1, t -map and GM ROIs, respectively). The line-fitting algorithm used accounted for data variance on both the PET and the ASL axis [357], and the resulting slopes in all 3 ROI types were similar. χ^2 values had high probabilities ($q = 92\%$ - 98%), well below the threshold for rejection of the fit (9.488 for 4 degrees of freedom at $p=0.05$). Furthermore, the two-tailed t -test was used to assess whether the slopes were significantly different from unity. The t -values obtained for all 3 ROIs (-0.10, -0.35 and -0.06 for the V1, t -map and GM ROIs, respectively) suggest that the slopes of the MR-PET linear fits do not differ statistically from unity.

A3.6 Discussion

Arterial spin labeling (ASL)-based perfusion fMRI techniques are fast, non-invasive, have high resolution (temporal and spatial), and are widely accessible. Furthermore, ASL can easily be used in conjunction with other MR techniques to provide information on a variety of physiological parameters in a single session. The goal of this study was to compare PET and FAIR ASL, under conditions extensively used in numerous brain flow-metabolism studies [174, 178, 357, 420]. The FAIR and PET data were fit to a straight line taking into account the variations in both modalities. The resulting slopes were not significantly different from unity, though large standard deviations were associated with the fit. Furthermore, our results showed a consistent monotonic increase in the CBF percent change (ΔCBF) with stimulus intensity in the FAIR CBF data which could not be observed consistently with PET due to its low SNR. On average, FAIR ΔCBF values were slightly lower than those measured with PET under the same conditions. Also, a lower SNR was observed in the FAIR group-average time course, likely due to inter-subject variability and group outliers. Despite these differences, the regional ΔCBF values measured with FAIR were highly correlated with PET measurements.

When comparing PET and fMRI data, a key step was the transformation of both datasets into the same frame of reference and to have the same spatial resolution, since the numerous registration steps could potentially introduce errors. First of all, PET data had to be aligned between runs and also to the surface-coil fMRI data, which was in turn manually registered to the head-coil MR anatomical images through a process susceptible to inter-subject variations. Subsequently, PET and MR scans were transformed into Talairach space along with the chosen ROI masks, allowing for additional image degradation. Moreover, since the fMRI data consisted of a single slice, no blurring could be performed in the slice direction, and hence the slice resolution of the FAIR images did not match that of the PET volume data. In some cases where the fMRI slice may have been positioned above the activated area, PET data would reflect activation while the FAIR data may not, resulting in FAIR Δ CBF values being lower than those of PET. This may be one of the sources of the systematic Δ CBF underestimation using this single-slice FAIR implementation. Furthermore, since the scan sessions were usually on different days, measurements are prone to various intra-subject variations. In fact, intra-subject variability as high as 16% has been reported in the literature for trained subjects [111, 112], and simple factors such as caffeine intake can alter the CBF response. Other sources of errors include subject motion and respiration. PET data were acquired with lower temporal resolution and over longer scan periods, thus the effects of motion would be reduced through data averaging. In addition, as all PET scans were aligned to the first run, the effect of potential movement between runs was greatly reduced. Although this process does not account for motion within runs, the need for in-plane motion correction was reduced due to the use of image blurring. On the other hand, each fMRI image was acquired in <100 ms, and motion could have potentially shifted the location of the activated region out of the ROI mask, resulting in an underestimation of the activation as well as diminished SNR. Complete 3D retrospective motion correction was not possible for the MR data, since the surrounding regions were not scanned, but visual examination suggested minimal displacement between runs or between frames in one run. Nonetheless, for both PET and MR, inter-session positioning differences could result in a slight data misalignment and therefore comparison of slightly shifted brain regions.

An additional source of potential error could originate from the experimental setup. Although the PET experiments were designed to reproduce the conditions found in the MR environment as closely as possible, some elements in the experimental setup were difficult to reproduce. These include factors such as head and mirror orientations, sensory stimulation induced by MR scanner noise and vibration, the presence of arterial and venous lines during the PET experiment, and the duration of the study. Changes in mirror orientation might occur between subjects and scans. While this should not have a large impact on the activation if the subject maintains fixation on the centre, the quality of the subjects' attention could be influenced by the degree of ease with which the stimulus was viewed. Sensory stimulation from the high background noise and vibration in the MR scanner, absent in the PET environment, could have added an additional variability. This factor was, however, previously reported to have little impact on the analysis [357]. On the other hand, in the PET experiments, the stress associated with having an arterial line and multiple injections could also have affected the subject's response. Moreover, the scan durations for PET and fMRI were different; subject motion generally increases during longer scans. In the fMRI experiments, nearly 36 minutes of continuous stimulation was used with no breaks between runs, whereas in PET, the scan sessions were shorter (4 minutes), and the subjects were given breaks, relieving strain on subject attention.

As we mentioned, the dependence of FAIR CBF estimates on transit delay as well as label width has been previously discussed [284, 357]. The transit delay is influenced by the label gap size, and an underestimation of the delay leads to CBF underestimation. The quantification and correction of the underestimation would require ASL acquisitions at several different inversion times for each flow condition. However, such measurements could not be included in this study given the number of graded flow increases being investigated. Instead, in the FAIR implementation used in this study, we made an effort to minimize this influence by using a substantially smaller gap size (3 mm) than typically reported in the literature [357, 407]. In addition, we used body coil transmission to achieve a very large label width, thereby minimizing CBF estimation errors due to labeling slab size.

Finally, it should be noted that while the single-slice FAIR sequence we used did not allow the measurement of absolute CBF, the literature has recently described various quantitative and multi-slice ASL sequences such as Q2TIPS [398] and QUIPSS II with BASSI pulse tagging [100, 118], which would better suit future fMRI studies. Multi-slice perfusion sequences provide a definite advantage when studying large ROIs, reducing the dependence on slice placement, facilitating visualization of global CBF changes, and benefiting the clinical utility of ASL perfusion imaging. In addition, multi-channel acquisitions and higher field strengths can provide higher global SNR while abolishing the need for surface-coil functional scans. This would reduce the number of steps needed for registration of fMRI and PET data by eliminating the subject-dependent manual registration step between head and surface coil anatomical scans. Improved data SNR and reduced post-processing variability would permit further exploration of Δ CBF variation with stimulation intensity.

In recently published studies involving CBF measurements by our group [49, 306], the QUIPSS II technique was employed [100, 118]. However, as stated earlier, the current study was motivated by the need to assess the accuracy and validity of the FAIR method with its known technical limitations, particularly given the importance attached to results published in recent years based on FAIR measurements [101, 174, 357, 408, 409]. In addition, we wanted to address the intense interest in a comprehensive evaluation of the relative quality of perfusion imaging using MRI and PET, the latter being the *de facto* golden standard technique for perfusion imaging. The chief finding of the present study is that there was no significant difference between measurements of CBF change using PET and FAIR under matched levels of graded visual stimulation and hypercapnia. These findings directly support the argument that FAIR, while leaving room for improvement, provides a valid measure of CBF changes under our experimental conditions, characterized by an accuracy well within the range measured using H_2^{15}O PET. The other important observation is that CBF measurements made using PET have a much lower SNR than those made using ASL-fMRI, stresses the immense importance in validating the latter for a wide array of applications.

A3.7 Acknowledgments

We are indebted to Dr. Alain Dagher for his help in the PET protocol. We would like to extend our gratitude to Drs. Plourde, Fiset and Chartrand at the McGill University Health Centre for placing and supervising the arterial lines. We also thank Peter Neelin, Sylvain Milot, Kate Hanratty and Aki Zografos for their help with the data analysis. This work was supported by the Natural Sciences and Engineering Research Council of Canada (NSERC) and the Canadian Institutes of Health Research (CIHR).

Bibliography

1. Levitt, M.H. and R. Freeman, *Compensation for Pulse Imperfections in NMR Spin-echo experiments*. J Magn Reson, 1981. **43**: p. 65-80.
2. Attwell, D. and C. Iadecola, *The neural basis of functional brain imaging signals*. Trends Neurosci, 2002. **25**(12): p. 621-5.
3. Attwell, D. and S.B. Laughlin, *An energy budget for signaling in the grey matter of the brain*. J Cereb Blood Flow Metab, 2001. **21**(10): p. 1133-45.
4. Malonek, D. and A. Grinvald, *Interactions between electrical activity and cortical microcirculation revealed by imaging spectroscopy: implications for functional brain mapping* Science 1996 **272** p. 551-554
5. Hoge, R.D., J. Atkinson, B. Gill, et al., *Investigation of BOLD signal dependence on cerebral blood flow and oxygen consumption: the deoxyhemoglobin dilution model*. Magn Reson Med, 1999. **42**(5): p. 849-63.
6. Buxton, R.B. and L.R. Frank, *A model for the coupling between cerebral blood flow and oxygen metabolism during neural stimulation*. J Cereb Blood Flow Metab, 1997. **17**(1): p. 64-72.
7. Berger, H., *Über das Elektroencephalogramm des Menschen*. Archiv für Psychiatrie und Nervenkrankheiten, 1929. **87**: p. 527-570.
8. Ginsberg, M.D., F. Yoshii, S. Vibusresth, et al., *Human task-specific somatosensory activation*. Neurology, 1987. **37**: p. 1301-8.
9. Brodmann, K., *Beitrage zur histologischen lokalisation der grosshirnrinde Gritte mitteilung: Die rindenfelder der neideren affen* J. Psychol. Neurol. Lpz., 1905(4): p. 177-226.
10. Sorensen, A.G., *Future prospects for fMRI in the clinic*. J Magn Reson Imaging, 2007. **23**: p. 941-4.
11. Leenders, K.L., D. Perani, A.A. Lammertsma, et al., *Cerebral blood flow, blood volume and oxygen utilization*. Brain, 1990. **113**: p. 27-47.
12. Sanelli, P.C., G. Nicola, A.J. Tsiouris, et al., *Reproducibility of postprocessing of quantitative CT perfusion maps*. AJR Am J Roentgenol, 2007. **188**: p. 212-8.
13. Kwong, K.K., J.W. Belliveau, D.A. Chesler, et al., *Dynamic magnetic resonance imaging of human brain activity during primary sensory stimulation*. Proc. Natl. Acad. Sci. USA, 1992. **89**: p. 5675-5679.
14. Ogawa, S., D.W. Tank, R. Menon, et al., *Intrinsic signal changes accompanying sensory stimulation: functional brain mapping with magnetic resonance imaging* Proc Natl Acad Sci U S A., 1992. **89**(13): p. 5951-5.
15. McRobbie, D.W., E.A. Moore, M.J. Graves, et al., *MRI From Picture to Proton*. 2nd ed. 2007, Cambridge: Cambridge University Press.
16. Nishimura, D.G., *Principles of Magnetic Resonance Imaging*. 1996: Stanford University
17. Logothetis, N.K. and B.A. Wandell, *Interpreting the BOLD signal*. Annu Rev Physiol, 2004. **66**: p. 735-69.

18. Duvernoy, H.M., S. Delon and J.L. Vannson, *Cortical blood vessels of the human brain*. Brain Res. Bull, 1981. **7**: p. 519-79.
19. Nolte, J., *The Human Brain: An Introduction to Its Functional Anatomy*. Fourth Edition ed. 1999, St. Louis: Mosby, Inc.
20. Roland, P.E., *Brain Activation* 1993 New York, NY Wiley-Liss 7
21. Gjedde, A., *Brain energy metabolism and haemodynamic response*, in *Functional MRI: An Introduction to Methods*, P. Jezzard, P.M. Matthews, and S.M. Smith, Editors. 2001, Oxford University Press: Oxford.
22. Hamel, E., *Perivascular nerves and the regulation of cerebrovascular tone*. J Appl Physiol, 2006. **100**(3): p. 1059-64.
23. Girouard, H. and C. Iadecola, *Neurovascular coupling in the normal brain and in hypertension, stroke, and Alzheimer disease*. J Appl Physiol, 2006. **100**(1): p. 328-35.
24. Burke, M. and C. Buhrlé, *BOLD response during uncoupling of neuronal activity and CBF*. NeuroImage, 2006. **32**(1): p. 1-8.
25. Zonta, M., M.C. Angulo, S. Gobbo, et al., *Neuron-to-astrocyte signaling is central to the dynamic control of brain microcirculation*. Nat Neurosci, 2003. **6**(1): p. 43-50.
26. Hyder, F., A.B. Patel, A. Gjedde, et al., *Neuronal-glial glucose oxidation and glutamatergic-GABAergic function*. J Cereb Blood Flow Metab, 2006. **26**: p. 865-77.
27. Silver, I.A. and M. Erecinska, *Extracellular glucose concentration in mammalian brain: Continuous monitoring of changes during increased neuronal activity and upon limitation in oxygen supply in normo-, hypo-, and hyperglycemic animals*. J Neurosci, 1994. **14**: p. 5068-76.
28. Buxton, R.B., *Introduction to Functional Magnetic Resonance Imaging*. 2003, Cambridge: Cambridge University Press.
29. Shulman, R.G., F. Hyder and D.L. Rothman, *Cerebral energetics and the glycogen shunt: neurochemical basis of functional imaging*. Proc Natl Acad Sci U S A, 2001. **98**(11): p. 6417-22.
30. Marrett, S. and A. Gjedde, *Changes of blood flow and oxygen consumption in visual cortex of living humans*. Adv. Exp. Med. Biol., 1997. **413**: p. 205-208.
31. Shulman, R.G., F. Hyder and D.L. Rothman, *Lactate efflux and the neuroenergetic basis of brain function*. NMR Biomed, 2001. **14**: p. 389-96.
32. Hyder, F., R.G. Shulman and D.L. Rothman, *A model for the regulation of cerebral oxygen delivery* J Appl Physiol, 1998. **85**: p. 554-564.
33. Hoge, R.D. and G.B. Pike, *Oxidative metabolism and the detection of neuronal activation via imaging*. J Chem Neuroanat, 2001. **22**(1-2): p. 43-52.
34. Ford, M.D., N. Alperin, S.H. Lee, et al., *Characterization of volumetric flow rate waveforms in the normal internal carotid and vertebral arteries*. Physiol Meas, 2005. **26**: p. 477-88.
35. Scheel, P., C. Ruge and M. Schoning, *Flow velocity and flow volume measurements in the extracranial carotid and vertebral arteries in healthy adults: reference data and the effects of age*. Ultrasound Med Biol, 2000. **26**: p. 1261-6.
36. Fahrig, R., H. Nikolov, A.J. Fox, et al., *A three-dimensional cerebrovascular flow phantom*. Med Phys, 1999. **26**: p. 1589-99.

37. Silverthorn, D., *Human Physiology - An Integrated Approach*. 1997, Prentice Hall: Upper Saddle River. p. 453-517.
38. Piechnik, S.K., P.A. Chiarelli and P. Jezzard, *Modelling vascular reactivity to investigate the basis of the relationship between cerebral blood volume and flow under CO₂ manipulation*. NeuroImage, 2008. **39**: p. 107-118.
39. Doepp, F., S.J. Schreiber, T. von Munster, et al., *How does the blood leave the brain? -- A systematic ultrasound analysis of cerebral venous drainage patterns*. Neuroradiol, 2004. **46**: p. 565-70.
40. Hutchinson, E., B. Stefanovic, A. Koretsky, et al., *Spatial flow-volume dissociation of the cerebral microcirculatory response to mild hypercapnia*. NeuroImage, 2006. **32**: p. 520-530.
41. Devor, A., P. Tian, N. Nishimura, et al., *Suppressed neuronal activity and concurrent arteriolar vasoconstriction may explain negative blood oxygenation level-dependent signal*. J Neurosci, 2007. **27**: p. 4452-9.
42. Sanders, J.A. and W.W. Orrison, *Functional magnetic resonance resonance imaging*, in *Functional Brain Imaging*. 1995, Mosby-Year Book, Inc.: St. Louis, MO. p. 250-253.
43. Roy, C.S. and C.S. Sherrington, *On the regulation of the blood supply of the brain*. J Physiol, 1890. **11**: p. 85-105.
44. Raichle, M.E., *Behind the scenes of functional brain imaging: a historical and physiological perspective* Proc Natl Acad Sci U. S. A., 1998. **95**: p. 765-772.
45. Frostig, R.D., E.E. Lieke, D.Y. Tso, et al., *Cortical functional architecture and local coupling between neuronal activity and the microcirculation revealed by in vivo high-resolution optical imaging*. Proc Natl Acad Sci U S A., 1990. **87**(16): p. 6082-6086.
46. Grubb, R.L., M.E. Phelps and J.O. Eichling, *The effects of vascular changes in PaCO₂ on cerebral blood volume, blood flow and vascular mean transit time*. Stroke, 1974. **5**: p. 630-639.
47. Sicard K, S.Q., Brevard ME, Sullivan R, Ferris CF, King JA, Duong TQ., *Regional cerebral blood flow and BOLD responses in conscious and anesthetized rats under basal and hypercapnic conditions: implications for functional MRI studies*. J Cereb Blood Flow Metab, 2003. **23**(4): p. 472-481.
48. Hoge, R.D., B. Gill, J. Atkinson, et al. *Investigation of CMRO₂/CBF coupling in human V1 using fMRI* in *Proceedings of the 4th International Conference on Functional Mapping of the Human Brain*. 1998 Montreal
49. Stefanovic, B., J.M. Warnking, K.M. Rylander, et al., *The effect of global cerebral vasodilation on focal activation hemodynamics*. NeuroImage, 2006. **30**(3): p. 726-34.
50. Lassen, N.A., *Cations as mediators of functional hyperemia in the brain.*, in *Brain Work and Metan Activity: Quantitative Studies with Radioactive Tracers.*, N.A. Lassen, et al., Editors. 1991, Munksgaard: Coperhagen. p. 68-77.
51. Iadecola, C., *Regulation of the cerebral microcirculation during neural activity: is nitric oxide the missing link?* Trends Neurosci, 1993. **16**(6): p. 206-14.
52. Iadecola, C., D.A. Pelligrino, M.A. Moskowitz, et al., *Nitric oxide synthase inhibition and cerebrovascular regulation*. J Cereb Blood Flow Metab, 1994. **14**(2): p. 175-92.

53. Kassissia, I.G., C.A. Goresky, C.P. Rose, et al., *Tracer oxygen distribution is barrier-limited in the cerebral microcirculation*. *Circ. Res.*, 1995. **77**: p. 1201-1211.
54. Gjedde, A., S. Ohta, H. Kuwabara, et al. *Is oxygen diffusion limiting for blood-brain transfer of oxygen?* in *Brain work and mental activity*. 1991. Copenhagen Munksgaard
55. Jones, M., J. Berwick, N. Hewson-Stoate, et al., *The effect of hypercapnia on the neural and hemodynamic responses to somatosensory stimulation*. *NeuroImage*, 2005. **27**(3): p. 609-23.
56. Sanders JA, O.W., *Functional magnetic resonance resonance imaging*, in *Functional Brain Imaging*. 1995, Mosby-Year Book, Inc.: St. Louis, MO. p. 250-253.
57. LeBihan, D., *Diffusion and Perfusion Magnetic Resonance Imaging* 1995 New York Raven Press
58. Hoogenraad, F.G., J.R. Reichenbach, E.M. Haacke, et al., *In vivo measurement of changes in venous blood-oxygenation with high resolution functional MRI at 0.95 Tesla by measuring changes in susceptibility and velocity* *Magn Reson Med*, 1998. **39**(1): p. 97-107.
59. Wright, G.A., B.S. Hu and A. Macovski, *II Rabi Award Estimating oxygen saturation of blood in vivo with MR imaging at 15 T* *J Magn Reson Imaging*, 1991. **1**(3): p. 275-83.
60. Norris, D., *Principles of magnetic resonance assessment of brain function*. *J Magn Reson Imaging* 2006. **23**: p. 794-807.
61. Jensen, J.H. and R. Chandra, *NMR relaxation in tissues with weak magnetic inhomogeneities*. *Magn Reson Med*, 2001. **44**: p. 144-56.
62. Brooks, R.A., *T2-shortening by strongly magnetized spheres: a chemical exchange model*. *Magn Reson Med*, 2002. **47**(2): p. 388-91
63. Stefanovic, B. and G.B. Pike, *Human whole-blood relaxometry at 15 T: Assessment of diffusion and exchange models*. *Magn Reson Med* 2004. **52**(4): p. 716-23.
64. Gardener, A.G., P.A. Gowland and S.T. Francis. *Measuring blood oxygenation at 235 T using a multi-echo sequence* 2004. Proc. 12th ISMRM, Kyoto, Japan.
65. Michaeli, S., D.J. Sorce, D. Idiyatullin, et al., *Transverse relaxation in the rotating frame induced by chemical exchange*. *J Magn Reson*, 2004. **169**(2): p. 293-9.
66. Golay, X., M.J. Silvennoinen, J. Zhou, et al., *Measurement of tissue oxygen extraction ratios from venous blood T2: increased precision and validation of principle*. *Magn Reson Med.* , 2001. **46**(2): p. 282-91.
67. Meyer, B., S. Roricht, H. Graf von Einsiedel, et al., *Inhibitory and excitatory interhemispheric transfers between motor cortical areas in normal humans and patients with abnormalities of the corpus callosum*. *Brain.* , 1995. **118** p. 429-40
68. Huttunen, J.K., O. Grohn and M. Penttonen, *Coupling between simultaneously recorded BOLD response and neuronal activity in the rat somatosensory cortex*. *NeuroImage*, 2008. **39**: p. 775-85.
69. Logothetis, N.K., *The underpinnings of the BOLD functional magnetic resonance imaging signal*. *J Neurosci*, 2003. **23**(10): p. 3963-71.

70. van Zijl, P.C.M., S.M. Eleff, J.A. Ulatowski, et al., *Quantitative assessment of blood flow, blood volume and blood oxygenation effects in functional magnetic resonance imaging*. Nature Medicine 1998. **4**(2): p. 159-67.
71. Sharan, M., M.D. Jones, Jr, R.C. Koehler, et al., *A compartmental model for oxygen transport in brain microcirculation*. Ann. Biomed. Eng., 1989. **17**: p. 13-38.
72. Boxerman, J.L., P.A. Bandettini, K.K. Kwong, et al., *The intravascular contribution to fMRI signal change: Monte Carlo modeling and diffusion-weighted studies in vivo*. Magn Reson Med, 1995. **34**(1): p. 4-10.
73. Norris, D.G., *High field human imaging*. J Magn Reson Imaging 2003. **18**(5): p. 519-29.
74. Kim, S.G., K. Hendrich, X. Hu, et al., *Potential pitfalls of functional MRI using conventional gradient-recalled echo techniques*. NMR Biomed, 1994. **7**(1-2): p. 69-74.
75. Jochimsen, T.H., D.G. Norris, T. Mildner, et al., *Quantifying the intra- and extravascular contributions to spin-echo fMRI at 3 T* Magn Reson Med 2004. **52**(4): p. 724-32
76. Michelich, C.R., A.W. Song and J.R. MacFall, *Dependence of gradient-echo and spin-echo BOLD fMRI at 4 T on diffusion weighting*. NMR Biomed, 2006. **19**: p. 566-72.
77. Yacoub, E., T.Q. Duong, P.F. van De Moortele, et al., *Spin-echo fMRI in humans using high spatial resolutions and high magnetic fields*. Magn Reson Med, 2003. **49**(4): p. 655-64.
78. Bandettini, P.A., K.K. Kwong, T.L. Davis, et al., *Characterization of cerebral blood oxygenation and flow changes during prolonged brain activation* Hum Brain Mapp 1997. **5**(2): p. 93-109
79. Jezzard, P. and S. Clare, *Principles of nuclear magnetic resonance and MRI*, in *Functional MRI: an introduction to methods*, P. Jezzard, P.M. Matthews, and S.M. Smith, Editors. 2001, Oxford University Press: Oxford.
80. Mayhew, J., Y. Zheng, Y. Hou, et al., *Spectroscopic analysis of changes in remitted illumination: the response to increased neural activity in brain*. NeuroImage, 1999. **10**: p. 304-26.
81. Triantafyllou, C., R.D. Hoge, Krueger, et al., *Comparison of physiological noise at 15 T, 3 T and 7 T and optimization of fMRI acquisition parameters*. NeuroImage, 2005. **26**: p. 243-50.
82. Hulvershorn, J., L. Bloy, E.E. Gualtieri, et al., *Spatial sensitivity and temporal response of spin echo and gradient echo bold contrast at 3 T using peak hemodynamic activation time*. NeuroImage, 2004. **24**: p. 216-33.
83. Worsley, K.J., C.H. Liao, J. Aston, et al., *A general statistical analysis for fMRI data*. NeuroImage, 2002. **15**(1): p. 1-15.
84. Kety, S.S. and C.F. Schmidt, *The nitrous oxide method for the quantitative determination of cerebral blood flow in man: theory, procedure and normal values*. J Clin Invest, 1948. **27**: p. 476-83.
85. Raichle, M.E., W.R.W. Martin, P. Herscovitch, et al., *Brain blood flow measured with intravenous H₂O: Implementation and validation*. J Nucl Med, 1983. **24**: p. 790-798.

86. Eastwood, J.D., M.H. Lev, T. Azhari, et al., *CT perfusion scanning with deconvolution analysis: pilot study in patients with acute middle cerebral artery stroke*. Radiology, 2002. **222**: p. 227-36.
87. Østergaard, L., R.M. Weisskoff, D.A. Chesler, et al., *High resolution measurement of cerebral blood flow using intravascular tracer bolus passages Part I: Mathematical approach and statistical analysis* 1996 **36** (5): p. 715-25
88. Østergaard, L., A.G. Sorensen, K.K. Kwong, et al., *High resolution measurement of cerebral blood flow using intravascular tracer bolus passages Part II: Experimental comparison and preliminary results* 1996. **36** (5): p. 726-36
89. Jaszewski, G., G. Strangman, J. Wagner, et al., *Differences in the hemodynamic response to event-related motor and visual paradigms as measured by near-infrared spectroscopy* NeuroImage, 2003. **20**(1): p. 479-88
90. Leung, T.S., I. Tachtsidis, M.M. Tisdall, et al., *Estimating a modified Grubb's exponent in healthy human brains with near infrared spectroscopy and transcranial Doppler*. Physiol Meas, 2009. **30**: p. 1-12.
91. Hoge, R.D., M.A. Franceschini, R.J.M. Covolan, et al., *Simultaneous recording of task-induced changes in blood oxygenation, volume, and flow using diffuse optical imaging and arterial spin-labeling MRI*. NeuroImage, 2005. **25**: p. 701-7.
92. Williams, D.S., J.A. Detre, J.S. Leigh, et al., *Magnetic resonance imaging of perfusion using spin inversion of arterial water* Proc Natl Acad Sci U S A., 1992. **89**(1): p. 212-6.
93. Detre, J.A., J.S. Leigh, D.S. Williams, et al., *Perfusion imaging* Vol. 23. 1992: Metabolic Magnetic Resonance Research Center, University of Pennsylvania School of Medicine, Philadelphia 19104. 37-45.
94. Kwong, K.K., J.W. Belliveau, D.A. Chesler, et al., *Dynamic magnetic resonance imaging of human brain activity during primary sensory stimulation*. Proc Natl Acad Sci U S A., 1992. **89**(12): p. 5675-9.
95. Schwarzbauer, C., S.P. Morrissey and A. Haase, *Quantitative magnetic resonance imaging of perfusion using magnetic labeling of water proton spins within the detection slice*. Magn Reson Med, 1996. **35**(4): p. 540-6.
96. Edelman, R.R., B. Siewert, D.G. Darby, et al., *Qualitative mapping of cerebral blood flow and functional localization with echo-planar MR imaging and signal targeting with alternating radio frequency*. Radiology, 1994. **192**(2): p. 513-20.
97. Kim, S.G., *Quantification of relative cerebral blood flow change by flow-sensitive alternating inversion recovery (FAIR) technique: application to functional mapping*. 1995. **34**(3): p. 293-301.
98. Kwong, K.K., D.A. Chesler, R.M. Weisskoff, et al., *MR perfusion studies with T1-weighted echo planar imaging*. Magn Reson Med, 1995. **34**(6): p. 878-87.
99. Golay, X., J. Hendrikse and T.C. Lim, *Perfusion imaging using arterial spin labeling* Top Magn Reson Imaging 2004. **15**(1): p. 10-27
100. Warnking, J.M. and G.B. Pike, *Reducing contamination while closing the gap: BASSI RF pulses in PASL*. Magn Reson Med, 2006. **55**(4): p. 865-73.
101. Feng, C.M., S. Narayana, J.L. Lancaster, et al., *CBF changes during brain activation: fMRI vs PET*. NeuroImage, 2004. **22**(1): p. 443-6.

102. Wong, E.C., R.B. Buxton and L.R. Frank, *Implementation of quantitative perfusion imaging techniques for functional brain mapping using pulsed arterial spin labeling* NMR Biomed, 1997. **10**: p. 237-249
103. Wong, E.C., R.B. Buxton and L.R. Frank, *Quantitative imaging of perfusion using a single subtraction (QUIPSS and QUIPSS II)*. Magn Reson Med, 1998. **39**(5): p. 702-8.
104. Alsop, D.C. and J.A. Detre, *Reduced transit-time sensitivity in noninvasive magnetic resonance imaging of human cerebral blood flow*. J Cereb Blood Flow Metab, 1996 **16**(6): p. 1236-49.
105. Edelman, R.R., B. Siewert, D.G. Darby, et al., *Qualitative mapping of cerebral blood flow and functional localization with echo-planar MR imaging and signal targeting with alternating radio frequency*. Radiology, 1994 **192**(2): p. 513-20.
106. Perthen, J.E., M. Bydder, K. Restom, et al., *SNR and functional sensitivity of BOLD and perfusion-based fMRI using arterial spin labeling with spiral SENSE at 3 T*. Magn Reson Imaging., 2008. **26**: p. 513-22.
107. Aguirre, G.K., E. Zarahn and D.C. Alsop, *Experimental design and the relative sensitivity of BOLD and perfusion fMRI*. NeuroImage, 2002. **15**: p. 488-500.
108. Luh, W.M., E.C. Wong, P.A. Bandettini, et al., *Comparison of simultaneously measured perfusion and BOLD signal increases during brain activation with T1-based tissue identification*. Magn Reson Med, 2000. **44**(1): p. 137-43.
109. Ye, F.Q., K.F. Berman, T. Ellmore, et al., *H₂¹⁵O PET validation of steady-state arterial spin tagging cerebral blood flow measurements in humans*. Magn Reson Med, 2000. **44**(3): p. 450-6.
110. Lin, W., C.P. Derdeyn, A. Celik, et al., *Regional cerebral blood volume: a comparison between MR and PET in human subjects*. Proceedings of the 6th Meeting of the International Society for Magn Reson Med, 1998.
111. Grandin, C.B., A. Bol, A.M. Smith, et al., *Absolute CBF and CBV measurements by MRI bolus tracking before and after acetazolamide challenge: repeatability and comparison with PET in humans*. NeuroImage, 2005. **26**(2): p. 525-35.
112. Carroll, T.J., V. Teneggi, M. Jobin, et al., *Absolute quantification of cerebral blood flow with magnetic resonance, reproducibility of the method, and comparison with H₂¹⁵O positron emission tomography*. J Cereb Blood Flow Metab, 2002. **22**(9): p. 1149-56.
113. Østergaard, L., D.F. Smith, P. Vestergaard-Poulsen, et al., *Absolute cerebral blood flow and blood volume measured by magnetic resonance imaging bolus tracking: comparison with positron emission tomography values* J Cereb Blood Flow Metab, 1998 **18**(4): p. 425-32.
114. Chen, J.J., M. Wieckowska, E. Meyer, et al., *Cerebral Blood Flow Measurement using fMRI and PET: A Cross-Validation Study*. Int J Biomed Imaging, 2008. **2008**: p. 516359.
115. Hernandez, L., C.A. Branch and J.A. Helpert. *Measurement of CBF with Arterial Spin Labeling: Correlate with Microspheres*. in *Proceedings of the 6th Meeting of the International Society for Magn Reson Med*. 1998. Sydney: Center for Advanced Brain Imaging, The Nathan Kline Institute for Psychiatric Research, Orangeburg, New York, Department of Radiology, Albert Einstein College of

- Medicine, Bronx, New York, and New York University, New York, and Department of Biomedical Engineering, University of North Carolina.
116. Silva, A.C. and S.G. Kim, *Pseudo-continuous arterial spin labeling technique for measuring CBF dynamics with high temporal resolution* Magn Reson Med 1999. **42**(3): p. 425-9
 117. Wang, J., D.C. Alsop, L. Li, et al., *Comparison of quantitative perfusion imaging using arterial spin labeling at 1.5 and 4.0 Tesla* Magn Reson Med, 2002. **48**(2): p. 242-54.
 118. Warnking, J.M. and G.B. Pike, *Bandwidth-modulated adiabatic RF pulses for uniform selective saturation and inversion.* Magn Reson Med 2004. **52**(5): p. 1190-9
 119. Ye, F.Q., J.A. Frank, D.R. Weinberger, et al., *Noise reduction in 3D perfusion imaging by attenuating the static signal in arterial spin tagging (ASSIST).* Magn Reson Med, 2000. **44**: p. 92-108.
 120. Rempp, K.A., G. Brix, F. Wenz, et al., *Quantification of regional cerebral blood flow and volume with dynamic susceptibility contrast-enhanced MR imaging.* . Radiology, 1994. **193**: p. 637-41.
 121. Calamante, F., D.L. Thomas, G.S. Pell, et al., *Measuring cerebral blood flow using magnetic resonance imaging techniques.* J Cereb Blood Flow Metab, 1999. **19**: p. 701-735.
 122. Silvennoinen, M.J., M.I. Kettunen and R.A. Kauppinen, *Effects of hematocrit and oxygen saturation level on blood spin-lattice relaxation.* Magn Reson Med, 2003. **49**(3): p. 568-71.
 123. Lu, H., D.A. Soltysik, B.D. Ward, et al., *Temporal evolution of the CBV-fMRI signal to rat whisker stimulation of variation duration and intensity: a linearity analysis.* NeuroImage, 2005. **26**: p. 432-40.
 124. Sanganahalli, B.G., P. Herman, H. Blumenfeld, et al., *Oxidative neuroenergetics in event-related paradigms.* J Neurosci, 2009. **29**(6): p. 1707-18.
 125. Ferrari, M., D.A. Wilson, D.F. Hanley, et al., *Effects of graded hypotension on cerebral blood flow, blood volume, an dmean transit time in dogs.* Am J Physiol, 1992. **262**: p. H1908-14.
 126. Lee, S.P., T.Q. Duong, G. Yang, et al., *Relative changes of cerebral arterial and venous blood volumes during increased cerebral blood flow: implications for BOLD fMRI.* Magn Reson Med, 2001. **45**(5): p. 791-800.
 127. Hutchison, E.B., B. Stefanovic, A.P. Koretsky, et al., *Spatial flow-volume dissociation of the cerebral microcirculatory response to mild hypercapnia.* NeuroImage, 2006. **32**: p. 520-30.
 128. Toyoda, H., K. Kashikura, T. Okada, et al., *Source of nonlinearity of the BOLD response revealed by simultaneous fMRI and NIRS.* NeuroImage, 2008. **39**: p. 997-1013.
 129. Boas, D.A., T. Gaudette, G. Strangman, et al., *The accuracy of near infrared spectroscopy and imaging during focal changes in cerebral hemodynamics.* NeuroImage, 2003. **13**: p. 76-90.
 130. Stewart, G.N., *Researches on the circulation time in organs and on the influences which affect it.* J Physiol, 1894. **15**: p. parts I-III.

131. Cha, S., *Perfusion MR imaging: basic principles and clinical applications*. Magn Reson Imaging Clin N Am, 2003. **11**(3): p. 403-13.
132. Belliveau, J.W., D.N. Kennedy, R.C. McKinstry, et al., *Functional mapping of the human visual cortex by magnetic resonance imaging*. Science, 1991. **254**(5032): p. 716-9.
133. Dunn, J.F., M.A. Roche, R. Springett, et al., *Monitoring angiogenesis in brain using steady-state quantification of DeltaR2 with MION infusion*. Magn Reson Med, 2004. **51**(1): p. 55-61.
134. Mandeville, J.B., J.J.A. Marota, B.E. Kosofsky, et al., *Dynamic functional imaging of relative cerebral blood volume during rat forepaw stimulation* Magn Reson Med, 1998. **39**: p. 615-624.
135. Zhao, F., P. Wang, K. Hendrich, et al., *Spatial specificity of cerebral blood volume-weighted fMRI responses at columnar resolution*. NeuroImage, 2005. **27**(2): p. 416-24.
136. Lu, H., C.A. Scholl, Y. Zuo, et al., *Quantifying the blood oxygenation level dependent effect in cerebral blood volume -- weighted functional MRI at 9.4 T*. Magn Reson Med, 2007. **58**: p. 616-21.
137. Perles-Barbacaru, A. and H. Lahrech, *A new magnetic resonance imaging method for mapping the cerebral blood volume fraction: the rapid steady-state T1 method*. J Cereb Blood Flow Metab, 2007. **27**: p. 618-31.
138. Zhao, F., P. Wang, K. Hendrich, et al., *Cortical layer-dependent BOLD and CBV responses measured by spin-echo and gradient-echo fMRI: insights into hemodynamic regulation*. NeuroImage, 2006. **30**(4): p. 1149-60.
139. Wu, E.X., K.K. Wong, M. Andrassy, et al., *High-resolution in vivo CBV mapping with MRI in wild-type mice*. Magn Reson Med, 2003. **49**(4): p. 765-70.
140. Wu, G., F. Luo, Z. Li, et al., *Transient relationships among BOLD, CBV, and CBF changes in rat brain as detected by functional MRI*. Magn Reson Med, 2002. **48**(6): p. 987-93.
141. Leite, F.P., D. Tsao, W. Vanduffel, et al., *Repeated fMRI using iron oxide contrast agent in awake, behaving macaques at 3 Tesla*. Neuroimage, 2002. **16**(2): p. 283-94.
142. Keilholz, S.D., A.C. Silva, M. Raman, et al., *BOLD and CBV-weighted functional magnetic resonance imaging of the rat somatosensory system*. Magn Reson Med, 2006. **55**(2): p. 316-24.
143. Scheffler, K., E. Seifritz, R. Haselhorst, et al., *Titration of the BOLD effect: Separation and quantitation of blood volume and oxygenation changes in the human cerebral cortex during neuronal activation and ferumoxide infusion* 1999. **42**: p. 829-836.
144. An, H. and W. Lin, *Cerebral venous and arterial blood volumes can be estimated separately in humans using magnetic resonance imaging*. Magn Reson Med, 2002. **48**(4): p. 583-8.
145. Mandeville, J.B., J.J.A. Marota, C. Ayata, et al. *Evidence for a Cerebral Post-arteriole Windkessel* in *J. Cereb. Blood. Flow Metab.* 1998
146. Herman, P., B.G. Sanganahalli and F. Hyder, *Multimodal measurements of blood plasma and red blood cell volumes during functional brain activation*. J Cereb Blood Flow Metab, 2009. **29**: p. 19-24.

147. Harel, N., J. Lin, S. Moeller, et al., *Combined imaging-histological study of cortical laminar specificity of fMRI signals*. NeuroImage, 2006. **29**: p. 879-887.
148. Lu, H., M. Law, G. Johnson, et al., *Novel approach to the measurement of absolute cerebral blood volume using vascular-space-occupancy magnetic resonance imaging*. Magn Reson Med, 2005. **54**(6): p. 1403-11.
149. Scouten, A. and R.T. Constable, *Application and limitations of whole-brain MAGIC VASO functional imaging*. Magn Reson Med, 2007. **58**: p. 306-15.
150. Scouten, A. and R.T. Constable, *VASO-based calculations the dynamic CSF volume*. Magn Reson Med, 2008. **58**: p. 308-15.
151. Mandeville, J.B., J.J.A. Marota, C. Ayata, et al., *MRI measurement of the temporal evolution of relative CMRO₂ during rat forepaw stimulation* Magn. Reson. Med., 1999. **42** (5): p. 944-951.
152. Lu, H., X. Golay, J.J. Pekar, et al., *Sustained poststimulus elevation in cerebral oxygen utilization after vascular recovery*. J Cereb Blood Flow Metab, 2004. **24**(7): p. 764-70.
153. Kim, T. and S.G. Kim, *Quantification of cerebral arterial blood volume and cerebral blood flow using MRI with modulation of tissue and vessel (MOTIVE) signals*. Magn Reson Med, 2005. **54**(2): p. 333-42.
154. Kim, T., K.S. Hendrich and S.G. Kim, *Functional MRI with magnetization transfer effects: determination of BOLD and arterial blood volume changes*. Magn Reson Med, 2008. **60**: p. 1518-23.
155. Stefanovic, B. and G.B. Pike, *Venous refocusing for volume estimation: VERVE functional magnetic resonance imaging*. Magn Reson Med, 2005. **53**(2): p. 339-47.
156. Wright, G.A., D.G. Nishimura and A. Macovski, *Flow-Independent Magnetic Resonance Angiography*. 1991. **17**: p. 126-140.
157. Thulborn, K.R., J.C. Waterton, P.M. Matthews, et al., *Oxygenation dependence of the transverse relaxation time of water protons in whole blood at high field*. Biochimica et Biophysica Acta, 1982. **714**(2): p. 265-70.
158. Siesjo, B., *Brain Energy Metabolism* 1978 New York Wiley 101-110
159. Herman, P., H.K. Trubel and F. Hyder, *A multiparametric assessment of oxygen efflux from the brain*. J Cereb Blood Flow Metab, 2006. **26**: p. 79-91.
160. Wu, H.M., M. Bergsneider, T.C. Glenn, et al., *Measurement of the global lumped constant for 2-deoxy-2-[18F]fluoro-D-glucose in normal human brain using [15O] water and 2-deoxy-2-[18F]fluoro-D-glucose positron emission tomography imaging. A method with validation based on multiple methodologies*. Mol Imaging Biol, 2003. **5**: p. 32-41.
161. Boas, D.A., G. Strangman, J.P. Culver, et al., *Can the cerebral metabolic rate of oxygen be estimated with near-infrared spectroscopy?* . Phys Med Biol 2003. **48**(15): p. 2405-18
162. Zhu, X.H., N. Zhang, Y. Zhang, et al., *In vivo ¹⁷O NMR approaches for brain study at high field*. NMR Biomed, 2005. **18**: p. 83-103.
163. Du, F., X.H. Zhu, Y. Zhang, et al., *Tightly coupled brain activity and cerebral ATP metabolic rate*. Proc Natl Acad Sci U S A, 2008. **105**: p. 6409-14.
164. Barinaga, M., *What makes brain neurons run?* . Science 1997 **276** p. 196-198

165. Villringer, A., *Understanding functional neuroimaging methods based on neurovascular coupling*. Advances in Experimental Medicine and Biology, 1997. **413**: p. 177-93.
166. Hoge, R.D. and G.B. Pike, *Oxidative metabolism and the detection of neuronal activation via imaging*. 2001 **22**: p. 43-52.
167. Thulborn, K.R., *A BOLD move for fMRI*. Nature Medicine, 1998. **4**(2): p. 155-6.
168. Fox, P.T. and M.E. Raichle, *Focal physiological uncoupling of cerebral blood flow and oxidative metabolism during somatosensory stimulation in human subjects*. Proc Natl Acad Sci U S A., 1986. **83**(4): p. 1140-4.
169. Ohta, S., E. Meyer, C.J. Thompson, et al., *Oxygen consumption of the living human brain measured after a single inhalation of positron emitting oxygen* J Cereb Blood Flow Metab 1991 **12** p. 179-192
170. Fox, P.T., M.E. Raichle, M.A. Mintun, et al., *Nonoxidative glucose consumption during focal physiologic neural activity*. Science, 1988. **241**(4864): p. 462-4.
171. Marrett, S., H. Fujita, E. Meyer, et al., *Stimulus specific increase of oxidative metabolism in human visual cortex in Quantification of Brain Function* 1993 Elsevier Science Publishers p. 217-224
172. Vafaei, M., E. Meyer, S. Marrett, et al. *Frequency-Dependent Changes in Cerebral Metabolic Rate of Oxygen CMRO₂ in the Human Striate Cortex in Proceedings of the Third International Conference on Functional Mapping of the Human Brain*. 1997 Copenhagen
173. Seitz, R.J. and P.E. Roland, *Vibratory Stimulation Increases and Decreases the Regional Cerebral Blood Flow and Oxidative Metabolism: a Positron Emission Tomography (PET) Study* Acta Neurol. Scand., 1992 **86** p. 60-67
174. Davis, T.L., K.K. Kwong, R.M. Weisskoff, et al., *Calibrated functional MRI: Mapping the dynamics of oxidative metabolism* Proc Natl Acad Sci U S A., 1998. **95** p. 1834-1839
175. Hoge, R.D., J. Atkinson, B. Gill, et al., *Linear coupling between cerebral blood flow and oxygen consumption in activated human cortex*. Proc Natl Acad Sci U S A, 1999. **96**(16): p. 9403-8.
176. Hyder, F., R.P. Kennan, N.R. Sibson, et al. *Cerebral Oxygen Delivery In Vivo: NMR Measurements of CBF and CMRO₂ at Different Levels of Brain Activity*. in *Proceedings of the 6th Meeting of the International Society for Magn Reson Med*. 1998. Sydney: Departments of Molecular Biophysics and Biochemistry, Diagnostic Radiology, Psychiatry, and Neurology, Yale University, New Haven Connecticut.
177. Atkinson, J.D., R.D. Hoge, B. Gill, et al. *BOLD, CBF, and CMRO₂ in the Human Primary Motor Cortex*. in *Proceedings of the Sixth International Conference on Functional Mapping of the Human Brain*. 2000 San Antonio
178. Kastrup, A., G. Kruger, T. Neumann-Haefelin, et al., *Changes of cerebral blood flow, oxygenation, and oxidative metabolism during graded motor activation* NeuroImage, 2002. **15**(1): p. 74-82
179. Kim, S.G., E. Rostrup, H.B. Larsson, et al., *Determination of relative CMRO₂ from CBF and BOLD changes: significant increase of oxygen consumption rate during visual stimulation*. Magn Reson Med, 1999. **41**(6): p. 1152-61.

180. Uludag, K., D.J. Dubowitz, E.J. Yoder, et al., *Coupling of cerebral blood flow and oxygen consumption during physiological activation and deactivation measured with fMRI* NeuroImage, 2004. **23**(1): p. 148-55
181. Stefanovic, B., J.M. Warnking and G.B. Pike, *Hemodynamic and metabolic responses to neuronal inhibition* NeuroImage, 2004. **22**(2): p. 771-8
182. Nagaoka, T., F. Zhao, P. Wang, et al., *Increases in oxygen consumption without cerebral blood volume change during visual stimulation under hypotension condition.* J Cereb Blood Flow Metab, 2006. **26**(8): p. 1043-51.
183. Gjedde, A. *Cerebrovascular Disease* 1997 Philadelphia Lippincott-Raven
184. Hudetz, A.G., *Mathematical Model of Oxygen Transport in the Cerebral Cortex* Brain Research 1999. **817**: p. 75-83.
185. Zheng, Y., D. Johnston, J. Berwick, et al., *A three-compartment model of the hemodynamic response and oxygen delivery to brain.* NeuroImage, 2005. **28**(4): p. 925-39.
186. Brown, G.G., L.T. Eyler Zorrilla, B. Georgy, et al., *BOLD and perfusion response to finger-thumb apposition after acetazolamide administration: differential relationship to global perfusion.* J Cereb Blood Flow Metab, 2003. **23**(7): p. 829-37.
187. Cohen, E.R., K. Ugurbil and S.G. Kim, *Effect of basal conditions on the magnitude and dynamics of the blood oxygenation level-dependent fMRI response.* J Cereb Blood Flow Metab 2002. **22**(9): p. 1042-53.
188. Bandettini, P.A., W.M. Luh, T.L. Davis, et al. *Simultaneous Measurement of Cerebral Perfusion and Oxygenation Changes During Neuronal Activation and Hypercapnia in Proceedings of the International Society for Magn Reson Med* 1997
189. Bruhn, H., A. Kleinschmidt, H. Boecker, et al., *The effect of acetazolamide on regional cerebral blood oxygenation at rest and under stimulation as assessed by MRI.* 1994. **14**(5): p. 742-8.
190. Hyder, F., *Neuroimaging with calibrated FMRI.* Stroke, 2004. **35**(11 Suppl 1): p. 2635-41.
191. Zappe, A.C., K. Uludag, A. Oeltermann, et al., *The influence of moderate hypercapnia on neural activity in the anesthetized nonhuman primate.* Cereb Cortex, 2008(Epublished ahead of print).
192. Hoge, R.D., J. Atkinson, B. Gill, et al., *Young Investigator's Rabi Award: Investigation of BOLD signal dependence on cerebral blood flow and oxygen consumption: the deoxyhemoglobin dilution model.* Magn Reson Med, 1999. **42**: p. 849-863.
193. Friston, K.J., P. Fletcher, O. Josephs, et al., *Event-Related fMRI: Characterizing Differential Responses* NeuroImage, 1998 **7** (1): p. 30-40
194. Ances, B.M., E. Zarahn, J.H. Greenberg, et al., *Coupling of neural activation to blood flow in the somatosensory cortex of rats is time-intensity separable, but not linear.* J Cereb Blood Flow Metab, 2000. **20**: p. 921-30.
195. Fujita, N., K. Matsumoto, H. Tanaka, et al., *Quantitative study of changes in oxidative metabolism during visual stimulation using absolute relaxation rates.* NMR Biomed, 2006. **19**(1): p. 60-8.

196. Fujita, N., M. Shinohara, H. Tanaka, et al., *Quantitative mapping of cerebral deoxyhemoglobin content using MR imaging*. NeuroImage, 2003. **20**(4): p. 2071-83.
197. Sicard, K.M. and T.Q. Duong, *Effects of hypoxia, hyperoxia, and hypercapnia on baseline and stimulus-evoked BOLD, CBF, and CMRO2 in spontaneously breathing animals*. NeuroImage, 2005. **25**(3): p. 850-8.
198. Ances, B.M., O. Leontiev, J.E. Perthen, et al., *Regional differences in the coupling of cerebral blood flow and oxygen metabolism changes in response to activation: Implications for BOLD-fMRI*. NeuroImage, 2008. **39**: p. 1510-21.
199. Ito, H., I. Kanno, M. Ibaraki, et al., *Changes in human cerebral blood flow and cerebral blood volume during hypercapnia and hypocapnia measured by positron emission tomography*. J Cereb Blood Flow Metab, 2003. **23**(6): p. 665-70.
200. Ito, H., K. Takahashi, J. Hatazawa, et al., *Changes in human regional cerebral blood flow and cerebral blood volume during visual stimulation measured by positron emission tomography*. J Cereb Blood Flow Metab, 2001. **21**(5): p. 608-12.
201. Kida, I., D.L. Rothman and F. Hyder, *Dynamics of changes in blood flow, volume, and oxygenation: implications for dynamic functional magnetic resonance imaging calibration*. J Cereb Blood Flow Metab, 2007. **27**: p. 690-696.
202. Glover, G.H., *Deconvolution of impulse response in event-related BOLD fMRI*. NeuroImage, 1999. **9**(4): p. 416-29.
203. Handwerker, D.A., J.M. Ollinger and M. D'Esposito, *Variation of BOLD hemodynamic responses across subjects and brain regions and their effects on statistical analyses*. NeuroImage, 2004. **21**(4): p. 1639-51.
204. Bagshaw, A.P., Y. Aghakhani, C.G. Benar, et al., *EEG-fMRI of focal epileptic spikes: analysis with multiple haemodynamic functions and comparison with gadolinium-enhanced MR angiograms* Hum Brain Mapp 2004. **22**(3): p. 179-92
205. Fukuda, M., P. Wang, C.H. Moon, et al., *Spatial specificity of the enhanced dip inherently induced by prolonged oxygen consumption in cat visual cortex: implication for columnar resolution functional MRI*. NeuroImage, 2006. **30**(1): p. 70-87.
206. Menon, R.S., S. Ogawa, X. Hu, et al., *BOLD based functional MRI at 4 Tesla includes a capillary bed contribution: echo-planar imaging correlates with previous optical imaging using intrinsic signals*. Magn Reson Med, 1995. **33**: p. 453-459.
207. Kim, D.S., T.Q. Duong and S.G. Kim, *High-resolution mapping of iso-orientation columns by fMRI*. Nature Neuroscience, 2000. **3**(2): p. 164-9.
208. Martinez, A., F. DiRusso, L. Anllo-Vento, et al., *Putting spatial attention on the map: timing and localization of stimulus selection processes in striate and extrastriate visual areas*. Vision Res, 2001. **41**(10-11): p. 1437-57.
209. Sheth, S.A., M. Nemoto, M. Guiou, et al., *Columnar specificity of microvascular oxygenation and volume responses: implications for functional brain mapping*. J Neurosci, 2004. **24**(3): p. 634-41.
210. Shtoyerman, E., A. Arieli, H. Slovin, et al., *Long-term optical imaging and spectroscopy reveal mechanisms underlying the intrinsic signal and stability of cortical maps in V1 of behaving monkeys*. J Neurosci, 2000. **20**(21): p. 8111-21.

211. Yacoub, E., A. Shmuel, J. Pfeuffer, et al., *Investigation of the initial dip in fMRI at 7 Tesla*. NMR Biomed, 2001. **14**(7-8): p. 408-12.
212. Yacoub, E. and X. Hu, *Detection of the early negative response in fMRI at 15 Tesla* Magn Reson Med 1999. **41**(6): p. 1088-92
213. Buxton, R.B., *The elusive initial dip*. NeuroImage 2001 **13** p. 953-958
214. Vanzetta, I. and A. Grinvald, *Evidence and lack of evidence for the initial dip in the anesthetized rat: implications for human functional brain imaging*. NeuroImage, 2001. **13**(6 Pt 1): p. 959-67.
215. Buxton, R.B., K. Uludag, D.J. Dubowitz, et al., *Modeling the hemodynamic response to brain activation*. NeuroImage, 2004. **23 Suppl 1**: p. S220-33.
216. Hoge, R.D., J. Atkinson, B. Gill, et al., *Stimulus-dependent BOLD and perfusion dynamics in human VI* NeuroImage, 1999. **9**(6 Pt 1): p. 573-85.
217. Nakai, T., K. Matsuo, C. Kato, et al., *Post-stimulus response in hemodynamics observed by functional magnetic resonance imaging—difference between the primary sensorimotor area and the supplementary motor area*. Magn Reson Imaging., 2000. **18**: p. 1215-9.
218. Zhao, F., T. Jin, P. Wang, et al., *Improved spatial localization of post-stimulus BOLD undershoot relative to positive BOLD*. NeuroImage, 2007. **34**: p. 1084-92.
219. Yacoub, E., K. Ugurbil and N. Harel, *The spatial dependence of the poststimulus undershoot as revealed by high-resolution BOLD- and CBV-weighted fMRI*. J Cereb Blood Flow Metab, 2006. **26**(5): p. 634-44.
220. Buxton, R.B., E.C. Wong and L.R. Frank, *Dynamics of blood flow and oxygenation changes during brain activation: the balloon model*. Magn Reson Med, 1998. **39**(6): p. 855-64.
221. Shmuel, A., M. Augath, A. Oeltermann, et al., *Negative functional MRI response correlates with decreases in neuronal activity in monkey visual area VI*. Nat Neurosci, 2006. **9**(4): p. 569-77.
222. Jin, T. and S.G. Kim, *Cortical layer-dependent dynamic blood oxygenation, cerebral blood flow and cerebral blood volume responses during visual stimulation*. NeuroImage, 2008. **43**: p. 1-9.
223. Shen, Q., H. Ren and T.Q. Duong, *CBF, BOLD, CBV, and CMRO2 fMRI signal temporal dynamics at 500-msec resolution*. J Magn Reson Imaging, 2008. **27**: p. 599-606.
224. Gold, L. and M. Lauritzen, *Neuronal deactivation explains decreased cerebellar blood flow in response to focal cerebral ischemia or suppressed neocortical function*. Proc Natl Acad Sci U S A., 2002. **99**: p. 7699-7704.
225. Shmuel, A., E. Yacoub, J. Pfeuffer, et al., *Sustained negative BOLD, blood flow and oxygen consumption response and its coupling to the positive response in the human brain* Neuron, 2002. **36**(6): p. 1195-210
226. Devor, A., I. Ulbert, A.K. Dunn, et al., *Coupling of the cortical hemodynamic response to cortical and thalamic neuronal activity*. Proc Natl Acad Sci U S A., 2005. **102**: p. 3822-7.
227. Kannurpatti, S. and B. Biswall, *Negative functional response to sensory stimulation and its origins*. J Cereb Blood Flow Metab, 2004. **24**: p. 703-712.
228. Logothetis, N.K., J. Pauls, M. Augath, et al., *Neurophysiological investigation of the basis of the fMRI signal*. Nature, 2001. **412**(6843): p. 150-7.

229. Smith, A.T., A.L. Williams and K.D. Singh, *Negative BOLD in the visual cortex: evidence against blood stealing*. Hum Brain Mapp, 2004. **21**: p. 213-20.
230. Raichle, M., A. MacLeod, A. Snyder, et al., *A default mode of brain function*. Proc Natl Acad Sci U S A., 2001. **98**: p. 676-682.
231. Frayne, R., B.G. Goodyear, P. Dickhoff, et al., *Magnetic resonance imaging at 30 Tesla: challenges and advantages in clinical neurological imaging* Invest Radiol 2003. **38**(7): p. 385-402
232. *Environmental Health Criteria 232 -- Static Fields*. 2006, World Healthy Organization.
233. Breger RK, R.A., Fischer ME, Papke RA, Haughton VM., *T1 and T2 measurements on a 1.5-T commercial MR imager*. Radiology, 1989. **171**(1): p. 273-276.
234. Breger RK, W.F., Charles HC, MacFall JR, Haughton VM., *Reproducibility of relaxation and spin-density parameters in phantoms and the human brain measured by MR imaging at 1.5 T*. Magn Reson Med, 1986. **3**(5): p. 649-62.
235. Wansapura, J., S. Holland, R. Dunn, et al., *NMR relaxation times in the human brain at 30 Tesla*. J Magn Reson Imaging, 1999 **9**(4): p. 531-8.
236. Breger, R., A. Rimm, M. Fischer, et al., *T1 and T2 measurements on a 15-T commercial MR imager*. Radiology, 1989. **171**(1): p. 273-276.
237. Breger, R., F. Wehrli, H. Charles, et al., *Reproducibility of relaxation and spin-density parameters in phantoms and the human brain measured by MR imaging at 15 T*. Magn Reson Med, 1986. **3**(5): p. 649-62.
238. Kruger, G., A. Kastrup and G.H. Glover, *Neuroimaging at 15 T and 30 T: comparison of oxygenation-sensitive magnetic resonance imaging*. Magn Reson Med, 2001. **45**(4): p. 595-604.
239. Fischer, H., P. Rinck, Y. van Haverbeke, et al., *Nuclear relaxation of human brain gray and white matter: analysis of field dependence and implications for MRI*. Magn Reson Med, 1990. **16**(2): p. 317-34.
240. Michaeli, S., M. Garwood, X.H. Zhu, et al., *Proton T2 relaxation study of water, N-acetylaspartate, and creatine in human brain using Hahn and Carr-Purcell spin echoes at 4T and 7T*. Magn Reson Med, 2002. **47**(4): p. 629-33.
241. Hennig, J., M. Weigel and K. Scheffler, *Multiecho sequences with variable refocusing flip angles: optimization of signal behavior using smooth transitions between pseudo steady states (TRAPS)*. Magn Reson Med. , 2003. **49**(3): p. 527-35
242. Busse, R.F., H. Hariharan, A. Vu, et al., *Fast spin echo sequences with very long echo trains: design of variable refocusing flip angle schedules and generation of clinical T2 contrast*. Magn Reson Med, 2006. **55**(5): p. 1030-7.
243. Oja, J.M., J. Gillen, R.A. Kauppinen, et al., *Venous blood effects in spin-echo fMRI of human brain* Magn Reson Med 1999. **42**(4): p. 617-26
244. Gati, J.S., R.S. Menon, K. Ugurbil, et al., *Experimental determination of the BOLD field strength dependence in vessels and tissue* 1997. **38**(2): p. 296-302.
245. Brooks, R.A., F. Moiny and P. Gillis, *On T2-shortening by weakly magnetized particles: the chemical exchange model*. Magn Reson Med, 2001. **45**: p. 1014-1021.

246. Yacoub, E., A. Shmuel, J. Pfeuffer, et al., *Imaging brain function in humans at 7 Tesla* Magn Reson Med 2001. **45**(4): p. 588-94
247. Silvennoinen, M.J., C.S. Clingman, X. Golay, et al., *Comparison of the dependence of blood R2 and R2* on oxygen saturation at 15 and 47 Tesla*. Magn Reson Med, 2003. **49**(1): p. 47-60.
248. Matwiyoff, N.A., C. Gasparovic, R. Mazurchuk, et al., *On the origin of paramagnetic inhomogeneity effects in whole blood*. Magn Reson Imaging., 1991. **20**: p. 144-150.
249. Gillis, P., S. Peto, F. Moiny, et al., *Proton transverse nuclear magnetic relaxation in oxidized blood: a numerical approach*. Magn Reson Med, 1995. **33**(1): p. 93-100.
250. Stainsby, J.A. and G.A. Wright, *Monitoring Blood Oxygen State in Muscle Microcirculation With Transverse Relaxation*. Magn Reson Med, 2005. **45**: p. 662-672.
251. Bryant, R.G., K. Marill, C. Blackmore, et al., *Magnetic Relaxation in Blood and Blood Clots*. Magn Reson Med, 1990. **13**: p. 133-144.
252. Matwiyoff NA, Gasparovic C, Mazurchuk R, et al., *On the origin of paramagnetic inhomogeneity effects in whole blood*. Magn Reson Imaging., 1991. **20**: p. 144-150.
253. Meyer, M., O. Yu, B. Eclancher, et al., *NMR relaxation rates and blood oxygenation level*. Magn Reson Med, 1995. **34**: p. 234-241.
254. Zhao, J., C. Clingman, M. Narvainen, et al., *Oxygenation and hematocrit dependence of transverse relaxation rates of blood at 3T*. Magn Reson Med, 2007. **58**: p. 592-596.
255. Sled, J.G. and G.B. Pike, *Correction for B1 and B0 variations in quantitative T2 measurements using MRI*. Magn Reson Med, 2000. **43**(4): p. 589-593.
256. Spees, W.M., D.A. Yablonskiy, M.C. Oswood, et al., *Water proton MR properties of human blood at 15 Tesla: magnetic susceptibility, T1, T2, T2*, and non-Lorentzian signal behavior* Magn Reson Med 2001. **45**(4): p. 533-42
257. Morariu, V., V. Pop, O. Popescu, et al., *Effects of temperature and pH on the water exchange through erythrocyte membrane: nuclear magnetic resonance studies*. J Membr Biol, 1981. **62**: p. 1-5.
258. Dharmakumar, R., J. Hong, J.H. Brittain, et al., *Oxygen-sensitive contrast in blood for steady-state free precession imaging*. Magn Reson Med, 2005. **53**(3): p. 574-83.
259. Kuchel, P., A. Coy and P. Stilbs, *NMR "diffusion-diffraction" of water revealing alignment of erythrocytes in a magnetic field and their dimensions and membrane transport characteristics*. Magn Reson Med, 1997. **37**: p. 637-643.
260. Higashi, T., A. Yamagishi, T. Takeuchi, et al., *Orientation of erythrocytes in a strong static magnetic field*. Blood, 1993. **82**(4): p. 1328-1334.
261. Bottomley, P.A., T.H. Foster, R.E. Argersinger, et al., *A review of normal tissue hydrogen NMR relaxation times and relaxation mechanisms from 1-100 MHz: dependence on tissue type, NMR frequency, temperature, species, excision and age*. 1984. **11**(4): p. 425-448.

262. Whittall, K.P., A.L. MacKay, D.A. Graeb, et al., *In vivo measurement of T2 distributions and water contents in normal human brain*. Magn Reson Med, 1997. **37**(1): p. 34-43.
263. Georgiades, C., R. Itoh, X. Golay, et al., *MR imaging of the human brain at 1.5T: regional variations in transverse relaxation rates in the cerebral cortex*. . AJNR Am J Neuroradiol, 2001. **22**: p. 1732–1737.
264. Ye, F.Q., W.R. Wayne Martin and P.S. Allen, *Estimation of the iron concentration in excised gray matter by means of proton relaxation measurements*. Magn Reson Med, 1996. **35**: p. 285-9.
265. Hirai, T., Y. Korogi, Y. Sakamoto, et al., *T2 shortening in the motor cortex: effect of aging and cerebrovascular diseases*. Radiology 1996. **199**: p. 799–803.
266. Chen, J.C., P.A. Hardy, W. Kucharczyk, et al., *MR of human postmortem brain tissue: correlative study between T2 and assays of iron and ferritin in Parkinson and Huntington disease* AJNR Am J Neuroradiol 1993. **14**(2): p. 275-81
267. Brooks, R., P. Luthert, D. Gadian, et al., *Does signal-attenuation on high-field T2-weighted MRI of the brain reflect regional cerebral iron deposition? Observations on the relationship between regional cerebral water proton T2 values and iron levels*. . J Neurol Neurosurg Psychiatry, 1989. **52**: p. 08–111.
268. Bartha, R., S. Michaeli, H. Merkle, et al., *In vivo H2O T2 measurement in the human occipital lobe at 4T and 7T by Carr-Purcell MRI: detection of microscopic susceptibility contrast*. . Magn Reson Med, 2002. **47**: p. 742–750.
269. Hardy, P.A. and R.M. Henkelman, *Transverse Relaxation Rate Enhancement Caused by Magnetic Particles*. 1989. **7**: p. 265-275.
270. Jensen, J.H., R. Chandra and H. Yu, *Quantitative model for the interecho time dependence of the CPMG relaxation rate in iron-rich gray matter*. Magn Reson Med, 2001. **46**: p. 159-65.
271. Stefanovic, B., J.G. Sled and G.B. Pike, *Quantitative T2 in the occipital lobe: the role of the CPMG refocusing rate*. J Magn Reson Imaging, 2003. **18**(3): p. 302-9.
272. Poon, C.S. and R.M. Henkelman, *Practical T2 quantitation for clinical applications*. Journal of Magnetic Resonance Imaging 1992. **2**(5): p. 541-53.
273. Bezdek, J.C., L.O. Hall and L.P. Clarke, *Review of MR Image Segmentation Techniques Using Pattern Recognition*. Med. Phys., 1993. **20**(4): p. 1033-1048.
274. Duda, R. and P. Hart, *Pattern Classification and Scene Analysis*. 1973: Wiley.
275. Zhou, J., X. Golay and P. van Zijl, *Inverse T2 contrast at 1.5 Tesla between gray matter and white matter in the occipital lobe of normal adult human brain*. . Magn Reson Med, 2001. **46**: p. 401–406.
276. Anderson, C.M., M.J. Kaufman, S.B. Lowen, et al., *Brain T2 relaxation times correlate with regional cerebral blood volume*. MAGMA, 2005. **18**: p. 3-6.
277. McCormick, P.W., M. Steward, M.G. Goetting, et al., *Regional cerebrovascular oxygen saturation measured by optical spectroscopy in humans*. Stroke, 1991. **22**: p. 596-602.
278. Foltz, W.D., N. Merchant, E. Downar, et al., *Coronary venous oximetry using MRI*. Magn Reson Med, 1999. **42**(5): p. 837-48.
279. Lu, H., M. Law, G. Johnson, et al., *Novel approach to the measurement of absolute cerebral blood volume using vascular-space-occupancy magnetic resonance imaging*. Magn Reson Med, 2005. **54**: p. 1403-11.

280. Helenius, J., J. Perkio, L. Soenne, et al., *Cerebral hemodynamics in a healthy population measured by dynamic susceptibility contrast MR imaging*. Acta Radiol, 2003. **44**: p. 538-46.
281. An, H. and W. Lin, *Impact of intravascular signal on quantitative measures of cerebral oxygen extraction and blood volume under normo- and hypercapnic conditions using an asymmetric spin echo approach*. Magn Reson Med, 2003. **50**: p. 708-16.
282. Kaneko, K., Y. Kuwabara, F. Mihara, et al., *Validation of the CBF, CBV, and MTT values by perfusion MRI in chronic occlusive cerebrovascular disease: a comparison with ¹⁵O-PET*. Acad Radiol, 2004. **11**: p. 489-97.
283. Murphy, B.D., A.J. Fox, D.H. Lee, et al., *White matter thresholds for ischemic penumbra and infarct core in patients with acute stroke*. Radiology, 2008. **247**: p. 818-25.
284. Wong, E.C., R.B. Buxton and L.R. Frank, *Implementation of quantitative perfusion imaging techniques for functional brain mapping using pulsed arterial spin labeling* NMR Biomed, 1997 **10** p. 237-249
285. Lu, H., X. Golay, J.J. Pekar, et al., *Functional magnetic resonance imaging based on changes in vascular space occupancy*. Magn Reson Med, 2003. **50**(2): p. 263-74.
286. Lu, H., C. Clingman, X. Golay, et al., *Determining the longitudinal relaxation time (T1) of blood at 30 Tesla*. Magn Reson Med 2004. **52**(3): p. 679-82
287. Kay, I. and R.M. Henkelman, *Practical implementation and optimization of one-shot T1 imaging* Magn Reson Med 1991. **22**(2): p. 414-24
288. Miura, S. and Y. Ichikawa, *Interaction of NADPH-adrenoferreredoxin reductase with NADP+ and adrenoferreredoxin Equilibrium and dynamic properties investigated by proton nuclear magnetic resonance* Journal of Biological Chemistry 1994 **269** (11): p. 8001-6
289. Gomori, J., R. Grossman, C. Yu-IP, et al., *NMR relaxation times of blood: dependence on field strength, oxidation state, and cell integrity*. J comput Assist Tomogr, 1987. **11**: p. 684-690.
290. Wong, E.C., T.T. Liu, W.M. Luh, et al., *T1 and T2 selective method for improved SNR in CSF-attenuated imaging: T2-FLAIR* Magn Reson Med 2001. **45**(3): p. 529-32
291. Sedlacik, J., A. Rauscher and J.R. Reichenbach, *Obtaining blood oxygenation levels from MR signal behavior in the presence of single venous vessels*. Magn Reson Med, 2007. **58**: p. 1035-44.
292. Nagdyman, N., P. Ewert, B. Peters, et al., *Comparison of different near-infrared spectroscopic cerebral oxygenation indices with central venous and jugular venous oxygenation saturation in children*. Pediatr Anesth, 2007. **18**: p. 160-6.
293. Buxton, R.B., K. Miller, L.R. Frank, et al. *BOLD Signal Dynamics: the Balloon Model with Viscoelastic Effects*. 1998. Sydney: Departments of Radiology and Psychiatry, University of California, San Diego and San Diego Supercomputer Center.
294. Kida, I., D.L. Rothman and F. Hyder, *Dynamic of changes in blood flow, volume, and oxygenation: implications for dynamic functional magnetic resonance imaging calibration*. J Cereb Blood Flow Metab, 2007. **27**: p. 690-696.

295. Mandeville, J.B., J.J.A. Marota, C. Ayata, et al., *Evidence for a cerebral postarteriole windkessel with delayed compliance*. J Cereb Blood Flow Metab, 1999. **19**: p. 679-89.
296. Biswal, B., A.G. Hudetz, F.Z. Yetkin, et al., *Hypercapnia Reversibly Suppresses Low-Frequency Fluctuations in the Human Motor Cortex During Rest Using Echo-Planar MRI* Journal of Cerebral Blood Flow and Metabolism 1997 **17** p. 301-308
297. Wang, Z., J.C. Lin, W. Mao, et al., *SAR and temperature: simulations and comparison to regulatory limits for MRI*. J Magn Reson Imaging, 2007. **26**: p. 437-441.
298. Boss, A., H. Graf, A. Berger, et al., *Tissue warming and regulatory responses induced by radio frequency energy deposition on a whole-body 3-Tesla magnetic resonance imager*. J Magn Reson Imaging, 2007. **26**: p. 1334-1339.
299. Chiarelli, P.A., D. Bulte, D. Gallichan, et al., *Flow-metabolism coupling in human visual, motor and supplementary motor areas assessed by magnetic resonance imaging*. Magn Reson Med, 2007. **57**: p. 538-547.
300. Balestrino, M. and G.G. Somjen, *Concentration of carbon dioxide, interstitial pH and synaptic transmission in hippocampal formation of the rat*. J Physiol, 1988. **396**: p. 247-66.
301. Hillman, M.C., A. Devor, M.B. Mouchard, et al., *Depth-resolved optical imaging and microscopy of vascular compartment dynamics during somatosensory stimulation*. NeuroImage, 2007. **35**: p. 89-104.
302. Ances, B., O. Leontiev, J. Perthen, et al., *Regional differences in the coupling of cerebral blood flow and oxygen metabolism changes in response to activation: Implications for BOLD-fMRI*. NeuroImage, 2008. **39**: p. 1510-1521.
303. Chen, J.J. and G.B. Pike. *Dynamic measurement of functional changes in venous blood volume at 3 T*. in *Proceedings of the 15th Meeting of the ISMRM*. 2007. Berlin.
304. Engelbrecht, V., M. Rassek, S. Preiss, et al., *Age-dependent changes in magnetization transfer contrast of white matter in the pediatric brain* Ajnr: American Journal of Neuroradiology 1998 **19** (10): p. 1923-9
305. Chen, J.J. and G.B. Pike, *Human whole blood T2 relaxometry at 3 Tesla*. Magn Reson Med, 2008. **61**: p. 249-54.
306. Stefanovic, B., J.M. Warnking, E. Kobayashi, et al., *Hemodynamic and metabolic responses to activation, deactivation and epileptic discharges*. NeuroImage, 2005. **28**(1): p. 205-15.
307. Sedlacik, J., A. Rauscher and J.R. Reichenbach, *Obtaining blood oxygenation levels from MR signal behavior in the presence of single venous vessels*. Magn Reson Med, 2007. **58**: p. 1035-1044.
308. Nagdyman, N., P. Ewert, B. Peters, et al., *Comparison of different near-infrared spectroscopic cerebral oxygenation indices with central venous and jugular venous oxygenation saturation in children*. Pediatr Anesth, 2007. **18**: p. 160-166.
309. Li, T., T. Haefelin, B. Chan, et al., *Assessment of hemodynamic response during focal neural activity in human using bolus tracking, arterial spin labeling and BOLD techniques*. NeuroImage, 2000. **12**: p. 442-451.

310. Gu, H., H. Lu, F.Q. Ye, et al., *Noninvasive quantification of cerebral blood volume in humans during functional activation*. NeuroImage, 2006. **30**: p. 377-87.
311. Francis, S.T., J.A. Pears, S. Butterworth, et al., *Measuring the change in CBV upon cortical activation with high temporal resolution using Look-Locker EPI and Gd-DTPA*. Magn Reson Med, 2003. **50**: p. 483-492.
312. Zhao, F., T. Jin, P. Wang, et al., *Improved spatial localization of post-stimulus BOLD undershoot relative to positive BOLD*. NeuroImage, 2007. **34**: p. 1084-1092.
313. Kim, T., K.S. Hendrich, K. Masamoto, et al., *Arterial versus total blood volume changes during neural activity-induced cerebral blood flow changes: implication for BOLD fMRI*. J Cereb Blood Flow Metab, 2007. **27**: p. 1235-47.
314. Piechnik, S.K., P.A. Chiarelli and P. Jezzard, *Modelling vascular reactivity to investigate the basis of the relationship between cerebral blood volume and flow under CO₂ manipulation*. NeuroImage, 2008. **39**: p. 107-118.
315. Rostrup, E., G.M. Knudsen, I. Law, et al., *The relationship between cerebral blood flow and volume in humans*. NeuroImage, 2005. **24**: p. 1-11.
316. Hsu, R. and S.T. W., *Analysis of oxygen exchange between arterioles and surrounding capillary-perfused tissue*. J Biomech Eng, 1992. **114**: p. 227-32.
317. Hillman, E.M.C., A. Devor, M.B. Bouchard, et al., *Depth-resolved optical imaging and microscopy of vascular compartment dynamics during somatosensory stimulation*. NeuroImage, 2007. **35**: p. 89-104.
318. Monos, E., *How does the vein wall respond to pressure?* Int. Union Physiol. Sci./Am. Physiol. Soc., 1993. **8**: p. 124-128.
319. Buxton, R.B., E.C. Wong and L.R. Frank, *Dynamics of blood flow and oxygenation changes during brain activation: The balloon model* Magn Reson Med, 1998. **39**(6): p. 855-64.
320. Kuroda, Y., M. Murakami, J. Tsuruta, et al., *Effects of sevoflurane and isoflurane on the ratio of cerebral blood flow/metabolic rate for oxygen in neurosurgery*. J. Anesth., 2000. **14**: p. 124-128.
321. Qiu, M., R. Ramani, M. Swetye, et al., *Anesthetic effects on regional CBF, BOLD, and the coupling between task-induced changes in CBF and BOLD: an fMRI study in normal human subjects*. Magn Reson Med, 2008. **60**: p. 987-96.
322. Krüger, G., A. Kleinschmidt and J. Frahm, *Dynamic MRI sensitized to cerebral blood oxygenation and flow during sustained activation of human visual cortex*. Magn Reson Med, 1996. **35**: p. 797-800.
323. Frahm, J., G. Kruger, K.D. Merboldt, et al., *Dynamic uncoupling and recoupling of perfusion and oxidative metabolism during focal brain activation in man*. Magn Reson Med, 1996. **35**(2): p. 143-8.
324. Donahue, M.J., R.D. Stevens, M. de Boorder, et al., *Hemodynamic changes after visual stimulation and breath holding provide evidence for an uncoupling of cerebral blood flow and volume from oxygen metabolism*. J Cereb Blood Flow Metab, 2009. **29**: p. 176-85.
325. Fransson, P., K.-D.M. Gunnar Kruger and J. Frahm, *MRI of functional deactivation: temporal and spatial characteristics of oxygenation-sensitive responses in human visual cortex* NeuroImage, 1999. **9**: p. 611-618.

326. Jones, R.A., *Origin of the signal undershoot in BOLD studies of the visual cortex.* NMR Biomed, 1999. **12**: p. 299-308.
327. Mildner, T., D.G. Norris, C. Schwarzbauer, et al., *A qualitative test of the balloon model for BOLD-based MR signal changes at 3T* Magn Reson Med 2001. **46**(5): p. 891-9
328. Yacoub, E. and X. Hu, *Detection of the early decrease in fMRI signal in the motor area* Magn Reson Med 2001. **45**(2): p. 184-90
329. Mandeville, J.B., J.J.A. Marota, C. Ayata, et al., *Evidence of a Cerebrovascular Postarteriole Windkessel With Delayed Compliance.* J Cereb Blood Flow Metab, 1999. **19**: p. 679-689.
330. Mandeville, J.B., B.G. Jenkins, B.E. Kosofsky, et al., *Regional sensitivity and coupling of BOLD and CBV changes during stimulation of rat brain.* Magn Reson Med, 2001. **45**(3): p. 443-7.
331. Nakai, T., K. Matsuo, C. Kato, et al., *Post-stimulus response in hemodynamics observed by functional magnetic resonance imaging—difference between the primary sensorimotor area and the supplementary motor area.* Magn Reson Imaging, 2000. **18**: p. 1215-1219.
332. Obata, T., T.T. Liu, K.L. Miller, et al., *Discrepancies between BOLD and flow dynamics in primary and supplementary motor areas: application of the balloon model to the interpretation of BOLD transients* NeuroImage, 2004. **21**(1): p. 144-53
333. Kong, Y., Y. Zheng, D. Johnston, et al., *A model of the dynamic relationship between blood flow and volume changes during brain activation.* J Cereb Blood Flow Metab, 2004. **24**(12): p. 1382-92.
334. Friston, K.J., A. Mechelli, R. Turner, et al., *Nonlinear responses in fMRI: the balloon model, volterra kernels, and other hemodynamics.* NeuroImage, 2000. **12**: p. 466-77.
335. Silva, A.C., A.P. Koretsky and J.H. Duyn, *Functional MRI Impulse Response for BOLD and CBV Contrast in Rat Somatosensory Cortex.* Magn Reson Med, 2007. **57**: p. 1110-1118.
336. Obrig, H., C. Hirth, J.G. Junge-Hulsing, et al., *Cerebral oxygenation changes in response to motor stimulation.* J Appl Physiol, 1996. **81**: p. 1174-83.
337. Kruger, G., A. Kleinschmidt and J. Frahm, *Stimulus dependence of oxygenation-sensitive MRI responses to sustained visual activation* NMR Biomed, 1998. **11**: p. 75-79.
338. Frahm, J., G. Kruger, K.-D. Merboldt, et al., *Dynamic uncoupling and recoupling of perfusion and oxidative metabolism during focal brain activation in man.* Magn Reson Med, 1998. **35**: p. 143-148.
339. Kruger, G., A. Kleinschmidt and J. Frahm, *Dynamic MRI sensitized to cerebral blood oxygenation and flow during sustained activation of human visual cortex.* Magn Reson Med, 1998. **35**: p. 797-800.
340. Frahm, J., J. Baudewig, K. Kallenberg, et al., *The post-stimulation undershoot in BOLD fMRI of human brain is not caused by elevated cerebral blood volume.* NeuroImage, 2008. **40**: p. 473-481.
341. Hoge, R.D., J. Atkinson, B. Gill, et al., *Stimulus-dependent BOLD and perfusion dynamics in human VI.* NeuroImage, 1999. **9**: p. 573-585.

342. Irikura, K., K.I. Maynard and M.A. Moskowitz, *Importance of Nitric Oxide Synthase Inhibition to the Attenuated Vascular Responses Induced by Topical L-Nitroarginine During Vibrissal Stimulation* J. Cereb. Blood. Flow Metab., 1994 **14** p. 45-48
343. Behzadi, Y. and T.T. Liu, *An arteriolar compliance model of the cerebral blood flow response to neural stimulus*. NeuroImage, 2005. **25**: p. 1100-1111.
344. Chen, J.J. and G.B. Pike. *Measuring hemodynamic contributions to the BOLD post-stimulus undershoot*. in *Proceedings of the 14th International Meeting of the Organization for Human Brain Mapping*. 2008. Melbourne.
345. Chen, J.J., K. Advani and G.B. Pike. *Characterization of the BOLD post-stimulus undershoot*. in *Proceedings of the 15th Meeting of the ISMRM*. 2007. Berlin.
346. Chen, J.J., K. Advani and G.B. Pike. *Analysis of the biomechanical origin of the BOLD post-stimulus undershoot*. in *Proceedings of the 13th International Meeting of the Organization for Human Brain Mapping*. 2007. Chicago.
347. MacIntosh, B.J., L.M. Klassen and R.S. Menon, *Transient hemodynamics during a breath hold challenge in a two part functional imaging study with simultaneous near-infrared spectroscopy in adult humans*. NeuroImage, 2003. **20**(2): p. 1246-52.
348. Schroeter, M.L., T. Kupka, T. Mildner, et al., *Investigating the post-stimulus undershoot of the BOLD signal—A simultaneous fMRI and fNIRS study*. NeuroImage, 2006. **30**: p. 349-358.
349. Huppert, T.J., R.D. Hoge, S.G. Diamond, et al., *A temporal comparison of BOLD, ASL, and NIRS hemodynamic responses to motor stimuli in adult humans*. NeuroImage, 2006. **29**: p. 368-382.
350. Jones, M., J. Berwick, D. Johnston, et al., *Concurrent optical imaging spectroscopy and laser-Doppler flowmetry: the relationship between blood flow, oxygenation, and volume in rodent barrel cortex*. NeuroImage, 2001. **13**: p. 1002-1015.
351. Yang, Y., W. Engelen, H. Pan, et al., *A CBF-based event-related brain activation paradigm: characterization of impulse-response function and comparison to BOLD*. NeuroImage, 2000. **12**: p. 287-297.
352. Chen, Y. and T. Parrish. *Is ASL-BOLD equivalent to standard BOLD?* in *13th Annual Meeting of the Organization for Human Brain Mapping*. 2007. Chicago.
353. Ye, F.Q., J.A. Frank, D.R. Weinberger, et al., *Noise reduction in 3D perfusion imaging by attenuating the static signal in arterial spin tagging (ASSIST)*. Magn Reson Med, 2000. **44**: p. 92-100.
354. Cox, R.W., *AFNI: software for analysis and visualization of functional magnetic resonance neuroimages*. Comput Biomed Res, 1996. **29**(3): p. 162-73.
355. Lu, H., M.J. Donahue and P.C.M.v. Zijl, *Detrimental effects of BOLD signal in arterial spin labeling fMRI at high field strength*. Magn Reson Med, 2006. **56**: p. 546-552.
356. Chen, J.J. and G.B. Pike. *Steady-state relationship between cerebral blood flow and venous blood volume*. in *Proceedings of the 16th Meeting of the ISMRM*. 2008. Toronto.

357. Hoge, R.D., J. Atkinson, B. Gill, et al., *Young Investigator's Award: Investigation of BOLD signal dependence on cerebral blood flow and oxygen consumption: the deoxyhemoglobin dilution model*. Magn Reson Med, 1999. **42**: p. 849-863.
358. Leite, F.P., D. Tsao, W. Vanduffel, et al., *Repeated fMRI using iron oxide contrast agent in awake, behaving macaques at 3 Tesla* NeuroImage, 2002. **16**(2): p. 283-94
359. Aubert, A. and R. Costalat, *A model of the coupling between brain electrical activity, metabolism, and hemodynamics: application to the interpretation of functional neuroimaging*. NeuroImage, 2002. **17**: p. 1162-1181.
360. Martindale, J., J. Mayhew, J. Berwick, et al., *The hemodynamic impulse response to a single neural event*. J Cereb Blood Flow Metab, 2003. **23**: p. 546-555.
361. Malonek, D., U. Dirnagl, U. Lindauer, et al., *Vascular imprints of neuronal activity: Relationships between the dynamics of cortical blood flow, oxygenation, and volume changes following sensory stimulation* Proc of the Natl Acad Sci USA, 1997 **94** (26): p. 14826-31
362. Hoge, R.D., M.A. Franceschini, R.J.M. Covolan, et al., *Simultaneous recording of task-induced changes in blood oxygenation, volume, and flow using diffuse optical imaging and arterial spin-labeling MRI*. NeuroImage, 2005. **25**: p. 701-707.
363. Malonek, D., U. Dirnagl, U. Lindauer, et al., *Vascular imprints of neuronal activity: Relationships between the dynamics of cortical blood flow, oxygenation, and volume changes following sensory stimulation* Proc of the Natl Acad Sci USA, 1997. **94**(26): p. 14826-31.
364. Boden, S., H. Obrig, C. Köhncke, et al., *The oxygenation response to functional stimulation: Is there a physiological meaning to the lag between parameters?* NeuroImage, 2007. **36**: p. 100-107.
365. Yang, Y., H. Gu and E.A. Stein, *Simultaneous MRI acquisition of blood volume, blood flow, and blood oxygenation information during brain activation*. Magn Reson Med, 2004. **52**(6): p. 1407-17.
366. Okazawa, H., H. Yamauchi, K. Sugimoto, et al., *Effects of acetazolamide on cerebral blood flow, blood volume, and oxygen metabolism: a positron emission tomography study with healthy volunteers*. J Cereb Blood Flow Metab, 2001. **21**: p. 1472-9.
367. Buckner, R.L., J. Goodman, M. Burock, et al., *Functional-anatomic correlates of object priming in humans revealed by rapid presentation event-related fMRI*. Neuron, 1998. **20**: p. 285-296.
368. Jezzard, P., P.M. Matthews and S.M. Smith, *Functional MRI: An Introduction to Methods*. 2003, Oxford: Oxford University Press, USA.
369. Cavaglia, M., S.M. Dombrowski, J. Drazba, et al., *Regional variation in brain capillary density and vascular response to ischemia*. Brain Res., 2001. **910**: p. 81-93.
370. Duvernoy, H.M., S. Delon and J.L. Vannson, *Cortical blood vessels of the human brain*. Brain Res. Bulletin, 1981. **7**: p. 519-579.
371. Fox, M.D., A.Z. Snyder, D.M. Barch, et al., *Transient BOLD responses at block transitions*. NeuroImage, 2005. **28**: p. 956-966.
372. Vafaei, M.S. and A. Gjedde, *Spatially dissociated flow-metabolism coupling in brain activation*. NeuroImage, 2004. **21**: p. 507-515.

373. Lindauer, U., J. Gethmann, M. Kuhl, et al., *Neuronal activity-induced changes of local cerebral microvascular blood oxygenation in the rat: effect of systemic hyperoxia or hypoxia*. Brain Res., 2003. **975**(1-2): p. 135-40.
374. Huttunen, J.K., O. Gröhn and M. Penttonena, *Coupling between simultaneously recorded BOLD response and neuronal activity in the rat somatosensory cortex*. NeuroImage, 2007. **39**: p. 775-785.
375. Osborne, P.G., *Hippocampal and striatal blood flow during behavior in rats: chronic laser Doppler flowmetry study*. . Physiol. Behav. , 1997. **61**: p. 485-492.
376. Simons, D.J., G.E. Carvell, A.E. Hershey, et al., *Responses of barrel cortex neurons in awake rats and effects of urethane anesthesia*. Exp. Brain Res., 1992. **91**: p. 259-272.
377. Palmer, J., A. de Crespigny, S. Williams, et al., *High-resolution mapping of discrete representational areas in rat somatosensory cortex using blood volume-dependent functional MRI*. NeuroImage, 1999. **9**: p. 383-392.
378. Harel, N., S.P. Lee, T. Nagaoka, et al., *Origin of negative blood oxygenation level-dependent fMRI signals*. J Cereb Blood Flow Metab, 2002. **22**: p. 908-17.
379. Kannurpatti, S.S. and B.B. Biswall, *Negative functional response to sensory stimulation and its origins*. J Cereb Blood Flow Metab, 2004. **24**: p. 703-12.
380. Singh, K.D. and I.P. Fawcett, *Transient and linearly graded deactivation of the human default-mode network by a visual detection task*. NeuroImage, 2008. **41**: p. 100-112.
381. Krainik, A., M. Hund-Georgiadis, S. Zysset, et al., *Regional impairment of cerebrovascular reactivity and BOLD signal in adults after stroke*. Stroke, 2005. **36**: p. 1146-52.
382. Wise, R.D., K. Ide, M.J. Poulin, et al., *Resting fluctuations in arterial carbon dioxide induce significant low frequency variations in BOLD signal*. NeuroImage, 2004. **21**: p. 1652-64.
383. Slessarev, M., J. Han, A. Mardimae, et al., *Prospective targetting and control of end-tidal CO₂ and O₂ concentration*. J Physiol, 2007. **15**: p. 1207-19.
384. Poulin, M.J., P.J. Liang and P.A. Robbins, *Dynamics of the cerebral blood flow response to step changes in end-tidal PCO₂ and PO₂ in humans*. J App Physiol, 1996. **81**: p. 1084-95.
385. Prisman, E., M. Slessarev, J. Han, et al., *Comparison of the effects of independently-controlled end-tidal PCO₂ and PO₂ on blood oxygen level-dependent (BOLD) fMRI*. J Magn Reson Imaging, 2008. **27**: p. 185-91.
386. Donahue, M.J., H. Lu, C.K. Jones, et al., *Theoretical and experimental investigation of the VASO contrast mechanism*. Magn Reson Med, 2006. **56**: p. 1261-73.
387. Scouten, A. and R.T. Constable, *Applications and limitations of whole-brain MAGIC VASO functional imaging*. Magn Reson Med, 2007. **58**: p. 306-15.
388. Lindquist, M.A., C.-H. Zhang, G. Glover, et al., *Rapid three-dimensional functional magnetic resonance imaging of the initial negative BOLD response*. J Magn Reson 2008. **191**: p. 100-11.
389. Hennig, J., M. Weigel and K. Scheffler, *Calculation of flip angles for echo trains with predefined amplitudes with the extended phase graph (EPG)-algorithm*:

- principles and applications to hyperecho and TRAPS sequences.* Magn Reson Med, 2004. **51**: p. 68-80.
390. Tannus, A. and M. Garwood, *Adiabatic pulses.* NMR Biomed, 1997. **10**: p. 423-34.
391. Nelson, T. and S. Tung, *Temperature dependence of proton relaxation times in vivo.* Magn Reson Imaging, 1987. **5**: p. 189-199.
392. D'Arceuil, H., S. Westmoreland and A. de Crespigny, *An approach to high resolution diffusion tensor imaging in fixed primate brain.* NeuroImage, 2007. **35**: p. 553-565.
393. Benga, G., V. Borza, O. Popescu, et al., *Water exchange through erythrocyte membranes: nuclear magnetic resonance studies on resealed ghosts compared to human erythrocytes.* J Membr Biol, 1986. **89**: p. 127-130.
394. Le Bihan, D., J. Delannoy and R.L. Levin, *Temperature mapping with MR imaging of molecular diffusion: application to hyperthermia.* Radiology, 1989. **171**: p. 853-7.
395. Delannoy, J., C.N. Chen, R. Turner, et al., *Noninvasive temperature imaging using diffusion MRI.* Magn Reson Med, 1991. **19**: p. 333-9.
396. Mills, R., *Self-diffusion in normal and heavy water in the range 1-45 °C.* J Phys Chem, 1973. **77**: p. 685-88.
397. Detre, J.A., W. Zhang, D.A. Roberts, et al., *Tissue specific perfusion imaging using arterial spin labeling.* NMR Biomed, 1994. **7**(1-2): p. 75-82.
398. Luh, W.M., E.C. Wong, P.A. Bandettini, et al., *QUIPSS II with thin-slice T1I periodic saturation: a method for improving accuracy of quantitative perfusion imaging using pulsed arterial spin labeling.* 1999. **41**(6): p. 1246-1254.
399. Pasley, B.N., B.A. Inglis and R.D. Freeman, *Analysis of oxygen metabolism implies a neural origin for the negative BOLD response in human visual cortex.* NeuroImage, 2007. **36**: p. 269-276.
400. Zhang, Y., H.K. Song, J. Wang, et al., *Spatially-confined arterial spin-labeling with FAIR.* J Magn Reson Imaging, 2005. **22**: p. 119-124.
401. Walsh, E., K. Minimatsu, J. Leppo, et al., *Radioactive microsphere validation of a volume localized continuous saturation perfusion measurement.* Magn Reson Med, 1994. **31**: p. 147-153.
402. Ewing, J., Y. Cao, R. Knight, et al., *Arterial spin labeling: validity testing and comparison studies.* J Magn Reson Imaging, 2005. **22**: p. 737-740.
403. Østergaard, L., P. Johannsen, P. Host-Poulsen, et al., *Cerebral blood flow measurements by magnetic resonance imaging bolus tracking: comparison with H₂¹⁵O positron emission tomography values.* J Cereb Blood Flow Metab, 1998. **18**: p. 935-940.
404. Lin, W., A. Celik, C. Derdeyn, et al., *Quantitative measurements of cerebral blood flow in patients with unilateral carotid artery occlusion: a PET and MR study.* J Magn Reson Imaging, 2001. **14**(6): p. 659-67.
405. Liu, H.L., P. Kochunov, J. Hou, et al., *Perfusion-weighted imaging of interictal hypoperfusion in temporal lobe epilepsy using FAIR-HASTE: comparison with H₂¹⁵O PET measurements.* Magn Reson Med, 2001. **45**: p. 431-435.

406. Zaini, M.R., S.C. Strother, J.R. Anderson, et al., *Comparison of matched BOLD and FAIR 40T-fMRI with [¹⁵O]water PET brain volumes*. Med Phys, 1999. **26**(8): p. 1559-67.
407. Buxton, R.B., L.R. Frank, E.C. Wong, et al., *A general kinetic model for quantitative perfusion imaging with arterial spin labeling*. Magn Reson Med, 1998. **40**(3): p. 383-96.
408. Kim, S.G. and N.V. Tsekos, *Perfusion imaging by a flow-sensitive alternating inversion recovery (FAIR) technique: application to functional brain imaging*. Magn Reson Med, 1997. **37**(3): p. 425-35.
409. Li, T., M. Moseley and G. Glover, *A FAIR study of motor cortex activation under normo- and hypercapnia induced by breath challenge*. NeuroImage, 1999. **10**(562-9).
410. Vafaei, M.S., E. Meyer, S. Marrett, et al., *Frequency-Dependent Changes in Cerebral Metabolic Rate of Oxygen During Activation of Human Visual Cortex*. J. Cereb. Blood. Flow Metab., 1999 **19** p. 272-277
411. Gemano, G. and E.J. Hoffman, *A study of data loss and mispositioning due to pileup in 2-D detectors in PET*. IEEE Trans. Nucl. Sci., 1990. **37**: p. 671-675.
412. Ollinger, J.M., G.C. Johns and B.M. T., *Model based scatter correction for fully 3D PET*. IEEE Trans. Nucl. Sci. Med. Imaging Conf. San Francisco, 1993: p. 1249-1251.
413. Ranger, N.T., C.J. Thompson and A.C. Evans, *The application of masked orbiting transmission source for attenuation correction in PET*. J. Nucl. Med., 1989. **30**: p. 1056-1068.
414. Hoffman, E.J., T.M. Geurrero, G. Germano, et al., *PET system calibration and correction for quantitative and spatially accurate images*. IEEE Trans. Nucl. Sci., 1989. **36**: p. 1108-1120.
415. Ohta, S., E. Meyer, H. Kuwabara, et al., *Cerebral [¹⁵O] water clearance in humans determined by PET: I Theory and normal values*. J Cereb Blood Flow Metab, 1996.
416. Sereno, M.I., A.M. Dale, J.B. Reppas, et al., *Borders of multiple visual areas in humans revealed by functional magnetic resonance imaging*. Science, 1995. **268**: p. 889-893.
417. Evans, A.C., S. Marrett, P. Neelin, et al., *Anatomical mapping of functional activation in stereotactic coordinate space*. NeuroImage, 1992. **1**(1): p. 43-65.
418. Collins, D.L., P. Neelin, T.M. Peters, et al., *Automatic 3D registration of MR volumetric data in standardized Talairach space*. J Comput Assist Tomogr, 1994. **18**(2): p. 192-205.
419. Woods, R.P., S.R. Cherry and J.C. Mazziotta, *Rapid automated algorithm for aligning and reslicing PET images*. J comput Assist Tomogr, 1992. **16**: p. 620-633.
420. Rostrup, E., I. Lae, M. Blinkenberg, et al., *Regional differences in the CBF and BOLD responses to hypercapnia: a combined PET and fMRI study*. NeuroImage, 2000. **11**(87-97).